

UNITED STATES AIR FORCE
SUMMER RESEARCH PROGRAM -- 1997
SUMMER FACULTY RESEARCH PROGRAM FINAL REPORTS

VOLUME 4A

ROME LABORATORY

RESEARCH & DEVELOPMENT LABORATORIES

5800 Uplander Way

Culver City, CA 90230-6608

Program Director, RDL
Gary Moore

Program Manager, AFOSR
Major Linda Steel-Goodwin

Program Manager, RDL
Scott Licoscas

Program Administrator, RDL
Johnetta Thompson

Program Administrator, RDL
Rebecca Kelly-Clemmons

Submitted to:

AIR FORCE OFFICE OF SCIENTIFIC RESEARCH

Bolling Air Force Base

Washington, D.C.

December 1997

20010319 066

AQ401-06-1193

REPORT DOCUMENTATION PAGE

AFRL-SR-BL-TR-00-

Public reporting burden for this collection of information is estimated to average 1 hour per response, including the time for reviewing instructions, searching existing data sources, gathering the required data, reviewing the collection of information, and completing and reviewing the collection of information. Send comments regarding this burden estimate or any other aspect of this collection of information, including suggestions for reducing the burden, to Washington Headquarters Services, Directorate for Information Operations and Reports, 1215 Jefferson Davis Highway, Suite 1204, Arlington, VA 22202-4302, and to the Office of Management and Budget, Paperwork Project, Washington, DC 20503.

Completing and reviewing this form for information

1. AGENCY USE ONLY (Leave blank)		2. REPORT DATE December, 1997		3. REPORT TYPE AND DATES COVERED	
4. TITLE AND SUBTITLE 1997 Summer Research Program (SRP), Summer Faculty Research Program (SFRP), Final Reports, Volume 4A, Rome Laboratory				5. FUNDING NUMBERS F49620-93-C-0063	
6. AUTHOR(S) Gary Moore					
7. PERFORMING ORGANIZATION NAME(S) AND ADDRESS(ES) Research & Development Laboratories (RDL) 5800 Uplander Way Culver City, CA 90230-6608				8. PERFORMING ORGANIZATION REPORT NUMBER	
9. SPONSORING/MONITORING AGENCY NAME(S) AND ADDRESS(ES) Air Force Office of Scientific Research (AFOSR) 801 N. Randolph St. Arlington, VA 22203-1977				10. SPONSORING/MONITORING AGENCY REPORT NUMBER	
11. SUPPLEMENTARY NOTES					
12a. DISTRIBUTION AVAILABILITY STATEMENT Approved for Public Release				12b. DISTRIBUTION CODE	
13. ABSTRACT (Maximum 200 words) The United States Air Force Summer Research Program (USAF-SRP) is designed to introduce university, college, and technical institute faculty members, graduate students, and high school students to Air Force research. This is accomplished by the faculty members (Summer Faculty Research Program, (SFRP)), graduate students (Graduate Student Research Program (GSRP)), and high school students (High School Apprenticeship Program (HSAP)) being selected on a nationally advertised competitive basis during the summer intersession period to perform research at Air Force Research Laboratory (AFRL) Technical Directorates, Air Force Air Logistics Centers (ALC), and other AF Laboratories. This volume consists of a program overview, program management statistics, and the final technical reports from the SFRP participants at the Rome Laboratory.					
14. SUBJECT TERMS Air Force Research, Air Force, Engineering, Laboratories, Reports, Summer, Universities, Faculty, Graduate Student, High School Student				15. NUMBER OF PAGES	
				16. PRICE CODE	
17. SECURITY CLASSIFICATION OF REPORT Unclassified	18. SECURITY CLASSIFICATION OF THIS PAGE Unclassified	19. SECURITY CLASSIFICATION OF ABSTRACT Unclassified	20. LIMITATION OF ABSTRACT UL		

GENERAL INSTRUCTIONS FOR COMPLETING SF 298

The Report Documentation Page (RDP) is used in announcing and cataloging reports. It is important that this information be consistent with the rest of the report, particularly the cover and title page. Instructions for filling in each block of the form follow. It is important to **stay within the lines** to meet **optical scanning requirements**.

Block 1. Agency Use Only (Leave blank).

Block 2. Report Date. Full publication date including day, month, and year, if available (e.g. 1 Jan 88). Must cite at least the year.

Block 3. Type of Report and Dates Covered. State whether report is interim, final, etc. If applicable, enter inclusive report dates (e.g. 10 Jun 87 - 30 Jun 88).

Block 4. Title and Subtitle. A title is taken from the part of the report that provides the most meaningful and complete information. When a report is prepared in more than one volume, repeat the primary title, add volume number, and include subtitle for the specific volume. On classified documents enter the title classification in parentheses.

Block 5. Funding Numbers. To include contract and grant numbers; may include program element number(s), project number(s), task number(s), and work unit number(s). Use the following labels:

C - Contract	PR - Project
G - Grant	TA - Task
PE - Program Element	WU - Work Unit Accession No.

Block 6. Author(s). Name(s) of person(s) responsible for writing the report, performing the research, or credited with the content of the report. If editor or compiler, this should follow the name(s).

Block 7. Performing Organization Name(s) and Address(es). Self-explanatory.

Block 8. Performing Organization Report Number. Enter the unique alphanumeric report number(s) assigned by the organization performing the report.

Block 9. Sponsoring/Monitoring Agency Name(s) and Address(es). Self-explanatory.

Block 10. Sponsoring/Monitoring Agency Report Number. (If known)

Block 11. Supplementary Notes. Enter information not included elsewhere such as: Prepared in cooperation with....; Trans. of....; To be published in.... When a report is revised, include a statement whether the new report supersedes or supplements the older report.

Block 12a. Distribution/Availability Statement. Denotes public availability or limitations. Cite any availability to the public. Enter additional limitations or special markings in all capitals (e.g. NOFORN, REL, ITAR).

DOD - See DoDD 5230.24, "Distribution Statements on Technical Documents."
DOE - See authorities.
NASA - See Handbook NHB 2200.2.
NTIS - Leave blank.

Block 12b. Distribution Code.

DOD - Leave blank.
DOE - Enter DOE distribution categories from the Standard Distribution for Unclassified Scientific and Technical Reports.
Leave blank.
NASA - Leave blank.
NTIS -

Block 13. Abstract. Include a brief (*Maximum 200 words*) factual summary of the most significant information contained in the report.

Block 14. Subject Terms. Keywords or phrases identifying major subjects in the report.

Block 15. Number of Pages. Enter the total number of pages.

Block 16. Price Code. Enter appropriate price code (*NTIS only*).

Blocks 17. - 19. Security Classifications. Self-explanatory. Enter U.S. Security Classification in accordance with U.S. Security Regulations (i.e., UNCLASSIFIED). If form contains classified information, stamp classification on the top and bottom of the page.

Block 20. Limitation of Abstract. This block must be completed to assign a limitation to the abstract. Enter either UL (unlimited) or SAR (same as report). An entry in this block is necessary if the abstract is to be limited. If blank, the abstract is assumed to be unlimited.

SFRP FINAL REPORT TABLE OF CONTENTS

i-xviii

1. INTRODUCTION	1
2. PARTICIPATION IN THE SUMMER RESEARCH PROGRAM	2
3. RECRUITING AND SELECTION	3
4. SITE VISITS	4
5. HBCU/MI PARTICIPATION	4
6. SRP FUNDING SOURCES	5
7. COMPENSATION FOR PARTICIPATIONS	5
8. CONTENTS OF THE 1996 REPORT	6

APPENDICIES:

A. PROGRAM STATISTICAL SUMMARY	A-1
B. SRP EVALUATION RESPONSES	B-1

SFRP FINAL REPORTS

PREFACE

Reports in this volume are numbered consecutively beginning with number 1. Each report is paginated with the report number followed by consecutive page numbers, e.g., 1-1, 1-2, 1-3; 2-1, 2-2, 2-3.

Due to its length, Volume 4 is bound in two parts, 4A and 4B. Volume 4A contains #1-18. Volume 4B contains reports #19-31. The Table of Contents for Volume 4 is included in both parts.

This document is one of a set of 16 volumes describing the 1997 AFOSR Summer Research Program. The following volumes comprise the set:

<u>VOLUME</u>	<u>TITLE</u>
1	Program Management Report
	<i>Summer Faculty Research Program (SFRP) Reports</i>
2A & 2B	Armstrong Laboratory
3A & 3B	Phillips Laboratory
4A & 4B	Rome Laboratory
5A , 5B & 5C	Wright Laboratory
6	Arnold Engineering Development Center, United States Air Force Academy and Air Logistics Centers
	<i>Graduate Student Research Program (GSRP) Reports</i>
7A & 7B	Armstrong Laboratory
8	Phillips Laboratory
9	Rome Laboratory
10A & 10B	Wright Laboratory
11	Arnold Engineering Development Center, United States Air Force Academy, Wilford Hall Medical Center and Air Logistics Centers
	<i>High School Apprenticeship Program (HSAP) Reports</i>
12A & 12B	Armstrong Laboratory
13	Phillips Laboratory
14	Rome Laboratory
15A & 15B	Wright Laboratory
16	Arnold Engineering Development Center

SRP Final Report Table of Contents

Author	University/Institution Report Title	Armstrong Laboratory Directorate	Vol-Page
R Jean M Andino	University of Florida , Gainesville , FL Atmospheric Reactions of Volatile Paint Components a Modeling Approach	AL/EQL	2- 1
R Anthony R Andrews	Ohio University , Athens , OH Novel Electrochemiluminescence Reactions and Instrumentation	AL/EQL	2- 2
R Stephan B Bach	Univ of Texas at San Antonio , San Antonio , TX Investigation of Sampling Interfaces for Portable Mass Spectrometry and a survey of field Portable	AL/OEA	2- 3
R Marilyn Barger	Florida A&M-FSU College of Engineering , Tallahassee , FL Analysis for The Anaerobic Metabolites of Toulene at Fire Training Area 23 Tyndall AFB, Florida	AL/EQL	2- 4
R Dulal K Bhaumik	University of South Alabama , Mobile , AL The Net Effect of a Covariate in Analysis of Covariance	AL/AOEP	2- 5
R Marc L Carter, PhD, PA	Hofstra University , Hempstead , NY Assessment of the Reliability of Ground Based Observers for the Detecton of Aircraft	AL/OEO	2- 6
R Huseyin M Cekirge	Florida State University , Tallahassee , FL Developing a Relational Database for Natural Attenuation Field Data	AL/EQL	2- 7
R Cheng Cheng	Johns Hopkins University , Baltimore , MD Investigation of Two Statistical Issues in Building a Classification System	AL/HRM	2- 8
R Gerald P Chubb	Ohio State University , Columbus , OH Use of Air Synthetic Forces For GCI Training Exercises	AL/HR1	2- 9.
R Sneed B Collard, Jr.	University of West Florida , Pensacola , FL Suitability of Ascidians as Trace Metal Biosensors-Biomonitors In Marine Environments An Assessment	AL/EQL	2- 10
R Catherine A Cornwell	Syracuse University , Syracuse , NY Rat Ultrasound Vocalization Development and Neurochemistry in Stress-Sensitive Brain Regions	AL/OER	2- 11

SRP Final Report Table of Contents

Author	University/Institution Report Title	Armstrong Laboratory Directorate	Vol-F
DR Baolin Deng	New Mexico Tech , Socorro , NM Effect of Iron Corrosion Inhibitors on Reductive Degradation of Chlorinated Solvents	AL/EQL _____	2-
DR Micheal P Dooley	Iowa State University , Ames , IA Copulatory Response Fertilizing Potential, and Sex Ratio of Offsprings Sired by male rats Ecposed in	AL/OER _____	2-
DR Itiel E Dror	Miami University , Oxford , OH The Effect of Visual Similarity and Reference Frame Alignment on the Recognition of Military Aircraft	AL/HRT _____	2-
DR Brent D Foy	Wright State University , Dayton , OH Advances in Biologivcally-Based Kinetic Modeling for Toxicological Applications	AFRL/HES _____	2-
DR Irwin S Goldberg	St. Mary's Univ , San Antonio , TX Mixing and Streaming of a Fluid Near the Entrance of a Tube During Oscillatory Flow	AL/OES _____	2-
DR Ramesh C Gupta	University of Mainè at Orono , Orono , ME A Dynamical system approach in Biomedical Research	ALOES _____	2-
DR John R Herbold	Univ of Texas at San Antonio , San Antonio , TX A Protocol for Development of Amplicons for a Rapid and Efficient Methoiid of Genotyping Hepatitis C	AL/AOEL _____	2-
DR Andrew E Jackson	Arizona State University , Mesa , AZ Development fo a Conceptual Design for an Information Systems Infrastructure To Support the Squadron	AL/HRA _____	2-
DR Charles E Lance	Univ of Georgia Res Foundation , Athens , GA Replication and Extension of the Schmidt, Hunter, and Outerbridge (1986) Model of Job Performance R	AL/HRT _____	2-
DR David A Ludwig	Univ of N.C. at Greensboro , Greensboro , NC Mediating effect of onset rate on the relationship between+ Gz and LBNP Tolerance	AL/AOCY _____	2-
DR Robert P Mahan	University of Georgia , Athens , GA The Effects of Task Structure on Cognitive Organizing Principles Implaicatins for Complex Display	AL/CFTO _____	2-

Author	University/Institution Report Title	Armstrong Laboratory Directorate	Vol-Page
R Phillip H Marshall	Texas Tech University , Lubbock , TX Preliminary report on the effects of varieties of feedback training on single target time-to-contac	AL/HRM	2- 23
R Bruce V Mutter	Bluefield State College , Bluefield , WV	AL/EQP	2- 24
R Allen L Nagy	Wright State University , Dayton , OH The Detection of Color Breakup In Field Sequential Color Displays	AL/CFHV	2- 25
R Brent L Nielsen	Auburn University , Auburn , AL Rapid PCR Detection of Vancomycin Resistance of Enterococcus Species in infected Urine and Blood	AL/AOEL	2- 26
R Thomas E Nygren	Ohio State University , Columbus , OH Group Differences in perceived importance of swat workload dimensions: Effects on judgment and perf	AL/CFHP	2- 27
R Edward H Piepmeier	Oregon State University , Corvallis , OR	AL/AOHR	2- 28
R Judy L Ratliff	Murray State Univ , Murray , KY Accumulation of Strontium and Calcium by Didemnum Conchyliatum	AL/EQL	2- 29
R Joan R Rentsch	Wright State University , Dayton , OH the Effects of Individual Differences and Team Processed on Team Member Schema Similarity and task P	AL/CFHI	2- 30
R Paul D Retzlaff	Univ of Northern Colorado , Greeley , CO The Armstrong Laboratory Aviation Personality Survey (ALAPS) Norming and Cross - Validation	AL/AOCN	2- 31
R David B Reynolds	Wright State University , Dayton , OH Modeling Heat Flux Through Fabrics Exposed to a Radiant Source and Analysis of Hot Air Burns	AL/CFBE	2- 32
R Barth F Smets	University of Connecticut , Storrs , CT Desorption and Biodegradation of Dinitrotoluenes in aged soils	AL/EQL	2- 33

SRP Final Report Table of Contents

Author	University/Institution Report Title	Phillips Laboratory Directorate	Vol-Pag
DR Graham R Allan	National Avenue , Las Vegas , NM Temporal and Spatial Characterisation of a Synchronously-Pumped Periodically-Poled Lithium Niobate O	PL/LIDD	3-
DR Mark J Balas	Univ of Colorado at Boulder , Boulder , CO Nonlinear Tracking Control for a Precision Deployable Structure Using a Partitioned Filter Approach	PL/SX	3-
DR Mikhail S Belen'kii	Georgia Inst of Technology , Atlanta , GA Multiple Aperture Averaging Technique for Measurement Full Aperture Tilt with a Laser Guide Star and	PL/LIG	3-
DR Gajanan S Bhat	Univ of Tennessee , Knoxville , TN Spinning Hollow Fibers From High Performance Polymers	PL/RK	3-
DR David B Choate	Transylvania Univ , Lexington , KY Blackhole Analysis	PL/VTMR	3-
DR Neb Duric	University of New Mexico , Albuquerque , NM Image Recovery Using Phase Diversity	AFRL/DEB	3-
DR Arthur B Edwards	9201 University City Blvd. , Charlotte , NC Theory of Protons in Buried Oxides	PL/VTMR	3-
DR Gary M Erickson	Boston University , Boston , MA Modeling The Magnetospheric Magnetic Field	PL/GPSG	3-
DR Hany A Ghoneim	Rochester Inst of Technol , Rochester , NY Focal Point Accuracy Assessment of an Off-Axis Solar Concentrator	PL/RKES	3-
DR Subir Ghosh	Univ of Calif, Riverside , Riverside , CA Designing Propulsion Reliability of Space Launch Vehicles	PL/RKBA	3- 1
DR George W Hanson	Univ of Wisconsin - Milwaukee , Milwaukee , WI Asymptotic analysis of the Natural system modes of coupled bodies in the large separation, Low-Frequency	AFRL/DEH	3- 1

SRP Final Report Table of Contents

Author	University/Institution Report Title	Phillips Laboratory Directorate	Vol-Page
DR Brian D Jeffs	Brigham Young University , Provo , UT Blind Bayesian Restoration of Adaptive Optics Images Using Generalized Gaussian Markov Random Field	AFRL/DES _____	3- 12
DR Christopher H Jenkins	S Dakota School of Mines/Tech , Rapid City , SD Mechnics of Surface Precosion for Membrane Reflectors	PL/VTVS _____	3- 13
DR Dikshitulu K Kalluri	University of Lowell , Lowell , MA Mode Conversion in a Time-Varying Magnetoplasma Medium	PL/GPID _____	3- 14
DR Aravinda Kar	University of Central Florida , Orlando , FL Measurement of the Cutting Performance of a High Beam Quality Chemical Oxygen-Iodine Laser on Aerosp	AFRL/DEO _____	3- 15
DR Bernard Kirtman	Univ of Calif, Santa Barbara , Santa Barbara , CA Quantum Chemical Characterization of the elctronic Structure and Reactions of Silicon Dangling Bon	PL/VTMR _____	3- 16
DR Spencer P Kuo	Polytechnic University , Farmingdale , NY Excitation of Oscillating Two Stream Instability by Upper Hybrid Pump Waves in Ionospheric Heating	PL/GPI _____	3- 17
DR Henry A Kurtz	Memphis State University , Memphis , TN H2 Reactions at Dangling Bonds in SiO2	PL/VTMR _____	3- 18
DR Min-Chang Lee	Massachusetts Inst of Technology , Cambridge , MA Laboratory Studies of Ionospheric Plasma Effects Produced by Lightning-induced Whistler Waves	PL/GPSG _____	3- 19
DR Donald J Leo	University of Toledo , Toledo , OH Microcontroller-Based Implementation of Adaptive Structural Control	AFRL/VSD _____	3- 20
DR Hua Li	University of New Mexico , Albuquerque , NM	PL/LIDD _____	3- 21
DR Hanli Liu	Univ of Texas at Arlington , Arlington , TX Expermental Validation of Three-Dimensional Reconstruction of Inhomogenety Images in Turbid Media	AFRL/DEB _____	3- 22

SRP Final Report Table of Contents

Author	University/Institution Report Title	Phillips Laboratory Directorate	Vol-Pa
DR M. Arfin K Lodhi	Texas Tech University , Lubbock , TX Thermoelectric Energy Conversion with solid Electrolytes	PL/VTRP	3-
DR Tim C Newell	University of New Mexico , Albuquerque , NM Study of Nonlinear Dynamics in a Diode Pumped Nd:YAG laser	PL/LIGR	3-
DR Michael J Pangia	Georgia College & State University , Milledgeville , GA Preparatory Work Towards a Computer Simulation of Electron beam Operations on TSS 1	PL/GPSG	3-
DR Vladimir O Papitashvili	Univ of Michigan , Ann Arbor , MI Modeling of Ionospheric Convectin from the IMF and Solar Wind Data	PL/GPSG	3-
DR Jaime Ramirez-Angulo	New Mexico State University , Las Cruces , NM	PL/VTMR	3-
DR Louis F Rossi	University of Lowell , Lowell , MA Analysis of Turbulent Mixing in the Stratosphere & Troposphere	PL/GPOL	3-
DR David P Stapleton	University of Central Oklahoma , Edmond , OK Atmospheric Effects Upon Sub-Orbital Boost glide Spaceplane Trajectories	PL/RKBA	3-
DR Jenn-Ming Yang	Univ of Calif, Los Angeles , Los Angeles , CA Thermodynamic Stability and Oxidation Behavior of Refractory (Hf, Ta, Zr) Carbide/boride Composites	PL/RKS	3-

SRP Final Report Table of Contents

Author	University/Institution Report Title	Rome Laboratory Directorate	Vol-Page
DR A. F Anwar	University of Connecticut , Storrs , CT Properties of Quantum Wells Formed In AlGaIn/GaN Heterostructures	RL/ERAC	4- 1
DR Milica Barjaktarovic	Wilkes University , Wilkes Barre , PA Assured Software Design: Privacy Enhanced Mail (PEM) and X.509 Certificate Specification	AFRL/IFG	4- 2
DR Stella N Batalama	SUNY Buffalo , Buffalo , NY Adaptive Robust Spread-Spectrum Receivers	AFRL/IFG	4- 3
DR Adam W Bojanczyk	Cornell University , Ithaca , NY Lowering the Computational Complexity of Stap Radar Systems	RL/OCSS	4- 4
DR Nazeih M Botros	So. Illinois Univ-Carbondale , Carbondale , IL A PC-Based Speech Synthesizing Using Sinusoidal Transform Coding (STC)	RL/ERC-1	4- 5
DR Nikolaos G Bourbakis	SUNY Binghamton , Binghamton , NY Eikones-An Object-Oriented Language For Image Analysis & Process	AFRL/IF	4- 6
DR Peter P Chen	Louisiana State University , Baton Rouge , LA Reconstructing the information Warfare Attack Scenario Guessing what Actually Had Happened Based on	RL/CA-II	4- 7
DR Everett E Crisman	Brown University , Providence , RI A Three-Dimensional, Dielectric Antenna Array Re-Configurable By Optical Wavelength Multiplexing	RL/ERAC	4- 8
DR Digendra K Das	SUNYIT , Utica , NY A Study of the Emerging Diagnostic Techniques in Avionics	RL/ERSR	4- 9
DR Venugopala R Dasigi	Southern Polytechnic State Univ , Marietta , GA Information Fusion for text Classification-an Experimental Comparison	AFRL/IFT	4- 10
DR Richard R Eckert	SUNY Binghamton , Binghamton , NY Enhancing the Rome Lab ADII virtual environment system	AFRL/IFSA	4- 11

SRP Final Report Table of Contents

Author	University/Institution Report Title	Rome Laboratory Directorate	Vol-P
DR Micheal A Fiddy	University of Lowell, Lowell, MA Target Identification from Limited Backscattered Field Data	RL/ERCS	4-
DR Lili He	Nothern Illinois University, Dekalb, IL the Study of Caaractreistics of CdS Passivation on InP	RL/EROC	4-
DR Edem Ibragimov	Michigan Tech University, Houghton, MI Effects of Surface Scattering in 3-D Optical Mass Storage	RL/IRAP	4-
DR Phillip G Kornreich	Syracuse University, Syracuse, NY Analysis of Optically Active Material Layer Fibers	RL/OCPA	4-
DR Kuo-Chi Lin	University of Central Florida, Orlando, FL A Study on The Crowded Airspace Self Organized Criticality	AFRL/IFSB	4-
Dr. Beth L Losiewicz	Colorado College, Colorado Spring, CO The Miami Corpus Latin American Dialect Database continued Research and Documentation	RL/IRAA	4-
DR John D Norgard	Univ of Colorado at Colorado Springs, Colorado Spring, CO Microwave Holography using Infrared Thermograms of Electromagnetic Fields	RL/ERST	4-
DR Jeffrey B Norman	Vassar College, Poughkeepsie, NY Gain Spectra of Beam-Coupling In Photorefractive Semiconductors	RL/OCPA	4-
DR Dimitrios N Pados	State Univ. of New York Buffalo, Buffalo, NY Joint Domain Space-Time Adaptive Processing w/Small Training Data Sets	AFRL/SNR	4-
DR Brajendra N Panda	University of North Dakota, Grand Forks, ND A Model to Attain Data Integrity After System Invasion	AFRL/IFG	4-
DR Michael A Pittarelli	SUNY OF Tech Utica, Utica, NY Phase Transitions in probability Estimation and Constraint Satisfaction Problems	AFRL/IFT	4-

SRP Final Report Table of Contents

Author	University/Institution Report Title	Rome Laboratory Directorate	Vol-Page
R Salahuddin Qazi	SUNY OF Tech Utica , Utica , NY Low Data rate Multimedia Communication Using Wireless Links	RL/IWT	4- 24
R Arindam Saha	Mississippi State University , Mississippi State , MS An Implementationa of the message passing Interface on Rtems	RL/OCSS	4- 25
R Ravi Sankar	University of South Florida , Tampa , FL A Study of Integrated and Intelligent Network Management	RL/C3BC	4- 26
R Mark S Schmalz	University of Florida , Gainesville , FL Errors inherent in Reconstruction of Targets From multi-Look Imagery	AFRL/IF	4- 27
R John L Stensby	Univ of Alabama at Huntsville , Huntsville , AL Simple Real-time Tracking Indicator for a Frequency Feedback Demodulator	RL/IRAP	4- 28
R Micheal C Stinson	Central Michigan University , Mt. Pleasant , MI Destructive Objects	RL/CAII	4- 29
R Donald R Ucci	Illinois Inst of Technology , Chicago , IL Simulation of a Robust Locally Optimum Receiver in correlated Noise Using Autoregressive Modeling	RL/C3BB	4- 30
R Nong Ye	Arizona State University , Tempe , AZ A Process Engineering Approach to Continuous Command and Control on Security-Aware Computer Networks	AFRL/IFSA	4- 31

SRP Final Report Table of Contents

Author	University/Institution Report Title	Wright Laboratory Directorate	Vol-Pa
DR William A Baeslack	Ohio State University , Columbus , OH	WL/MLLM _____	5-
DR Bhavik R Bakshi	Ohio State University , Columbus , OH Modeling of Materials Manufacturing Processes by Nonlinear Continuum Regression	WL/MLIM _____	5-
DR Brian P Beecken	Bethel College , St. Paul , MN Contribution of a Scene Projector's Non-Uniformity to a Test Article's Output Image Non-Uniformity	AFRL/MN _____	5-
DR John H Beggs	Mississippi State University , Mississippi State , MS The Finite Element Method in Electromagnetics For Multidisciplinary Design	AFRL/VA _____	5-
DR Kevin D Belfield	University of Detroit Mercy , Detroit , MI Synthesis of Novel Organic Compounds and Polymers for two Photon Asorption, NLO, and Photorefractive	WL/MLBP _____	5-
DR Raj K Bhatnagar	University of Cincinnati , Cincinnati , OH A Study of Intra-Class Variability in ATR Systems	AFRL/SN _____	5-
DR Victor M Birman	Univ of Missouri - St. Louis , St Louis , MO Theoretical Foundations for Detection of Post-Processing Cracks in Ceramic Matrix Composites Based o	WL/FIBT _____	5-
DR Gregory A Blaisdell	Purdue University , West Lafayette , IN A Review of Benchmark Flows for Large Eddy Simulation	AFRL/VA _____	5-
DR Octavia I Camps	Pennsylvania State University , University Park , PA MDL Texture Segmentation Compressed Images	WL/MNGA _____	5-
DR Yiding Cao	Florida International Univ , Miami , FL A Feasibility Study of Turbine Disk Cooling by Employing Radially Rotating Heat Pipes	WL/POTT _____	5- 1
DR Reaz A Chaudhuri	University of Utah , Salt Lake City , UT A Novel Compatibility/Equilibrium Based Iterative Post-Processing Approach For Axisymmetric brittle	WL/MLBM _____	5- 1

SRP Final Report Table of Contents

Author	University/Institution Report Title	Wright Laboratory Directorate	Vol-Page
DR Mohamed F Chouikha	Howard University , Washington , DC Detection Techniques Use in Forward-Looking Radar Signal Processing a Literature Review	WL/AAMR _____	5- 12
DR Milton L Cone	Embry-Riddle Aeronautical University , Prescott , AZ Scheduling in the Dynamic System Simulation Testbed	WL/AACF _____	5- 13
DR Robert C Creese	West Virginia University , Morgantown , WV Feature Based Cost Modeling	WL/MTI _____	5- 14
DR William Crossley	Purdue University , West Lafayette , IN Objects and Methods for Aircraft Conceptual Design and Optimization in a Knowledge-Based Environment	WL/FIBD _____	5- 15
DR Gene A Crowder	Tulane University , New Orleans , LA Vibrational Analysis of some High-Energy Compounds	WL/MNM _____	5- 16
DR Richard W Darling	University of South Florida , Tampa , FL Geometrically Invariant NonLinear recursive Filters, with Application to Target Tracking	WL/MNAG _____	5- 17
DR Robert J DeAngelis	Univ of Nebraska - Lincoln , Lincoln , NE Quantitative Description of Wire Textures In Cubic Metals	WL/MNM _____	5- 18
DR Bill M Diong	Pan American University , Edinburg , TX Analysis and Control Design for a Novel Resonant DC-DC Converter	WL/POOC _____	5- 19
DR John K Douglass	University of Arizona , Tucson , AZ Guiding Missiles "On The Fly:" Applications of Neurobiological Principles to Machine Vision For Arms	AFRL/MN _____	5- 20
DR Mark E Eberhart	Colorado School of Mines , Golden , CO Modeling The Charge Redistribution Associated with Deformation and Fracture	WL/MLLM _____	5- 21
DR Gregory S Elliott	Rutgers:State Univ of New Jersey , Piscataway , NJ On the Development of Planar Doppler Velocimetry	WL/POPT _____	5- 22

Author	University/Institution Report Title	Wright Laboratory Directorate	Vol-Pag
DR Elizabeth A Ervin	University of Dayton , Dayton , OH Eval of the Pointwise K-2 Turbulence Model to Predict Transition & Separtion in a Low Pressure	WL/POTT	5- 2
DR Altan M Ferendeci	University of Cincinnati , Cincinnati , OH Vertically Interconnected 3D MMICs with Active Interlayer Elements	WL/AADI	5- 2
DR Dennis R Flentge	Cedarville College , Cedarville , OH Kinetic Study of the Thermal Decomposition of t-Butylphenyl Phosphate Using the System for Thermal D	WL/POSL	5- 2
DR George N Frantziskonis	University of Arizona , Tucson , AZ Multiscale Material Characterization and Applications	WL/MLLP	5- 2
DR Zewdu Gebeyehu	Tuskegee University , Tuskegee , AL Synthesis and Characterization of Metal-Xanthic Acid and -Amino Acid Complexes Useful Ad Nonlinear	WL/MLPO	5- 2
DR Richard D Gould	North Carolina State U-Raleigh , Raleigh , NC Reduction and Analysis of LDV and Analog Raw Data	WL/POPT	5- 2
DR Michael S Grace	University of Virginia , Charlottesville , VA Structure and Function of an Extremely Sensitive Biological Infrared Detector	WL/MLPJ	5- 2
DR Gary M Graham	Ohio University , Athens , OH Indicial Response Model for Roll Rate Effects on A 65-Degree Delta wing	WL/FIGC	5- 3
DR Allen G Greenwood	Mississippi State University , Mississippi Sta , MS An Object-Based approach for Integrating Cost Assessment into Product/Process Design	WL/MTI	5- 3
DR Rita A Gregory	Georgia Inst of Technology , Atlanta , GA Range Estimating for Research and Development Alternatives	WL/FIVC	5- 3
DR Mark T Hanson	University of Kentucky , Lexington , KY Anisotropy in Epic 96&97: Implementation and Effects	WL/MNM	5- 3

SRP Final Report Table of Contents

author	University/Institution Report Title	Wright Laboratory Directorate	Vol-Page
DR Majeed M Hayat	University of Dayton , Dayton , OH A Model for Turbulence and Photodetection Noise in Imaging	WL/AAJT	5- 34
DR Larry S Helmick	Cedarville College , Cedarville , OH NMA Study of the Decomposition Reaction Path of Demnum fluid under Tribological Conditions	WL/MLBT	5- 35
DR William F Hosford	Univ of Michigan , Ann Arbor , MI INTENSITY OF [111]AND [100] TEXTURAL COMPONENTS IN COMPRESSION-FORGED TANTALUM	AFRL/MN	5- 36
DR David E Hudak	Ohio Northern University , Ada , OH A Study fo a Data-Parallel Imlementation of An Implicit Solution fo the 3D Navier-Stokes Equations	WL/FIMC	5- 37
DR David P Johnson	Mississippi State University , Mississippi , MS An Innovative Segmented Tugsten Penetrating Munition	WL/MNAZ	5- 38
DR Ismail I Jouny	Lafayette College , Easton , PA	WL/AACT	5- 39
DR Edward T Knobbe	Oklahoma State University , Stillwater , OK Organically Modified silicate Films as Corrosion Resistant Treatments for 2024-T3 Alumium Alloy	WL/MLBT	5- 40
DR Seungug Koh	University of Dayton , Dayton , OH Numerically Efficinet Direct Ray Tracing Algorithms for Automatic Target Recognition using FPGAs	WL/AAST	5- 41
DR Ravi Kothari	University of Cincinnati , Cincinnati , OH A Function Approximation Approach for Region of Interest Selection in synthetic Aperture Radar Image	WL/AACA	5- 42
DR Douglas A Lawrence	Ohio University , Athens , OH On the Analysis and Design of Gain scheduled missile Autopilots	WL/MNAG	5- 43
DR Robert Lee	Ohio State University , Columbus , OH Boundary Conditions applied to the Finite Vlume Time Domain Method for the Solution of Maxwell's Equ	WL/FIM	5- 44

SRP Final Report Table of Contents

Author	University/Institution Report Title	Wright Laboratory Directorate	Vol-I
DR Junghsen Lich	Wright State University , Dayton , OH Develop an Explosive Simulated Testing Apparatus for Impact Physics Research at Wright Laboratory	WL/FIV	5-
DR James S Marsh	University of West Florida , Pensacola , FL Distortion Compensation and Elimination in Holographic Reocnstruction	WL/MNSI	5-
DR Mark D McClain	Cedarville College , Cedarville , OH A Molecular Orbital Theory Analysis of Oligomers of 2,2'-Bithiazole and Partially Reduced 3,3'-Dimet	WL/MLBP	5-
DR William S McCormick	Wright State University , Dayton , OH Some Observations of Target Recognition Using High Range Resolution Radar	WL/AACR	5-
DR Richard O Mines	University of South Florida , Tampa , FL Testing Protocol for the Demilitarization System at the Eglin AFB Herd Facility	WLMN/M	5-
DR Dakshina V Murty	University of Portland , Portland , OR A Useful Benchmarking Method in Computational Mechanics, CFD, adn Heat Tansfer	WL/FIBT	5-
DR Krishna Naishadham	Wright State University , Dayton , OH	WL/MLPO	5-
DR Serguei Ostapenko	University of South Florida , Tampa , FL	WL/MLPO	5-
DR Yi Pan	University of Dayton , Dayton , OH Improvement of Cache Utilization and Parallel Efficiency of a Time-Dependnet Maxwell Equation Solver	AFRL/VA	5-
DR Rolfe G Petschek	Case Western Reserve Univ , Cleveland , OH AB INITIO AUANTUM CHEMICAL STUDIES OF NICKEL DITHIOLENE COMPLEX	WL/MLPJ	5-
DR Kishore V Pochiraju	Stevens Inst of Technology , Hoboken , NJ Refined Reissner's Variational Solution in the Vicinity of Stress Singularities	AFRL/ML	5-

SRP Final Report Table of Contents

Author	University/Institution Report Title	Wright Laboratory Directorate	Vol-Page
R Muhammad M Rahman	University of South Florida , Tampa , FL Computation of Free Surface Flows with Applications in Capillary Pumped Loops, Heat Pipes, and Jet I	WL/POOB _____	5- 56
R Mateen M Rizki	Wright State University , Dayton , OH Classification of High Range Resolution Radar Signatures Using Evolutionary Computation	WL/AACA _____	5- 57
R Shankar M Sastry	Washington University , St Louis , MO	WL/MLLM _____	5- 58
R Martin Schwartz	University of North Texas , Denton , TX Computational Studies of Hydrogen Abstraction From Haloalkanes by the Hydroxyl Radical	WL/MLBT _____	5- 59
R Rathinam P Selvam	Univ of Arkansas , Fayetteville , AR Computation of Nonlinear Viscous Panel Flutter Using a Full-Implicit Aeroelastic Solver	WL/FIMC _____	5- 60
R Yuri B Shtessel	Univ of Alabama at Huntsville , Huntsville , AL Smoothed Sliding Mode control Approach For Addressing Actuator Deflection and Deflection Rate Saturation	AFRL/VA _____	5- 61
R Mario Sznajder	Pennsylvania State University , University Park , PA Suboptimal Control of Nonlinear Systems via Receding Horizon State Dependent Riccati Equations	WL/MNAG _____	5- 62
R Barney E Taylor	Miami Univ. - Hamilton , Hamilton , OH Photoconductivity Studies of the Polymer 6FPBO	WLMLBP _____	5- 63
R Joseph W Tedesco	Auburn University , Auburn , AL high Velocity Penetration of Layered Concrete Targets with Small Scale Ogive-nose Steel projectiles	WL/MNSA _____	5- 64
R Krishnaprasad Thirunarayan	Wright State University , Dayton , OH A VHDL MODEL SYNTHESIS APPLET IN TCL/TK	WL/AAST _____	5- 65

SRP Final Report Table of Contents

Author	University/Institution Report Title	Wright Laboratory Directorate	Vol-P:
DR Karen A Tomko	Wright State University , Dayton , OH Grid Level Parallelization of an Implicit Solution of the 3D Navier-Stokes Equations	WL/FIMC _____	5-
DR Max B Trueblood	University of Missouri-Rolla , Rolla , MO A Study of the Particulate Emissions of a Well-Stirred Reactor	WL/POSC _____	5-
DR Chi-Tay Tsai	Florida Atlantic University , Boca Raton , FL Dislocation Dynamics in Heterojunction Bipolar Transistor Under Current Induced Thermal St	WL/AA _____	5-
DR John L Valasek	Texas A&M University , College Station , TX Two Axis Pneumatic Vortex Control at High Speed and Low Angle-of-Attack	WL/FIMT _____	5-
DR Mitch J Wolff	Wright State University , Dayton , OH An Experimental and Computational Analysis of the Unsteady Blade Row Potential Interaction in a Tr	WL/POTF _____	5-
DR Rama K Yedavalli	Ohio State University , Columbus , OH Improved Aircraft Roll Maneuver Performance Using Smart Deformable Wings	WL/FIBD _____	5-

Author	University/Institution Report Title	Arnold Engineering Development Center Directorate	Vol-Page
R Csaba A Biegl	Vanderbilt University , Nashville , TN Parallel processing for Turbine Engine Modeling and Test Data validation	AEDC/SVT _____	6- 1
R Frank G Collins	Tennessee Univ Space Institute , Tullahoma , TN Design of a Mass Spectrometer Sampling Probe for The AEDC Impulse Facility	AEDC _____	6- 2
R Kenneth M Jones	N Carolina A&T State Univ , Greensboro , NC	AEDC/SVT _____	6- 3
R Kevin M Lyons	North Carolina State U-Raleigh , Raleigh , NC Velocity Field Measurements Using Filtered-Rayleigh Scattering	AEDC/SVT _____	6- 4
R Gerald J Micklow	Univ of Alabama at Tuscaloosa , Tuscaloosa , AL	AEDC/SVT _____	6- 5
DR Michael S Moore	Vanderbilt University , Nashville , TN Extension and Installation of the Model-Integrated Real-Time Imaging System (Mirtis)	AEDC/SVT _____	6- 6
DR Robert L Roach	Tennessee Univ Space Institute , Tullahoma , TN Investigation of Fluid Mechanical Phenomena Relating to Air Injection Between the Segments of an Arc	AEDC _____	6- 7
DR Nicholas S Winowich	University of Tennessee , Knoxville , TN	AEDC _____	6- 8
DR Daniel M Knauss	Colorado School of Mines , Golden , CO Synthesis of salts With Delocalized Anions For Use as Third Order Nonlinear Optical Materials	USAFA/DF _____	6- 9
DR Jeffrey M Bigelow	Oklahoma Christian Univ of Science & Art , Oklahoma City , OK Raster-To-Vector Conversion of Circuit Diagrams: Software Requirements	OCALC/TI _____	6- 10

SRP Final Report Table of Contents

Author	University/Institution Report Title	Arnold Engineering Development Center Directorate	Vol-P
DR Paul W Whaley	Oklahoma Christian Univ of Science & Art , Oklahoma City , OK A Probabilistic framework for the Analysis of corrosion Damage in Aging Aircraft	OCALC/L _____	6- _____
DR Bjong W Yeigh	Oklahoma State University , Stillwater , OK Logistics Asset Management : Models and Simulations	OCALC/TI _____	6- _____
DR Michael J McFarland	Utah State University , Logan , UT Delisting of Hill Air Force Base's Industrial Wastewater Treatment Plant Sludge	OC-ALC/E _____	6- _____
DR William E Sanford	Colorado State University , Fort Collins , CO Nuerical Modeling of Physical Constraints on in-Situ Cosolvent Flushing as a Groundwater Remedial Op	OO-ALC/E _____	6- _____
DR Sophia Hassiotis	University of South Florida , Tampa , FL Fracture Analysis of the F-5, 15%-Spar Bolt	SAALC/TI _____	6- 1
DR Devendra Kumar	CUNY-City College , New York , NY A Simple, Multiversion Concurrency Control Protocol For Internet Databases	SAALC/LD _____	6- 1
DR Ernest L McDuffie	Florida State University , Tallahassee , FL A Propossed Exjpert System for ATS Capability Analysis	SAALC/TI _____	6- 1
DR Prabhaker Mateti	Wright State University , Dayton , OH How to Provide and Evaluate Computer Network Security	SMALC/TI _____	6- 1
DR Mansur Rastani	N Carolina A&T State Univ , Greensboro , NC Optimal Structural Design of Modular Composite bare base Shelters	SMALC/L _____	6- 1
DR Joe G Chow	Florida International Univ , Miami , FL Re-engineer and Re-Manufacture Aircraft Sstructural Components Using Laser Scanning	WRALC/TI _____	6- 2

1. INTRODUCTION

The Summer Research Program (SRP), sponsored by the Air Force Office of Scientific Research (AFOSR), offers paid opportunities for university faculty, graduate students, and high school students to conduct research in U.S. Air Force research laboratories nationwide during the summer.

Introduced by AFOSR in 1978, this innovative program is based on the concept of teaming academic researchers with Air Force scientists in the same disciplines using laboratory facilities and equipment not often available at associates' institutions.

The Summer Faculty Research Program (SFRP) is open annually to approximately 150 faculty members with at least two years of teaching and/or research experience in accredited U.S. colleges, universities, or technical institutions. SFRP associates must be either U.S. citizens or permanent residents.

The Graduate Student Research Program (GSRP) is open annually to approximately 100 graduate students holding a bachelor's or a master's degree; GSRP associates must be U.S. citizens enrolled full time at an accredited institution.

The High School Apprentice Program (HSAP) annually selects about 125 high school students located within a twenty mile commuting distance of participating Air Force laboratories.

AFOSR also offers its research associates an opportunity, under the Summer Research Extension Program (SREP), to continue their AFOSR-sponsored research at their home institutions through the award of research grants. In 1994 the maximum amount of each grant was increased from \$20,000 to \$25,000, and the number of AFOSR-sponsored grants decreased from 75 to 60. A separate annual report is compiled on the SREP.

The numbers of projected summer research participants in each of the three categories and SREP "grants" are usually increased through direct sponsorship by participating laboratories.

AFOSR's SRP has well served its objectives of building critical links between Air Force research laboratories and the academic community, opening avenues of communications and forging new research relationships between Air Force and academic technical experts in areas of national interest, and strengthening the nation's efforts to sustain careers in science and engineering. The success of the SRP can be gauged from its growth from inception (see Table 1) and from the favorable responses the 1997 participants expressed in end-of-tour SRP evaluations (Appendix B).

AFOSR contracts for administration of the SRP by civilian contractors. The contract was first awarded to Research & Development Laboratories (RDL) in September 1990. After completion of the

1990 contract, RDL (in 1993) won the recompetition for the basic year and four 1-year options.

2. PARTICIPATION IN THE SUMMER RESEARCH PROGRAM

The SRP began with faculty associates in 1979; graduate students were added in 1982 and high school students in 1986. The following table shows the number of associates in the program each year.

YEAR	SRP Participation, by Year			TOTAL
	SFRP	GSRP	HSAP	
1979	70			70
1980	87			87
1981	87			87
1982	91	17		108
1983	101	53		154
1984	152	84		236
1985	154	92		246
1986	158	100	42	300
1987	159	101	73	333
1988	153	107	101	361
1989	168	102	103	373
1990	165	121	132	418
1991	170	142	132	444
1992	185	121	159	464
1993	187	117	136	440
1994	192	117	133	442
1995	190	115	137	442
1996	188	109	138	435
1997	148	98	140	427

Beginning in 1993, due to budget cuts, some of the laboratories weren't able to afford to fund as many associates as in previous years. Since then, the number of funded positions has remained fairly constant at a slightly lower level.

3. RECRUITING AND SELECTION

The SRP is conducted on a nationally advertised and competitive-selection basis. The advertising for faculty and graduate students consisted primarily of the mailing of 8,000 52-page SRP brochures to chairpersons of departments relevant to AFOSR research and to administrators of grants in accredited universities, colleges, and technical institutions. Historically Black Colleges and Universities (HBCUs) and Minority Institutions (MIs) were included. Brochures also went to all participating USAF laboratories, the previous year's participants, and numerous individual requesters (over 1000 annually).

RDL placed advertisements in the following publications: *Black Issues in Higher Education*, *Winds of Change*, and *IEEE Spectrum*. Because no participants list either *Physics Today* or *Chemical & Engineering News* as being their source of learning about the program for the past several years, advertisements in these magazines were dropped, and the funds were used to cover increases in brochure printing costs.

High school applicants can participate only in laboratories located no more than 20 miles from their residence. Tailored brochures on the HSAP were sent to the head counselors of 180 high schools in the vicinity of participating laboratories, with instructions for publicizing the program in their schools.

High school students selected to serve at Wright Laboratory's Armament Directorate (Eglin Air Force Base, Florida) serve eleven weeks as opposed to the eight weeks normally worked by high school students at all other participating laboratories.

Each SFRP or GSRP applicant is given a first, second, and third choice of laboratory. High school students who have more than one laboratory or directorate near their homes are also given first, second, and third choices.

Laboratories make their selections and prioritize their nominees. AFOSR then determines the number to be funded at each laboratory and approves laboratories' selections.

Subsequently, laboratories use their own funds to sponsor additional candidates. Some selectees do not accept the appointment, so alternate candidates are chosen. This multi-step selection procedure results in some candidates being notified of their acceptance after scheduled deadlines. The total applicants and participants for 1997 are shown in this table.

1997 Applicants and Participants			
PARTICIPANT CATEGORY	TOTAL APPLICANTS	SELECTEES	DECLINING SELECTEES
SFRP	490	188	32
(HBCU/MI)	(0)	(0)	(0)
GSRP	202	98	9
(HBCU/MI)	(0)	(0)	(0)
HSAP	433	140	14
TOTAL	1125	426	55

4. SITE VISITS

During June and July of 1997, representatives of both AFOSR/NI and RDL visited each participating laboratory to provide briefings, answer questions, and resolve problems for both laboratory personnel and participants. The objective was to ensure that the SRP would be as constructive as possible for all participants. Both SRP participants and RDL representatives found these visits beneficial. At many of the laboratories, this was the only opportunity for all participants to meet at one time to share their experiences and exchange ideas.

5. HISTORICALLY BLACK COLLEGES AND UNIVERSITIES AND MINORITY INSTITUTIONS (HBCU/MIs)

Before 1993, an RDL program representative visited from seven to ten different HBCU/MIs annually to promote interest in the SRP among the faculty and graduate students. These efforts were marginally effective, yielding a doubling of HBCU/MI applicants. In an effort to achieve AFOSR's goal of 10% of all applicants and selectees being HBCU/MI qualified, the RDL team decided to try other avenues of approach to increase the number of qualified applicants. Through the combined efforts of the AFOSR Program Office at Bolling AFB and RDL, two very active minority groups were found, HACU (Hispanic American Colleges and Universities) and AISES (American Indian Science and Engineering Society). RDL is in communication with representatives of each of these organizations on a monthly basis to keep up with the their activities and special events. Both organizations have widely-distributed magazines/quarterlies in which RDL placed ads.

Since 1994 the number of both SFRP and GSRP HBCU/MI applicants and participants has increased ten-fold, from about two dozen SFRP applicants and a half dozen selectees to over 100 applicants and two dozen selectees, and a half-dozen GSRP applicants and two or three selectees to 18 applicants and 7 or 8 selectees. Since 1993, the SFRP had a two-fold applicant increase and a two-fold selectee increase. Since 1993, the GSRP had a three-fold applicant increase and a three to four-fold increase in selectees.

In addition to RDL's special recruiting efforts, AFOSR attempts each year to obtain additional funding or use leftover funding from cancellations the past year to fund HBCU/MI associates. This year, 5 HBCU/MI SFRPs declined after they were selected (and there was no one qualified to replace them with). The following table records HBCU/MI participation in this program.

SRP HBCU/MI Participation, By Year				
YEAR	SFRP		GSRP	
	Applicants	Participants	Applicants	Participants
1985	76	23	15	11
1986	70	18	20	10
1987	82	32	32	10
1988	53	17	23	14
1989	39	15	13	4
1990	43	14	17	3
1991	42	13	8	5
1992	70	13	9	5
1993	60	13	6	2
1994	90	16	11	6
1995	90	21	20	8
1996	119	27	18	7

6. SRP FUNDING SOURCES

Funding sources for the 1997 SRP were the AFOSR-provided slots for the basic contract and laboratory funds. Funding sources by category for the 1997 SRP selected participants are shown here.

1997 SRP FUNDING CATEGORY	SFRP	GSRP	HSAP
AFOSR Basic Allocation Funds	141	89	123
USAF Laboratory Funds	48	9	17
HBCU/MI By AFOSR (Using Procured Addn'l Funds)	0	0	N/A
TOTAL	9	98	140

SFRP - 188 were selected, but thirty two canceled too late to be replaced.

GSRP - 98 were selected, but nine canceled too late to be replaced.

HSAP - 140 were selected, but fourteen canceled too late to be replaced.

7. COMPENSATION FOR PARTICIPANTS

Compensation for SRP participants, per five-day work week, is shown in this table.

1997 SRP Associate Compensation

PARTICIPANT CATEGORY	1991	1992	1993	1994	1995	1996	1997
Faculty Members	\$690	\$718	\$740	\$740	\$740	\$770	\$770
Graduate Student (Master's Degree)	\$425	\$442	\$455	\$455	\$455	\$470	\$470
Graduate Student (Bachelor's Degree)	\$365	\$380	\$391	\$391	\$391	\$400	\$400
High School Student (First Year)	\$200	\$200	\$200	\$200	\$200	\$200	\$200
High School Student (Subsequent Years)	\$240	\$240	\$240	\$240	\$240	\$240	\$240

The program also offered associates whose homes were more than 50 miles from the laboratory an expense allowance (seven days per week) of \$50/day for faculty and \$40/day for graduate students. Transportation to the laboratory at the beginning of their tour and back to their home destinations at the end was also reimbursed for these participants. Of the combined SFRP and GSRP associates, 65 % (194 out of 286) claimed travel reimbursements at an average round-trip cost of \$776.

Faculty members were encouraged to visit their laboratories before their summer tour began. All costs of these orientation visits were reimbursed. Forty-three percent (85 out of 188) of faculty associates took orientation trips at an average cost of \$388. By contrast, in 1993, 58 % of SFRP associates took

orientation visits at an average cost of \$685; that was the highest percentage of associates opting to take an orientation trip since RDL has administered the SRP, and the highest average cost of an orientation trip. These 1993 numbers are included to show the fluctuation which can occur in these numbers for planning purposes.

Program participants submitted biweekly vouchers countersigned by their laboratory research focal point, and RDL issued paychecks so as to arrive in associates' hands two weeks later.

This is the second year of using direct deposit for the SFRP and GSRP associates. The process went much more smoothly with respect to obtaining required information from the associates, only 7% of the associates' information needed clarification in order for direct deposit to properly function as opposed to 10% from last year. The remaining associates received their stipend and expense payments via checks sent in the US mail.

HSAP program participants were considered actual RDL employees, and their respective state and federal income tax and Social Security were withheld from their paychecks. By the nature of their independent research, SFRP and GSRP program participants were considered to be consultants or independent contractors. As such, SFRP and GSRP associates were responsible for their own income taxes, Social Security, and insurance.

8. CONTENTS OF THE 1997 REPORT

The complete set of reports for the 1997 SRP includes this program management report (Volume 1) augmented by fifteen volumes of final research reports by the 1997 associates, as indicated below:

1997 SRP Final Report Volume Assignments

LABORATORY	SFRP	GSRP	HSAP
Armstrong	2	7	12
Phillips	3	8	13
Rome	4	9	14
Wright	5A, 5B	10	15
AEDC, ALCs, WHMC	6	11	16

APPENDIX A -- PROGRAM STATISTICAL SUMMARY

A. Colleges/Universities Represented

Selected SFRP associates represented 169 different colleges, universities, and institutions.
GSRP associates represented 95 different colleges, universities, and institutions.

B. States Represented

SFRP -Applicants came from 47 states plus Washington D.C. Selectees represent 44 states.

GSRP - Applicants came from 44 states. Selectees represent 32 states.

HSAP - Applicants came from thirteen states. Selectees represent nine states.

Total Number of Participants	
SFRP	189
GSRP	97
HSAP	140
TOTAL	426

Degrees Represented			
	SFRP	GSRP	TOTAL
Doctoral	184	0	184
Master's	2	41	43
Bachelor's	0	56	56
TOTAL	186	97	298

SFRP Academic Titles	
Assistant Professor	64
Associate Professor	70
Professor	40
Instructor	0
Chairman	1
Visiting Professor	1
Visiting Assoc. Prof.	1
Research Associate	9
TOTAL	186

Source of Learning About the SRP		
Category	Applicants	Selectees
Applied/participated in prior years	28%	34%
Colleague familiar with SRP	19%	16%
Brochure mailed to institution	23%	17%
Contact with Air Force laboratory	17%	23%
<i>IEEE Spectrum</i>	2%	1%
<i>BIIHE</i>	1%	1%
Other source	10%	8%
TOTAL	100%	100%

APPENDIX B -- SRP EVALUATION RESPONSES

1. OVERVIEW

Evaluations were completed and returned to RDL by four groups at the completion of the SRP. The number of respondents in each group is shown below.

Table B-1. Total SRP Evaluations Received

Evaluation Group	Responses
SFRP & GSRPs	275
HSAPs	113
USAF Laboratory Focal Points	84
USAF Laboratory HSAP Mentors	6

All groups indicate unanimous enthusiasm for the SRP experience.

The summarized recommendations for program improvement from both associates and laboratory personnel are listed below:

- A. Better preparation on the labs' part prior to associates' arrival (i.e., office space, computer assets, clearly defined scope of work).
- B. Faculty Associates suggest higher stipends for SFRP associates.
- C. Both HSAP Air Force laboratory mentors and associates would like the summer tour extended from the current 8 weeks to either 10 or 11 weeks; the groups state it takes 4-6 weeks just to get high school students up-to-speed on what's going on at laboratory. (Note: this same argument was used to raise the faculty and graduate student participation time a few years ago.)

2. 1997 USAF LABORATORY FOCAL POINT (LFP) EVALUATION RESPONSES

The summarized results listed below are from the 84 LFP evaluations received.

1. LFP evaluations received and associate preferences:

Table B-2. Air Force LFP Evaluation Responses (By Type)

Lab	Evals Recv'd	How Many Associates Would You Prefer To Get ?								(% Response)			
		SFRP				GSRP (w/Univ Professor)				GSRP (w/o Univ Professor)			
		0	1	2	3+	0	1	2	3+	0	1	2	3+
AEDC	0	-	-	-	-	-	-	-	-	-	-	-	-
WHMC	0	-	-	-	-	-	-	-	-	-	-	-	-
AL	7	28	28	28	14	54	14	28	0	86	0	14	0
USAF A	1	0	100	0	0	100	0	0	0	0	100	0	0
PL	25	40	40	16	4	88	12	0	0	84	12	4	0
RL	5	60	40	0	0	80	10	0	0	100	0	0	0
WL	46	30	43	20	6	78	17	4	0	93	4	2	0
Total	84	32%	50%	13%	5%	80%	11%	6%	0%	73%	23%	4%	0%

LFP Evaluation Summary. The summarized responses, by laboratory, are listed on the following page. LFPs were asked to rate the following questions on a scale from 1 (below average) to 5 (above average).

2. LFPs involved in SRP associate application evaluation process:
 - a. Time available for evaluation of applications:
 - b. Adequacy of applications for selection process:
3. Value of orientation trips:
4. Length of research tour:
5.
 - a. Benefits of associate's work to laboratory:
 - b. Benefits of associate's work to Air Force:
6.
 - a. Enhancement of research qualifications for LFP and staff:
 - b. Enhancement of research qualifications for SFRP associate:
 - c. Enhancement of research qualifications for GSRP associate:
7.
 - a. Enhancement of knowledge for LFP and staff:
 - b. Enhancement of knowledge for SFRP associate:
 - c. Enhancement of knowledge for GSRP associate:
8. Value of Air Force and university links:
9. Potential for future collaboration:
10.
 - a. Your working relationship with SFRP:
 - b. Your working relationship with GSRP:
11. Expenditure of your time worthwhile:

(Continued on next page)

12. Quality of program literature for associate:
 13. a. Quality of RDL's communications with you:
 b. Quality of RDL's communications with associates:
 14. Overall assessment of SRP:

Table B-3. Laboratory Focal Point Responses to above questions

	<i>AEDC</i>	<i>AL</i>	<i>USAFA</i>	<i>PL</i>	<i>RL</i>	<i>WHMC</i>	<i>WL</i>
<i># Evals Recv'd</i>	0	7	1	14	5	0	46
<i>Question #</i>							
2	-	86 %	0 %	88 %	80 %	-	85 %
2a	-	4.3	n/a	3.8	4.0	-	3.6
2b	-	4.0	n/a	3.9	4.5	-	4.1
3	-	4.5	n/a	4.3	4.3	-	3.7
4	-	4.1	4.0	4.1	4.2	-	3.9
5a	-	4.3	5.0	4.3	4.6	-	4.4
5b	-	4.5	n/a	4.2	4.6	-	4.3
6a	-	4.5	5.0	4.0	4.4	-	4.3
6b	-	4.3	n/a	4.1	5.0	-	4.4
6c	-	3.7	5.0	3.5	5.0	-	4.3
7a	-	4.7	5.0	4.0	4.4	-	4.3
7b	-	4.3	n/a	4.2	5.0	-	4.4
7c	-	4.0	5.0	3.9	5.0	-	4.3
8	-	4.6	4.0	4.5	4.6	-	4.3
9	-	4.9	5.0	4.4	4.8	-	4.2
10a	-	5.0	n/a	4.6	4.6	-	4.6
10b	-	4.7	5.0	3.9	5.0	-	4.4
11	-	4.6	5.0	4.4	4.8	-	4.4
12	-	4.0	4.0	4.0	4.2	-	3.8
13a	-	3.2	4.0	3.5	3.8	-	3.4
13b	-	3.4	4.0	3.6	4.5	-	3.6
14	-	4.4	5.0	4.4	4.8	-	4.4

3. 1997 SFRP & GSRP EVALUATION RESPONSES

The summarized results listed below are from the 257 SFRP/GSRP evaluations received.

Associates were asked to rate the following questions on a scale from 1 (below average) to 5 (above average) - by Air Force base results and over-all results of the 1997 evaluations are listed after the questions.

1. The match between the laboratories research and your field:
2. Your working relationship with your LFP:
3. Enhancement of your academic qualifications:
4. Enhancement of your research qualifications:
5. Lab readiness for you: LFP, task, plan:
6. Lab readiness for you: equipment, supplies, facilities:
7. Lab resources:
8. Lab research and administrative support:
9. Adequacy of brochure and associate handbook:
10. RDL communications with you:
11. Overall payment procedures:
12. Overall assessment of the SRP:
13.
 - a. Would you apply again?
 - b. Will you continue this or related research?
14. Was length of your tour satisfactory?
15. Percentage of associates who experienced difficulties in finding housing:
16. Where did you stay during your SRP tour?
 - a. At Home:
 - b. With Friend:
 - c. On Local Economy:
 - d. Base Quarters:
17. Value of orientation visit:
 - a. Essential:
 - b. Convenient:
 - c. Not Worth Cost:
 - d. Not Used:

SFRP and GSRP associate's responses are listed in tabular format on the following page.

Table B-4. 1997 SFRP & GSRP Associate Responses to SRP Evaluation

	Arnold	Brooks	Edwards	Eglin	Griffis	Hanscom	Kelly	Kirtland	Lackland	Robins	Tyndall	WPAFB	average
# res	6	48	6	14	31	19	3	32	1	2	10	85	257
1	4.8	4.4	4.6	4.7	4.4	4.9	4.6	4.6	5.0	5.0	4.0	4.7	4.6
2	5.0	4.6	4.1	4.9	4.7	4.7	5.0	4.7	5.0	5.0	4.6	4.8	4.7
3	4.5	4.4	4.0	4.6	4.3	4.2	4.3	4.4	5.0	5.0	4.5	4.3	4.4
4	4.3	4.5	3.8	4.6	4.4	4.4	4.3	4.6	5.0	4.0	4.4	4.5	4.5
5	4.5	4.3	3.3	4.8	4.4	4.5	4.3	4.2	5.0	5.0	3.9	4.4	4.4
6	4.3	4.3	3.7	4.7	4.4	4.5	4.0	3.8	5.0	5.0	3.8	4.2	4.2
7	4.5	4.4	4.2	4.8	4.5	4.3	4.3	4.1	5.0	5.0	4.3	4.3	4.4
8	4.5	4.6	3.0	4.9	4.4	4.3	4.3	4.5	5.0	5.0	4.7	4.5	4.5
9	4.7	4.5	4.7	4.5	4.3	4.5	4.7	4.3	5.0	5.0	4.1	4.5	4.5
10	4.2	4.4	4.7	4.4	4.1	4.1	4.0	4.2	5.0	4.5	3.6	4.4	4.3
11	3.8	4.1	4.5	4.0	3.9	4.1	4.0	4.0	3.0	4.0	3.7	4.0	4.0
12	5.7	4.7	4.3	4.9	4.5	4.9	4.7	4.6	5.0	4.5	4.6	4.5	4.6
Numbers below are percentages													
13a	83	90	83	93	87	75	100	81	100	100	100	86	87
13b	100	89	83	100	94	98	100	94	100	100	100	94	93
14	83	96	100	90	87	80	100	92	100	100	70	84	88
15	17	6	0	33	20	76	33	25	0	100	20	8	39
16a	-	26	17	9	38	23	33	4	-	-	-	30	
16b	100	33	-	40	-	8	-	-	-	-	36	2	
16c	-	41	83	40	62	69	67	96	100	100	64	68	
16d	-	-	-	-	-	-	-	-	-	-	-	0	
17a	-	33	100	17	50	14	67	39	-	50	40	31	35
17b	-	21	-	17	10	14	-	24	-	50	20	16	16
17c	-	-	-	-	10	7	-	-	-	-	-	2	3
17d	100	46	-	66	30	69	33	37	100	-	40	51	46

4. 1997 USAF LABORATORY HSAP MENTOR EVALUATION RESPONSES

Not enough evaluations received (5 total) from Mentors to do useful summary.

5. 1997 HSAP EVALUATION RESPONSES

The summarized results listed below are from the 113 HSAP evaluations received.

HSAP apprentices were asked to rate the following questions on a scale from
1 (below average) to 5 (above average)

1. Your influence on selection of topic/type of work.
2. Working relationship with mentor, other lab scientists.
3. Enhancement of your academic qualifications.
4. Technically challenging work.
5. Lab readiness for you: mentor, task, work plan, equipment.
6. Influence on your career.
7. Increased interest in math/science.
8. Lab research & administrative support.
9. Adequacy of RDL's Apprentice Handbook and administrative materials.
10. Responsiveness of RDL communications.
11. Overall payment procedures.
12. Overall assessment of SRP value to you.
13. Would you apply again next year? Yes (92 %)
14. Will you pursue future studies related to this research? Yes (68 %)
15. Was Tour length satisfactory? Yes (82 %)

	Arnold	Brooks	Edwards	Eglin	Griffiss	Hanscom	Kirtland	Tyndall	WPAFB	Totals
# resp	5	19	7	15	13	2	7	5	40	113
1	2.8	3.3	3.4	3.5	3.4	4.0	3.2	3.6	3.6	3.4
2	4.4	4.6	4.5	4.8	4.6	4.0	4.4	4.0	4.6	4.6
3	4.0	4.2	4.1	4.3	4.5	5.0	4.3	4.6	4.4	4.4
4	3.6	3.9	4.0	4.5	4.2	5.0	4.6	3.8	4.3	4.2
5	4.4	4.1	3.7	4.5	4.1	3.0	3.9	3.6	3.9	4.0
6	3.2	3.6	3.6	4.1	3.8	5.0	3.3	3.8	3.6	3.7
7	2.8	4.1	4.0	3.9	3.9	5.0	3.6	4.0	4.0	3.9
8	3.8	4.1	4.0	4.3	4.0	4.0	4.3	3.8	4.3	4.2
9	4.4	3.6	4.1	4.1	3.5	4.0	3.9	4.0	3.7	3.8
10	4.0	3.8	4.1	3.7	4.1	4.0	3.9	2.4	3.8	3.8
11	4.2	4.2	3.7	3.9	3.8	3.0	3.7	2.6	3.7	3.8
12	4.0	4.5	4.9	4.6	4.6	5.0	4.6	4.2	4.3	4.5
Numbers below are percentages										
13	60%	95%	100%	100%	85%	100%	100%	100%	90%	92%
14	20%	80%	71%	80%	54%	100%	71%	80%	65%	68%
15	100%	70%	71%	100%	100%	50%	86%	60%	80%	82%

**PROPERTIES OF QUANTUM WELLS FORMED IN Al_{1-x}GaN/GaN
HETEROSTRUCTURES**

A.F. M. Anwar
Associate Professor
Department of Electrical and Systems Engineering

University of Connecticut
Storrs, CT 06269-2157

Final Report for:
Summer Research Program
Phillips Laboratory

Sponsored by:
Air Force Office of Scientific Research
Bolling Air Force Base, Washington, DC

And

Phillips Laboratory

September 1997

PROPERTIES OF QUANTUM WELLS FORMED IN AlGaN/GaN HETEROSTRUCTURES

A. F. M. Anwar

Associate Professor

Electrical and Systems Engineering Department

The University of Connecticut

Storrs, CT 06269-2157

Abstract

Calculated sheet carrier concentration as a function of Al mole fraction in the quantum well formed at the GaN/AlGaN heterointerface is calculated and compared to experimental data. Close agreement between experiment and theory is observed. The calculated sheet carrier concentration reflect the maximum carrier concentration possible in the GaN QW for a given Al mole fraction and can not possibly be used to argue in favor of either interface charge or piezoelectric effect as giving rise to the carriers. Based on experimental data the charge density in the AlGaN layer is estimated to be $4 \times 10^{12} \text{ cm}^{-2}$.

The temperature dependence of the quantum well properties formed in $\text{Al}_{0.25}\text{Ga}_{0.75}\text{N}/\text{GaN}/\text{Al}_{0.25}\text{Ga}_{0.75}$ and $\text{Al}_{0.25}\text{Ga}_{0.75}\text{N}/\text{GaN}$ are presented. The 2DEG concentration increases with temperature, however, the rate of increase slows down with increasing gate bias implying gain compression with increasing temperature. Calculations show that gain compression is less in $\text{Al}_{0.25}\text{Ga}_{0.75}\text{N}/\text{GaN}/\text{Al}_{0.25}\text{Ga}_{0.75}$ structures than in $\text{Al}_{0.25}\text{Ga}_{0.75}\text{N}/\text{GaN}$ based FETs. The presence of the second barrier in $\text{Al}_{0.25}\text{Ga}_{0.75}\text{N}/\text{GaN}/\text{Al}_{0.25}\text{Ga}_{0.75}$ structures gives rise to a well confined two dimensional electron gas as compared to the single barrier structures where the average distance of the electron cloud can be as high as 300Å at 500K under a low gate bias. The behavior of the average distance of the electron cloud indicates that the unity gain cut-off frequency is temperature dependent in single barrier structures, specially at low gate bias. Double barrier structures, on the other hand, may provide with device where the unity gain cut-off frequency is independent of temperature.

The calculations are based upon a simple technique to determine valence band alignments. Calculated values are compared to experimental data showing excellent agreement. A calculated valence band discontinuity of 0.42eV for AlN/GaN is well within the experimental bounds.

PROPERTIES OF QUANTUM WELLS FORMED IN AlGa_N/Ga_N HETEROSTRUCTURES

A. F. M. Anwar

1. Introduction

AlGa_N/Ga_N high electron mobility transistors (HEMTs) are currently being pursued for applications in high power and high temperature microwave circuitry [1-2]. The high bandgap of the Ga_N channel material allows higher breakdown fields and the low intrinsic carrier concentration allows for better control over free carrier concentration. The low field electron mobility is comparable to that of Si and the peak velocity is close to that of GaAs but occurs at a very high field making it an excellent candidate for high frequency and high speed application as has recently been demonstrated by Khan et. al.[3], Shur et. al. [4], Redwing et. al.[5] and Binari et. al. [1-2] for Ga_N/AlGa_N HFETs.

The microwave and the dc performance of the device depends critically upon the behavior of the two dimensional electron gas (2DEG) density and its dependence upon bias and temperature. In this report Schrödinger and Poisson's equations are solved self-consistently to model the QW. More importantly, a method to determine the valence band alignment is introduced that is extended to include Ga_N-based heterostructures.

Some of the HEMT structures reported by Binari et. al. [1-2] and Redwing et. al.[5] had appreciable two dimensional electron gas (2DEG) concentration though the AlGa_N supply layer was undoped. Dangling bonds at the Ga_N/AlGa_N heterointerface may give rise to interface charge that may explain the observed 2DEG concentration. Moreover, charge at the metal AlGa_N interface may modify or may be fully responsible for the 2DEG concentration as well. This observation is reminiscent of the Si/SiO₂ technology where interface charge at the interface created enough band bending so that channel carriers were present at zero bias. Recently, an alternative explanation towards the formation of the 2DEG concentration using piezoelectric effect has been proposed by Asbeck et. al. [14] is paper theoretical 2DEG concentration is compared to the experimental data to show excellent agreement, though piezoelectric effect was not incorporated in the calculation. This may suggest that experimental sheet carrier

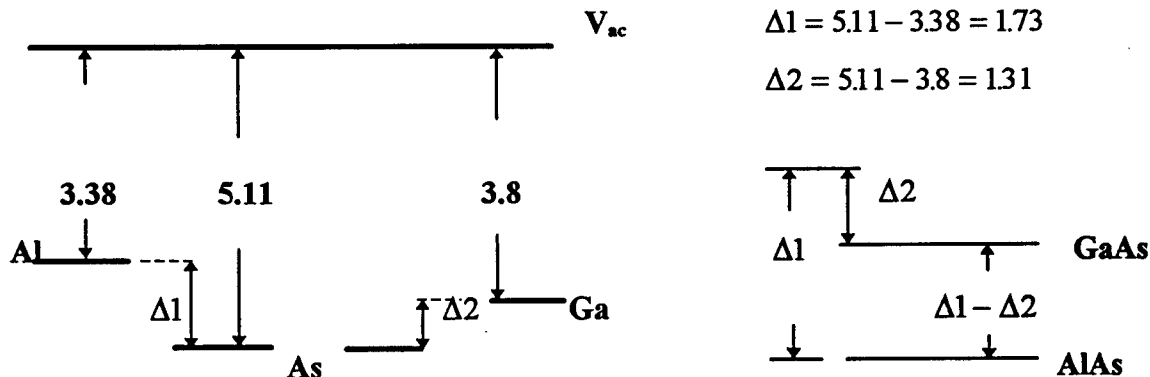
concentration versus Al mole fraction data may not be sufficient to conclude on the effect of piezoelectric effect on the formation of 2DEG in GaN.

2. VALENCE BAND ALIGNMENT

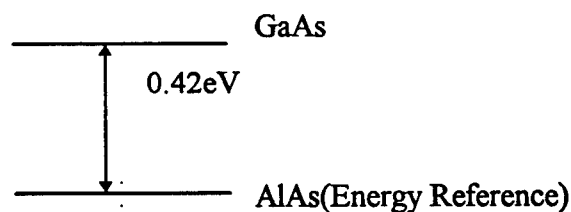
In this section a simple technique to determine valence band alignment is presented. In this technique the vacuum level is used as the energy reference. For a set of compound semiconductors the work function of the elements are used in constructing the valence band alignments. In the following few paragraphs the method is discussed with examples:

2.1 Theory/Computation

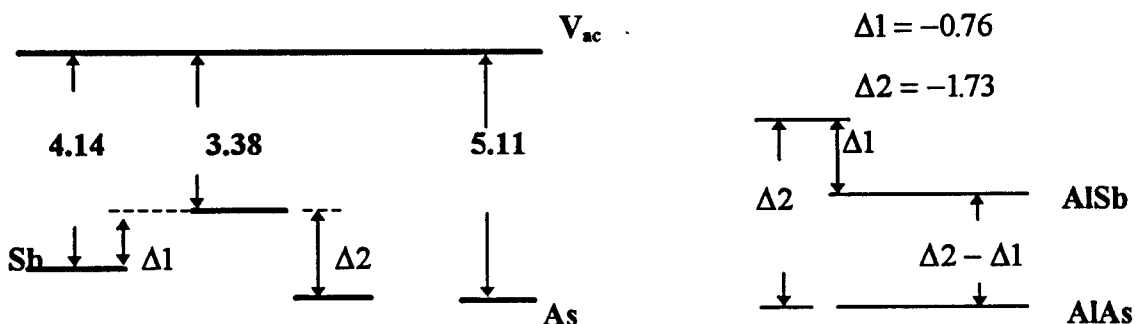
a) AlAs/GaAs system



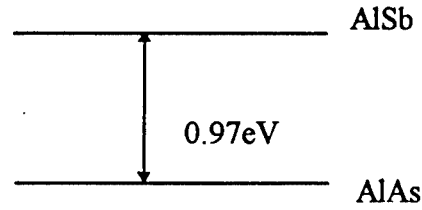
A higher $\Delta 1$ places AlAs below GaAs by $(\Delta 1 - \Delta 2 =) 0.42\text{eV}$.



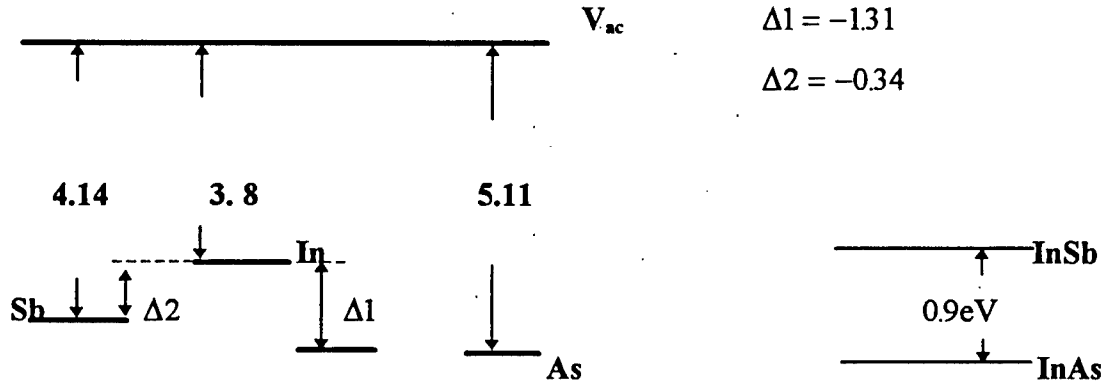
b) To establish a common reference, we inspect AlAs/AlSb system:



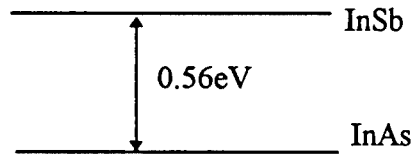
$$\Delta E_v|_{AlAs/AlSb} = -0.76 - (-1.73) = 0.97\text{eV}$$



c) InAs/InSb

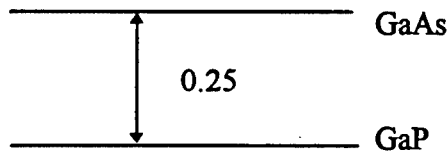


However, this yields a value not supported by experiment. We therefore, use the other value for As : 4.72eV and the resulting $\Delta E_v = 0.56\text{eV}$



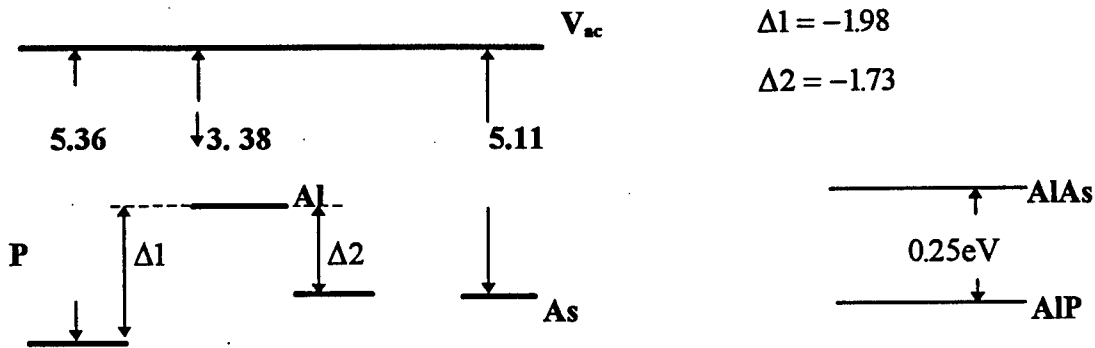
2.2 Phosphides and Nitrides

In this section the method is extended to include binaries containing Phosphides and Nitrides . The workfunction of P is not available, therefore, needs to be calculated first. From the known $\Delta E_v = 0.25$ in GaAs/GaP system [6] the workfunction of P is determined to be 5.36 eV.



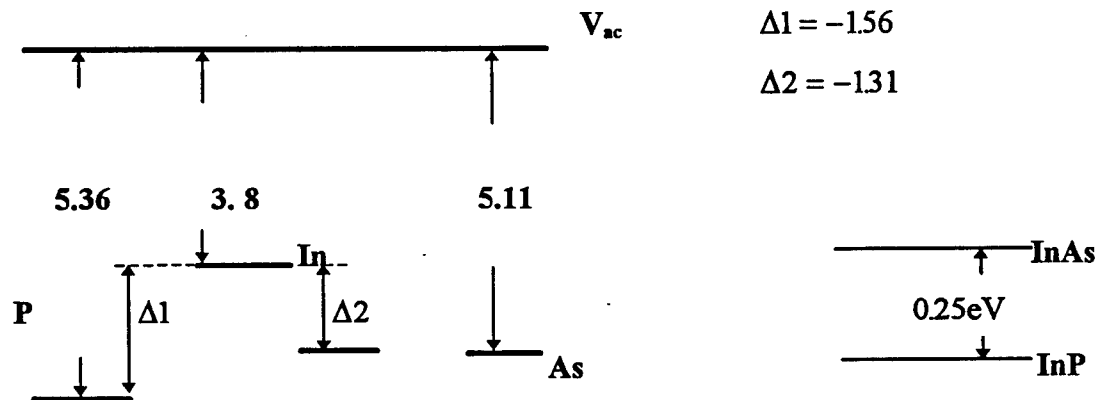
Using the calculated value of phosphorus workfunction the band alignment of the following binaries are obtained.

a) AlAs/AlP



a) $\Delta E_v = 0.5$ for AlP/GaP and is supported by the data presented by Tiwari et. al. [6]. Relating the ionization potential and workfunction (Michaelson's relationship), the workfunction of N is determined to be 7.265 eV (ionization potential=14.53 eV (CRC Manual) and electron affinity=0 is assumed). The resulting VB energy places AlN 2.155 eV below AlAs and GaN 0.42 above AlN.

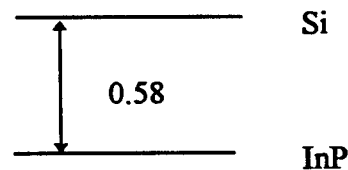
b) InP/InAs



2.3 Binary vs. Elemental Semiconductor Band Alignment

The technique developed for binaries is modified to include binary elemental semiconductor interface. Instead of using the workfunction data ionization energy is used for the computation of valence band alignments. For Si/InP and Si/CdS interface the computed valence band discontinuities are 0.58 eV and 1.98 eV, respectively.

$$\begin{aligned} \phi_{\text{InP}} &= 5.7 \text{ eV} \\ \phi_{\text{Si}} &= 5.12 \text{ eV} \\ \Delta E_v &= 5.7 - 5.12 = 0.58 \text{ eV} \end{aligned}$$

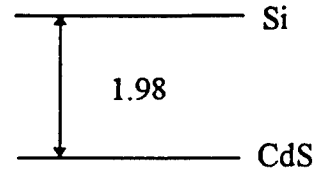


Again, from Ruan et. al. [7]

$$\phi_{\text{CdS}} = 7.1\text{eV}$$

$$\phi_{\text{Si}} = 5.12\text{eV}$$

$$\Delta E_v = 1.98\text{eV}$$

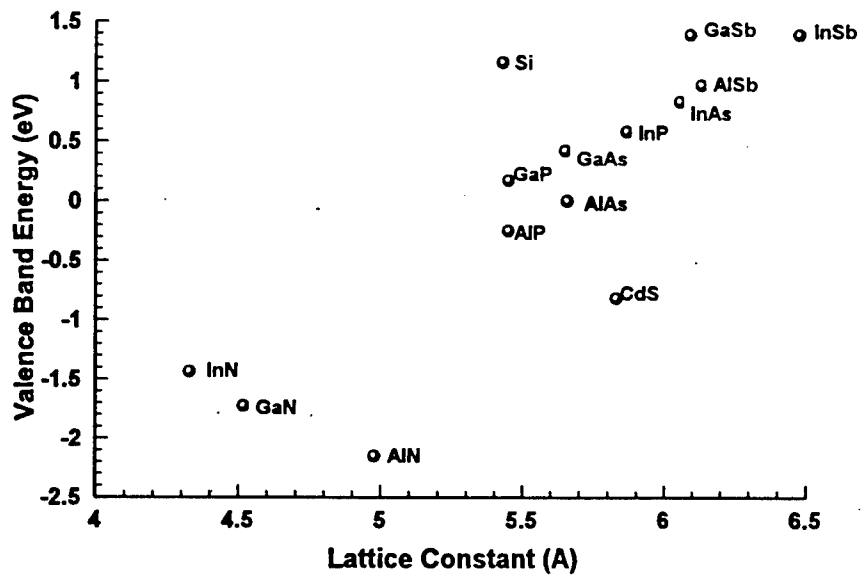


2.4 Data

Computed results are compared to experiment and other theoretical calculations and are tabulated in the table.

	Theory	Exp.	Ruan	EAR
GaAs/CdS	1.24		1.19	1.6
AlAs/CdS	0.82		0.7	1.08
GaSb/CdS	2.21		1.85	2.25
GaP/CdS	0.99		0.64	1.04
InP/CdS	1.4	1.63	0.97	1.4
AlSb/InAs	0.14		0.03	0.06

Valence band alignments with AlAs as reference is shown in the following figure.



3.1 Determination of Conduction Band Offset

The band offset is required among other material parameters to solve for the QW and determine the 2DEG concentration. The first measured valence band alignment using XPS was reported by Martin et. al.[8], giving a valence band discontinuity of $0.8 \pm 0.3\text{eV}$ for wurzite GaN/AlN heterointerface. Suzuki et. al [9] using **k.p** method and taking into account the effect of strain calculated a value close to 0.8eV . Using the method of work functions of elements a valence band discontinuity of 0.42eV was calculated for GaN/AlN heterointerface. In this calculation the effect of strain or the presence of dangling bonds at the heterointerface was not taken into account.

A conduction band discontinuity of 1.2eV is obtained for zincblende GaN/AlN heterointerface at room temperature. The conduction band discontinuity was obtained by using a band gap of 3.4 eV for GaN and 5.1 eV for AlN. For $\text{Al}_x\text{Ga}_{1-x}\text{N}$ the minimum conduction band energy was calculated based on the relationships reported by Fan et. al. Based on calculated valence band offset in GaN/ $\text{Al}_x\text{Ga}_{1-x}\text{N}$ it is found that the conduction band offset may be given as: $\Delta E_c = 0.75\Delta E_g$, where ΔE_g is the difference in bandgaps of GaN and $\text{Al}_x\text{Ga}_{1-x}\text{N}$. In Fig.1, The temperature dependence of the conduction band offset at GaN/ $\text{Al}_x\text{Ga}_{1-x}\text{N}$ heterointerface is shown. The plot is obtained by assuming the usual form of temperature dependent bandgap for GaN in the form $E_g^{\text{GaN}}(T) = 3.056 + 5.08 \times 10^{-4}T^2 / (T - 996)$ [10], where T is the temperature in $^\circ\text{K}$. The measured bandgap of AlN changes slightly over the temperature range of 77°K to 300°K and data beyond this temperature range is absent. In this paper the bandgap of AlN is assumed to be independent of temperature. As observed from the figure that with increasing temperature ΔE_c increases and is due to the faster decrease of the GaN bandgap with respect to the AlGa_N bandgap with temperature.

3.2 QW Calculation

In AlGa_N/GaN systems the QW is formed in GaN (see Fig. 1). Following the method previously developed by the present authors [11], the one electron Schrödinger equation, under effective mass approximation, can be written as

$$-(\hbar^2/2) \frac{d}{dx} \left(\frac{1}{m^*} \frac{d\zeta_i}{dx} \right) + (V(x) - E_i) \zeta_i = 0 \quad (1)$$

where m^* is the electron effective mass, \hbar is the reduced Planck's constant, ζ_i is the envelope wave function, E_i is the energy eigen value, $V(x)$ is the potential energy and the subscript i denotes the i th subband. For simplicity the potential energy function is approximated by three straight lines with slopes a_1 , a_2 and a_3 , respectively, and is expressed as

$$V(x) = \begin{cases} V_0 & x < 0 \\ a_j x + \Delta E_j & x_{j-1} < x < x_j, j = 1, 2, 3 \end{cases}$$

where $\Delta E_1 = 0$, $\Delta E_2 = (a_1 - a_2)x_1$, $\Delta E_3 = \Delta E_2 + \Delta E_{c2} + L(a_2 - a_3)$, ΔE_{c2} is the conduction band discontinuity at the second heterointerface, $L = x_2 - x_0$ is the width of the well, $x_0 = 0$ is the position of the first heterointerface, and x_3 is the distance from the first heterointerface in which 99% of the electrons reside. The solution to the Schrödinger equation, for different regions, may be written as

$$\zeta_j(x) = \alpha_{1,0} e^{\beta x} + \alpha_{2,0} e^{-\beta x} \quad j=0$$

$$\zeta_j(x) = \alpha_{1,j} \text{Ai}(\xi_j) + \alpha_{2,j} \text{Bi}(\xi_j) \quad j=1, 2, 3$$

where $\beta = \sqrt{(2m_0^* / \hbar^2)(\Delta E_{c1} - E)}$, ΔE_{c1} is the conduction band discontinuity at the first heterointerface, m_0^* is the electron effective mass in the buffer (GaN for normal HEMTs.), Ai and Bi are the Airy and the complementary function, respectively,

$$\xi_i = \gamma_i \left(x + \frac{\Delta E_i - E}{\alpha_j} \right), \text{ with } \gamma_i = ((2m_j^* \alpha_j) / \hbar^2)^{1/3} \text{ and } \alpha_{k,j} \text{'s } (k=1, 2 \& j=0, 1, 2, 3) \text{ are the}$$

arbitrary constants. Here the subscript j refers to region j and the superscript i , whenever used, will refer to the i th subband. The eigen values and eigen functions are determined by applying the two boundary conditions at any interface (a) continuity of the wave function and (b) continuity of the first derivative by taking into account the proper effective mass.

Having formulated the Schrödinger equation Poisson's equation is formulated:

$$\epsilon \frac{d^2 \phi}{dx^2} = q \sum_i n_{si} \zeta_i^2(x) + q N_A \quad (2)$$

where $n_{si} = \frac{m_{GaN}^* kT}{\pi \hbar^2} \ln(1 + e^{(E_F - E_i)/kT})$ is the number of electrons per unit area, $\xi_i(x)$ is the envelope wave function in the i th subband, N_A is the acceptor density in the unintentionally doped buffer layer, m_{GaN}^* refers to the effective mass in the channel, T is the temperature and E_F is the Fermi level at the interface relative to the conduction band in the channel at $x=0$. In these equations we have chosen the potential energy at the interface as the reference. The Fermi level E_F is expressed as

$$E_F = q[\phi(0) - \phi(W)] + E_{F0} + \Delta E_{c2} \quad (3)$$

where $\phi(0) - \phi(W)$ is the total band bending in the buffer layer $\phi(0) = 0$, W is the depletion depth, $E_{F0} = -\left[\frac{E_g(T)}{2} + kT \ln \frac{N_A}{n_i(T)}\right]$ is the position of the Fermi level with

respect to the conduction band in the bulk buffer and $n_i(T)$ is the intrinsic carrier concentration in buffer layer. The slopes α_j of the straight lines, which approximate the shape of the QW, are proportional to the average electric field determined by Poisson's equation. By integrating eqn. (2) twice with respect to x , the slopes can be expressed in the form

$$\alpha_j = (q^2 / \epsilon)(f_j n_{si} + N_A W), \quad j=1,2,3 \quad (4)$$

where

$$f_i = 1 - \sum_i \frac{n_{si}}{n_s} \frac{1}{x_j - x_{j-1}} \int_{x_{j-1}}^{x_j} dx \int_{-\infty}^x \zeta_i^2(x') dx', \quad j=1,2,3 \quad (5)$$

and $n_{si} = \sum_i n_{si}$ is the channel electron density in cm^{-2} . By solving the one electron Schrödinger equation for the given potential we can obtain the eigen energies and the wave functions for the system. The eigen energies and the wave functions determine the shape of the electron distribution in the quantum well which is then used to solve Poisson's equation. The two equations are solved self-consistently until we have accounted for 99% of the carriers in the quantum well.

3.3 Results and Discussion

QWs formed at the GaN/Al_{0.25}Ga_{0.75}N heterointerface is considered. The effective mass of GaN and AlN is assumed to be $0.19m_0$, respectively, where m_0 is the free electron mass. The electron effective mass of Al_xGa_{1-x}N is obtained by a linear interpolation between the values for GaN and AlN.

In Fig.2, the conduction band profiles obtained by solving Schrödinger and Poisson's equations self-consistently are plotted for 300K and 500K. On the same plot the 2DEG distributions are also plotted along with the Fermi levels that lie very close to the tip of the conduction band discontinuity. The plots are obtained for a 2DEG concentration $1.8 \times 10^{12} \text{ cm}^{-2}$. The conduction band profiles can be explained by noticing the fact that $n_i(300\text{K})$ is 12 orders of magnitude less than $n_i(500\text{K})$. This difference in n_i is due to (a) the higher effective density of states at higher temperatures and (b) a decrease in bandgap of GaN with increasing temperature. Moreover, the conduction band offset increases from 0.313eV at room temperature to 0.361eV at 500K. Assuming fully ionized acceptor in GaN at both temperatures the Fermi level moves closer to the intrinsic Fermi level with increasing temperature. Therefore, less band bending in GaN is required to obtain the same 2DEG concentration at 500K than at 300K. At room temperature a higher fraction of the 2DEG concentration is in the first subband due to the close proximity of the Fermi level to the first eigen energy. On the other hand, at 500K a larger separation between the first eigen energy and the Fermi level implies a lesser degree of occupation of the first subband that allows the higher subbands to be populated.

In Fig 3, the 2DEG concentration is plotted as a function of temperature with gate bias as a parameter. The structures simulated were GaN/AlGa_{0.25}N single heterointerface and Al_{0.25}Ga_{0.75}N/GaN/Al_{0.25}Ga_{0.75}N double heterointerface HEMTs. In both structures the gate is followed by a 200 Å doped epilayer with a donor doping density of $5 \times 10^{18} \text{ cm}^{-3}$ and a 20 Å spacer layer. The QW is adjacent to the spacer layer. The barrier potential ϕ_b is assumed to be 1.1 eV [12]. As observed in both structures the 2DEG concentration increases with temperature. With increasing temperature the rate of increase

of the 2DEG concentration decreases implying a compression in the device transconductance. Moreover, the gain compression is more severe in single barrier HEMTs than in the double barrier structures.

In Fig. 4, the average distance of the electron cloud from the first heterointerface (closest to the gate) $x_{av} = \frac{1}{n_s} \int_0^\infty x n_{si} dx$ is plotted as a function of temperature. Due to the presence of the second barrier x_{av} for the double barrier structures are small equals half the well width at low 2DEG concentration (at lower temperatures as evident from Fig.3). For increasing gate bias in DH structures the QW becomes more triangular at the first heterointerface and x_{av} decreases. The extremely low 2DEG concentration at low gate bias allows the higher sub-bands to be occupied in a SH structure giving rise to a high x_{av} . With increasing gate bias and temperature the 2DEG concentration increases making possible the occupancy of the lower sub-bands giving a low x_{av} and is very clearly demonstrated for a gate bias of -1.5V. x_{av} is directly related to the calculation of the gate-source capacitance in HEMTs: $C_{GS} = \epsilon / (d + \Delta d)$, where d is the total distance between the gate metal and the first heterointerface and $\Delta d = \frac{\epsilon_{AlGaIn}}{\epsilon_{GaN}} x_{av}$ and ϵ 's are the dielectric constants. In SH structures, at lower gate bias, x_{av} are comparable to d and decreases a lot in magnitude with increasing bias at a higher temperatures. C_{GS} , therefore, is very sensitive to any change in temperature at lower gate bias and may make the unity gain cut-off frequency bias and temperature dependent. However, at higher gate bias, in SH structures, x_{av} is very weakly dependent upon temperature making both C_{GS} and f_T temperature independent. On the other hand, in DH structures x_{av} is always weakly dependent upon temperature and is primarily decided by the applied gate bias.

4.1 Sheet Carrier Calculation

A large strain is induced at the AlGaIn/GaN interface due to the mismatch in lattice constants. The biaxial stress generates a piezoelectric polarization P_z , where the z direction is along the [0001] direction in the wurzite crystal and is given by $P_z = 2d_{31}(c_{11} + c_{12} - 2c_{13}^2 / c_{33})u_{xx}$. d_{31} is the piezoelectric constant and is the important

component of piezoelectric tension for the [0001] direction. c_{ij} 's are the elastic stiffness coefficient and u_{xx} is the component of the strain tensor along the x direction. As has been shown by Bykhovski et. al. [13] the surface carrier density comparable to the 2DEG concentration may be present that necessitates the accounting of piezoelectric effect in AlGaIn/GaN-based device simulation.

Asbeck et. al. [14] provides the band diagram utilizing charge induced due to piezoelectric effect and uses that to explain their experimental Al mole fraction versus sheet carrier (2DEG) concentration data. In this paper the 2DEG concentration is calculated for varying Al mole fraction by solving Schrödinger and Poisson's equations self-consistently. The theoretical result explains the experimental data reported by Asbeck et. al. [14] though piezoelectric effect was not included in the simulation.

Following the method reported by the present authors Schrödinger and Poisson's equations are solved self-consistently. The GaN layer is assumed to be unintentionally doped p-type with an acceptor doping concentration of $1 \times 10^{14} \text{ cm}^{-3}$. The conduction band offset is given by $\Delta E_c = 0.75\Delta E_g$ where ΔE_g is the difference in band gaps of the GaN and AlGaIn layers. In Fig.1, the calculated 2DEG concentration is plotted as a function of the Al mole fraction. The computation is carried out at room temperature. The simulated 2DEG concentration represents the maximum confined electron density in the quantum well (QW) and is obtained by aligning the Fermi level as close to the top of the QW as possible. On the same plot experimental data reported by Asbeck et. al. [14] is shown and the agreement is excellent. It should be pointed out that the experimental data was obtained under a floating gate condition. The close agreement between the experimental data and the theoretical results implies that the 2DEG concentration is dictated by the QW itself and a plot of 2DEG concentration versus Al mole fraction may not be representative of piezoelectric effect or interface charge.

4.2 Gate Voltage Calculation

Instead of plotting the 2DEG concentration with varying Al mole fraction a more conclusive plot may result if the 2DEG concentration is plotted as a function of the gate voltage for layers grown under differing conditions (MOCVD versus MBE). Under different growth conditions the interface charge density will be different implying varying

gate voltage for the same 2DEG concentration. A careful C-V measurement then will supply the interface charge density. However, the invariance in gate voltage for the same 2DEG concentration in structures grown under different growth conditions may point to a different explanation.

To comment on the magnitude of the charge in question we use the experimental data reported by Binari et. al. [1] The structure under consideration consists of a 500 Å of $\text{Al}_{0.15}\text{Ga}_{0.85}$ on top of a 3 μm GaN. Using a off state 2DEG concentration of $1 \times 10^{10} \text{ cm}^{-2}$ the gate is at a potential of 0.85 V, however, Binari et. al. [1] reports a pinch off voltage of -4 V. In order to get -4 V a charge of the amount of $4.03 \times 10^{12} \text{ cm}^{-2}$ has to exist in the AlGaIn layer. The charge density may easily be the interface charge density required to explain Binari et. al. [1] data.

5. Conclusion

The temperature dependence of the properties of QWs formed in AlGaIn/GaN and AlGaIn/GaN/AlGaIn are presented. With increasing temperature both structures show gain compression, however, the double barrier structures are more stable. x_{av} calculations indicate that the DH structures may provide a f_T that is less sensitive to temperature variation.

6. References

1. S. C. Bianri, J. M. Redwing, G. Kelner and W. Kruppa, "AlGaIn/GaN HEMTs grown on SiC substrates," Electron. Lett., vol. 33, No. 3, p. 242, 1997.
2. S. C. Binari, " GaN FETs for high temperature and microwave applications," Electrochem. Soc. Proc., 95-21, p. 136, 1995.
3. M. A. Khan, Q. Chen, M. S. Shur, B. T. Dermott and J. A. Higgins, " Microwave operation of GaN/AlGaIn Doped channel heterostructure field effect transistors," IEEE Electron Dev. Lett., vol. 17, No.7, p. 325, 1996.
4. M. S. Shur and M. A. Khan, " GaN/AlGaIn heterostructure devices: photodetectors and field effect transistors," MRS Bull., p. 44, Feb., 1997

5. J. M. Redwing, M. A. Tischler, J. S. Flynn, S. Elhamri, M. Ahoujja, R. S. Newrock and W. C. Mitchel, "Two-dimensional electron gas properties of AlGa_N/Ga_N heterostructures grown on 6H-SiC and sapphire substrates," Appl. Phys. Lett., vol. 69, p. 963, 1996
6. S. Tiwari, and D. J. Frank, "Empirical fit to band discontinuities and barrier heights in III-V alloy systems," APL, vol. 60(5), p. 630, 1992.
7. Y-C Ruan and W. Y. Ching, "An effective dipole theory for band lineups in semiconductor heterojunctions," J. Appl. Phys., vol. 62, No. 7, p. 2885, 1987.
8. G. Martin, S. Strite, A. Botchkarev, A. Agarwal, A. Rockett and H. Morkoc, "Valence-band discontinuity between Ga_N and Al_N measured by x-ray photoemission spectroscopy," Appl. Phys. Lett., vol. 65, No. 5, p. 610, 1994.
9. M. Suzuki and T. Uenoyama, "Strain effect on electronics and optical properties of Ga_N/AlGa_N quantum-well lasers," J. Appl. Phys., vol. 80, No. 12, p. 6868, 1996.
10. S. Strite and H. Morkoc, "Ga_N, Al_N, and In_N: a review," J. Vac. Sci. Technol., vol. B 10, No. 4, p. 1237, 1992.
11. A. F. M. Anwar and R. T. Webster, "An envelope function description of the quantum well formed in Al_xGa_{1-x}As_ySb_{1-y}/InAs/Al_xGa_{1-x}As_ySb_{1-y} heterostructures," J. Appl. Phys., vol. 80, No. 12, p. 6827, 1996.
12. F. Stengel, S. N. Mohammad and H. Morkoc, "Theoretical investigation of electrical characteristics of AlGa_N/Ga_N modulation doped field-effect transistors," J. Appl. Phys. vol. 80, No. 5, p. 3031, 1996.
13. A. Bykhovski, B. Gelmont and M. Shur, "The influence of the strain-induced electric field on the charge distribution in Ga_N-Al_N-Ga_N structure," J. Appl. Phys., vol. 74, No. 11, p. 6734, 1993.
14. P. M. Asbeck, E. T. Yu, S. S. Lau, G. J. Sullivan, J. Van Hove and J. Redwing, "Piezoelectric charge densities in AlGa_N/Ga_N HFETs," Electron. Lett., p. 241, Aug. 1997.

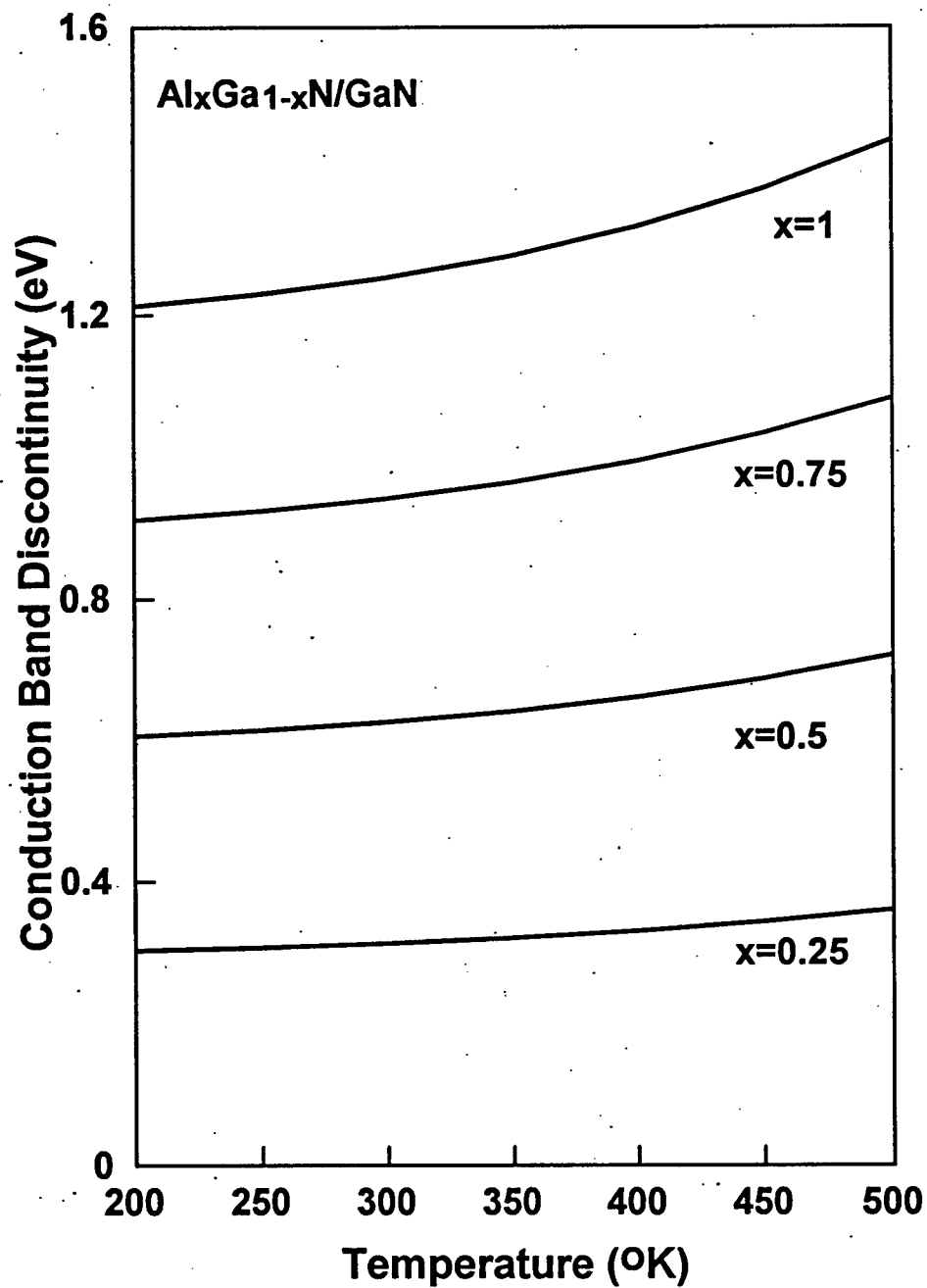


Figure 1 Conduction band offset in a GaN/AlGa_xN heterointerface with Al-mole fraction as a parameter.

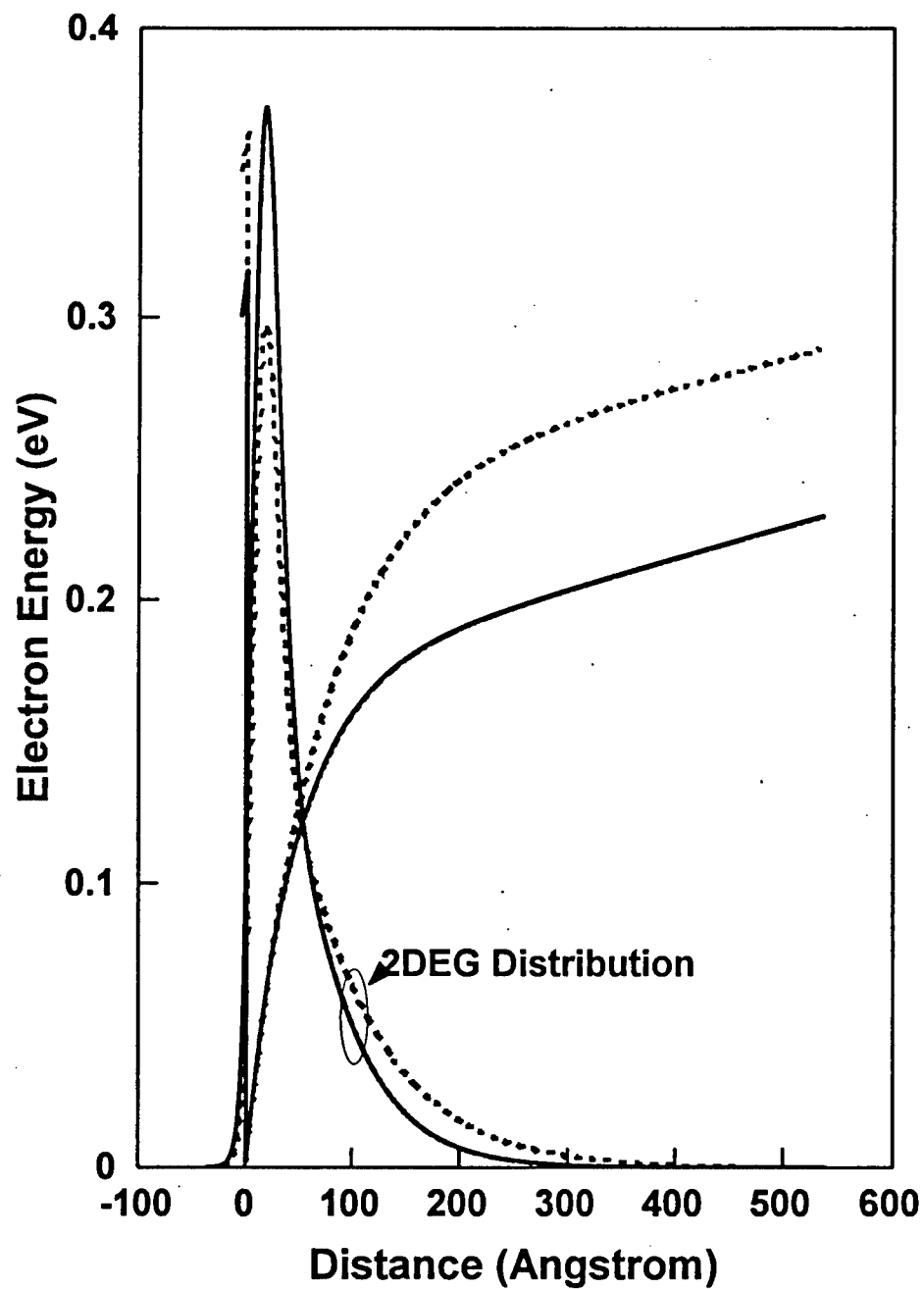


Figure 2 Conduction band profile is plotted as a function of distance for 300K (solid line) and 500K (dashed line). The 2DEG distribution is also shown.

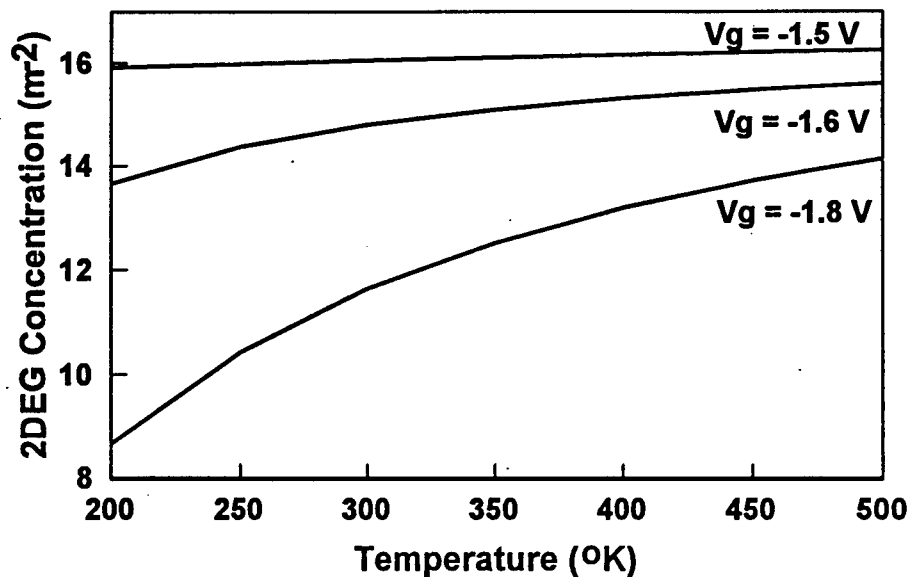


Figure 3(a) $\log_{10}(2\text{DEG})$ concentration is plotted as a function of temperature for varying gate bias for AlGa_N/Ga_N heterointerface. An Al-mole fraction of 0.25 is considered.

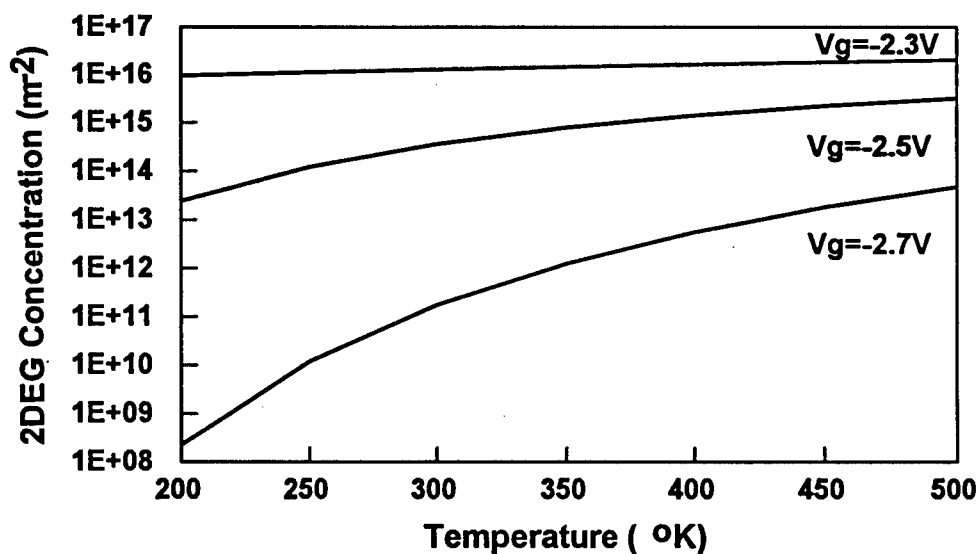


Figure 3(b) 2DEG concentration in AlGa_N/Ga_N/AlGa_N system is plotted as a function of temperature for different gate bias.

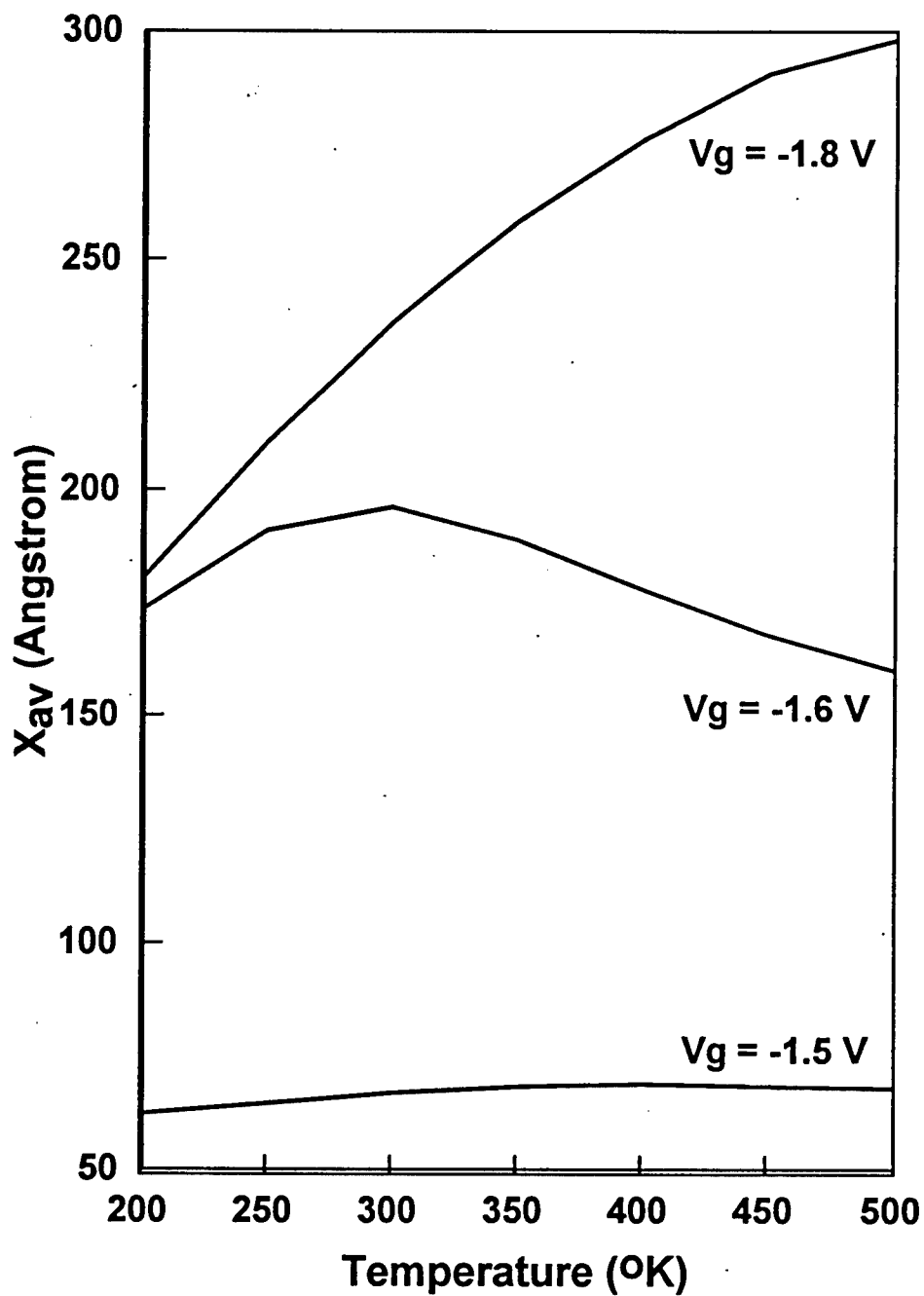


Figure 4(a) Average electron distance from the first heterointerface in AlGaIn/GaN is plotted as a function of temperature.

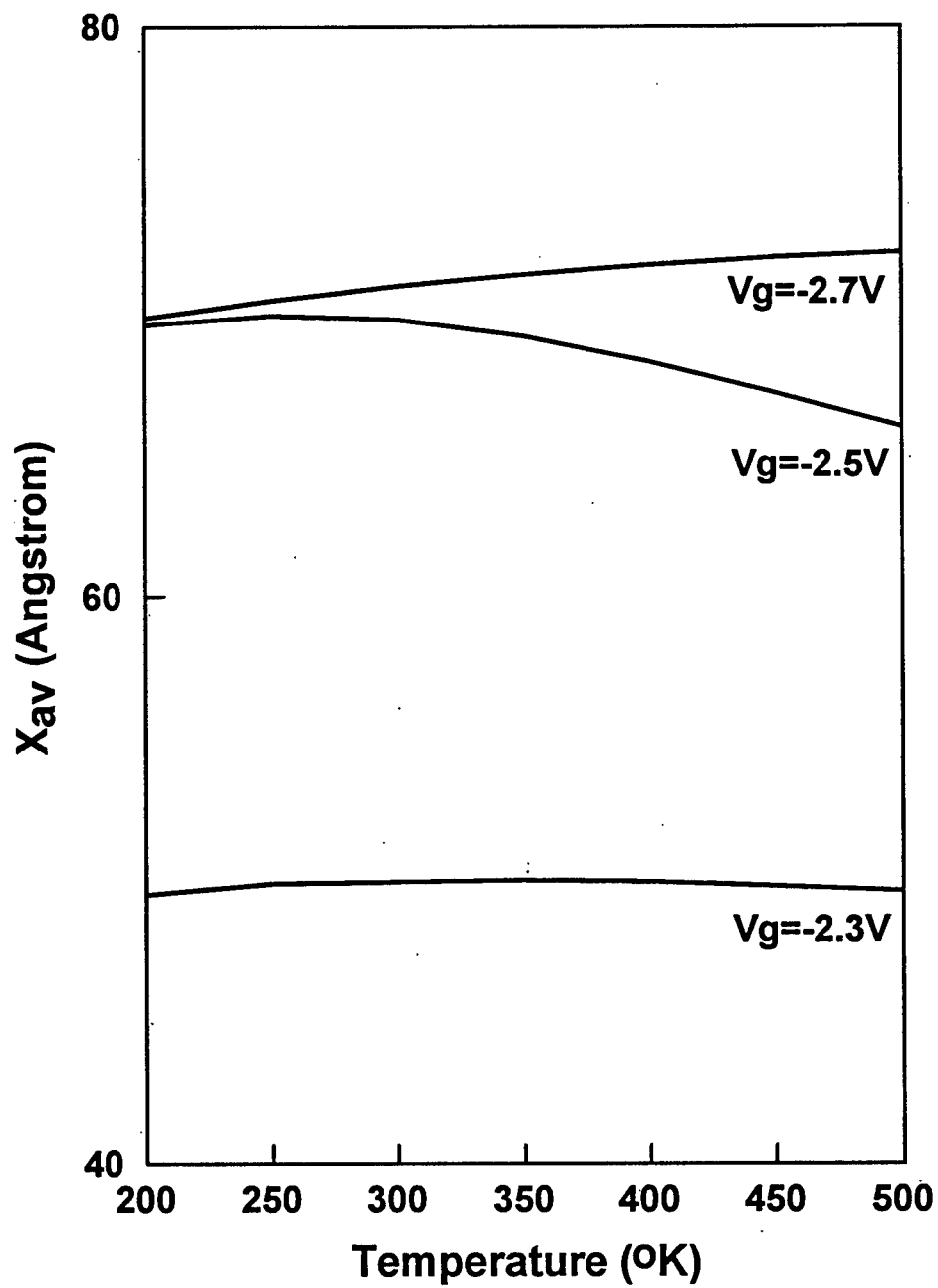


Figure 4(b) Average electron distance from the first heterointerface in AlGaIn/GaN/AlGaIn system is plotted as a function of temperature.

**ASSURED SOFTWARE DESIGN: PRIVACY ENHANCED MAIL (PEM) AND
X.509 CERTIFICATE SPECIFICATION**

Milica Barjaktarovic
Assistant Professor
Department of Electrical and Computer Engineering

Wilkes University
Stark Learning Center
Wilkes-Barre, PA 18766

Final Report for:
Summer Faculty Research Program
Rome Laboratory

Sponsored by:
Air Force Office of Scientific Research
Bolling Air Force Base, DC

And

Rome Laboratory
Rome, NY

September 30, 1997

ASSURED SOFTWARE DESIGN: PRIVACY ENHANCED MAIL (PEM) AND X.509 CERTIFICATE SPECIFICATION

Milica Barjaktarović
Assistant Professor
Department of Electrical and Computer Engineering
Wilkes University
Wilkes-Barre PA 18766

Abstract

In this document we present two related projects:

- Formal specification and verification of the Privacy Enhanced mail (PEM) control sequence. The sequence is specified in the language PROMELA based on Hoare's process algebra CSP, and verified using AT&T's model checker SPIN. The contribution of our work is to show that software can be constructed by formal design procedures. The control path is written in a process algebra based on the data path described in higher order logic. The control path is verified using a model checker, and the data path is verified using a theorem prover.
- Semi-formal specification of X.509 certificates. This specification will be translated into HOL.

Chapter 1

Introduction

The issues of system design, building and testing are crucial in hardware and software systems, especially in complex systems, and especially with hardware/software co-design.

We address these issues by proposing a design and testing methodology based on formal methods. We demonstrate our approach on a case study, the Privacy Enhanced Mail (PEM) software. We also further this work by semi-formally specifying X.509 certificates which PEM uses. PEM is a representative of more complex secure e-mail systems, such as MISSI.

In this document we present two related projects:

- Formal specification and verification of Privacy Enhanced mail (PEM) control sequence. The sequence is specified in the language PROMELA based on Hoare's process algebra CSP, and verified using AT&T's model checker SPIN. The contribution of our work is to show that software can be constructed by formal design procedures. The control path is written in a process algebra based on the data path described in higher order logic [3]. The control path is verified using a model checker, and the data path is verified using a theorem prover.
- Semi-formal specification of X.509 certificates. This specification will be translated into HOL.

Chapter 2

Promela and SPIN

Promela is a language based on CSP and implemented in C. SPIN is the publicly distributed automated verification tool which supports Promela [4, 6, 5, 12].

Promela uses processes (we can think of them as “C functions executed concurrently.”) Processes are executed by being called from another process using the `run` statement. The main process is called `init`.

Promela uses channels for communication. A channel is a FIFO queue of a certain capacity. For example, a channel which can store N byte-long messages is declared as:

```
chan channel = [N] of {byte}
```

Zero-capacity channels do not have capability to store messages, and are used for synchronization (i.e. handshaking.) The following syntax is used to append a message type `msg_type` with values `expr1` and `expr2` to channel `q`: `q!msg_type(expr1, expr2)`. `q?msg` means “receive message `msg` on channel `q`.”

Promela has twelve types of statements: assertion, expression, selection, assignment, goto, break, repetition, atomic, send, receive, printf, and timeout. `skip` statement is analogous to C *continue* statement. Assertions, expressions and printf statements are similar to C.

Selection statement is similar to C *if* construct, except that Promela requires that one option be executed, and will deadlock if no option is executable. Repetition statement is similar to C *do* loop. It is executed repeatedly until a `break` statement is executed or a `goto` statement transfers control outside of the loop. Atomic sequence is indicated by the keyword `atomic` and allows a block of critical code to be executed without interruption.

SPIN can use `assert` statements, `never` claims and Linear Temporal Logic (LTL) statements for validation. Assert statements state properties of data at a given state. Never claims state properties of data at one or more states.

An `atomic` statement marks the specification section that is to be executed without interruptions; i.e. it is a semaphore protecting critical code, and is used for streamlining the model.

Chapter 3

PEM

In this chapter we present the PROMELA specification of the PEM model based on functions specified and verified in HOL [3]. Therefore, we provide the the control path given the data path. Both control and data paths are verified: the control path is verified using the model checker SPIN [4], and the data path is verified using the theorem prover HOL. The data path verification ensures that the data structures have the desired properties. The control path assures that the correct data is used. Properties that we want to check for are integrity, privacy, and authenticity.

3.1 PEM Algorithm

MIC stands for “message integrity check.” From [11, 10, 2, 9], we extract the following algorithm:

```
Sender:
generate MIC
sign MIC using the sender's private key
if msg_type == ENCRYPTED
    generate DEK
    generate other parameters
    encrypt msg using DEK
    encrypt the signed MIC using DEK

Receiver:
get and verify sender's certification path
extract sender's public key from the certificate
if msg_type == ENCRYPTED
    use receiver's private key to extract DEK
    decrypt msg text
    decrypt signed MIC
    use sender's public key to unsign MIC
    calculate MIC on the msg
    compare calculated and received MICs
else /*if msg_type != ENCRYPTED*/
```

use sender's public key to extract MIC
compute MIC on the msg

3.1.1 Observations

The sender needs to get the receiver's certification path only if he is sending an encrypted message.

The receiver must always get sender's certification path, because he must check the signature on the MIC.

Data Encryption Key (DEK) is encrypted using the recipient's public key, and decrypted using recipient's private key.

MIC is signed using the sender's private key, and unsigned using the sender's public key; encrypted using DEK, and decrypted using DEK.

3.2 Differences and Similarities Between PEM and MISSI

PEM and MISSI: both have a single path through the certification hierarchy to any user.

Note: X.509 allows for multiple certification paths. Although both PEM and MISSI are based on X.509 certificates, they do so in a restricted way.

PEM and MISSI: both have the same certificates (X.509), and the same certificate verification process.

PEM:

Does not have an access control mechanism, e.g. FORTEZZA card.

Does not use network Guard.

How does a user know if the Root certificate is valid - the trust in the certification path is based on the trusted Root certificate, yet in PEM it seems that the Root certificate is not protected any better than any other certificate.

MISSI:

Does use network Guard.

Stores Root certificate on the FORTEZZA card and hence provides additional protection.

Comparison between the PEM and MISSI algorithms is shown below. DEK stands for Data Encryption Key. MEK stands for Message Encryption Key. DEK and MEK are just different names for the key used to encrypt data.

PEM:

Algorithm used for:	applied to plaintext	applied to DEK

hash	RSA-MD2, RSA-MD5	
signature	DES-EDE, DES-ECB, RSA	
encryption	DES-CBC	RSA

MISSI:

Algorithm	applied to	applied to
used for:	plaintext	MEK

hash	SHA-1	
signature	DSA	
encryption	SKIPJACK	NSA-designed

Comparison between the PEM and MISSI encryption algorithms is shown below. MISSI has one more layer of encryption than PEM. PEM uses only one key, DEK, to encrypt data. MISSI uses two keys: one to encrypt data (MEK) and one to encrypt MEK (TEK). TEK stands for Token Encryption Key.

PEM:	MISSI:
generate DEK	generate MEK
encrypt data using DEK	encrypt data using MEK
	generate TEK using sender's private key, receiver's public key, and random numbers
encrypt DEK using receiver's public key	encrypt MEK using TEK
	construct a token which includes MEK
	encrypt token using TEK

The algorithms for the PEM and MISSI sender and receiver are relatively similar. The functions used, based on the PEM algorithm presented in [3], do not map directly to MISSI functions, but the similarity is present.

According to [3], the PEM algorithm can be expressed using the functions used in [3]. We present the PEM algorithm in the following table. We also compare the PEM and MISSI algorithms. Actions common to both PEM and MISSI are presented in the middle. In the table, we tried to physically align the PEM and MISSI entries that correspond to each other.

PEM	MISSI
	Sender:
	get receiver's certification path
verify the cert path	msp_check_signature
hash	msp_submit
sign	
encryptP	

```

encryptS

Receiver:
for all messages:
    get certification path
    verify certification path
if msg_type == MIC_ONLY or
    msg_type == MIC_CLEAR
    get text
if msg_type == ENCRYPTED
    getEN_msg_message
    ENCRYPTED_is_PrivateS
    ENCRYPTED_is_Authentic2
if msg_type == MIC_ONLY
    MIC_ONLY_is_Intact
if msg_type == MIC_CLEAR
    MIC_CLEAR_is_Intact

```

The following are crude descriptions of MISSI functions:

```

msp_check_sign:
    verify certification path

msp_submit:
    hash
    sign
    encrypt
    construct the token

msp_status:
    extract sender's certification path from the message
    if not encrypted, extract message text

msp_deliver:
    if encrypted, decrypt message, verify
    hash and check the signature

```

3.3 PROMELA Model

We constructed a PROMELA model which represents a sender and a receiver connected via a WAN. The outline of the model is presented in the section 3.2. A sample PROMELA specification for the sender hashing and message signing is:

```

if
::( msg_type == ENCRYPTED
|| msg_type == MIC_CLEAR

```

```

|| msg_type == MIC_ONLY) ->
hash[wkst]!plaintext, MDalgid; /*generate_MIC;*/
from_hash[wkst]?MIC;
sign[wkst]!MIC,sPRkey, sign_algid;
    /*sign MIC using private key of sender*/
from_sign[wkst]?signed_MIC;

```

We use the following notation: calling a function is modeled as producing an output on the channel named with the function name (e.g. “hash”). The function returns the output via the channel `from_functionname`; e.g. `from_hash` models the output of the hash function.

We model each function as a “black box” which takes an input and returns the output. The contents of the “box” are left to implementers, and are outlined in the HOL specifications. What we provide here is analogous to C function declarations and a main program.

A sample PROMELA specification for the receiver is:

```

mic_only_is_intact:
    MIC_ONLY_is_Intact[wkst]!d1,d2,d3,d4,d5,d6,d7,d8,d9,d10,d11,d12;
    from_MIC_ONLY_is_Intact[wkst]?rsp;
    if
    :: (rsp == OK) -> skip;
    :: (rsp != OK) -> error_;
    fi;

```

The label `mic_only_is_intact` is used to mark reaching this place in the specification for testing purposes.

3.4 Results

We test our model using the Linear Temporal Logic (LTL) response formula: every time p is true, q must eventually happen, or:

$$\Box(p \rightarrow q)$$

We are interested in authenticity, message integrity, and privacy.

We ran the above formula for the following pairs of p and q :

```

#define p (sent_msg_type == ENCRYPTED)
#define q (PEM_UA[3]@authenticate)

#define p (sent_msg_type == MIC_ONLY)
#define q (PEM_UA[3]@authenticate)

#define p (sent_msg_type == MIC_CLEAR)

```



```

#define q  (PEM-UA[3]@authenticate)

#define p  (sent_msg_type == MIC_ONLY)
#define q  (PEM-UA[3]@mic_only_is_intact)

#define p  (sent_msg_type == MIC_CLEAR)
#define q  (PEM-UA[3]@mic_clear_is_intact)

#define p  (sent_msg_type == ENCRYPTED)
#define q  (PEM-UA[3]@encrypted_is_private)

#define p  (sent_msg_type == ENCRYPTED)
#define q  (PEM-UA[3]@encrypted_is_intact)

```

SPIN produces the following result, which indicate that the formulas are true:

```

(Spin Version 2.9.7 -- 18 April 1997)
  + Partial Order Reduction

```

Full statespace search for:

```

    never-claim          +
    assertion violations + (if within scope of claim)
    acceptance  cycles  - (not selected)
    invalid endstates   - (disabled by never-claim)

```

State-vector 944 byte, depth reached 207, errors: 0

```

    6163 states, stored
    1716 states, matched
    7879 transitions (= stored+matched)
    4412 atomic steps

```

Chapter 4

X.509 Definitions

In this chapter we present our specification of X.509 certificates.

4.1 Underlying Assumptions

The following discussion is based on public key cryptography (PKC), in which, for all users X : $X_p \cdot X_s = X_s \cdot X_p$. X_p represents a user's public key, and X_s represents private key.

Each user is identified by its possession of its private key (assuming that the private key remains confidential to the user) [7] p.57. This requirement means that each public-private key pair is unique.

Each user possesses a unique Distinguished Name (DN) [7] p.57.

Certificates may or may not be protected in the Directory.

Certificates are unforgeable, i.e. only a Certification Authority (CA) can modify the certificate without being detected [7] p.57.

Sender and receiver must use the same hash and crypto functions, and clocks must be logically synchronized by bilateral agreements.

4.2 Certification Hierarchy and Certificate Definition

Certification hierarchy is defined in [7], and in this section we present the most important portions.

There is an unbroken chain of trusted points in the Directory between the users requiring to authenticate. For example, have a common point of trust and link it to each user by an unbroken chain of trusted points [7] p.57.

A certification authority of any user may or may not be unique. That is, it is possible to have certificates issued by different authorities [7] p.57.

If user A has a certificate issued by CA, CA must be an entry in Directory Information Tree (DIT) [7] p.58.

The above two requirements allow for a certification hierarchy graph of any depth. We show a hypothetical X.509 certification hierarchy in Figure 4.1. MISSI allows a certification hierarchy tree

of depth 4.

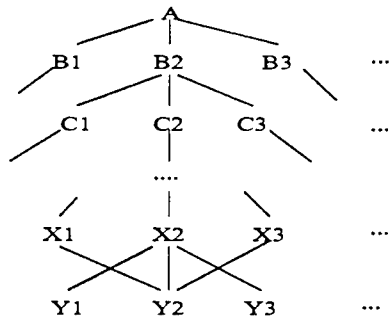


Figure 4.1: A possible PEM certification hierarchy.

A CA hierarchy may or may not coincide with DIT hierarchy. Therefore, users who have CAs in the hierarchy may establish a certification path between them using the Directory without any prior information [7] p.58. Note: a CA hierarchy is the same as a certification hierarchy.

4.2.1 Forward and Reverse Certificates

A **certificate** is a file containing the user's public information, signed by the certification authority that issued the certificate. A certificate of user A issued by CA contains:

$$CA \ll A \gg = CA\{SN, AI, CA, A, A_p, T^A\}$$

where: SN = serial number; AI = algorithm id; CA = name of the certification authority that issued the certificate; A = user name, i.e. name of the entity whose certificate it is, name of the subject of the certificate; A_p = public key of the subject of the certificate; and T^A = certificate validity period [7] p. 57.

In summary, a certificate associates the public key and the unique DN of the user it describes.

Certificates are stored in the Directory. The Directory entry of each user A who is participating in strong authentication, contains the certificate(s) of A.

Certificates are held with Directory entries as attributes of type UserCertificate, CACertificate, or CrossCertificatePair (containing both forward and reverse certificates) [7] p.59.

The Directory entry of each Certification Authority X contains a number of certificates. These certificates are of two types. First there are forward certificates of X generated by other Certification Authorities. Second, there are reverse certificates generated by X itself which are the certified public keys of other certification authorities.

.... Each CA may store one (forward?) certificate and one reverse certificate designated as corresponding to its superior CA. [7] p.58.

For example, let us assume that the Certification Authority Y issued a certificate to the user X. Forward certificate $Y \ll X \gg$ has the following properties:

issuer_name = Y
subject_name = X
subject_key_info = X_p

In logic, we can express the forward certificate properties as:

```
subject_of(certificate) = X AND issuer_of(certificate)=Y ->
is_forward_cert(certificate)
<=>
rank(X) < rank(Y) AND is_cert_authority(Y)
AND on_issuue_list(Y,X)
```

Reverse certificate $X \ll Y \gg$ has the following properties:

issuer_name = X
subject_name = Y
subject_key_info = Y_p

In logic, we can express reverse certificate properties as:

```
subject_of(certificate) = Y AND issuer_of(certificate)=X ->
is_reverse_cert(certificate)
<=>
rank(X) <= rank(Y) AND is_cert_authority(X)
AND is_cert_authority(Y) AND NOT on_issuue_list(X,Y)
```

We can define "the rank of user A," i.e. rank(A), as the depth in the certification tree that the user is at, assuming that the root of the tree has the highest rank.

We observe that each user in the X.509 certificate hierarchy tree does not know what his rank is, unless that information is stored with the user; however, the standard does not explicitly mention such storing.

[1] p. 9, states that subjectKey BIT STRING DSS privileges contains the flag "is certification authority." We have not found any reference to this flag in the X.509 documentation, and we feel that it is necessary. Both the rank and the "is certification authority" flag are used to distinguish between forward and reverse certificates. Currently, the only way a user would know what type of certificate they have is by examining which slot of CrossCertificatePair the certificate was put into - either slot 0 (for forward certificates), or slot 1 (for reverse certificates).

The BNF notation for a certificate is the following:

```
Certificate ::= SIGNED SEQUENCE {
    version          [0]Version DEFAULT 1988
    serialNumber     SerialNumber
    signature        AlgorithmIdentifier
```

```

    issuer      Name
    validity    Validity
    subject     Name
    subjectPublicKeyInfo SubjectPublicKeyInfo}

Version      ::=  INTEGER {1988(0)}
SerialNumber ::=  INTEGER

Validity     ::= SEQUENCE {
    notBefore    UTCTime
    notAfter     UTCTime}

SubjectPublicKeyInfo ::= SEQUENCE {
    algorithm     AlgorithmIdentifier
    subjectKey     BIT STRING}

AlgorithmIdentifier ::= SEQUENCE {
    algorithm      OBJECT IDENTIFIER
    parameters     ANY DEFINED BY algorithm
                   OPTIONAL}

```

The BNF notation for Directory entries is as follows:

```

UserCertificate      ::= ATTRIBUTE
    WITH ATTRIBUTE-SYNTAX Certificate
CACertificate        ::= ATTRIBUTE
    WITH ATTRIBUTE-SYNTAX Certificate
CrossCertificatePair ::= ATTRIBUTE
    WITH ATTRIBUTE-SYNTAX CertificatePair
CertificatePair      ::= SEQUENCE {
    forward [0] Certificate OPTIONAL
    reverse [1] Certificate OPTIONAL
    -- at least one must be present --}

```

4.2.2 Certification Path

[7] p. 57, defines certification path as: **Certification path** is a list of certificates needed to allow a particular user to get the public key of another user. Each item in the list is a certificate of the certification authority of the next item on the list. If we use symbol $A \rightarrow B$ to mark the certification path from user A to user B, and $A \ll B \gg$ marks certificate of B issued by A, then:

$$A \rightarrow B = CA(A) \ll X_1 \gg X_1 \ll X_2 \gg \dots X_i \ll X_{i+1} \gg \dots CA(B) \ll B \gg$$

Logically, certification path forms an unbroken chain of trusted points in the Directory Information Tree between two users wishing to authenticate.

Users can get certification paths from various resources - either from the Directory and/or from the stored certification paths. However, once a user gets a certificate, it must validate it. (Note: a

user can be human or non-human. such as an application process).

Since the public key of any user X can be discovered by any user knowing the public key of CA(X), obtaining the certification path is a recursive process.

... We assume that each user knows his public and private keys, as well as the public keys of his certification authority.

[7] gives the following definitions, although we could not find a place where these definitions are either used or mentioned in the X.509 standard:

```
Certificates      ::= SEQUENCE{
  certificate      Certificate,
  certificationPath ForwardCertificationPath OPTIONAL }

ForwardCertificationPath ::= SEQUENCE OF CrossCertificates

CertificationPath  ::= SEQUENCE {
  userCertificate   Certificate,
  theCACertificates SEQUENCE OF CertificatePair OPTIONAL }

CrossCertificates  ::= SET OF Certificate
```

4.3 Assumptions About the Directory and Certificates

Certificates are publicly available from the Directory.

Each certificate is an attribute in the Directory.

User certificates are generated by some off-line CA which is completely separate from the Directory Service Agents (DSAs) in the Directory. The CA must be satisfied of the identity of a user before creating a certificate for the user.

CAs must not issue certificates for two users with the same name.

A user's key may be produced in one of three ways: the user generates his own key pair; a third party generates the user's key pair; or the CA generates the user's key pair [7] p.67.

All private keys remain known only to the user to whom they belong to.

4.3.1 X.509 Certification Hierarchy Example

We show a hypothetical X.509 certification hierarchy in Figure 4.2.

In this case, the Directory contents can be described as:

```
C: UserCertificate, X<<C>>

A: UserCertificate, X<<A>>

X: CACertificatePair, forward [0] W<<X>>
   backward[1] X<<W>>
   CACertificate, X<<Z>>
```

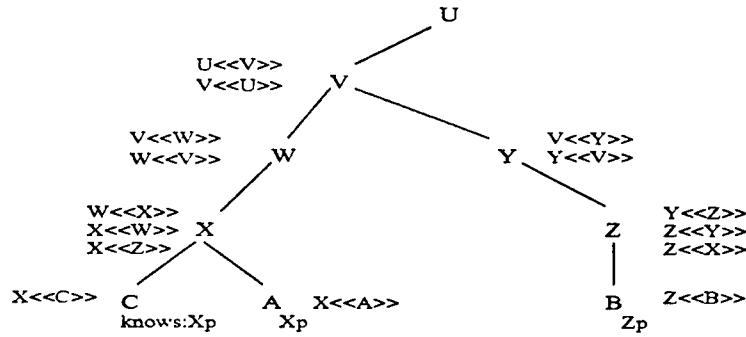


Figure 4.2: Example PEM certification hierarchy.

```

W: CACertificatePair, forward [0] V<<W>>
    backward[1] W<<V>>

V: CACertificatePair, forward [0] U<<V>>
    backward[1] V<<U>>

Y: CACertificatePair, forward [0] V<<Y>>
    backward[1] Y<<V>>

Z: CACertificatePair, forward [0] Y<<Z>>
    backward[1] Z<<Y>>
    CACertificate,      Z<<X>>

B: UserCertificate,   Z<<B>>

```

It is assumed that each user knows his public and private keys, as well as the public keys of his certification authority. For example, C and A know X_p , and B knows Z_p .

For the above example, the certification path from A to B is:

$X<<W>>$, $W<<V>>$, $V<<Y>>$, $Y<<Z>>$, $Z<>$.

4.4 Modeling Certificates in the Directory

[8] defines the structure of the X.509 Directory. The Directory is a distributed database with entries arranged in a tree.

The **Directory Information Base (DIB)** is made up of information about objects. It is composed of directory entries, each of which consists of a collection of information on one object. Each entry is made up of attributes, each with a type and one or more values. The entries of the DIB are arranged in the form of a tree, the **Directory Information Tree (DIT)** where the vertices represent the entries. ... Every entry has a distinguished name. [8] sec.6.

Attribute is the information of a particular type concerning an object and appearing in an entry describing that object in the DIB [8] sec.7.

Attribute type is that component of an attribute which indicates the class of information given by that attribute. [8] sec.7.

Attribute value is a particular instance of the class of information indicated by an attribute type [8] sec.7.

```
Attribute ::= SEQUENCE {  
    type          Attribute Type  
    values        SET OF Attribute Value  
    -- at least one value is required --}
```

```
Attribute Type ::= OBJECT IDENTIFIER
```

```
Attribute Value ::= ANY
```

In general, we can say that the Directory can be modeled as:

```
Directory is list of object_entry  
object_entry is pair (user_name, attribute)  
attribute is pair (attribute_type, attribute_values)  
  
attribute_type ::= UserCertificate | CACertificate | CertificatePair  
(* and other attribute types not related to certificates *)  
(* when they get added, the def for attribute value has to be changed *)  
  
attribute_values is set of signed_certificates
```

Each certificate consists of the portion that relates the user's name with the user's public key, and the appended signature. The certificate is issued by an issuer, who signs the certificate and appends the signature.

```
signed_certificate is pair (certificate, signature)  
  
certificate is tuple(Int, Int, AlgId, DN,  
                    validity_period, DN, subject_pub_key_info)  
  
(* version_no                *)  
(* SN                        *)  
(* signature algid           *)  
(* issuer distinguished name  *)  
(* validity period: notBefore, notAfter *)  
(* subject distinguished name *)  
(* subject public key info: algid, public key *)  
  
validity_period is pair (UTCTime, UTCTime)  
(* UTCTime is date/time, Coordinated Universal time *)
```



```

(* notBefore*)
(* notAfter *)

subject_public_key_info is pair (AlgId, bit_string)
(* algid for public key *)
(* public key          *)

algids is pair (algid, alg_params)

```

Users are allowed to store any portion of the certification path. The number of certificates which must be obtained from the Directory can be reduced in the following cases:

1. If the two users wishing to authenticate are served by the same certification authority, then the users can unwrap each other's certificates directly.
2. If the CAs of the users are arranged in a hierarchy, a user could store the public keys, certificates and reverse certificates of all certification authorities between the user and the root of the DIT. Typically, this would involve the user knowing the public keys and certificates of only three or four certification authorities. The user would then only be required to obtain the certification paths from the common point of trust.
3. If user A frequently communicates with users certified by certification authority X, A could learn the certification path to X and the return certification path from X, making it necessary only to obtain the certificate of the other user itself from the Directory.
4. Certification authorities can cross-certify one another by bilateral agreement in order to shorten the certification path.
5. If two users have communicated before and have learned one another's certificate, they are able to authenticate without any recourse to the Directory.

4.4.1 Updating Certificate Entries

Each CA shall maintain:

- a time-stamped list of certificates it issued which have been revoked
- a time-stamped list of revoked certificates of all CAs known to the CA and certified by the CA.

Both lists shall exist, even if empty. ... CA must keep expired certificates for a while, if non-repudiation is used [7], p.68.

Expired certificates should be removed from the Directory. The maintenance of the Directory entries affected by the CAs revocation lists is the responsibility of the Directory and its users, e.g. users update their entry.

4.5 MISSI Certificates

MISSI follows X.509 standard with some additional constraints.

In MISSI, there are only 4 or 5 levels in certification hierarchy: Policy Approving Authority (PAA), which acts as the "root" of the certification tree; Policy Creation Authorities (PCAs) and Certification Authorities (CAs) which issue certificates; Organizational Notaries (ONs), and users which do not issue certificates. Currently, ONs are not implemented.

PAA is the "trusted root" and each user keeps PAA's certificate on his FORTEZZA card.

MISSI certification hierarchy is a tree, where each user is authorized only by its subordinate certification authority.

Reverse certificates are not allowed in MISSI.

Figure 4.3 shows MISSI certification hierarchy tree and what certificates are stored in the Directory for each level.

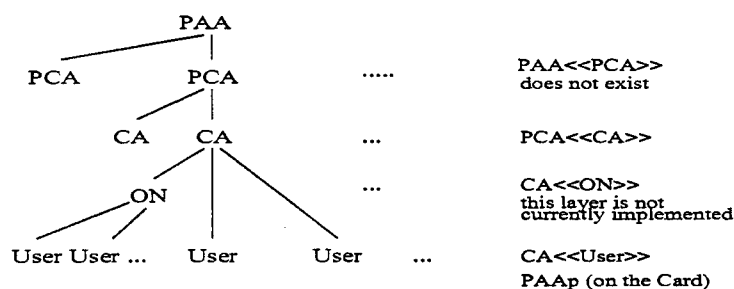


Figure 4.3: MISSI certification hierarchy.

```
forall cert, cert!: certificate, X,Y: user_name
```

```
MISSI_unique_cert:
```

```
issuer_of(cert) = X AND subject_of(cert) = Y
```

```
AND
```

```
issuer_of(cert1) = Z AND subject_of(cert1) = Y
```

```
<=> X = Z AND cert=cert1
```

Each user can log in as separate personalities, where each personality has its own DN and certificate(s).

Bibliography

- [1] *Interface Control Document for the FORTEZZA Message Security Protocol Software*. http://www.armadillo.huntsville.al.us/Fortezza_docs/obsolete.html, December 20 1994.
- [2] D. Balenson. Privacy Enhancement for Internet Electronic Mail: Part III: Algorithms, Modes, and Identifiers. RFC 1423, TIS, February 1993. <ftp://ds.internic.net>.
- [3] Dan Zhou and Shiu-Kai Chin. Verifying Privacy Enhanced Mail Functions with Higher Order Logic. In *DIMACS Workshop on Network Threats*. Rutgers University, Piscataway, NJ, December 4–6 1996.
- [4] Gerard J. Holtzman. *Validation and Verification of Communication Protocols*. Prentice Hall, New York, 1989.
- [5] Gerard J. Holzmann. Basic SPIN Manual. AT&T Bell Laboratories, Murray Hill, New Jersey, 079074.
- [6] Gerard J. Holzmann. Design and Validation of Protocols: a Tutorial. *Computer Networks and ISDN Systems*, 25:981–1017, 1993.
- [7] ITU-T. The Directory - Authentication Framework. X.509. 1989.
- [8] ITU-T. The Directory - Models. X.501, 1989.
- [9] B. Kaliski. Privacy Enhancement for Internet Electronic Mail: Part IV: Key Certification and Related Services. RFC 1424, RSA Laboratories, February 1993. <ftp://ds.internic.net>.
- [10] S. Kent. Privacy Enhancement for Internet Electronic Mail: Part II: Certificate-Based Key Management. RFC 1422, BBN, February 1993. <ftp://ds.internic.net>.

ADAPTIVE ROBUST SPREAD-SPECTRUM RECEIVERS

Stella N. Batalama
Associate Professor
Department of Electrical and Computer Engineering

University of New York at Buffalo
201 Bell Hall
Buffalo, NY 14260

Final Report for:
Summer Research Program
Rome Laboratory

Sponsored by:
Air Force Office of Scientific Research
Bolling Air Force Base, Washington, DC

And

Rome Laboratory

September 1997

ADAPTIVE ROBUST SPREAD-SPECTRUM RECEIVERS

Stella N. Batalama
Assistant Professor
Department of Electrical and Computer Engineering
State University of New York at Buffalo
E-mail: batalama@eng.buffalo.edu

Abstract

In military communications, Direct-Sequence Spread-Spectrum (DS-SS) transmissions are primarily considered as a single user communication strategy that exhibits advanced security characteristics in hostile environments. Still, the presence of other concurrent spread-spectrum signals is possible. These are intelligent hostile users that attempt to severely corrupt the signal of interest. They are highly correlated with the user of interest (aiming at perfect correlation) and completely unknown; thus no control can be exercised to, or knowledge can be acquired about, their spreading codes.

To tap on the relative merits of both non-linear and linear signal processing we propose the following DS-SS receiver for signal detection in non-Gaussian noise: A linear Minimum Mean Square Error (MMSE) or Minimum Variance Distortionless Response (MVDR) filter preceded by a vector of *adaptive* chip-based non-linearities. The novel characteristics of our approach are: First, the non-linear receiver front-end adapts itself to the unknown prevailing noise environment providing robust performance for a wide range of underlying noise distributions. Second, the linear tap-weight filter that follows the non-linearly processed chip-samples, results in a receiver that proves to be effective in combating the SS interference as well. In addition, an approximately optimum DS-SS receiver is derived which accounts for the dependence observed in the received samples due to the common interfering bits.

ADAPTIVE ROBUST SPREAD-SPECTRUM RECEIVERS

Stella N. Batalama

I. Introduction and Background

In military communications, Direct-Sequence Spread-Spectrum (DS-SS) transmissions are primarily considered as a single user communication strategy that exhibits advanced security characteristics in hostile environments. Still, the presence of other concurrent spread-spectrum signals is possible. These are intelligent hostile users that attempt to severely corrupt the signal of interest. They are highly correlated with the user of interest (aiming at perfect correlation) and completely unknown; thus no control can be exercised to, or knowledge can be acquired about, their spreading codes.

By now a considerable body of knowledge exists in the communications society and a number of single-user DS-SS interference suppression techniques have been developed [15] - [19]. Most of this work assumes Gaussian noise, primarily because other assumptions lead to mathematical difficulties. However, the Gaussian noise assumption has often been proven inadequate due to the significant impulsive nature of the background noise that results in low (but non-zero) probability of high amplitude spikes. Examples include physical or man-made impulsive interference sources such as lightening discharges, automobile ignitions, neon lights, or hostile electronic devices. In addition, the Gaussian noise is the worst type of noise in terms of minimizing channel capacity, since it is the most entropic among all infinite support, finite variance noise models. This implies that significant performance improvements can be achieved if the actual statistical characteristics of the impulsive noise are properly taken into account during receiver design. Various attempts have been made and significant effort has been placed in the development of non-Gaussian noise models. At the outset, two general groups of noise models have been identified. Those which are empirically motivated and have been developed to fit collected data and those which are physically motivated and attempt to directly model physical mechanisms [13]. Examples of physical models of non-Gaussian noise include the Class A noise [20] - [22], [24] which involves infinite sum of weighted Gaussians with increasing variances, the generalized Gaussian model [23], and the α -stable model [25] - [26]. On the other hand, highly tractable empirical model examples include the ϵ -contamination model such as the Gaussian ϵ -mixture and the Outlier model.

Signal detection in non-Gaussian noise is a well matured subject in the detection literature that has attracted interest since the early 60s. Optimum systems have been derived using non-Gaussian noise models in which the mathematical difficulties have been bypassed by adopting three critical assumptions: Independent samples, weak (or small) signal conditions, and large number of samples. The lack of knowledge of closed-form multivariate non-Gaussian probability density functions (pdfs) necessitated the first postulation. So, only first order pdfs are needed to determine the required multivariate pdfs of the received sample data vector on which

the detection algorithm is based. Further structural simplifications were achieved by the second postulation which characterizes the structures as locally optimum. The merits of the last assumption refer primarily to performance analysis/evaluation issues.

Locally optimum detection of one signal in non-Gaussian noise has been considered in [6], [8], [9] - [11]. In [8] a Neyman-Pearson approach chooses the locally optimum test by maximizing the slope of the power function at the origin while keeping a fixed false alarm rate. A Bayesian approach in [6] and [9] uses a first order Taylor expansion of the likelihoods in the likelihood ratio test. Under the assumption of independent samples the locally optimum receiver usually involves one or more non-linearities (depending on whether the samples are also identically distributed) followed by a matched-filtering operation. The optimum non-linearities are tailored to the particular (univariate) pdf of the assumed noise model. Receiver performance for specific non-linearities and corresponding noise models are reported in [13], [14]. The effect on performance when the critical assumptions are removed is examined in [12].

We note, however, that explicit apriori knowledge of the underlying noise statistics is generally not available in a realistic scenario and an alternative approach has been to use the conventional MF preceded by various ad-hoc (also reported as distribution free) non-linearities. The rationale behind their use is an attempt to de-emphasize the effects of large peaks.

To complete the presentation of critical system model considerations pertinent to this report, it remains to acknowledge and react to the presence of other spread-spectrum users that are highly correlated with the user of interest. DS-SS in non-Gaussian noise has been studied in [1], [2], [4], [14], [28] - [30]. Receiver proposals involve the use of either a conventional matched filter or a majority-vote receiver (that is a hard-limiter non-linearity per chip followed by a matched-filter operation matched to the signature of the user of interest). It was reported [14] that neither one of the above proposals is universally effective against the combination of SS interference and non-Gaussian noise. "In hopes of retaining good rejection of impulsive noise while allowing the signal cross-correlation properties to work against the multiple access interference", a sigmoid type non-linearity followed by a matched filter has also been examined [14].

To tap on the relative merits of both non-linear and linear signal processing we propose the following DS-SS receiver for signal detection in non-Gaussian noise: A linear Minimum Mean Square Error (MMSE) or Minimum Variance Distortionless Response (MVDR) filter preceded by a vector of *adaptive* chip-based non-linearities. The novel characteristics of our approach are: First, the non-linear receiver front-end adapts itself to the unknown prevailing noise environment providing robust performance for a wide range of underlying noise distributions. Second, the linear tap-weight filter that follows the non-linearly processed chip-samples, results in a receiver that proves to be effective in combating the SS interference as well. In addition, an approximately optimum DS-SS receiver is derived which accounts for the dependence observed in the received samples due to the common interfering bits.

In Section II we present the system model. In Section III we derive the approximately optimum DS-SS receiver. Distribution free non-linearities as well as noise models under consideration are introduced in Section

IV. Optimum rules for given non-linearities are also developed. Distribution free receivers are proposed in Section V. Their performance is evaluated through simulations that utilize importance sampling principles and is presented in Section VI.

II. System Model

We consider a binary DS-SS system where one SS user and $K - 1$ SS interferers transmit synchronously over a single non-Gaussian channel. The synchronous transmission framework is considered mainly for simplicity in the presentation since it is well known that every asynchronous system can be modelled as a synchronous one with higher effective multiuser population ($2K - 1$ virtual users in our case). The continuous-time received signal after carrier demodulation and low pass filtering is modeled as follows

$$r(t) = \sum_i \sum_{k=0}^{K-1} \sqrt{E_k} b_k(i) s_k(t - iT) + n(t), \quad (1)$$

where with respect to the k th user, E_k is the received energy, $b_k(i) \in \{-1, 1\}$ is the i th information bit, and $s_k(t)$ is the signature. T is the symbol period and $n(t)$ is the filtered channel non-Gaussian noise. We assume normalized signatures of the following form

$$s_k(t) = \sum_{j=1}^L c_k(j) P_{T_c}[t - (j-1)T_c], \quad (2)$$

where L is the system processing gain, $c_k(i) \in \{-1, 1\}$, $j = 1, \dots, L$, are the signature bits for the k th user, and $P_{T_c}(\cdot)$ is the spreading pulse with duration $T_c = T/L$. Focusing on one symbol interval, and after conventional chip-matched filtering and sampling at the chip rate $1/T_c$, the discrete time version of the received signal can be written as

$$\mathbf{r} = \sqrt{E_0} b_0 \mathbf{S}_0 + \sum_{k=1}^{K-1} \sqrt{E_k} b_k \mathbf{S}_k + \mathbf{n}. \quad (3)$$

We note that bold variables denote vectors in R^L , unless otherwise specified, or matrices. We also consider *user 0* as the user of interest. The problem we study in this work is the detection of the binary antipodal information signal of the user of interest in the presence of *unknown* spread-spectrum interference and additive non-Gaussian noise.

III. Approximately Optimum Receivers

The single-user detection problem in the presence of SS interference and non-Gaussian background noise can be casted as a multivariate binary hypothesis testing problem of the following form:

$$H_1 : \mathbf{r} = \sqrt{E_0} \mathbf{S}_0 + \sum_k \sqrt{E_k} b_k \mathbf{S}_k + \mathbf{n}, \quad (4)$$

$$H_0 : \mathbf{r} = -\sqrt{E_0} \mathbf{S}_0 + \sum_k \sqrt{E_k} b_k \mathbf{S}_k + \mathbf{n}, \quad (5)$$

where H_1 (H_0) corresponds to the transmission of +1 (or -1) by the user of interest. Let us define the combined interference-plus-noise (or *combined noise*) vector \mathbf{v} such that

$$\mathbf{v} = \sum_k \sqrt{E_k} b_k \mathbf{S}_k + \mathbf{n}. \quad (6)$$

Clearly, the vector \mathbf{v} is composed of L coordinates of the form

$$v_i = \sum_{k=1}^{K-1} \sqrt{E_k} b_k S_{ki} + n_i, \quad i = 1, \dots, L. \quad (7)$$

Assuming independent identically distributed non-Gaussian noise samples n_i , the combined noise vector is comprised by conditionally independent chip samples, conditioned on the interfering bit combination; that is

$$f_{i|b_k^{(p)}}(v_i | \{b_k^{(p)}\}) = f_n(v_i - \sum_k \sqrt{E_k} b_k S_{ki}), \quad (8)$$

where $f_n(\cdot)$ is the univariate noise density, S_{ki} denotes the i th signature bit of the k -th user, and $\{b_k^{(p)}\}$ is the p th interfering bit combination. The unconditional density of v_i is thus an equally weighted mixture of non-Gaussian noise densities (one per interference bit combination), i.e.

$$p_i(v_i) = \frac{1}{2^{K-1}} \sum_{p=1}^{2^{K-1}} f_n(v_i - \sum_k \sqrt{E_k} b_k^{(p)} S_{ki}). \quad (9)$$

Each mixture has a different mean that depends on the vector $[S_{1i}, S_{2i}, \dots, S_{(K-1)i}]$. In addition, due to the dependence of the combined noise coordinates on the particular interference bit combination, the multivariate pdf of the vector \mathbf{v} can not be identified as a product of univariate ones and appropriate dependence considerations should be taken into account when the combined noise approach is followed. The second-order dependence of the combined-noise coordinates is found to be

$$\begin{aligned} \rho_{i,j} &\triangleq E(v_i v_j) = E\left\{ \sum_{k=1}^{K-1} [\sqrt{E_k} b_k S_{ki} + n_i] \sum_{k=1}^{K-1} [\sqrt{E_k} b_k S_{kj} + n_j] \right\} = \\ &= \sum_{k=1}^{K-1} E_k S_{ki} S_{kj} + \sigma^2 \delta_{ij}. \end{aligned} \quad (10)$$

If $\mathbf{A}^{(k)}$ denotes the $L \times L$ signature autocorrelation matrix of user k , the correlation between the v_i and v_j coordinate of vector \mathbf{v} is given by

$$\rho_{ij} = \sum_{k=1}^{K-1} E_k \mathbf{A}_{ij}^{(k)} + \sigma^2 \delta_{ij}, \quad (11)$$

where $\mathbf{A}_{ij}^{(k)}$ is the (i, j) th element of matrix $\mathbf{A}^{(k)}$.

The strong dependence structure in the underlying model of spread-spectrum transmissions in the presence of SS interference and non-Gaussian noise suggests that receiver designs based on the assumption of independence between chips are less than optimum. Their suboptimality, however, is often justified by the intractability of the detectors that incorporate the dependence assumption. The rest of this section proceeds with the development of an approximately optimum receiver and reveals its intractability.

The likelihood ratio test for the hypothesis problem under consideration is

$$\Lambda(\mathbf{r}) = \frac{p(\mathbf{r}|H_1)}{p(\mathbf{r}|H_0)} \underset{H_0}{\gtrless} 1 \Rightarrow \frac{p_{\mathbf{v}}(\mathbf{r} - \sqrt{E_0}\mathbf{S}_0)}{p_{\mathbf{v}}(\mathbf{r} + \sqrt{E_0}\mathbf{S}_0)} \underset{H_0}{\gtrless} 1. \quad (12)$$

Under the assumption of sufficiently small signal energy ($E_0 \rightarrow 0$) we can approximate each likelihood per hypothesis by the first order Taylor expansion and the optimum decision rule (likelihood ratio) becomes

$$\begin{aligned} \frac{p_{\mathbf{v}}(\mathbf{r}) - \nabla_{\mathbf{r}}^T p_{\mathbf{v}}(\mathbf{r})\mathbf{S}_0}{p_{\mathbf{v}}(\mathbf{r}) + \nabla_{\mathbf{r}}^T p_{\mathbf{v}}(\mathbf{r})\mathbf{S}_0} &= \frac{(p_{\mathbf{v}}(\mathbf{r}) - \nabla_{\mathbf{r}}^T p_{\mathbf{v}}(\mathbf{r})\mathbf{S}_0)/p_{\mathbf{v}}(\mathbf{r})}{(p_{\mathbf{v}}(\mathbf{r}) + \nabla_{\mathbf{r}}^T p_{\mathbf{v}}(\mathbf{r})\mathbf{S}_0)/p_{\mathbf{v}}(\mathbf{r})} \underset{H_0}{\gtrless} 1 \\ \Rightarrow \frac{1 - \frac{\nabla_{\mathbf{r}}^T p_{\mathbf{v}}(\mathbf{r})}{p_{\mathbf{v}}(\mathbf{r})}\mathbf{S}_0}{1 + \frac{\nabla_{\mathbf{r}}^T p_{\mathbf{v}}(\mathbf{r})}{p_{\mathbf{v}}(\mathbf{r})}\mathbf{S}_0} \gtrless 1 &\Rightarrow \frac{-\nabla_{\mathbf{r}}^T p_{\mathbf{v}}(\mathbf{r})}{p_{\mathbf{v}}(\mathbf{r})}\mathbf{S}_0 \underset{H_0}{\gtrless} 0. \end{aligned} \quad (13)$$

Let us denote the optimum test by

$$\psi_0(\mathbf{r}) \triangleq \frac{-\nabla_{\mathbf{r}}^T p_{\mathbf{v}}(\mathbf{r})}{p_{\mathbf{v}}(\mathbf{r})}. \quad (14)$$

That is, $\psi_0(\mathbf{r}) = [\psi_{01}(\mathbf{r}), \dots, \psi_{0L}(\mathbf{r})]^T$ where

$$\psi_{0i}(\mathbf{r}) = \frac{-\frac{\partial}{\partial r_i} p_{\mathbf{v}}(\mathbf{r})}{p_{\mathbf{v}}(\mathbf{r})}. \quad (15)$$

Eq. (13) suggests that, to the extent that the combined effect of SS interference and non-Gaussian noise can be approximated by non-Gaussian colored noise and the small signal assumption holds, the optimum test is highly non-linear and it has memory, where memory refers to correlation across different chip samples. In addition, the resulting receiver involves a matched filter operation such that the non-linearly (and with memory) processed received vector samples are matched with the signature of the user of interest. Further simplification of (14) or (15) is dependent on the combined-noise effect characteristics. Next, we attempt to do such a simplification for a general noise model, the transformation noise model, that retains identical first order distributions and second order moments with those of the actual combined noise model.

Let us denote by \mathbf{z} a vector of L Gaussian random variables $\mathcal{N}(\mu_i, 1)$, where i denotes the coordinate index within vector \mathbf{z} . That is, \mathbf{z} is $\mathcal{N}(\boldsymbol{\Sigma}, \mathbf{1})$, where $\boldsymbol{\Sigma} = [\mu_1, \mu_2, \dots, \mu_L]^T$. Let \mathbf{H} be a linear operator such that $\mathbf{R} = \mathbf{H}\mathbf{H}^T$ where \mathbf{R} corresponds to a multivariate Gaussian distribution $\mathcal{N}(\boldsymbol{\Sigma}, \mathbf{R})$. We recall that given an autocorrelation matrix \mathbf{R} we can always find a unique lower triangular matrix \mathbf{H} (by Cholesky factorization). Let us denote by \mathbf{z}_c the random vector that corresponds to $\mathcal{N}(\boldsymbol{\Sigma}, \mathbf{R})$. Then the linear operator \mathbf{H} can be chosen such that

$$E\{\mathbf{z}_c \mathbf{z}_c^T\} = E\{(\mathbf{H}\mathbf{z})(\mathbf{H}\mathbf{z})^T\} = \mathbf{H}E\{\mathbf{z}\mathbf{z}^T\}\mathbf{H}^T = \mathbf{H}\mathbf{H}^T = \mathbf{R}. \quad (16)$$

Let also $\{g_i(\cdot)\}$, $i = 1, \dots, L$ be a set of zero memory non-linearities (if they exist) such that the vector $\mathbf{g}^{-1}(\cdot) \triangleq [g_1^{-1}(\cdot), g_2^{-1}(\cdot), \dots, g_L^{-1}(\cdot)]^T$ when applied to the vector \mathbf{z}_c in an element by element basis produces the vector \mathbf{v} with the desired univariate densities $p_i(v_i)$, i.e.

$$\mathbf{g}^{-1}(\mathbf{z}_c) \triangleq [g_1^{-1}(z_{c1}), g_2^{-1}(z_{c2}), \dots, g_L^{-1}(z_{cL})]^T = [v_1, v_2, \dots, v_L]^T. \quad (17)$$

We will show later how to choose such non-linearities. If such non-linearities exist then the noise \mathbf{v} is called transformation noise [5], [7]. Given the non-linearity vector $\mathbf{g}^{-1}(\cdot)$ the dependence structure of \mathbf{v} is determined by the dependence structure of \mathbf{z}_c (i.e. by \mathbf{R}). However, in practice we usually know \mathbf{R}_v (for example we can estimate \mathbf{R}_v in the absence of the desired signal). But then \mathbf{R}_{z_c} can be computed from \mathbf{R}_v through numerical integration [32].

The rest of this section refers to the selection of the non-linearities for our system model in (13)-(17). We recall that a very small number of multivariate densities can be described by closed form expressions [31]. Thus, our objective is to generate a combined noise vector \mathbf{v} with a particular dependence structure \mathbf{R}_v (that accounts for the SS interference) and a particular univariate non-Gaussian distribution $p_i(v_i)$. This can be considered as an approximation of the combined noise density $p_v(\mathbf{v})$ up to the second order statistics. We will denote this approximate density by $\tilde{p}_v(\mathbf{v})$. We also note that $p_i(\cdot)$, $i = 1, \dots, L$, have different mean but are otherwise identical. This fact actually dictates time varying non-linearities instead of a fixed non-linearity.

The noise vector \mathbf{v} obtained by passing the vector \mathbf{z} through the linear operator followed by the memoryless non-linearity vector $\mathbf{g}^{-1}(\cdot)$ is characterized by the following identity

$$\tilde{p}_v(\mathbf{v}) = \phi[\mathbf{g}(\mathbf{v})] \prod_{i=1}^m |g'_i(v_i)|, \quad (18)$$

where $\phi(\cdot)$ is the multivariate Gaussian $\mathcal{N}(\Sigma, \mathbf{R})$, $\mathbf{g}(\mathbf{v}) = [g_1(v_1), \dots, g_L(v_L)]^T$, and prime ($'$) denotes differentiation. Also m denotes the “depth” of dependence, i.e. the largest positive integer for which $\rho_{i,i+m} \neq 0$, for any $i \leq L$ and $m \leq L - i$. Here we assume without loss of generality that $m = L$. If however $m < L$ then $g_i(\cdot) = 0$, $\forall i > m$, and the vector $\mathbf{g}(\cdot)$ has only m coordinates. Thus, by (13) the approximately optimum non-linearity is now given by

$$\tilde{\psi}_0(\mathbf{r}) = [\tilde{\psi}_{01}(\mathbf{r}), \dots, \tilde{\psi}_{0L}(\mathbf{r})]^T, \quad (19)$$

where

$$\tilde{\psi}_{0i}(\mathbf{r}) = \frac{-\frac{\partial}{\partial r_i} \tilde{p}_v(\mathbf{r})}{\tilde{p}_v(\mathbf{r})}. \quad (20)$$

If we combine expressions (18), (19), (20), and (21) we obtain

$$\tilde{\psi}_0(\mathbf{r}) = - \left[\frac{\nabla \phi}{\phi}[\mathbf{g}(\mathbf{r})] \mathbf{g}'(\mathbf{r}) + \frac{\mathbf{g}''}{\mathbf{g}'}(\mathbf{r}) \right]^T, \quad (21)$$

where $\frac{\nabla \phi}{\phi}[\mathbf{g}(\mathbf{r})] \mathbf{g}'(\mathbf{r})$ identifies element by element vector multiplication. Thus, the non-linearities $g_i(\cdot)$ can be found by

$$g_i(x_i) = \Phi_i^{-1}[P_i(x_i)], \quad (22)$$

where Φ_i is the cdf of $\mathcal{N}(\mu_i, 1)$ and $P_i(\cdot)$ is the marginal cdf of the vector \mathbf{v} . Then, by differentiation, we obtain

$$g'_i(x_i) = \frac{p_i(x_i)}{\phi_i[g_i(x_i)]} \quad \text{and} \quad (23)$$

$$-\frac{g''_i}{g'_i}(x_i) = -\frac{p'_i}{p_i}(x_i) + \frac{\phi'_i}{\phi_i}[g_i(x_i)]g'_i(x_i). \quad (24)$$

We note that the transformation noise technique can be applied to any arbitrary multivariate noise density ϕ (as long as it is known analytically). If ϕ is $\mathcal{N}(\Sigma, \mathbf{R})$ then

$$-\frac{\nabla \phi}{\phi}(\mathbf{x}) = \mathbf{R}^{-1}\mathbf{x} \quad \text{and} \quad (25)$$

$$-\frac{g_i''}{g_i'}(x_i) = -\frac{p_i'}{p_i}(x_i) + g_i'(x_i)g_i(x_i). \quad (26)$$

In summary, the approximately optimum single-user DS-SS receiver in the presence of SS interference and non-Gaussian noise is structured as $[\tilde{\psi}_0(\mathbf{r})]^T \mathbf{S}_0$ where pertinent quantities are found by (21)-(26).

To build this receiver we need to know the matrix \mathbf{R} and the univariate densities $\tilde{p}_i(v_i)$, $i = 1, \dots, L$. The matrix \mathbf{R} can be numerically evaluated from matrix \mathbf{R}_v , [32], which in turn can be sample-average estimated in the absence of the desired user signal. On the other hand, the set $\{p_i(v_i)\}$, $i = 1, \dots, L$, requires a prohibitively intensive evaluation effort. This should be a set of densities that approximate sufficiently close the mixtures of non-Gaussians; to that extent, the original combined-noise multivariate distribution is approximated by an equivalent model with identical first order distributions and second order moments. We conclude this section by commenting that if we want to avoid the complexity that results from the numerical integration in calculating \mathbf{R} from \mathbf{R}_v we can use a reversed noise modeling as described in Appendix I.

IV. Distribution Free Non-linearities

It is clear that the independence assumption across received chip samples within a symbol period offers tremendous mathematical simplifications. However, the dependence structure imposed in the model by the presence of other spread spectrum interferers necessitates the use of multivariate models whose distributions cannot be identified as products of univariate ones any more. On the other hand, not many multivariate densities of closed-form are known.

The set of the weak-signal optimum non-linearities derived in the previous section is related to a particular multivariate density (cf. eq. (15) and (18)). Purely theoretically, for a given set of non-linearities we can always identify the noise model for which they are optimum by solving the differential equation in (18), i.e.

$$p_v(\mathbf{r}) = K \exp \int_0^{r_1} \dots \int_0^{r_L} \psi_{01}(\mathbf{y}) \dots \psi_{0L}(\mathbf{y}) dy_1 \dots dy_L, \quad (27)$$

where $\mathbf{y} = [y_1, \dots, y_L]^T$.

Similarly and still theoretically, we can identify the relationship between the optimum likelihood ratio test and the weak-signal optimum test by substituting (27) to the test in (12).

Clearly, the transformation noise model exhibits reasonable tractability and it can be considered as an approximation to the actual noise that retains identical to the actual model first order densities and second order moments as identified in the previous section. However, the most important contribution of the developments in the previous section to the rest of this work is the structure of the optimum receiver. The first term $[\mathbf{R}^{-1}g(\mathbf{r})]^T \mathbf{S}_0$ in (21) involves two parts. One that is related to the dependence structure which refers to the SS interference

effect in our case, and a second part that is related to the presence of non-Gaussian noise. In particular, the structure of the first term consists of the weak signal optimum non-linearity followed by the MMSE optimum detector for the same signal in Gaussian colored noise. This observation stands as our main motivation and justification to our proposal for non-linear DS-SS receivers. In fact, we propose receivers that involve a non-linear signal processing front-end followed by an MMSE (or MVDR) linear filter. The non-linear front-end consists of a set of memoryless non-linearities (one per chip sample of the received signal) that are in general non-identical. They limit the output excursions of the noise and have a whitening effect in the sense of a “smoother” output spectrum. A few comments on the proposed distribution-free non-linearities follow.

We consider only non-linearities that are odd-symmetric around the origin. This is justified by our choice to consider additive noise models with symmetric pdfs. In particular we consider the $\text{sgn}(\cdot)$ non-linear pre-processing per chip sample (also referred to as a hard-limiter), as well as two variable level soft-limiters such as the puncher and the clipper. All of them are shown in Fig. 1.

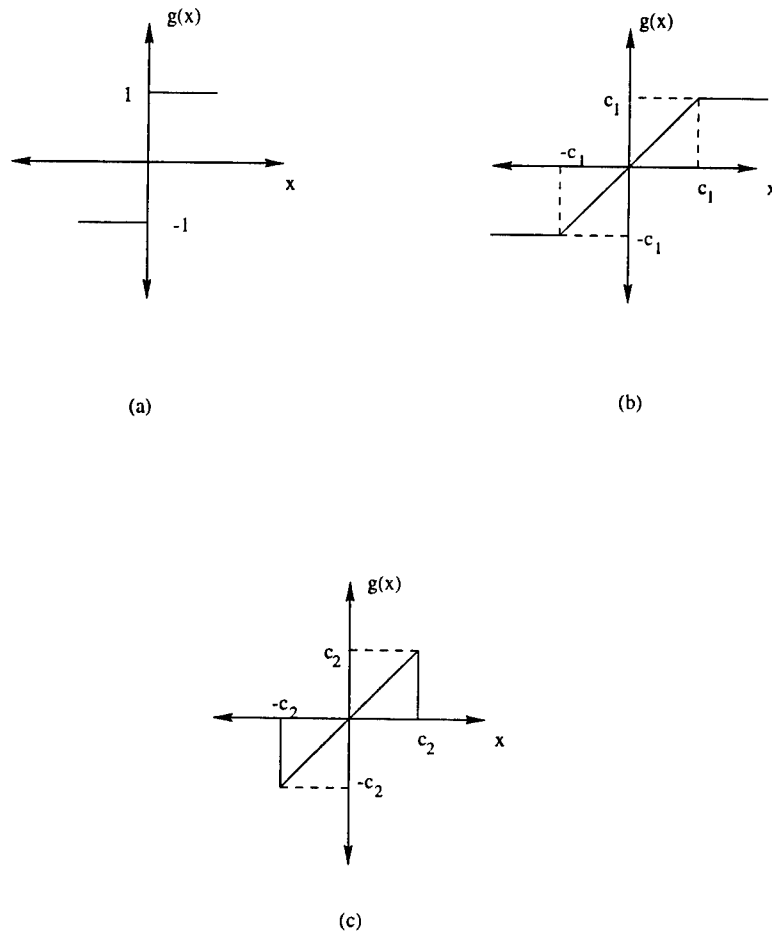


Figure 1: (a) Hard-limiter, (b) Clipper, (c) Puncher.

1. Optimum rules for fixed non-linearities

The hard-limiter non-linearity followed by a matched filter and a majority vote rule has been considered in [4] for a DS-SS system, while in [14] its performance has been evaluated under the convenient assumption of asymptotically long spreading codes. Although there is no optimality associated with either the selection of the sign non-linearity, or the matched filtering that follows, or even the final decision rule (majority vote), the operational simplicity of both the front and the back-end of the receiver is appealing. Appreciating the operational simplicity of both the sign non-linearity and the MF linear filter, we maintain these operations and we develop the optimum final decision rule for the system proposed in [4]. The optimum rule is given by the following proposition. The proof is included in Appendix II.

Proposition 1 *The optimum decision rule for the information bit of the user of interest in unknown SS interference and additive noise with univariate distribution F that assumes*

- (i) *a sign non-linearity per received chip sample followed by matched filtering (matched to the signature of the user of interest), and*
- (ii) *independent noise samples*

is given by

$$E_{b_{k,k=1,\dots,K-1}} \left\{ \prod_{i=1}^L \left[F \left(\frac{\sqrt{E_0} \frac{1}{L} + \sum_{k=1}^{K-1} \sqrt{E_k} b_k S_{ki} S_{0i}}{1/\sqrt{L}} \right) \right]^{\frac{1+u_i}{2}} \cdot \left[F \left(\frac{-\sqrt{E_0} \frac{1}{L} - \sum_{k=1}^{K-1} \sqrt{E_k} b_k S_{ki} S_{0i}}{1/\sqrt{L}} \right) \right]^{\frac{1-u_i}{2}} \right. \\ \left. - \prod_{i=1}^L \left[F \left(\frac{-\sqrt{E_0} \frac{1}{L} + \sum_{k=1}^{K-1} \sqrt{E_k} b_k S_{ki} S_{0i}}{1/\sqrt{L}} \right) \right]^{\frac{1+u_i}{2}} \cdot \left[F \left(\frac{\sqrt{E_0} \frac{1}{L} - \sum_{k=1}^{K-1} \sqrt{E_k} b_k S_{ki} S_{0i}}{1/\sqrt{L}} \right) \right]^{\frac{1-u_i}{2}} \right\} \quad (28)$$

where $u_i = \text{sgn}(r(i)S_{0i})$, $i = 1, \dots, L$. \square

The decision rule obtained by Proposition 1 is of exponential complexity in the number of spread spectrum interferers and it is analogous to the optimum multiuser detector in [27]. It can be used, however, to identify the level of suboptimality of the handy majority-vote receiver.

V. Non-linear DS-SS Receivers

To combine the best features of linear filtering and non-linear signal processing, we propose an adaptive non-linear receiver for the detection of the information bit of the user of interest in a non-Gaussian impulsive noise environment that exhibits the general structure of Fig. 2.

The receiver involves a non-linear pre-processing front-end followed by a linear tap-weight filter. The non-linearities are in general non identical. As discussed in Section III, approximately optimum performance can be obtained if the non-linearities are chosen on the basis of explicit apriori knowledge of the underlying combined-noise statistics. In realistic applications, however, this information is not usually available and our approach

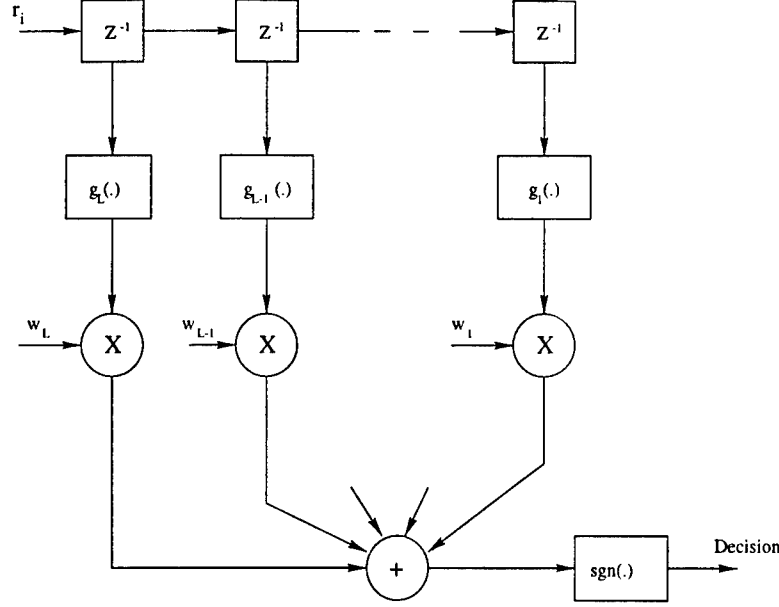


Figure 2: General structure of a non-linear DS-SS receiver

proceeds by choosing a distribution free non-linearity which adapts its parameters to the unknown prevailing noise environment. This way we develop a receiver that is efficient and robust for a wide range of underlying noise distributions. In particular, we choose to compare the performance of the sign non-linearity, the clipper, and the puncher. Out of these three non-linearities the hard-limiter is fixed while the other two are adaptive with respect to the cutoff parameter shown in Fig. 1.

The non-linearly processed chip samples drive a linear tap-weight filter $\mathbf{w} = [w_1, \dots, w_L]^T$ whose taps are determined according to the MMSE or MVDR criterion. Under both criteria the tap-weight filters are determined by the statistics of the non-linearly processed received signal samples. If $\mathbf{g}(\cdot) = [g_1(\cdot), \dots, g_L(\cdot)]$ denotes the vector of the non-linearities then the test statistic for the detection of the information bit of the user of interest is determined by the inner product

$$\langle \mathbf{g}(\mathbf{r}), \mathbf{w} \rangle \quad (29)$$

and \mathbf{w} is given by the following proposition. The proof is outlined in Appendix II.

Proposition 2 *Given the non-linearity $\mathbf{g}(\cdot)$ then*

(i) the MMSE linear tap-weight vector \mathbf{w} is given by

$$\mathbf{w} = \mathbf{R}^{-1} E\{\mathbf{g}(\mathbf{r})b_0\} \quad (30)$$

and

(ii) the MVDR linear tap-weight vector \mathbf{w} that is distortionless in the \mathbf{S}_0 direction is given by

$$\mathbf{w} = \frac{1}{\mathbf{S}_0^T \mathbf{R}^{-1} \mathbf{S}_0} \mathbf{R}^{-1} \mathbf{S}_0. \quad (31)$$

For both (i) and (ii) the matrix \mathbf{R} is given by

$$\mathbf{R} = E\{\mathbf{g}(\mathbf{r})\mathbf{g}^T(\mathbf{r})\}. \quad \square \quad (32)$$

The advantages of the particular parametric non-linearities (clipper and puncher) together with the adaptive evaluation of the cutoff parameter, result in a structure that exhibits the favorable characteristics of both conventional linear filtering and non-linear signal processing. Clearly, the cutoff parameter c is related to our confidence on the interval $[-c, c]$ and the fraction of the received data which we expect to fall in the linear region of the receiver non-linearity. Thus, the more Gaussian (non-impulsive) the environment is, the larger the cut-off parameter value and the closer to the conventional linear tap-weight MMSE or MVDR our receiver structure is. Thus the cutoff parameter c is expected to track the impulsiveness of the environment and the overall structure converges (as $c \rightarrow \infty$) to the conventional linear receiver when the channel exhibits Gaussian behavior.

While the merits of an adaptive non-linearity are clear, receiver operational robustness for a wide range of impulsiveness in the underlying noise environment necessitates particular attention to the design criterion chosen for the adaptive evaluation of c . Arguably, least squares criteria are not appropriate in non-Gaussian environments, largely due to their non-robustness against a small number of large errors (outliers) in the data set. This argument, together with the nature of the ultimate performance evaluation measure of digital communication systems, motivates the development of a simple and elegant algorithm that adapts c in a way that minimizes the probability of error (Bit-Error-Rate) at the output of the receiver.

In this context, let us assume without loss of generality that the receiver employs the same non-linearity per chip sample $g(\cdot, c)$ parametrized by the cutoff parameter c . Let us then denote the output of the receiver by $u(\mathbf{r}, c) \triangleq \text{sgn} \langle \mathbf{g}(\mathbf{r}, c), \mathbf{w} \rangle$. If we define $\rho(\cdot)$ such that

$$\rho(\mathbf{r}_0, \mathbf{r}_1; c) \triangleq \frac{1}{2} \{ \pi_0 [1 + u(\mathbf{r}_0, c)] + \pi_1 [1 - u(\mathbf{r}_1, c)] \}, \quad (33)$$

where $\pi_0 = \pi_1 = 1/2$ are the a priori probabilities of hypothesis H_0 and H_1 , then we observe that the probability of error is equal to

$$P_e(c) = E[\rho(\mathbf{r}_0, \mathbf{r}_1; c)], \quad (34)$$

where \mathbf{r}_0 and \mathbf{r}_1 correspond to received data vectors from H_0 and H_1 respectively. Thus, the so defined function $\rho(\cdot)$ (cf. eq. (33)) provides a measure for the distortion at the output of the receiver. Indeed, the bracket terms are both zero when the receiver makes the correct decision and strictly positive otherwise. Based on stochastic gradient techniques and exploiting the property in (34) we develop an adaptive procedure that iteratively adjusts the cutoff parameter c to minimize the probability of error at the output of the receiver:

$$c_{n+1} = c_n - \alpha_n x_n(c_n), \quad (35)$$

where

$$x_n(c) \stackrel{\text{def}}{=} \frac{1}{2d_n} [\rho(\mathbf{r}_{0,n}, \mathbf{r}_{1,n}; c + d_n) - \rho(\mathbf{r}_{0,n}, \mathbf{r}_{1,n}; c - d_n)], \quad (36)$$

and $\{d_n\}$ and $\{\alpha_n\}$ are monotonically decreasing sequences of positive numbers such that $\sum \alpha_n = \infty$, $\sum \alpha_n d_n < \infty$, and $\sum \alpha_n^2 d_n^{-2} < \infty$.

Summarizing, the proposed non-linear receiver structure involves adaptive non-linearities of the form of a puncher or a clipper and it is determined by the set of coupled expressions (30) or (31) and (33)-(36).

VI. Numerical and Simulation Comparisons

As mentioned in the introduction, non-Gaussian noise models can be categorized into two groups: Those that are empirically motivated and those that are physically motivated. In this work we consider the following noise models: the Laplace, the Cauchy, the Gaussian ϵ -mixture, and the Outlier model. The Laplace noise belongs to the class of generalized Gaussian densities. This class involves symmetric unimodal densities derived by generalizing the Gaussian density to obtain a variable rate of exponential decay [8], [23]. Their general form is given by

$$f_n(x) = [b \eta(\sigma_n, b) / 2\Gamma(1/b)] \exp\{-\eta(\sigma_n, b)|x|^b\}, \quad (37)$$

where $\eta(\sigma, b) \triangleq \sigma^{-1}[\Gamma(3/b)/\Gamma(1/b)]^{1/2}$, b is a positive constant that controls the rate of decay, $\Gamma(\cdot)$ is the gamma function, and σ_n^2 is the noise variance. The above expression for $b = 1$ reduces to the Laplace density, while for $b = 2$ it is the Gaussian pdf. The generalized Gaussian class has been used in the past to model non-Gaussian noise with a variable level of impulsive nature controlled by the rate of exponential decay. While the Laplace density is not the most representative one with respect to “heavy-tailness”, it is used here due to its mathematical tractability. A density with extremely heavy tails is the Cauchy density which has been chosen as a second noise model. The Cauchy model belongs to the α -stable class which has been recently introduced as a non-Gaussian impulsive noise class of densities [25] - [26].

The third model under consideration is the Gaussian ϵ -mixture model. The general form of the ϵ -mixture model is given by

$$f_\epsilon(x) = (1 - \epsilon)f_0(x) + \epsilon f_1(x), \quad (38)$$

where $\epsilon \in [0, 1]$ accounts for the probability under which the noise is f_1 distributed. The pdf f_0 is usually taken to be Gaussian representing the background noise (non-impulsive) such as receiver thermal noise. The contaminating pdf can be chosen arbitrarily. If $f_1(x)$ is taken to be Gaussian (with high variance) then we have the Gaussian ϵ -mixture model. In that case and for particular ranges of values for the ratio of the corresponding variances, the underlying noise model relates to the Class A model. We recall that the Class A model involves densities that can be written as an infinite series of weighted Gaussians with increasing variances. Suggested approximations involve M -term truncations [13]. The primary advantage of the ϵ -mixture model is analytic simplicity.

A similarly highly tractable empirical model is the outlier model which can also be considered as a limiting case of a mixture model with $f_1(\cdot)$ chosen to be a delta function at $\mp\infty$. In this case we can equivalently interpret the parameter ϵ as the percentage of outlying values.

In this section we consider three groups of receivers. The first one consists of receiver designs that take no provision for impulsive noise effects. They are the conventional signature matched-filter, the conventional decorrelator, and the conventional MVDR filter. The second group includes the hard-limiting majority-vote rule and the hard-limiting optimum fusion rule. Finally, three different MVDR designs are considered with hard-limiting, clipping, or punching front-end non-linear processing. As we explained earlier, the clipping or punching parameter may be selected adaptively by (35) and (36).

Fig. 3 presents full comparisons over the 0 to 16dB nominal SNR range for the Gaussian ϵ -mixture noise model.

Fig. 4 carries out the same studies for the Outlier ϵ -mixture model.

Fig. 5 accounts for Cauchy background noise over the 0 to 16dB signal power range.

Figs. 6, 7, and 8 present the same studies for Laplace distributed noise and various total SNR ranges. A quick overall comparison between Fig. 5 and Figs. 6, 7, and 8 indicates that the Laplace noise does not represent a severely impulsive operating environment.

Throughout these studies we assume presence of 3 (three) spread spectrum interferers. Their signature cross-correlation with the spread spectrum signal of interest is set equal to approximately 50%.

VII. Conclusions

We considered the problem of robust detection of a DS-SS signal in the presense of unknown highly correlatex SS interferers and additive non-Gaussian noise. The general structure of our proposed receiver exhibits the merits of both non-linear and linear signal processing. It is either a linear Minimum Mean Square Error (MMSE) or a linear Minimum Variance Distortionless Response (MVDR) filter preceded by a vector of *adaptive* chip-based non-linearities. The novel characteristics of our approach are: First, the non-linear receiver front-end adapts itself to the unknown prevailing noise environment providing robust performance for a wide range of underlying noise distributions. Second, the linear tap-weight filter that follows the non-linearly processed chip-samples, results in a receiver that proves to be effective in combating the SS interference as well. Numerical and simulation results included in this report compared the proposed receiver for three different distribution-free front-end non-linearities (hard-limiter, clipper, and puncher) as well as for particular non-Gaussian noise models (Laplace, Cauchy, Gaussian ϵ -mixture, and Outlier model).

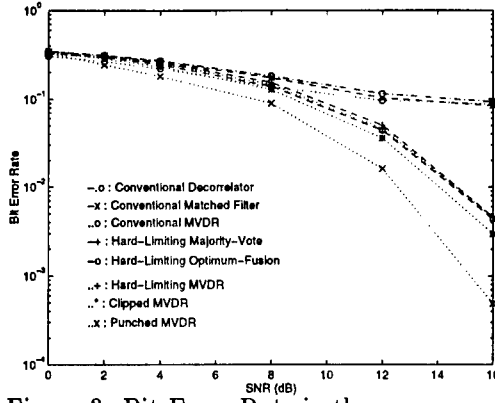


Figure 3: Bit-Error-Rate in the presence of unknown SS interference and Gaussian ϵ -mixture noise ($\epsilon = 0.2, \gamma^2 = 1000$).

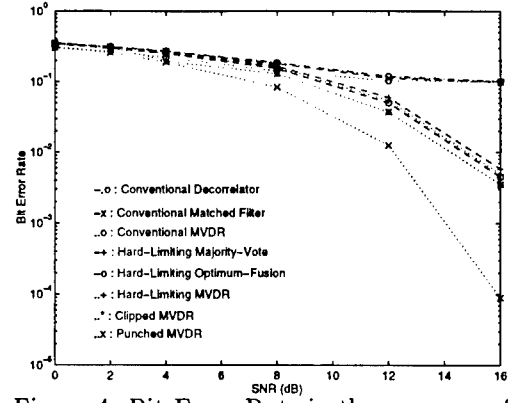


Figure 4: Bit-Error-Rate in the presence of unknown SS interference and Outlier noise ($\epsilon = 0.2$).

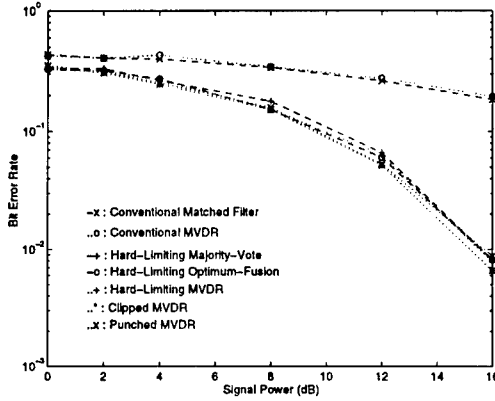


Figure 5: Bit-Error-Rate in the presence of unknown SS interference and Cauchy noise.

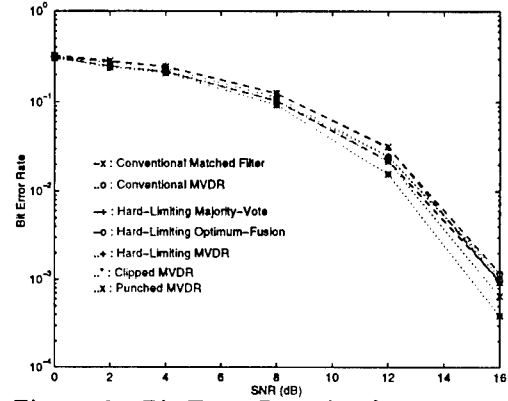


Figure 6: Bit-Error-Rate in the presence of unknown SS interference and Laplacian noise.

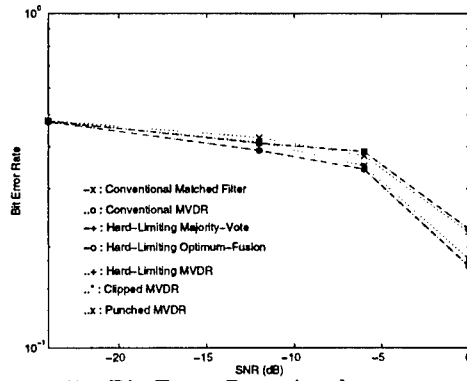


Figure 7: Bit-Error-Rate in the presence of unknown SS interference and Laplacian noise.

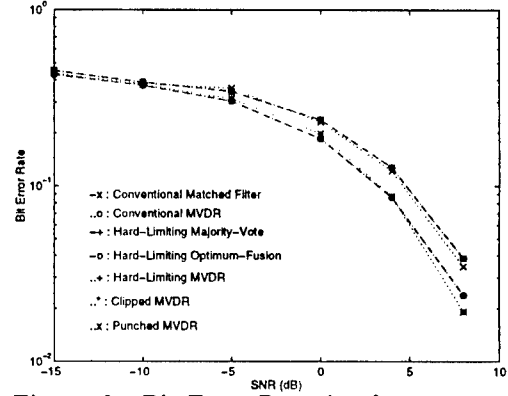


Figure 8: Bit-Error-Rate in the presence of unknown SS interference and Laplacian noise.

APPENDIX I

Let us denote by \mathbf{z} a vector of L i.i.d. $\mathcal{N}(0, 1)$ random variables and let $g^{-1}(\cdot)$ denote the zero memory invertible non-linearity (if it exists) that can transform the vector \mathbf{z} into a vector θ consisting of L i.i.d. random variables of a particular common non-Gaussian univariate pdf $p_i(\theta_i)$ and common variance σ^2 . Let us also denote by \mathbf{H} a lower triangular matrix of appropriate dimensionality determined by the set $\{\rho_{i,j}\}, i, j = 1, \dots, L$, such that $\mathbf{H}\theta = \mathbf{v}$. That is, given \mathbf{R}_v , \mathbf{H} is obtained by Cholesky factorization of \mathbf{R}_v :

$$\mathbf{R}_v = E\{\mathbf{v}\mathbf{v}^T\} = E\{(\mathbf{H}\theta)(\mathbf{H}\theta)^T\} = \mathbf{H}E\{\theta\theta^T\}\mathbf{H}^T = \sigma^2\mathbf{H}\mathbf{H}^T, \quad (39)$$

where σ^2 is the variance of θ_i , $i = 1, \dots, L$. If m is the dimensionality of the matrix \mathbf{H} controlled by the superposition of the signature autocorrelation matrices $\mathbf{A}^{(k)}$, then for a continuously differentiable univariate density $p_i(v_i)$, the multivariate density of the noise vector \mathbf{v} is

$$p_v(\mathbf{v}) = |\mathbf{H}^{-1}| \prod_{i=1}^m p_i[(\mathbf{H}^{-1}\mathbf{v})_i]. \quad (40)$$

Then, the optimum detector under small signal assumptions is

$$\psi(\mathbf{r}) = [\mathbf{H}^{-1}\mathbf{r}]^T \mathbf{g}(\mathbf{H}^{-1}\mathbf{r}), \quad (41)$$

with $g(r_i) = \frac{-p'_i}{p_i}(r_i)$. \square

APPENDIX II

Proof of Proposition 1:

The likelihood ratio test for the underlying structure is given by

$$\frac{\pi_1 P_1(u_1, \dots, u_L)}{\pi_0 P_0(u_1, \dots, u_L)} \underset{H_0}{\overset{H_1}{\gtrless}} 1 \Rightarrow P_1(u_1, \dots, u_L) - P_0(u_1, \dots, u_L) \underset{H_0}{\overset{H_1}{\gtrless}} 0, \quad (42)$$

where $P_1(\cdot)$ and $P_0(\cdot)$ denote probabilities under H_1 and H_0 respectively, and $\pi_1 = \pi_0 = 1/2$. We note that the binary random variables u_i are not independent; however they are conditionally independent. This implies that the test statistic can be simplified as follows

$$E_{b_k, k=1, \dots, K-1} \left\{ \prod_{i=1}^L P_1(u_i | \{b_k\}) - \prod_{i=1}^L P_0(u_i | \{b_k\}) \right\}. \quad (43)$$

Under H_1 ($b_0 = 1$),

$$w_i = \text{sgn}\{r(i)s(i)\} = \text{sgn}\left\{\left[\sqrt{E_0}S_{0i} + \sum_{k=1}^{K-1} \sqrt{E_k}b_k S_{ki} + n_i\right]S_{0i}\right\}, \quad (44)$$

which implies that $u_i = 1$ with probability $F\left(\frac{\sqrt{E_0}\frac{1}{L} + \sum_{k=1}^{K-1} \sqrt{E_k}b_k S_{ki}S_{0i}}{1/\sqrt{L}}\right)$. Similarly, $u_i = -1$ with probability $F\left(\frac{-\sqrt{E_0}\frac{1}{L} - \sum_{k=1}^{K-1} \sqrt{E_k}b_k S_{ki}S_{0i}}{1/\sqrt{L}}\right)$. Thus,

$$P_1(u_i | \{b_k\}) = \left[F\left(\frac{\sqrt{E_0}\frac{1}{L} + \sum_{k=1}^{K-1} \sqrt{E_k}b_k S_{ki}S_{0i}}{1/\sqrt{L}}\right) \right]^{\frac{1+u_i}{2}} \cdot \left[F\left(\frac{-\sqrt{E_0}\frac{1}{L} - \sum_{k=1}^{K-1} \sqrt{E_k}b_k S_{ki}S_{0i}}{1/\sqrt{L}}\right) \right]^{\frac{1-u_i}{2}}. \quad (45)$$

$P_0(u_i|\{b_k\})$ can be expressed in a similar manner.

For the special case where $F(\cdot)$ is the cdf of the Gaussian ϵ -mixture $[f(x) = (1-\epsilon)f_0(x) + \epsilon f_1(x)]$ distribution, the test can be further simplified to

$$\begin{aligned}
& E_{b_k, k=1, \dots, K-1} \left\{ \prod_{i=1}^L \left[1 - \left\{ (1-\epsilon)Q \left(\frac{\sqrt{E_0} \frac{1}{L} + \sum_{k=1}^{K-1} \sqrt{E_k} b_k S_{ki} S_{0i}}{\frac{1}{L} \sigma_1} \right) \right. \right. \right. \\
& \quad \left. \left. + \epsilon Q \left(\frac{\sqrt{E_0} \frac{1}{L} + \sum_{k=1}^{K-1} \sqrt{E_k} b_k S_{ki} S_{0i}}{\frac{1}{L} \sigma_2} \right) \right\} \right]^{\frac{1+\mathbf{u}_i}{2}} \cdot \\
& \quad \cdot \left[(1-\epsilon)Q \left(\frac{\sqrt{E_0} \frac{1}{L} + \sum_{k=1}^{K-1} \sqrt{E_k} b_k S_{ki} S_{0i}}{\frac{1}{L} \sigma_1} \right) + \epsilon Q \left(\frac{\sqrt{E_0} \frac{1}{L} + \sum_{k=1}^{K-1} \sqrt{E_k} b_k S_{ki} S_{0i}}{\frac{1}{L} \sigma_2} \right) \right]^{\frac{1-\mathbf{u}_i}{2}} - \\
& \quad - \prod_{i=1}^L \left[(1-\epsilon)Q \left(\frac{\sqrt{E_0} \frac{1}{L} - \sum_{k=1}^{K-1} \sqrt{E_k} b_k S_{ki} S_{0i}}{\frac{1}{L} \sigma_1} \right) + \epsilon Q \left(\frac{\sqrt{E_0} \frac{1}{L} - \sum_{k=1}^{K-1} \sqrt{E_k} b_k S_{ki} S_{0i}}{\frac{1}{L} \sigma_2} \right) \right]^{\frac{1+\mathbf{u}_i}{2}} \cdot \\
& \quad \cdot \left[1 - \left\{ (1-\epsilon)Q \left(\frac{\sqrt{E_0} \frac{1}{L} - \sum_{k=1}^{K-1} \sqrt{E_k} b_k S_{ki} S_{0i}}{\frac{1}{L} \sigma_1} \right) + \epsilon Q \left(\frac{\sqrt{E_0} \frac{1}{L} - \sum_{k=1}^{K-1} \sqrt{E_k} b_k S_{ki} S_{0i}}{\frac{1}{L} \sigma_2} \right) \right\} \right]^{\frac{1-\mathbf{u}_i}{2}} \right\}, \quad (46)
\end{aligned}$$

where σ_0^2 and σ_1^2 are the variances of f_0 and f_1 respectively, where $Q(x) = 1 - \Phi(x)$.

Proof of Proposition 2:

- (i) The filter \mathbf{w} in (30) is the Wiener solution for a linear tap-weight filter with input vector $\mathbf{g}(\mathbf{r})$.
- (ii) The filter \mathbf{w} in (31) is the solution to the optimization problem that minimizes the output variance under the constraint that $\mathbf{w}^T \mathbf{S}_0 = 1$. \square

References

- [1] B. Aazhang and H. V. Poor, "Performance of DS/SSMA communications in impulsive channels-Part 1: Linear correlation receivers," *IEEE Trans. Commun.*, vol. COM-35, No. 11, pp. 1179-1188, Nov. 1987.
- [2] L. A. Rusch and H. V. Poor, "Multiuser detection techniques for narrowband interference suppression in spread spectrum communications", *IEEE Trans. Commun.*, vol. 43, No. 2/3/4, pp. 1725-1737, Feb./Mar./Apr. 1995.
- [3] D. R. Anderson and P. A. Wintz, "Analysis of a spread-spectrum multiple-access system with a hard limiter", *IEEE Trans. Commun.*, vol. COM-17, No. 2, pp. 285-290, Apr. 1969.
- [4] B. Aazhang and H. V. Poor, "Performance of DS/SSMA communications in impulsive channels-Part II: Hard-limiting correlation receivers", *IEEE Trans. Commun.*, vol. 36, 1988
- [5] H. V. Poor and J. B. Thomas, "Memoryless discrete-time detection of a constant signal in m-dependent noise", *IEEE Trans. Info. Theory*, vol. II-25, No. 1, pp. 88-97, Jan. 1979.

- [6] A. D. Spaulding and D. Middleton, "Optimum reception in an impulsive interference environment-Part I: Coherent detection", *IEEE Trans. Commun.*, vol. COM-25, No. 9, pp. 910-923, Sept. 1977.
- [7] A. B. Martinez, P. F. Swaszek, and J. B. Thomas "Locally optimal detection in multivariate non-Gaussian noise", *IEEE Trans. Info. Theory*, vol. IT-30, No. 6, pp. 815-822, Nov. 1985.
- [8] J. H. Miller and J. B. Thomas, "Detectors for discrete-time signals in non-gaussian noise", *IEEE Trans. Info. Theory*, vol. IT-18, No. 2, pp. 241-250, Mar. 1972.
- [9] A. D. Spaulding and D. Middleton, "Optimum reception in an impulsive interference environment-Part II: Incoherent reception", *IEEE Trans. Commun.*, vol. COM-25, No. 9, pp. 924-934, Sept. 1977.
- [10] S. A. Kassam, "Locally robust array detectors for random signals", *IEEE Trans. Info. Theory*, vol. 24, No. 3, pp. 309-316, 1978.
- [11] J. Capon, "On the asymptotic efficiency of locally optimum detectors", *IRE Trans. Info. Theory*, pp. 67-71, 1961.
- [12] A. D. Spaulding, "Locally optimum and suboptimum detector performance in a non-gaussian interference environment", *IEEE Trans. Commun.*, vol. COM-33, No. 6, pp. 509-517, June 1985.
- [13] K. S. Vastola, "Threshold detection in narrow-band non-Gaussian noise", *IEEE Trans. Commun.*, vol. COM-32, No. 2, pp. 134-139, Feb. 1984.
- [14] B. Aazhang and H. V. Poor, "An analysis of nonlinear direct-sequence correlators", *IEEE Trans. Commun.*, vol. 37, No. 7, pp. 723-731, July 1989.
- [15] U. Madhow, M. L. Honig and S. Verdu, "Blind adaptive multiuser detection", *IEEE Trans. Info. Theory*, vol. 41, pp. 944-960, July 1995.
- [16] U. Madhow and M. L. Honig, "MMSE interference suppression for direct-sequence spread-spectrum CDMA", *IEEE Trans. Commun.*, vol. 42, pp. 3178-3188, Dec. 1994.
- [17] M. K. Varanasi and B. Aazhang, "Multistage detection in asynchronous code-division multiple access communications", *IEEE Trans Commun.*, vol. 38, pp. 509-519, April 1990.
- [18] A. Duel-Hallen, "Decorrelating decision-feedback multiuser detection for synchronous code-division multiple-access channels", *IEEE Trans. Commun.*, vol. 41, pp. 285-290, Feb. 1993.
- [19] D. A. Pados and S. N. Batalama, "Low complexity blind detection of DS-CDMA Signals: Auxiliary-Vector receivers", *IEEE Trans. Commun.*, to appear.
- [20] D. Middleton, "Statistical physical models of urban radio noise environments, Part I: Foundation", *IEEE Trans. Electrom. Compat.*, pp. 38-56, May 1972.

- [21] D. Middleton, "Man-made noise in urban environments and transportation systems", *IEEE Trans. Commun.*, pp. 1232-1241, Nov. 1973.
- [22] D. Middleton, "Statistical physical models of electromagnetic interference", *IEEE Trans. Electrom. Compat.*, pp. 106-127, Aug. 1972.
- [23] S. N. Batalama and D. Kazakos, "On the generalized Cramer-Rao bound for the estimation of the location", *IEEE Trans. Signal Proc.*, vol., No., pp. 487-492, Feb. 1997.
- [24] S. Kassam, *Signal Detection in non-Gaussian noise*, Springer-Verlag, 1988.
- [25] C. L. Nikias and M. Shao, *Signal Processing with Alpha-Stable distributions and applications*, Wiley, 1995.
- [26] A. Tsihrintzis and C. L. Nikias, "Performance of optimum and suboptimum receivers in the presence of impulsive noise modelled as an α -stable process", *IEEE Trans. Commun.*, vol., No., pp. , Apr. 1995.
- [27] S. Verdu, "Minimum probability of error for asynchronous Gaussian multiple-access channels," *IEEE Trans. Info. Theory*, vol. 32, pp. 85-96, Jan. 1986.
- [28] R. D. Lou and L. B. Milstein, "Error probability bounds and approximations for DS spread spectrum communication systems with multiple tone or multiple access interference", *IEEE Trans. Commun.*, vol. 32, No. 5, pp. 493-502, May 1984.
- [29] R. A. Iltis and L. B. Milstein, "Performance analysis of narrow-band interference rejection techniques in DS spread-spectrum systems", *IEEE Trans. on Commun.*, vol. 32, No. 1, pp. 1169-1177, Nov. 1984.
- [30] L. Li and L. B. Milstein, "Rejection of narrow-band interference in PN spread-spectrum systems using transversal filters", *IEEE Trans. on Commun.*, vol. 30, No. 5, pp. 925-928, May 1982.
- [31] N. L. Johnson and S. Kotz, *Distributions in Statistics: Continuous Multivariate Distributions*, Wiley 1972.
- [32] S. T. Li and J. L. Hammond, "Generation of pseudo-random numbers with specified univariate distributions and correlation coefficients", *IEEE Trans. Syst. Man Cyber.*, vol. SMC-5, No. 5, pp. 557-561, Sept. 1975.

LOWERING THE COMPUTATIONAL COMPLEXITY OF STAP RADAR SYSTEMS

Adam W. Bojanczyk
Associate Professor
Department of Electrical Engineering

Cornell University
335 Rhodes Hall
Ithaca, NY 14853-3801

Final Report for:
Summer Research Program
Rome Laboratory

Sponsored by:
Air Force Office of Scientific Research
Bolling Air Force Base, Washington, DC

And

Rome Laboratory

September 1997

LOWERING THE COMPUTATIONAL COMPLEXITY OF STAP RADAR SYSTEMS

Adam W. Bojanczyk
School of Electrical Engineering
Cornell University

Abstract

Space-time adaptive processing (STAP) refers to a class of methods for detecting targets using an array of sensors. The output of the array is weighted using data collected from the sensors over a given period of time. An optimal weight calculation method exists: however, this method is usually computationally impractical. Therefore, various suboptimal methods have been proposed to lower the computational burden of the optimal method. This paper describes one of such methods. The method attempts to exploit the structure and the low rank characteristics of the sample covariance matrix.

LOWERING THE COMPUTATIONAL COMPLEXITY OF STAP RADAR SYSTEMS

Adam W. Bojanczyk

1 Introduction

We consider a radar system where a series of pulses is sent and the echoes from these pulses are collected on a set of sensors. The returns are sampled, and the resulting data is processed with the objective of determining whether targets are present. This task is made more complex by the presence of interference, which may come from man-made jamming, sensor noise, multipath effects, or the motion of the platform [9].

If interference is localized in frequency and comes from a limited number of sources, it can be overcome using adaptive spatial weighting of the data. The weights applied to the data reduce the effects of interference and increase reception of the desired signal [4, 7]. For an airborne radar platform, interference due to platform motion is not localized in frequency [9]. In this case, a more thorough approach is to use a sub-array of tapped delay lines connected to each sensor [7]. The weights may then be adapted from data in both the time and space dimensions. This approach is referred to as *space-time adaptive processing*, or STAP.

Space-time adaptive processing can be very effective in nulling the interference but requires high computational power that only supercomputers can provide. In order for the STAP systems to be practical for the airborne radar applications their computational complexity must be lowered. In this note we describe one possible way of achieving this goal.

1.1 The STAP Problem

Consider an airborne radar platform with a linear array of N equidistant sensors. A series of M pulses is sent out by the radar, and the returned echoes are sampled and collected by the array shown in Figure 1.

After pre-processing, the returns from a particular distance from the radar are a set of complex signal vectors,

$$s_i \in \mathcal{C}^{N \times 1}, \quad i = 1, 2, \dots, M.$$

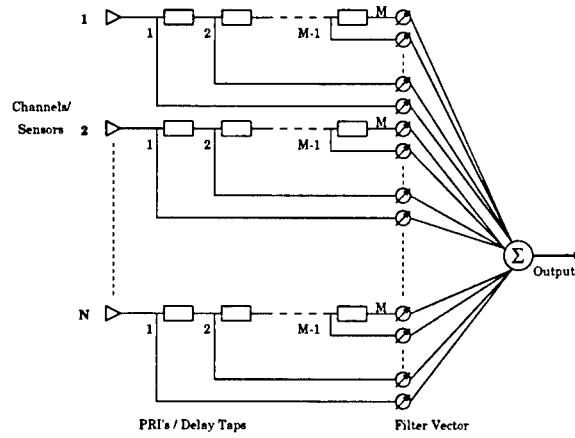


Figure 1: Space-time processing.

Define s , a *space-time snapshot*, as

$$s = \begin{bmatrix} s_1 \\ s_2 \\ \vdots \\ s_M \end{bmatrix}. \quad (1)$$

The object of radar processing is to decide whether a moving target is present at a given range in a particular direction. The direction is specified with a *steering vector* v . Target detection is accomplished through calculation of a *weight* vector w , dependent on v , which is applied to s to get the array output $y = w^H s$ for the particular range and direction. The output y is subjected to a binary decision-making process with an appropriate threshold function. If y is larger than the threshold, a target is considered present: if y is less than the threshold, no target is considered to be present at the location corresponding to the snapshot. The choice of the weight vector is obviously critical.

The process of target detection may be thought of as minimizing the array output in all directions but that of the target signal, assumed to be indicated by v . This has the effect of canceling ground clutter and jamming originating from directions other than the search direction. The average array output power is [2]

$$P = E(yy^H), \quad (2)$$

where $E(\cdot)$ denotes the expectation operator. Noting that $y = w^H s$, equation (2) may be

rewritten as

$$\begin{aligned} E(yy^H) &= E(w^H ss^H w) \\ &= w^H R w, \end{aligned} \quad (3)$$

where $R = E(ss^H)$ is the signal covariance matrix [4]. The direction is specified by introducing the constraint $v^H w = 1$, ensuring that signals originating in the direction of the steering vector are given maximal weighting. The problem of finding the weight vector can then be expressed using (3) as a constrained least-squares problem,

$$\min_{v^H w = 1} w^H R w. \quad (4)$$

If R is full rank then the solution to (4) [2, 9] is

$$w_{opt} = \frac{R^{-1}v}{v^H R^{-1}v}. \quad (5)$$

The covariance matrix R is generally unknown and is estimated from the space-time snapshots collected over some time interval with a constant timestep Δt . In this context, a snapshot taken at a particular time $T_0 + i\Delta t$ corresponds to a particular range and can also be referred to as a *range gate* with index i . Assume that a set of L range gates is collected. Let $s_{i,j}$ denote the value of the sensor data for a particular range gate i , with i varying from 1 to L , and a particular pulse j , with j varying from 1 to M , for all channels. Define

$$X_j = \begin{bmatrix} s_{1,j}^T \\ s_{2,j}^T \\ \vdots \\ s_{L,j}^T \end{bmatrix}, \quad (6)$$

and

$$X = \begin{bmatrix} X_1 & X_2 & \cdots & X_M \end{bmatrix}.$$

We refer to X as the data matrix. The covariance matrix can be estimated from A [6, 9] as follows

$$R \approx \hat{R} = \frac{1}{L} X^H X. \quad (7)$$

The minimization problem (4) for the matrix \hat{R} becomes,

$$\min_{v^H w = 1} w^H \hat{R} w$$

and is equivalent to the following constrained minimization problem

$$\min_{\|w\|_2=1} \|Xw\|_2. \quad (8)$$

The formulation (8) will be the starting point for the discussion in Section 2.

1.2 Optimal Space-time Processing

The weight vector w can be calculated by the so-called *sample matrix inversion* technique, or SMI. One possible implementation of the SMI technique is to compute the QR factorization of the data matrix X followed by triangular system solution. Matrix-vector multiplication between the such obtained weight vector and the data is used to compute the output vector y corresponding to each particular range and direction. Each such output is compared to a threshold to determine whether a target is present at the corresponding range. When the weight calculation and output vector formation steps are applied to the entire data matrix, the algorithm referred to as *joint-domain optimum* or *fully adaptive* space-time processing [1, 2, 10].

This method is not generally used for two reasons. First, the number of calculations required is $O(M^3N^3)$, which may be too large to process in the allotted time.¹ Second, the actual number of samples taken may be too small to allow statistically sufficient estimation of R from A for a particular range. For these reasons, various *heuristic* methods of space-time processing are used instead [9].

The goal of these methods is to reduce the amount of computation required to obtain the weight vector and at the same time to improve the statistical estimation of the underlying process. One kind of heuristics is to split the datacube into several smaller subcubes and process them independently in an analogous way as in the optimal method. The other kind of heuristics is based on the observation that the data matrix X is structured and often of low rank [9, 5, 11]. In this case, the space spanned by the columns of X is approximated by a lower dimensional subspace, called the *signal* space, determined by the dominant singular values of X . All subsequent processing is done in this lower dimensional space. The major

¹Ward [9] states that the product MN may range from 10^3 to 10^4 , leading to a computation requirement of 10^9 to 10^{12} flops for the optimal processing algorithm. An example in the same report [9, p. 28] gives a processing interval on the order of 10^{-2} seconds. The sustained computation rate required to meet these requirements is on the order of teraflops.

difficulty in this approach is to find a good low rank approximation of X . This problem is the focus of this note and is discussed in more detail the following sections.

2 STAP as a Linear Least Squares Problem

We will interpret the STAP problem as the constrained linear least squares problem (8):

$$\rho = \min_{s^H w = 1} \|Xw\|_2$$

where $X \in \mathcal{C}^{m \times n}$ is the complex data matrix, $s \in \mathcal{C}^n$ is the complex *steering* vector, and $w \in \mathcal{C}^n$ is the sought complex *weight* vector. For simplicity we assume that X is full rank (but most likely of a low *numerical* rank), and that the steering vector s is normalized, $\|s\|_2 = 1$.

In what follows the standard basis in \mathcal{C}^n will be denoted by $e_1^{(n)}, e_2^{(n)}, \dots, e_n^{(n)}$. Whenever the dimension n is clear from the context the superscript n will be omitted. The space spanned by columns of the matrix Y will be denoted by $\text{span}(X)$.

Using the SVD decomposition of X [3],

$$X = U\Sigma V^H, \quad (9)$$

and the fact that the L_2 norm is invariant under unitary transformations, the problem (8) is transformed to the equivalent problem

$$\rho = \min_{(s^H V)(V^H w) = 1} \|\Sigma(V^H w)\|_2 \quad (10)$$

Let H be a unitary transformation that maps the vector $V^H s$ onto the last coordinate e_n in the standard basis in \mathcal{C}^n ,

$$HV^H s = e_n = \begin{pmatrix} 0 \\ \vdots \\ 0 \\ 1 \end{pmatrix}. \quad (11)$$

On applying the transformation H (10) becomes

$$\rho = \min_{e_n^H (HV^H w) = 1} \|\Sigma H^H (HV^H w)\|_2. \quad (12)$$

Let

$$y = \begin{pmatrix} y_1 \\ \vdots \\ y_{n-1} \\ y_n \end{pmatrix} = HV^H w. \quad (13)$$

Thus

$$\rho = \min_{e_n^H y=1} \|(\Sigma H^H)y\|_2 \quad (14)$$

where

$$y_n = 1.$$

The right hand side in (14) can now be expanded as follows

$$\min_{e_n^H y=1} \|(\Sigma H^H)y\|_2 = \min_{(y_1, \dots, y_{n-1})} \|(\Sigma H^H) \begin{pmatrix} y_1 \\ \vdots \\ y_{n-1} \\ 0 \end{pmatrix} + (\Sigma H^H)e_n\|_2 \quad (15)$$

which at this point becomes an unconstrained problem.

Let B denote the first $n-1$ columns of ΣH^H and

$$B = P\Gamma Q^H$$

be the SVD of B , where $P \in \mathcal{C}^{n \times n}$ and $Q \in \mathcal{C}^{(n-1) \times (n-1)}$ are unitary, and

$$\Gamma = \begin{pmatrix} \gamma_1 & \cdots & 0 \\ 0 & \ddots & 0 \\ 0 & \cdots & \gamma_{n-1} \\ 0 & \cdots & 0 \end{pmatrix}.$$

Then (15) can be rewritten in the form

$$\min_{e_n^H y=1} \|(\Sigma H^H)y\|_2 = \min \left\| \begin{pmatrix} \gamma_1 & \cdots & 0 \\ 0 & \ddots & 0 \\ 0 & \cdots & \gamma_{n-1} \\ 0 & \cdots & 0 \end{pmatrix} Q^H \begin{pmatrix} y_1 \\ \vdots \\ y_{n-1} \end{pmatrix} + \begin{pmatrix} r_1 \\ \vdots \\ r_{n-1} \\ r_n \end{pmatrix} \right\|_2 = |r_n|, \quad (16)$$

where

$$r = \begin{pmatrix} r_1 \\ \vdots \\ r_{n-1} \\ r_n \end{pmatrix} = P^H \Sigma H^H e_n. \quad (17)$$

The minimizer of (16) is

$$\begin{pmatrix} y_1 \\ \vdots \\ y_{n-1} \end{pmatrix} = -Q \begin{pmatrix} \gamma_1 & \cdots & 0 \\ 0 & \ddots & 0 \\ 0 & \cdots & \gamma_{n-1} \end{pmatrix}^{-1} \begin{pmatrix} r_1 \\ \vdots \\ r_{n-1} \end{pmatrix}. \quad (18)$$

while that of (8) is

$$w = VH^H \begin{pmatrix} y_1 \\ \vdots \\ y_{n-1} \\ 1 \end{pmatrix} \quad (19)$$

The minimizer w can also be written in the form

$$w = VH^H \begin{pmatrix} Q & 0 \\ 0 & 1 \end{pmatrix} \text{diag}(\gamma_1, \dots, \gamma_{n-1}, 1)^{-1} \begin{pmatrix} r_1 \\ \vdots \\ r_{n-1} \\ 1 \end{pmatrix} \quad (20)$$

2.1 Low Rank Approximation of the Data Matrix

The relations (17) - (19) provide a constructive (but computationally inefficient) means for finding the minimizer of (8). The relation (16) has been developed with a different goal in mind. Namely, we want to address the question of finding a low dimension subspace $\text{span}(Y)$ of the space $\text{span}(X)$ for which a minimizer u^* of

$$\min_{s^H u = 1} \|Yu\| \quad (21)$$

yields a small value of $\|Xu^*\|$ in (8).

One way of selecting Y is to choose l left singular vectors of X , or l columns of the matrix U in (9) - this is equivalent to requiring that the minimizer u be a linear combination of the corresponding l columns of V .

We note that if the first l columns of U are chosen, that is Y is the best L_2 approximation of X , the value of $\|Xu^*\|$ might not be sufficiently small.

Indeed, let

$$Y_l = U \Sigma_l V^H, \quad \Sigma_l = \begin{pmatrix} \sigma_1 & & & \\ & \ddots & & \\ & & \sigma_l & \\ & & & 0 \end{pmatrix}$$

be the best, in L_2 norm, rank l approximation to X . Assume that the steering vector s is orthogonal to the first l columns of V . Then H in (11) will have the following form

$$H_l = \begin{pmatrix} I_l & 0 \\ 0 & G_{n-l} \end{pmatrix} \quad (22)$$

where I_l is the identity matrix in $\mathcal{C}^{l \times l}$ and $G_{n-l}^H G_{n-l} = I_{n-l}$.

Consider now the minimization problem (8) for the matrix Y_l ,

$$\rho_l = \min_{s^H u = 1} \|Y_l u\|$$

The relation (15) for Y_l takes on the form

$$\min_{(y_1, \dots, y_{n-1})} \left\| \Sigma_l H_l^H \begin{pmatrix} y_1 \\ \vdots \\ y_{n-1} \\ 0 \end{pmatrix} \right\|$$

as now $\Sigma_l H_l^H e_n$ in (15) is a zero vector. Thus the least norm solution to (14) for the matrix Y_l is $y^* = e_n$. For this y^* the norm in (15) corresponding to the matrix X has the value $\|\Sigma H^H e_n\| = \|r\|$ where r is defined by (17). This is not surprising as we assumed that the steering vector s was orthogonal to the right singular vectors corresponding to the largest singular values $\sigma_1, \dots, \sigma_l$.

The relation (16) gives an insight which of the l columns of U should be chosen. Let π be a permutation such that

$$\pi \begin{pmatrix} r_1 \\ \vdots \\ r_{n-1} \end{pmatrix} = \begin{pmatrix} r_{i_1} \\ \vdots \\ r_{i_{n-1}} \end{pmatrix}$$

where

$$|r_{i_1}| \geq |r_{i_2}| \geq \dots \geq |r_{i_{n-1}}|.$$

From (16) it is seen that if only l columns of Γ can be included in the minimization process the smallest norm will be obtained if the largest (in the magnitude) components of r are zeroed. This is realized by the vector y^* with components

$$\begin{pmatrix} y_1^* \\ \vdots \\ y_{n-1}^* \end{pmatrix} = -Q \begin{pmatrix} \gamma_1 & \cdots & 0 \\ 0 & \ddots & 0 \\ 0 & \cdots & \gamma_{n-1} \end{pmatrix}^{-1} \pi^{-1} \begin{pmatrix} r_1 \\ \vdots \\ r_l \\ 0 \end{pmatrix}, \quad (23)$$

minimizes the norm on the right hand side of (16) in the space spanned by columns i_1, \dots, i_l of the matrix Γ . From (24) the corresponding to y^* weight vector $w^{(l)}$ is given by

$$w^{(l)} = V H^H \begin{pmatrix} Q & 0 \\ 0 & 1 \end{pmatrix} \text{diag}(\gamma_1, \dots, \gamma_{n-1}, 1)^{-1} \pi^{-1} \begin{pmatrix} r_{i_1} \\ \vdots \\ r_{i_l} \\ 0 \\ 1 \end{pmatrix} \quad (24)$$

Thus $w^{(l)}$ is in the space spanned by the columns i_1, \dots, i_l of the matrix

$$V H^H \begin{pmatrix} Q & 0 \\ 0 & 1 \end{pmatrix}$$

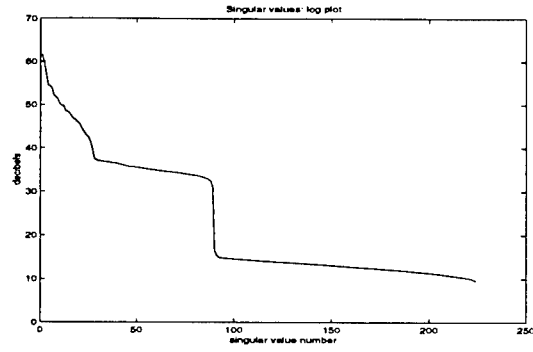
and hence it is not immediately obvious how to select a good l -dimensional subspace of $\text{span}(X)$ for minimization of (21) without knowing all (right) singular vectors of X . Some additional insight can be obtained from analyzing the following example.

Example 1: We generated a synthetic data cube using software developed by the Scientific Studies Corporation for Rome Laboratory [8].

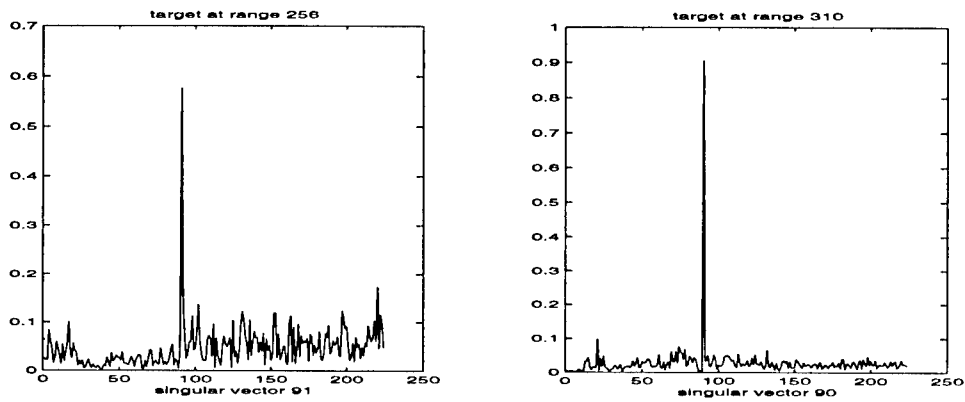
In this hypothetical scenario we considered a linear array with $N = 14$ sensors spaced at half wavelength installed on a moving platform. A subarray of $M = 16$ taps was associated with each sensor.

The clutter returns were simulated by spreading 361 equally spaced point scatterers over the angular sector. The clutter-to-noise parameter was calculated from the contribution of all clutter echos. There were four jammers placed at angles $-5^\circ, 5^\circ, 25^\circ$ and 65° , and their powers were 55, 45, 40 and 35 dB above the noise level, respectively. There were two targets at angles -30° and 40° , located at range gates 256 and 310, with normalized velocity 0.2 and 0.4, and SNR of 10 and 12 dB, respectively.

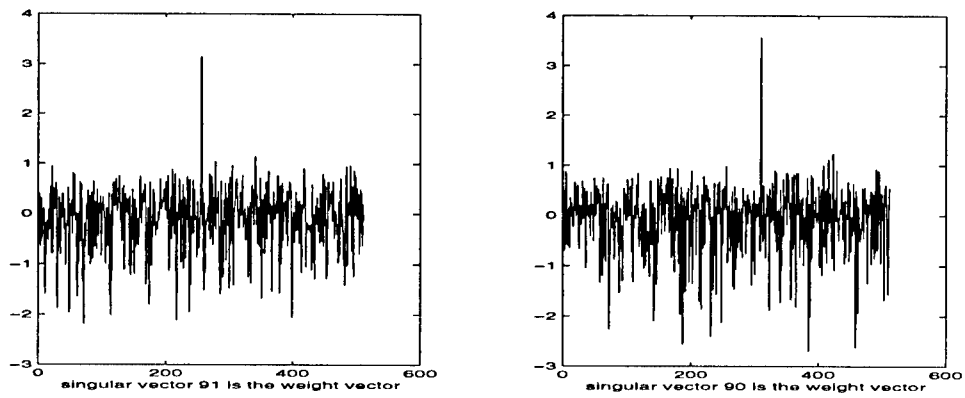
Space-time samples were collected from $L = 512$ ranges. The condition number of the corresponding data matrix X was $\text{cond}(X) = 1.5746e + 05$ and it had singular values distributed as shown in Figure 2(a). Two steering vectors s_1 and s_2 were picked so they were pointing exactly at the two targets.



(a) Distribution of singular values.



(b) Decomposition of the weight vectors in the basis of right singular vectors.



(c) Residuals corresponding to the weight vectors v_{90} and v_{91}

Figure 2: Characteristics of the data matrix X .

The analysis of Section 3 reveals that the optimal weight vectors w_1 and w_2 are almost aligned with the right singular vectors v_{90} and v_{91} (see the coefficients of the decomposition

of w_1 and w_2 in the basis of the right singular vectors which are plotted in Figure 2(b)).

σ_{88}	1.7939e+03
σ_{89}	1.3056e+03
σ_{90}	4.4900e+01
σ_{91}	3.5518e+01
σ_{92}	3.1487e+01
σ_{93}	3.1244e+01

Table 1: Singular values corresponding to the targets.

Table 1 lists two preceding and two succeeding singular values surrounding the singular values of interest. It reveals that the singular vectors v_{90} and v_{91} cannot be considered as belonging to the dominant subspace as the corresponding singular values σ_{90} and σ_{91} are not large (respectively to all subsequent singular values). This confirms observations made in Section 3 about possible inadequacy of the dominant subspace for finding weak targets.

However Table 1 also shows that σ_{90} and σ_{91} immediately follow the large singular values. Thus in order to capture enough information about weak targets one might have to extend the dominant subspace by singular vectors corresponding to singular values immediately succeeding the dominant singular values. In the next section we describe how an approximation to this desired subspace might be computed.

3 Approximate SVD

The singular value decomposition of a matrix X can be efficiently computed by the Golub Kahan algorithm [3]. The first step of the algorithm is a bidiagonalization of X which transforms X into an upper bidiagonal form,

$$U^H X V = B = \begin{pmatrix} \alpha_1 & \beta_1 & \cdots & 0 & \cdots \\ 0 & \alpha_2 & \ddots & 0 & \vdots \\ \vdots & \ddots & \ddots & \ddots & \vdots \\ \vdots & & \ddots & \ddots & \beta_{n-1} \\ 0 & \cdots & \cdots & 0 & \alpha_n \end{pmatrix}$$

This bidiagonalization can be realized by applying to X a sequence of $n - 1$ left and $n - 2$ right Householder transformations.

It turns out that the bidiagonalization of X does not have to be completed to provide a useful information about the matrix X [3]. Namely, it is often the case that after k steps of bidiagonalization the largest singular values of B_k ,²

$$B_k = B(1 : k, 1 : k)$$

tend to be very good approximations to the largest k singular values of X (the small singular values of X are usually not as well approximated). Thus if we are interested in the large singular values and the corresponding singular vectors, an incomplete bidiagonalization will often provide a very satisfactory approximation.

Let $B^{(k)}$ denote the matrix obtained from X after k steps of bidiagonalization via left and right Householder transformations. The matrix $B^{(k)} = U_k^H X V_k$, where U_k and V_k denote products of the bidiagonalizing Householder transformations, has the following form,

$$B^{(k)} = \begin{pmatrix} B_{k-1} & e_{k-1}\beta_{k-1} & 0 & \cdots & 0 \\ 0 & \alpha_k & b_{k,k+1}^{(k)} & \cdots & b_{k,n}^{(k)} \\ 0 & 0 & b_{k+1,k+1}^{(k)} & \cdots & b_{k+1,n}^{(k)} \\ \vdots & \vdots & \vdots & & \vdots \\ 0 & 0 & b_{m,k+1}^{(k)} & \cdots & b_{m,n}^{(k)} \end{pmatrix} \quad (25)$$

Note that if $b_{k,k+1}^{(k)} = 0$, the matrix $B^{(k)}$ becomes block diagonal. This will happen if X has rank k . If X has k very large and $n - k$ very small singular values, the norm of $B^{(k)}(:, k + 1 : n)$ will be small. Thus the singular values of X will naturally decouple into the so-called *signal* and *noise* singular values. The k largest singular values of X will be well approximated by the k largest singular values of $B^{(k)}$ which in turn will be very close to the singular values of B_k . This phenomenon is illustrated in Figure 3, for the case considered in Example 1, where the log of the magnitudes of the singular values of X (the dotted line) is compared against the log of the norm of consecutive columns of $B^{(k)}$ (the solid line), $k = 100$.

²Here we have adopted the MATLAB colon notation whereby $B(1 : l, 1 : k)$ denotes the submatrix of B consisting of the first k columns and the first l rows

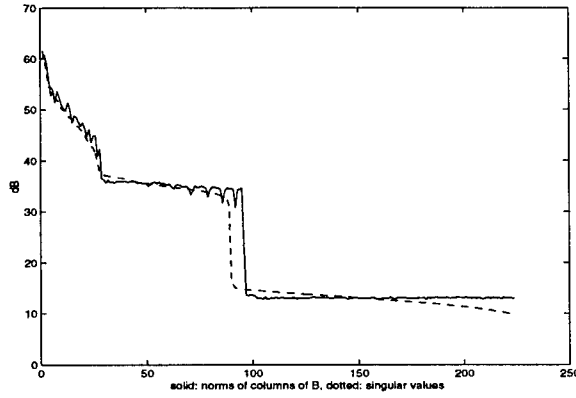


Figure 3: Partial bidiagonalization $k = 100$, singular values.

In an analogous way the first k right (left) singular vectors of X will almost belong to $\text{span}(V_k)$ ($\text{span}(U_k)$). Thus the first k column of U_k can be considered as a good approximation to the so-called *signal* subspace. This is illustrated in Figure 4 (for the case considered in Example 1) where the coefficients of the expansion of the steering vectors v_{90} and v_{91} in the basis of the columns of V_k are plotted against the columns numbers. Note that the steering vectors v_{90} and v_{91} almost completely lie in the subspace spanned by the first $k = 95$ columns of V_k .

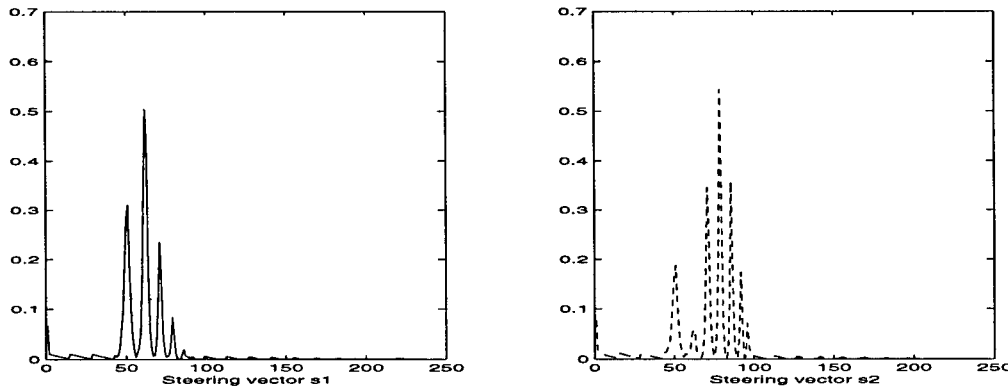


Figure 4: Partial bidiagonalization $k = 100$, decomposition of steering vectors.

3.1 New Heuristic and Its Preliminary Evaluation

The plots in Figures 3 and 4 suggest the following heuristic for finding targets. Perform bidiagonalization of the data matrix X until an appreciable gap is found between the norm

of column k of $B^{(k)}$ and the norm of column $k+1$ of $B^{(k+1)}$. If presence of l weaker targets is suspected, perform additional l steps of bidiagonalization. Solve the minimization problem (21) in the subspace spanned by the first $r = k + l$ column of U_r ,

$$\min_{(V_r^H s)^H u = 1} \|U_r u\| \quad (26)$$

where $V_r^H s$ is a 'rotated' steering vector.

Preliminary results about the effectiveness of the heuristic are shown in Figures 5 and 6 where we compared four STAP methods for the hypothetical scenario described in Example 1. Plots in Figure 5 correspond to the target located in the range gate 256 while plots in Figure 6 correspond to the target located in the range gate 310.

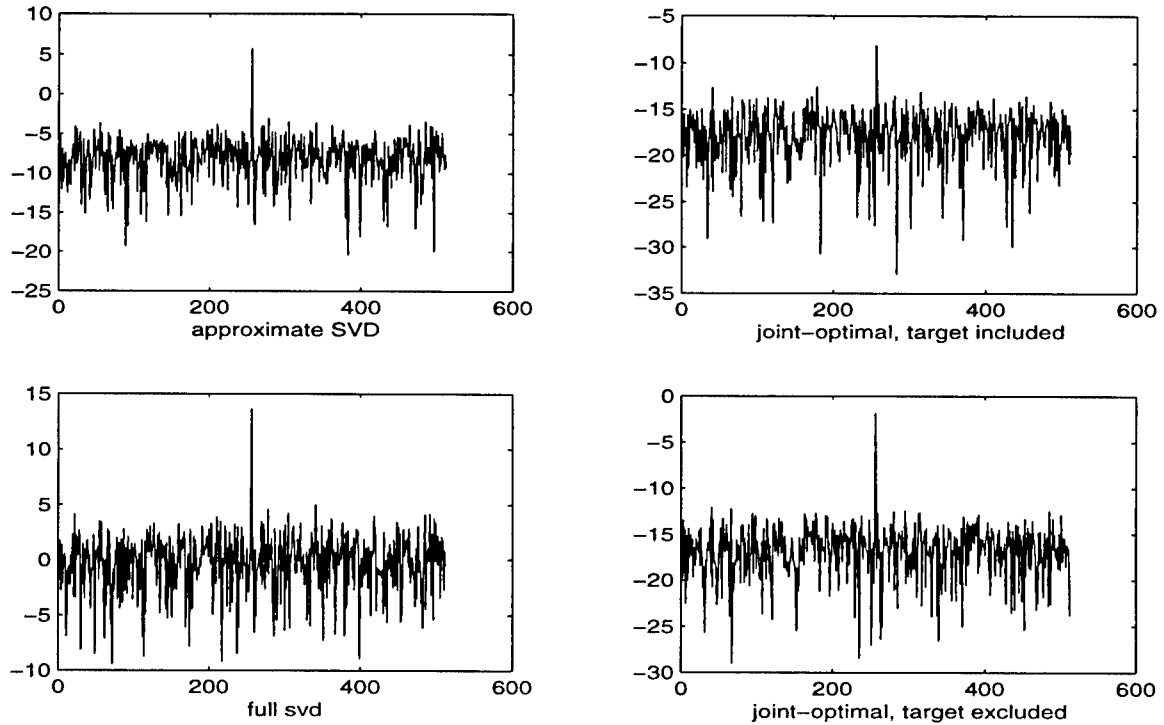


Figure 5: Target at range gate 256

Out of the four methods two were based on the Sample Matrix Inversion method SMI [1, 2, 10] while the other two could be considered as eigenspace methods.

For the SMI methods the covariance matrix was estimated from the data X according to (7). In the first method, *SMI-include*, the space-time sample from the range gate under

the test was included (the upper-right plot) while in the other, *SMI-exclude*, it was excluded (the lower-right plot).

Two eigenspace method were tested. In the first eigenspace method, *SVD-full*, (the lower-left plot) the complete SVD of X was computed and the weight vector was selected as that right singular vector which aligns best with the target's steering vector. The other eigenspace method, *SVD-approximate*, (the upper-left plot) was the one considered in this note where a partial bidiagonalization of X was calculated first and was followed by solving the constrained linear least squares problem (26).

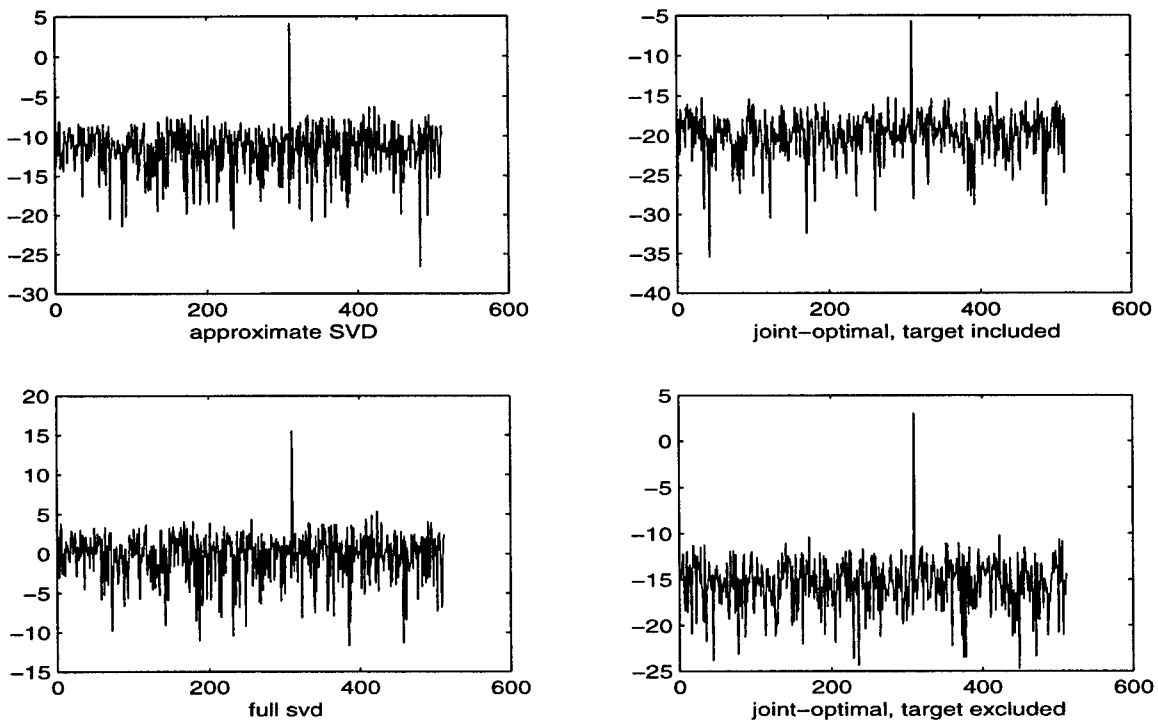


Figure 6: Target at range gate 310

The plots confirm that the join-optimal method, when the range gate under the test is excluded from the sample covariance matrix, produces the most visible indication of the target. However, as the location of the target cannot be know beforehand, the computations would have to be repeated for all possible location of the target. If all samples are included in the estimate of the covariance matrix, the peak corresponding to the target is still visible but to a lesser degree. On the other hand this process does not have to be repeated for all

ranges.

The eigenspace methods also process all samples simultaneously. As seen in Figures 5 and 6, the performance of the method *SVD-full* which computes the full singular value decomposition is close to the performance of the joint-optimal method *SMI-exclude*. The performance of the method *SVD-approximate*, which attempts to approximate the signal subspace only, is very satisfactory. At the same time *SVD-approximate* is the least expensive out of the four methods compared, at least for the case considered in Example 1.

This preliminary investigation suggests that the method *SVD-approximate* deserves more detailed analysis. We plan to undertake such an analysis and report more comparative results in a future note.

Acknowledgements: I would like to thank my host Dr. Mark Linderman for providing very friendly research environment during my visit to Rome Laboratory, and Drs Ralph Kohler, Mark Linderman, Richard Linderman, William Melvin, James Michels, and Michael Wickes for many fruitful discussions and willingness to share their expertise with the author.

References

- [1] Lawrence E. Brennan, Dana J. Piwinski, and Fred M. Staudaher. Comparison of space-time adaptive processing approaches using experimental airborne radar data. In *1993 National Radar Conference*, pages 176–181, March 1993.
- [2] Robert C. DiPietro. Extended factored space-time processing for airborne radar systems. In *Twenty-sixth Annual Asilomar Conference on Signals, Systems, and Computing*, pages 425–430, Pacific Grove, CA, 1992.
- [3] Gene H. Golub and Charles F. Van Loan. *Matrix Computations*. The John Hopkin University Press, Baltimore and London, third edition, 1997.
- [4] Simon Haykin. *Adaptive Filter Theory*. Prentice Hall, Englewood Cliffs, NJ, second edition, 1991.

- [5] Alexander Haimovich. The Eigencanceler: Adaptive Radar by Eigenanalysis Methods. *IEEE Transactions on Aerospace and Electronic Systems*, vol 32, no 2, April 1996, pp 532–542.
- [6] James H. Michels. Summary of space-time processing algorithms. Technical report, Rome Laboratory Advanced Concepts Branch, July 1995. Draft.
- [7] Robert A. Monzingo and Thomas W. Miller. *Introduction to Adaptive Arrays*. John Wiley and Sons, New York, 1983.
- [8] Jaime R. Roman and Dennis W. Davis. Multichannel System Identification and Detection Using Output Data Techniques. Technical report, Rome Laboratory Advanced Concepts Branch, October 1996.
- [9] James Ward. Space-time adaptive processing for airborne radar data systems. Technical Report 1015, Massachusetts Institute of Technology Lincoln Laboratory, Lexington, MA, September 1994.
- [10] James Ward and Allan O. Steinhardt. Multiwindow post-Doppler space-time adaptive processing. In *Proceedings of the IEEE Seventh SP Workshop on Statistical Signal and Array Processing*, pages 461–464, Quebec City, Qc, Canada, June 26-29 1994.
- [11] Ho Yang and Mary Ann Ingram. Design of Partially Adaptive Arrays Using Singular-Value Decomposition. *IEEE Transactions on Aerospace and Electronic Systems*, vol 45, no 3, May 1997, pp 843–850.

A PC-Based Speech Synthesizing Using Sinusoidal Transform Coding (STC)

**Nazeih M. Botros
Associate Professor
Department of Electrical Engineering**

**Southern Illinois University
Carbondale, Illinois 62901-6603**

**Final Report for:
Summer Faculty Research Program
Rome Laboratory, Hanscom Air Force Base, Boston, MA**

**Sponsored by:
Air Force Office of Scientific Research
Bolling Air Force Base, DC**

**and
Rome Laboratory**

August 1997

A REAL-TIME PC-Based Speech Synthesizing Using Sinusoidal Transform Coding (STC)

Nazeih M. Botros
Associate Professor
Department of Electrical Engineering

Abstract

In this research we investigate a real time speech synthesizing system using a PC platform. Synthesizing was carried out by using Sinusoidal Transform Coding (STC) technique. The proposed synthesizing system works on multi-speakers; the active speakers have their speech signal compressed to 4.8Kb/s while the inactive speakers have their speech signal compressed to 2.4 Kb/s. The code describing the operation of the system is written with C++ and is optimized to allow for a real-time operation.

Introduction

The ultimate goal of this project is to design a real-time PC-based multiple-speaker conferencing system. This system is a modified version of an existing system. In the system, the speech signal is synthesized by implementing the Sinusoidal Transform Coder (STC) technique. Figure 1. shows a block diagram of the proposed system. To achieve this goal, the following tasks have to be accomplished:

1. Investigating the STC technique. The technique was developed by Rome Laboratory through MIT-Lincoln Laboratory. The investigation includes collection and understanding of the literature pertaining to the technique. This task has been accomplished and the Reference Section of this report shows a list of the papers that have been investigated.
2. Investigating the existing C-code of the STC and the Window subprograms; the code was written by Rome Lab and Lincoln Lab. The STC code was written by Lincoln Lab on Sun-Unix platform and was ported on a PC platform by Rome Lab [19]. This task has been accomplished; the function of each segment of the code was identified. For example, the attached C-code is a subprogram entitled "ANA_INIT.CPP" to initialize: sampling windows, pitch coding parameters, and line spectrum parameters.
3. Optimization of the existing code, especially the STC code, so it can run efficiently on a real-time basis on a PC platform. To achieve this task, the existing code has to run successfully so that optimization procedure can be started and the performance of the developed code can be compared with that of the existing code. On the last day of my

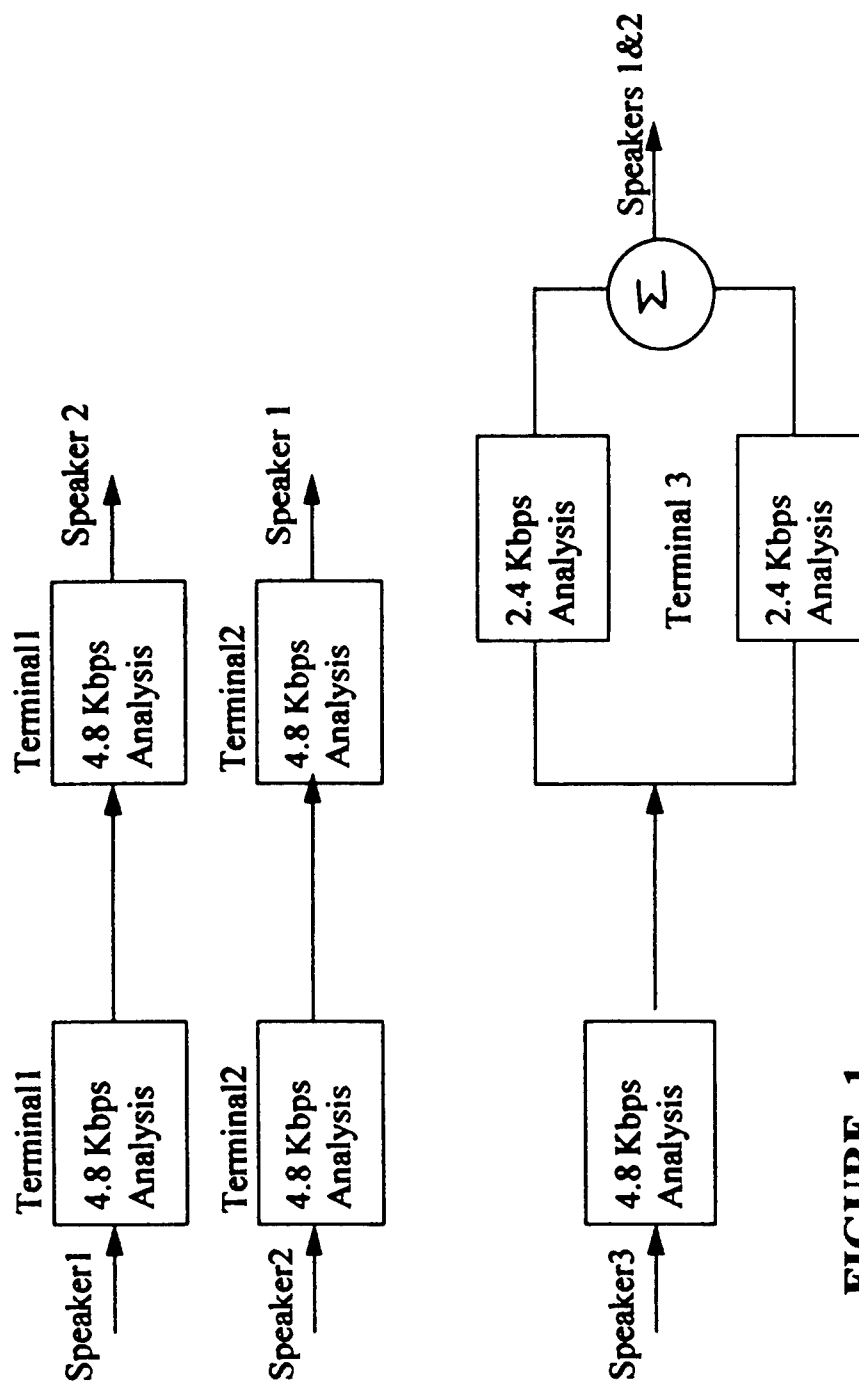


FIGURE 1.

eight-week tour we were able to run successfully several segments of the existing code.

Accordingly, the optimization task will be included in the Summer Extension Proposal to the Air Force Office of Scientific Research (AFOSR).

4. Integrating the bridge into a PC code so that any Air Force user with a PC can use the system without the need for a special hardware (bridge). This task will be included in the Summer Extension Proposal to the Air Force Office of Scientific Research (AFOSR).

The Sinusoidal Transform Coder

The Sinusoidal Transform Coder (STC) is a vocoding speech compression technique that has demonstrated synthetic speech of good quality at rates from 2400 b/s to 4800 b/s. The basic idea behind the technique is that speech signal can be modeled by amplitude, frequency, and phase of a train of sine waves, [1-6]. In the analysis phase, the time-domain speech signal is convolved with a window signal and the output signal of the convolution (frames) is transformed to the frequency domain using the Short Time Fourier Transform (STFT). The outcome of the STFT is amplitudes and phases of certain frequency components. In the synthesis phase the phases, and frequencies obtained from the analysis phase are used to generate sine waves, these waves are convolved (modulated) with the amplitudes to obtain a synthetic speech signal. The technique has gone through several modification procedures since it was developed in 1986. Speech of very high quality can be synthesized using a sinusoidal model when the amplitudes, frequencies, and phases are derived from a high-resolution analysis of the short-time Fourier Transform (STFT). If the measured sine wave frequencies are replaced by a harmonic set of frequencies in which the fundamental frequency is chosen to make the harmonic model a "best fit" to the measured sine wave data, then synthetic speech of high

quality can be obtained by sampling the STFT at the harmonic frequencies. The parameters of the resulting speech model are the pitch, voicing, and the sine wave amplitudes at the pitch harmonics. The sine wave amplitudes are coded by fitting a set of cepstral coefficients derivatives to an envelope of the measured sine wave amplitudes. The derivatives are obtained by taking the cosine transform of the cepstral coefficients. The output of the cosine is called channel gains. Additional steps are taken to reduce the number of bits of the coding. The amplitude envelope is warped to the usual speech frequency range (0 to 3 KHz) and the cepstral coefficients are quantized. also a frame fill techniques are used in order to give more temporal resolution to the coded amplitudes. Low rate coding is achieved by using a high-order (14 to 16) allpole model to represent the spline envelope. Moreover, 3 bits have been used as side information to allow some adaptivity in the quantization step-size. Figure 2. shows the fitting of an 14th order allpole to spline envelope. For multi-speakers system, The system, which consists of multiple speech terminals and a single conference bridge, allows conferees to communicate using 4800b/s STC when a single speaker is talking and at 2400 b/s when two speakers are active. The dual rate implementation of STC uses a 14th order allpole model at 2400 b/s and a 16th order allpole model at 4800 b/s.

To reduce the computations on the bridge, embedded coding is used such that the 2400 b/s representation of the speech signal is just a subset of the full 4800 b/s bit stream. The bit rate transformation is then accomplished by simply ignoring half of the bits. The core 2400 b/s 14th order allpole coder uses a total of 72 bits to synthesize two frames every 30 ms. At 4800 b/s, 61 of the additional 72 bits are used to code the residuals, the reflection coefficients, and the sample variances. The remaining 11 bits are used to improve the

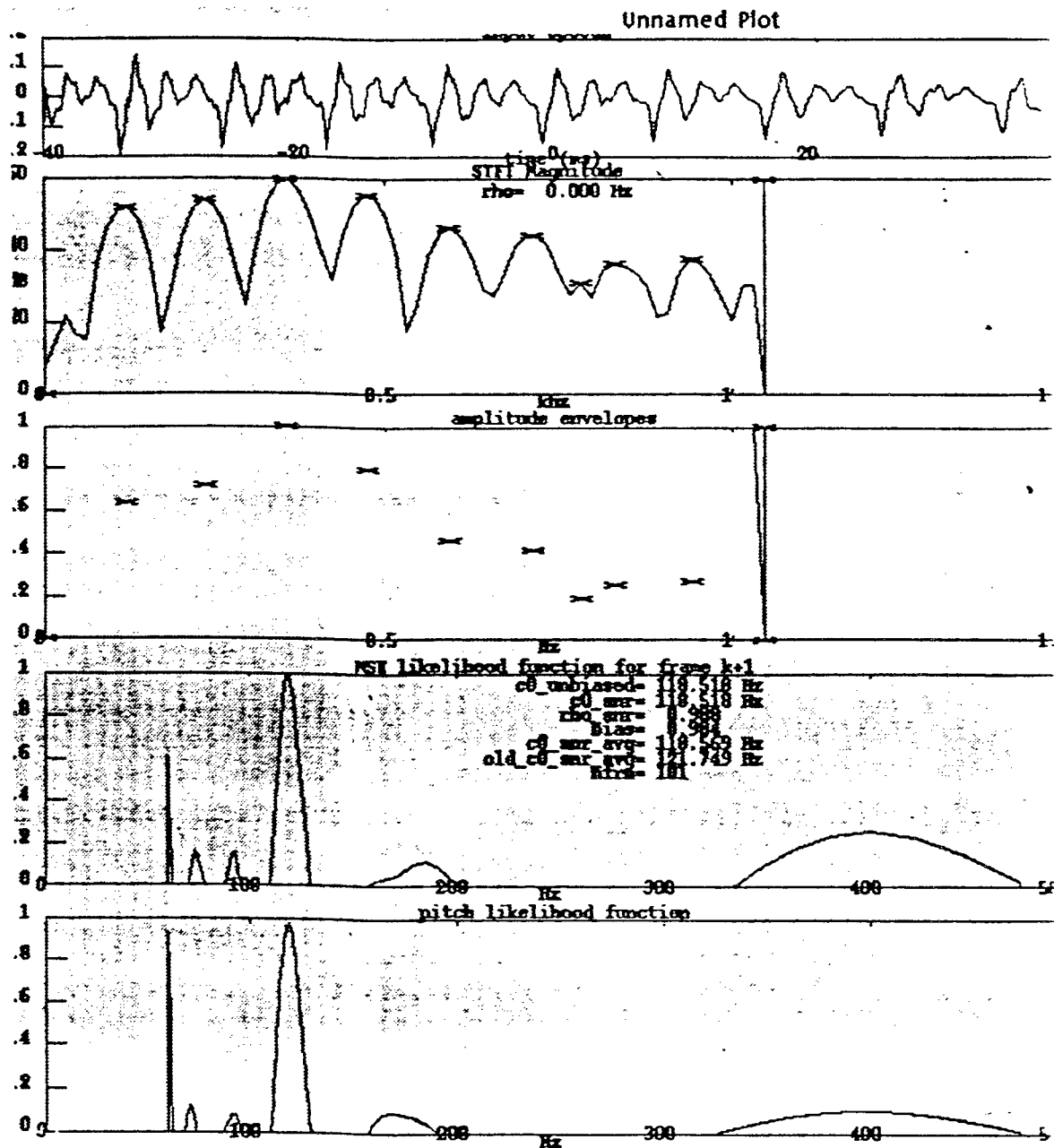


FIGURE 2.

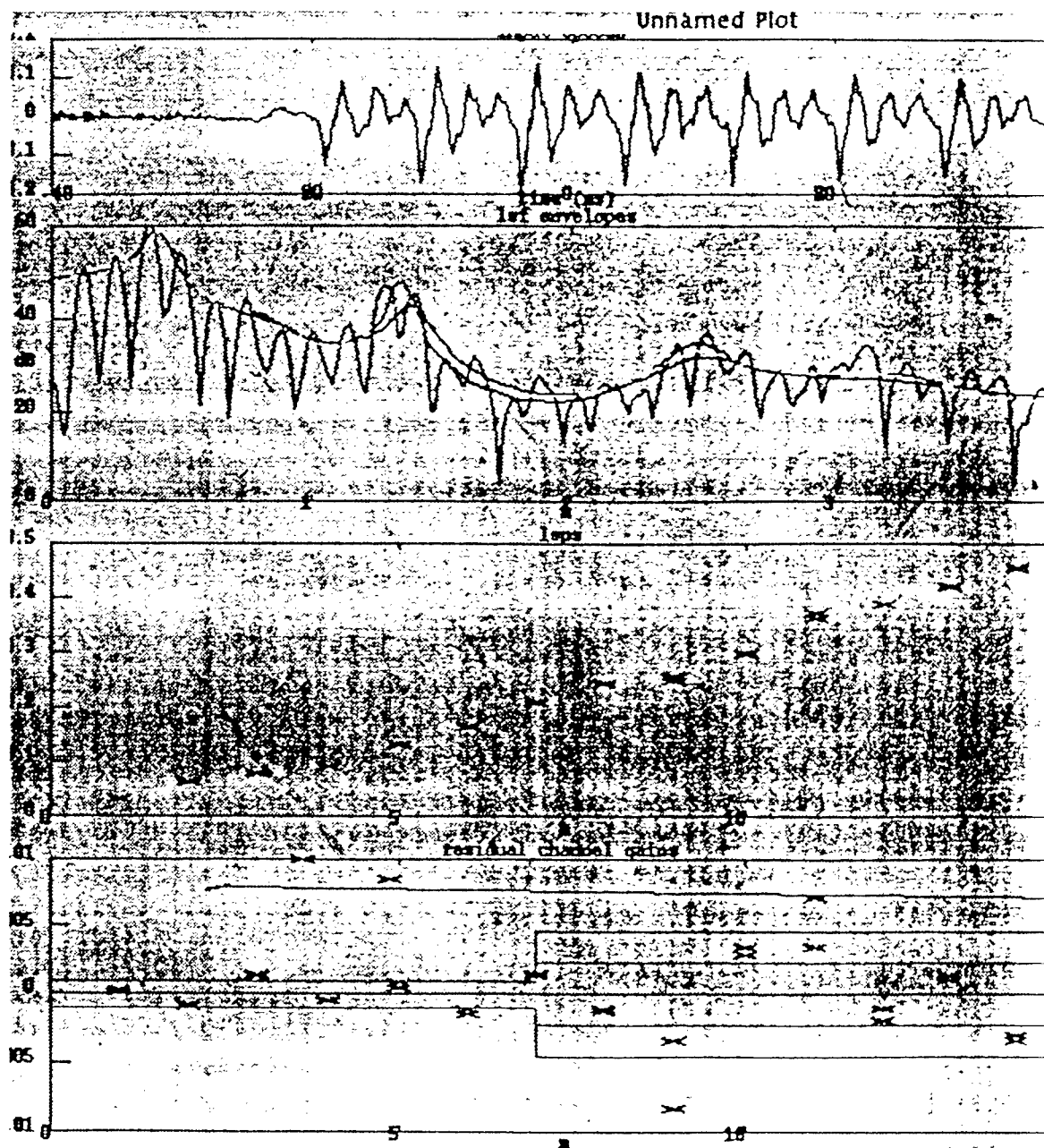


FIGURE 2 continue

coding of the pitch, voicing, and gain parameters. The embedded coder operates in real time using one 40 Mhz TMS320C30 for analysis and one 40 Mhz TMS320C30 for synthesis. This implementation is employed in the new version of the Air Force multimedia conferencing system.

REFERENCES

- [1] E. Singer, R.J. McAulay, R.B. Dunn, and T.F. Quatieri, "Embedded Dual-Rate Sinusoidal Transform Coding," Proc. IEEE Workshop on Speech Coding, Pocono Manor, PA, September 7-10, 1997.
- [2] E. Singer, R.J. McAulay, R.B. Dunn, and T.F. Quatieri, "Low Rate Coding of the Spectral Envelope Using Channel Gains," Proc. IEEE Int. Conf. Acoustics, Speech and Signal Processing, Atlanta, GA, May 7-10, 1996.
- [3] R.B. Dunn, R.J. McAulay, T.G. Champion, and T.F. Quatieri, "Sinewave Amplitude Coding Using a Mixed LSF/PARCOR Representation," IEEE Speech Coding Workshop, Annapolis, MD, September 20-22, 1995.
- [4] R.J. McAulay, T.F. Quatieri, and T.G. Champion, "Sinewave Amplitude Coding Using High-Order Allpole Models," EUSIPCO-94, Edinburgh, Scotland, UK, September 13-16, 1994.
- [5] R.J. McAulay, T. G. Champion, and T.F. Quatieri, "Sinewave Amplitude Coding Using Line Spectral Frequencies," Proc. of the IEEE Workshop on Speech Coding for Telecommunication St-Jovite, Quebec, Canada, Oct. 13-15, 1993.
- [6] R. J. McAulay and T.F. Quatieri, "The Application of Subband Coding to Improve Quality and Robustness of the Sinusoidal Transform Coder," Proc. IEEE-1993 Int. Conf. Acoustics, Speech and Signal Processing, Minneapolis, MN, April 27-30, 1993.
- [7] Paliwal and B.S. Atal, "Efficient Vector Quantization of LPC Parameters at 24 Bits/Frame," IEEE Transaction on Speech and Audio Processing, Vol. 1, No. 1, pp. 3-14, January 1993.

- [8] R. J. McAulay and T.F. Quatieri, "Low Rate Speech Coding Based on a Sinusoidal Model," Chapter 1.6, pp. 165-208 in *Advances in Speech Signal Processing*, S. Furui and M.M. Sondhi (Eds.), Marcel Dekker, New York, 1992.
- [9] T.G. Champion, "Multi-Speaker Conferencing Over Narrowband Channels, " *Proc. MILCOM-91*, pp. 1220-1223, 1991.
- [10] M. M. Sondhi and S. Furui, *Advances in Acoustics and Speech Processing*, New York City, NY, Marcel Deckker, 1991.
- [11] R. J. McAulay, and T.F. Quatieri, "Pitch Estimation and Voicing Detection Based on Sinusoidal Model," *Proc. IEEE 1990 Int. Conf. Acoustics, Speech and Signal Processing*, Albuquerque, NM, pp. 249-252, April 1990.
- [12] R. J. McAulay, and T. Champion, "Improved interoperable 2.4 kb/s LPC Using Sinusoidal Transform Coder Techniques," *Proc. IEEE 1990 Int. Conf. Acoustics, Speech and Signal Processing*, Albuquerque, NM, April 1990.
- [13] R. J. McAulay and T.F. Quatieri, "The Sinusoidal Transform Coder (STC): A High Performance Multi-Rate Speech Coder," *Military Speech Tech'89*, Washington, D.C., November 1989.
- [14] R.J. McAulay, T. M. Parks, T.F. Quatieri, and M. Sabin, "Sine-wave Amplitude Coding at Low Data Rates," *IEEE Workshop on speech Coding*, Vancouver, B.C., Canada, September 1989.
- [15] R. J. McAulay, and T.F. Quatieri, "Speech Analysis-Synthesis Based on a Sinusoidal Representation," *IEEE Trans. Acoustics, Speech and Signal Processsing*, ASSP-34, No. 4, pp. 744-754, August 1986.

- [16] F. K. Soong and B-H Juang, "Line Spectrum Pair (LSP) and Speech Data Compression," Proc. IEEE Int. Conf. Acoustics, Speech and Signal Processing, San Diego, CA, pp. 1.10.1-1.10.4, March 1984.
- [17] S. paul, " The Spectral Envelope Estimation," IEEE Trans. on Acoustics, Speech and Signal Processing, Vol. ASSP-29, No. 29, pp. 786-794, 1981.
- [18] F. takara and S. Saito, "A Statistical Method for Estimation of Speech Spectral Density and Formant Frequencies," Electron. Commun. Vol. 53-A, pp. 36-43, 1970.
- [19] Lt. Eric Miller "Speech Synthesizing," a Technical Report to Rome Lab, ERC-1, 1997.

```

trig_init ();

// Initialize constants and variables for plotting
#ifdef C30
    plotter_init ();
#endif

// Initialize the random number generator
nurand (1);      // random seed generation

// Initialize the dc-bias notch filter
notch_init ();

// Initialize fixed 60ms window for coarse pitch analysis...must precede
// "read_init()"
stft_init (&audio_in[0]);

// Initialize the fixed 22.5ms analysis window for LPC analysis
#ifdef INVERSE
    inverse_init (&residual[0]);
#endif

// Read in initial 60ms speech buffer from the disk...must follow
// "stft_init()"
#ifdef STANDALONE
    if (!analog_input && !hexfile_input)
    {
        read_init (nfrm, audio_in, SpBuf, &cleanup);
#ifdef INVERSE
        read_init (nfrm, residual, SpBuf, &cleanup);
#endif
    } else {
        // put noise in audio_in buffer

        sign = 5.0;
        for (i = 0; i < MS100; i++) {
            audio_in[i] = sign;
            sign = -sign;
        }
    }
#endif

// Initialize constants for coarse/fine pitch analysis

```

Example of a segment of the Code

```

        &nmb_r_indices48);
    else
        code_lsps_init (bit_rate, &bits_left48, order_allpole48, nbits_ff_lsp48,
            nbits_lsp48_k, nlevels_lsp48_k, nbits_lsp48_kp1, nlevels_lsp48_kp1,
            &nmb_r_indices48, dlsp48_pointer);

    // Summarize the bit allocation

#ifdef CODER_SUMMARY
    coder_summary (bit_rate, bits_left48, smpratex2, nbits_sync, nbits_vac,
        nbits_pitch48, nbits_ff_pitch48, nbits_voicing48, nbits_ff_voicing48,
        nbits_gain48, nbits_ff_gain48, order_allpole48, nbits_ff_lsp48,
        nbits_lsp48_k, nlevels_lsp48_k, nbits_lsp48_kp1, nlevels_lsp48_kp1);
#endif

    // Initialize displays for track plots

#ifdef C30
    plot_tracks_init ();
#endif

    // Clear all data for a cold start

    clear_data ();

    // Initialize timer0 to profile the real-time modules

#ifdef PROFILE_ANA
    InitTimer0( PROFILE_TIMER_PERIOD ); // 0.1 millisecond timer period
#endif

}

//*****

```



```

coarse_pitch_init ();
tracker_pitch_init ();
wideband_voicing_init ();

// Initialize the arrays for warping the envelope
warp_init ();
#ifdef MASKER
    masking_envelope_init ();
#endif

// Initialize the arrays used to invert the tridiagonal matrix for the
// harmonic spline envelope
#ifdef CUBIC_SPLINE
    harmonic_spline_init();
#endif

// Initialize the cosine table for speeding up as_to_lsp()
as_to_lsp_init (order_allpole48);

// Compute the total number of bits for parameter coding
set_bits (bit_rate, smprate2, &nbits_sync, &nbits_vac, &nbits_left48);

// Initialize the pitch coding parameters
code_pitch_init (nbits_pitch48, nbits_ff_pitch48, &nbits_left48, &slope1_pitch48,
    &nlevels_pitch48);

// Initialize the voicing coding table
code_voicing_init (nbits_voicing48, nbits_ff_voicing48, &nbits_left48,
    &slope_voicing48, &nlevels_voicing48);

// Initialize the gain coding table
code_gain_init (nbits_gain48, nbits_ff_gain48, &nbits_left48,
    &nlevels_gain48, &table_gain48, ALPHA48, &alpha48, &gain_min, &gain_max);

// Initialize the parameters for lsp coding
if (vq_lsp_flag)
    vq_lsp_init (bit_rate, &nbits_left48, order_allpole48, nbits_ff_lsp48,
        nbits_lsp48_k, nlevels_lsp48_k, nbits_lsp48_kp1, nlevels_lsp48_kp1,

```

Example of a segment of the Code

VISUAL TARGET TRACKING AND EXTRACTION FROM A SEQUENCE OF IMAGES

Nikolaos Bourbakis
Associate Director/Professor
Department of Electrical and Computer Engineering

Binghamton University
T.J. Watson School of Engineering & Applied Science
Center for Intelligent Systems
Binghamton, NY 13902

Final Report for:
Summer Faculty Research Program
Rome Laboratory

Sponsored by:
Air Force Office of Scientific Research
Bolling Air Force Base, DC

And

Rome Laboratory
Rome, NY

August, 1997

VISUAL TARGET TRACKING AND EXTRACTION FROM A SEQUENCE OF IMAGES

Nikolaos Bourbakis
Professor
Dept. of Electrical Engineering,
Dept. of Computer Science,
Associate Director
Center for Intelligent Systems
Binghamton University,

Richard Andel
Graduate Student
Dept. of Computer Science,
Binghamton University,

Abstract

This paper presents a methodology for visually tracking and extracting targets from a sequence of images (video). The methodology presented here consists of a combination of algorithms, such as heuristic segmentation, edge detection, thinning, region growing, fractals, feature extraction, graph with attributes, etc., appropriately selected according to the existing situation, such as moving target - still camera, still camera - moving target, moving target - moving camera. The new contribution of this paper is the combination of algorithms in a human like feedback geometric approach of processing low resolution information from consecutive images. Simulated results of the methodology are presented.

Keywords: Visual Target tracking, Feature Extraction, Fractals, Graphs, Processing sequences of images

VISUAL TARGET TRACKING AND EXTRACTION FROM A SEQUENCE OF IMAGES

**Nikolaos Bourbakis
Richard Andel**

1. Introduction

Technological advances in artificial intelligence and especially in heuristic search using fractals, pattern recognition and image understanding have provided the opportunity for the development of autonomous systems for Automatic Target Recognition (ATR) from still images [1-9]. ATR in pattern recognition and image understanding based method depends upon resolution for a successful classification. Several of these ATR methodologies can successfully applied to targets detection and identification in a sequence of images (video). In particular, Songhua et al. [4] employ the use of a wideband millimeter wave radar to receive high range resolution and extract the target's center. More specifically, they use the high range resolution to extract the target's features (shape, size, physical structure). Then, they use a heuristic feature extraction technique to detect the target's scattering centers, the number of strong scattering centers, the target's range extent, the range distance between scattering centers and the relative amplitude of the scattering center peaks for the recognition and location of the target in a single frame. A similar ATR radar algorithm was described by them, but on an incoherent low resolution radar. The authors used a semi-fuzzy clustering algorithm to extract the target's feature.

In addition to classical based ATR, researchers have also developed Neural Network based ATR algorithms. The major effort of using ANN algorithms for ATR is to train the neural net with various radar based information related with a specific type of targets, such ships and perform fast classification-recognition of the unknown target received by radar returns. In this type of ATR the training data set is very large, and becomes larger when additional noisy information, such as shift independent, scale, fluctuation, is considered. For these type of ATRs FFT, DMT and CT transformations are needed for the feature extraction and preprocessing, see Min et. al [3]. Most recently, neural nets researchers attempt to overcome with some of the weak points of the neural network ATR approaches, such as fluctuations of echoes, deformation, number of hidden layers and hidden neuron/layer, number and size of neural nets, etc. [1]. The neural net approach seems promissible but has to wait until the VLSI technology is able to support realistic neural nets

implementations.

The methodology proposed here attempts to visually track and extract the target's features in near real-time by using a human like feedback geometric approach and a limited amount of information (original coordinates, size) available from a sequence of images (video). In particular, the methodology presented here consists of a combination of algorithms, such as heuristic segmentation, edge detection, thinning, region growing, fractals, feature extraction, graphs, etc., appropriately selected according to the existing situation, such as moving target - still camera, still camera - moving target, moving target - moving camera. The new contribution of this method is the combination of algorithms in a human like (heuristic) feedback geometric approach of processing a small amount of information extracted from low resolution data from consecutive images. The human like approach is based on the way that humans maintain and interrelate portions of visual information from sequential views (frames) in order to detect motion and extract features from selected "objects". In the methodology presented here, we attempt to emulate this human perception by tracking motion of adjacent colors in a sequence of images. Simulated results of the methodology using sequences of images are presented.

2. The Methodology for Visual Target Tracking and Extraction

A classical ATR method may consist of four basic steps: 1) target detection, 2) target tracking, 3) features extraction, and 4) target recognition.

The methodology described by this paper presents only the visual target tracking and features extraction parts from a sequence of images.

2.1. Target's Specs

For any ATR system the target detection part starts with the determination of the targets' specs. More specifically, the specs of a target may vary from a single name (e.g. bus) to a more complex description (e.g. shapes, size, colors, texture, specialized features, etc), or some time something "unknown", which specs does not match with the specs of known targets.

In our case here, we assume that the target's specs are limited to a pair of coordinates (i,j) which point the target at the initial frame. Thus, the goal is to use this limited information (i,j) for the tracking and extraction of a target (T) from a sequence of images.

In a future step, our ATR system will accept target's specs and automatically detect the target without the use of initial coordinates [4,6].

2.2. Heuristic based Image Smoothing, Edge-Detection with Thinning

Initially, we apply a heuristic based edge detection - thinning and segmentation method to define and clean the image regions with specific colors [9]. In particular, an image has to be smoothed before an edge detection process in order noise to be removed, especially noise associated with the camera [15].

. Smoothing

During the smoothing process, the color value of a pixel is compared with the color of each its eight neighboring blocks, as shown in figure 1. Note that blocks of pixels are used here instead of single pixels. The average color of a block can be determined by using the neighborhood's member-ship functions with respect to the center pixel as shown in equation 1.

$$C_{ij,b} = \frac{\sum_{q=p}^{p'} \sum_{s=k}^{k'} \mu_{n_{sp}} \cdot C_{sq}}{\sum_{q=p}^{p'} \sum_{s=k}^{k'} \mu_{n_{sp}}} \quad (1)$$

where, k,p point to the low left and k',p' to the top right corner pixel in block b and C_{sq} represents the color vector of a pixel at the location sp. This equation evaluates the average color vector of a block b with respect to the center ij of the pixel. For smoothing, the color contrast between the center pixel and all the neighboring blocks must be measured.

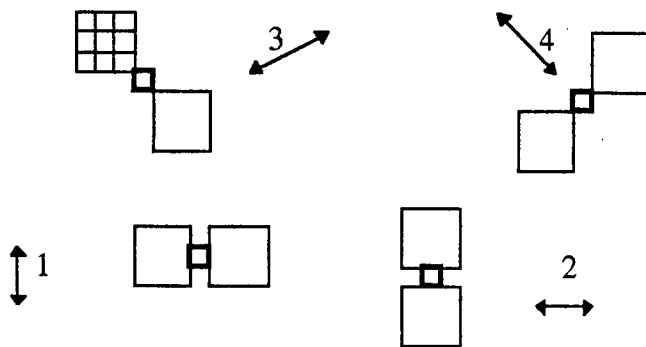


Fig. 1: Eight neighboring blocks of size 3x3 and four edge directions.

. Edge Detection with Thinning

Hue (h) , Intensity (I) and Saturation (s) are important parameters edges in images. These parameters can be computed by using RGB values from the equation (2).

$$\begin{aligned}
 x &= 0.49R + 0.31G + 0.20B \\
 y &= 0.177R + 0.812G + 0.011B \\
 z &= 0.00R + 0.01G + 0.99B \\
 l &= 116(y/y_0)^{1/3} \\
 a &= 500[(x/x_0)^{1/3} - (y/y_0)^{1/3}] \\
 b &= 200[(y/y_0)^{1/3} - (z/z_0)^{1/3}] \\
 I &= l ; s = [(a^2 + b^2)^{1/2}] ; h = \tan^{-1}(a/b) ;
 \end{aligned} \tag{2}$$

where, x,y,z are color values. The edge detection algorithm accepts smooth image input, evaluates the four edge directions (fig. 1), defines local maxs by using histogram information, thins the edges and restores the image.

2.3. Region Growing and Chain Coding for Extraction of Target's Regions

When the target's coordinates (i,j) are given their color (v) is defined and a region growing algorithm is applied to determine the shape and the size of the target's color region pointed by the coordinates (i,j).

. The basic steps of the region growing algorithm are:

*Define the starting pixel P(i,j);
 Create the neighborhood template 3x3 around P(i,j);
 Compare the color value (vx) of each neighbor pixel with starting pixel's one (v);
 If v ≠ vx then define the border pixels and save their coordinates in file and
 goto the next neighbor pixel;
 else continue with the next neighbor pixel;
 Repeat the process in a spiral manner;*

. The Chain code algorithm is used to select the coordinates from the designated file and converts them into a string S by using the eight directions D={0,1,2,3,4,5,6,7} of the chain code.

$$S = (i,j) \text{ } n_i(d_k) n_j(d_m) \dots n_r(d_t)$$

where $n_i, n_j, \dots, n_r \in \mathbb{Z}$ represent the number of pixels with the same direction,

$d_k, d_m, \dots, d_t \in D$ represent the chain code directions, and (i,j) represents pairs of coordinates related with the beginning of the string and its substrings if any.

2.4. Target's Region: Shape, Size, Graph and Framing

The target's region ($R_c \in T$) extracted by the region growing algorithm has a specific shape Sh represented by a chain coding string. This particular string is rearranged, by selecting its longest sub-string with the same direction to be at the beginning of $Sh \in R_c$, as shown in the following example:

original shape

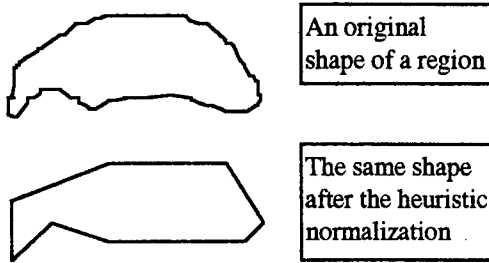
$Sh = d1d1d3d3d3d7d7d7d7d7d7d7d7d4...d4$

rearranged shape

$Sh' = d7d7d7d7d7d7d7d7d7d4...d4d1d1d3d3d3$

The size of a particular target's region is also extracted during the region growing algorithmic process and saved in a file as a number of pixels with the same color.

At this point the methodology creates a graph $G(R_c)$ with attributes for a more robust representation of the region R_c . In particular, a heuristic straight line segment recognition process is used to convert the string Sh' into a sequence of straight line segments, $Sh' = L1 L2 L3 L4 \dots$, as shown below:



At this point, the normalized shape is converted into a graph with attributes

$$G(R_c) = \overset{c}{N1} \overset{c}{a1} \overset{c}{2} \overset{p}{N2} \overset{s}{a2} \overset{s}{3} N3 \dots Nk \overset{c}{ak} \overset{c}{1} N1 \otimes N \overset{c}{aij} \overset{c}{Nj} \dots \otimes N \overset{c}{nanm} \overset{c}{Nm} \dots$$

where, a graph node N_i represents a straight line segment with the attributes (starting point, orientation, length, curvature); and an arc ax_{ij} represents a set relationships among line segments, such as (connectivity (c), parallelism (p), similarity (s), relative magnitude (rm),...).

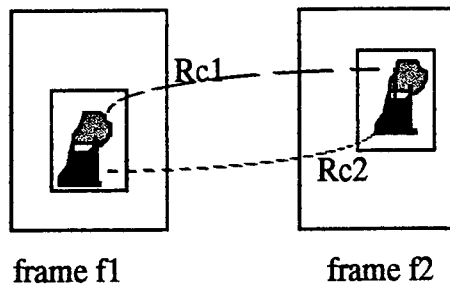
Finally, a frame around the target's region R_c can be generated. The frame is a rectangular area, which covers the region $R_c \in T$ and additional pixels from the surrounding area. The purpose of this frame is to define a smaller area at the original image frame, which will be used for a quick segmentation and determination of the rest target's parts (regions).

2.5. Tracking and Extraction of Target's Regions in Consecutive Frames

Humans have the ability to detect motion of color regions by comparing them in consecutive views (frames) . In particular, the human eye has the ability to approximately maintain a view for 1/10 of a second. This is enough time for the human visual system to compare differences occurred between two or more consecutive views and track the motion of different colors. Then, the visual system extracts the shapes of these regions, synthesizes them into a global shape which represents a moving "object", and attempts to recognize the "object" against to an existing set of relative representations.

We define here the process for tracking moving target 's regions in consecutive frames (images) by emulating the human perception of detecting and tracking motion of adjacent colors in a sequence of images. In particular, the algorithmic steps are:

- . Create a frame $W(Rc1)$ around the coordinates (i,j) at the frame $f1$;
- . Apply the heuristic segmentation on the frame $W(Rc1)$;
- . Define and extract the shape of a target's region $Rc1$ with color $(v1)$ by using the coordinates (i,j) ;
- . Generate the graph $G(Rc1)$;
- . Move to next frame $f2$ and develop a new frame $W(Rc1)$ around the coordinates (i,j) ;
- . Apply the heuristic segmentation process on the new frame $W(Rc1)$;
- . Search for the region $Rc1$ by using an S-S or S-D algorithmic procedure;
 - If $Rc1$ is found then extract it and generate its graph representation $G(Rc1')$;
 - Compare the two graphs $\{G(Rc1), G(Rc1')\}$;
 - If $G(Rc1)$ is similar to $G(Rc1')$, then search for an adjacent region $Rc2$ 'with color $(v2)$ at the frame $f2$ and extract its graph $G(Rc2')$;
 - Go back to frame $f1$ and search for a region $Rc2$ with same color $v2$;
 - If $Rc2$ is found then compare their graphs $\{G(Rc2), G(Rc2')\}$
 - if they are similar , then
 - synthesize these two regions into a new one as parts of the target;
- . Repeat the process for other adjacent regions;
- . When all target's regions have been found, then color them with the same color (vt) defining them as single color target T , generate the target's graph $G(T)$, and create a new frame $W(T)$ for it;
- . Go to the next frame $f3$ searching for the target T ;
- . Readjust the size of $W(T)$ if the target is moving in depth;
- else $Rc2'$ is background; then continue for another adjacent region;
- else the $Rc1'$ is background and move the frame $W(Rc1)$ around and repeat the process;



. Tracking Scenarios

We examine the methodology to track the regions (or parts) of a target under various scenarios, such as, (a) moving camera-moving target (MCMT), (b) moving camera- still target (MCST), (c) moving target-still camera (MTSC).

. Successive Spirals (SS) for MCMT

In this particular case, both the target and the camera are moving with different velocities (V_T , V_C) and in different directions as well, as shown in figure 2.

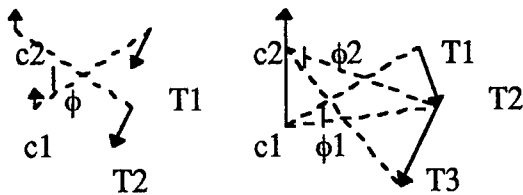


Figure 2.

The basic assumption here is that the target has to appear into two consecutive images (frames) in order to be tracked by the camera. If this assumption is true, then the camera has to rotate itself to the target's direction by an angle ϕ_i , $i=1,2,3...$ defined by the motion of the target. When the target appears at the first frame (f1), the methodology described here assumes that the target will be automatically detected by another process, or pointed by the user on the frame f1, thus the initial target's coordinates (i_0, j_0) are saved for the next processing steps. At this point, the methodology extracts the particular region pointed by its specific color value, as mentioned in the previous section. At the second frame (f2) the target will appear at any position, thus the methodology applies a spiral (Ss) scanning to detect the target at its new position (i_1, j_1) as shown in figure 3.

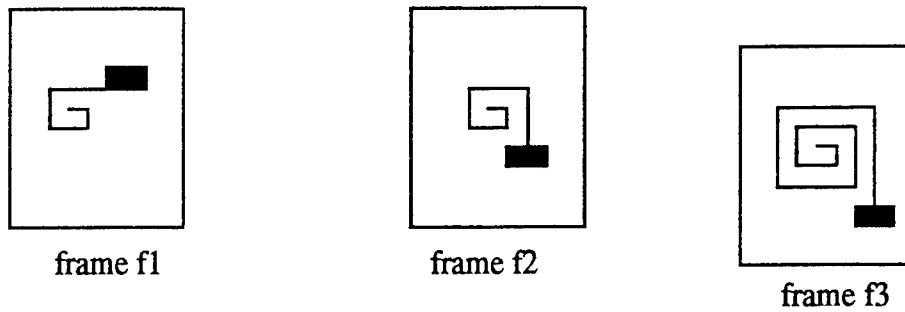


Figure 3.

Since the target is moving, there is always a non zero probability that it will change direction from frame to frame, thus the methodology applies always a spiral detection scanning, starting from the previous (i,j) , or the center of the frame $(f_j, j=2,3,...)$, to find the target. This proposed target detection approach works based on the target's color under the assumption that the color (v) of the region R_c will not drastically change from a frame f_j to the next one f_{j+1}

. *Spiral with Successive Diagonals (SDs) for (MTSC), or (MCST).*

In these cases, one of the two items used here is moving when the other remains in a fixed position. In particular, there is a case that the camera is still and the target is moving. Here, we assume that the target appears into two consecutive frames f_1 and f_2 as previously. Thus, the methodology firstly applies a spiral scanning to detect the target at the second frame. At this point the method saves the new co-ordinates (i_1, j_1) and develops trajectory vector for the motion of the target. Thus, at the next consecutive frame f_3 , the method does not apply a spiral scanning to detect the target, but a diagonal one in smaller area, which requires less scanning steps to find the target, as shown in figure 4.

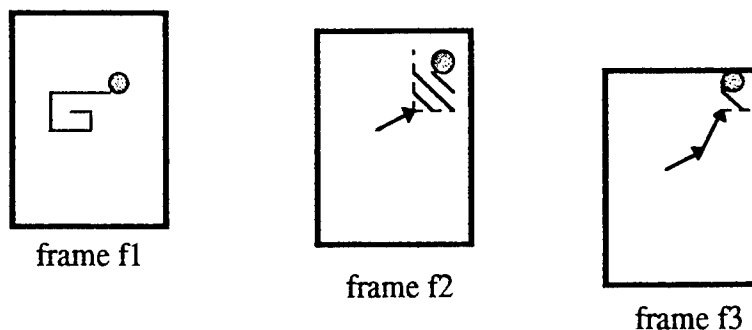


Figure 4.

. Target's region extraction and comparison

In case that the target's region R_c is detected, a region growing algorithm is applied by the methodology to extract the region's characteristics (size, color, shape). These three features are important for the identification of the correct region. Thus, a comparison takes place between the previous region's characteristics and the new ones. Since the color (v) is the same the emphasis is given at the two other features, size and shape. The comparison between two sizes $Sz1$ and $Sz2$ is very simple, since by size we mean the number of pixels with the same color (v). Thus, the methodology subtracts these sizes $|Sz1 - Sz2| \leq \epsilon$, where ϵ represents a heuristic acceptance range. Next, the method compares the graphs $G(Rc1)$ and $G(Rc2)$ by using a confidence function f for the graph matching process,

$$f(N_i, a_{ij}) = [(\#N/\#N') + (\#N_{same}/\#N'_{total}) + (\#a_{ij} \text{ same}/\#a'_{ij} \text{ total}) + (sub(a_{ij}(c))/seq(a'_{ij}(c))) + (\#a_{ij}(p)/\#a'_{ij}(p)) + (\#a_{ij}(s)/\#a'_{ij}(s))] \leq E$$

where E represents a heuristic threshold of acceptance

3. Illustrative Examples

For the illustrative examples, we used sequences of synthetic (4 consecutive frames) and real grey scale images, a PC pentium 200MHz, and a target of 950 pixels. Note that this methodology works for color sequences images as well.

3.1. Synthetic Sequence of Images

. Moving Target - Still Camera

. Methodology S-Ds

Results:

Frame f0 = 0 msecs

Frame f1 = 0.35 msecs, spiral

Frame f2 = 0.13 msecs, diagonal

Frame f3 = 0.07 msecs, diagonal

Total = 0.55 msecs

. Moving Camera - Moving Target using previous coordinates

. Methodology S-Ss

Results:

Frame f0 = 0 msec

Frame f1 = 0.35 msec, spiral

Frame f2 = 0.62 msec, spiral

Frame f3 = 0.31 msec, spiral

Total = 1.28 msec

. Moving Camera - Moving Target using central points

. Methodology S-Ss

Results:

Frame f0 = 0 msec

Frame f1 = 0.0045 msec, spiral

Frame f2 = 0.49 msec, spiral

Frame f3 = 2.72 msec, spiral

Total = 3.21 msec

3.2. Grey Scale Images

. Moving Target - Still Camera

. Methodology S-Ss

Results:

Frame f0 = 0 msec

Frame f1 = 12.5 msec, spiral

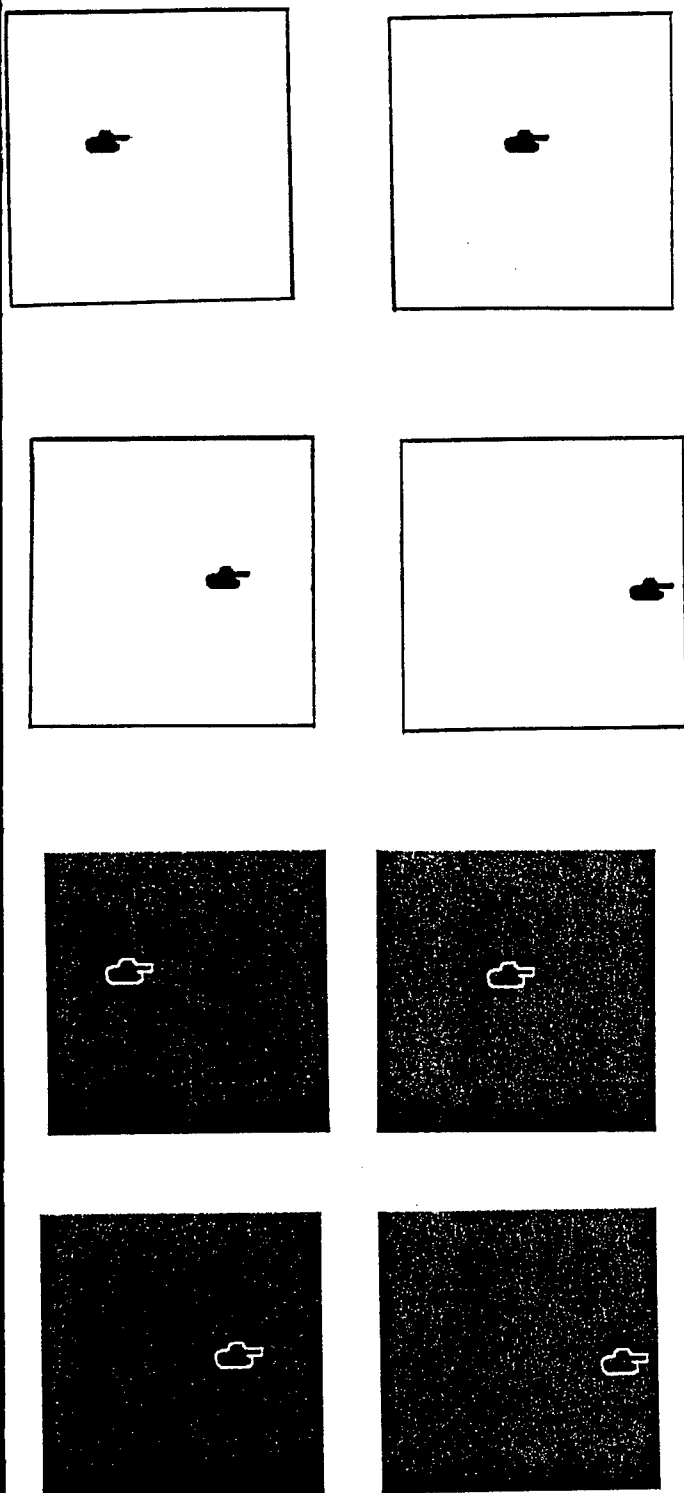
Frame f2 = 10.5 msec, spiral

Frame f3 = 10.5 msec, spiral

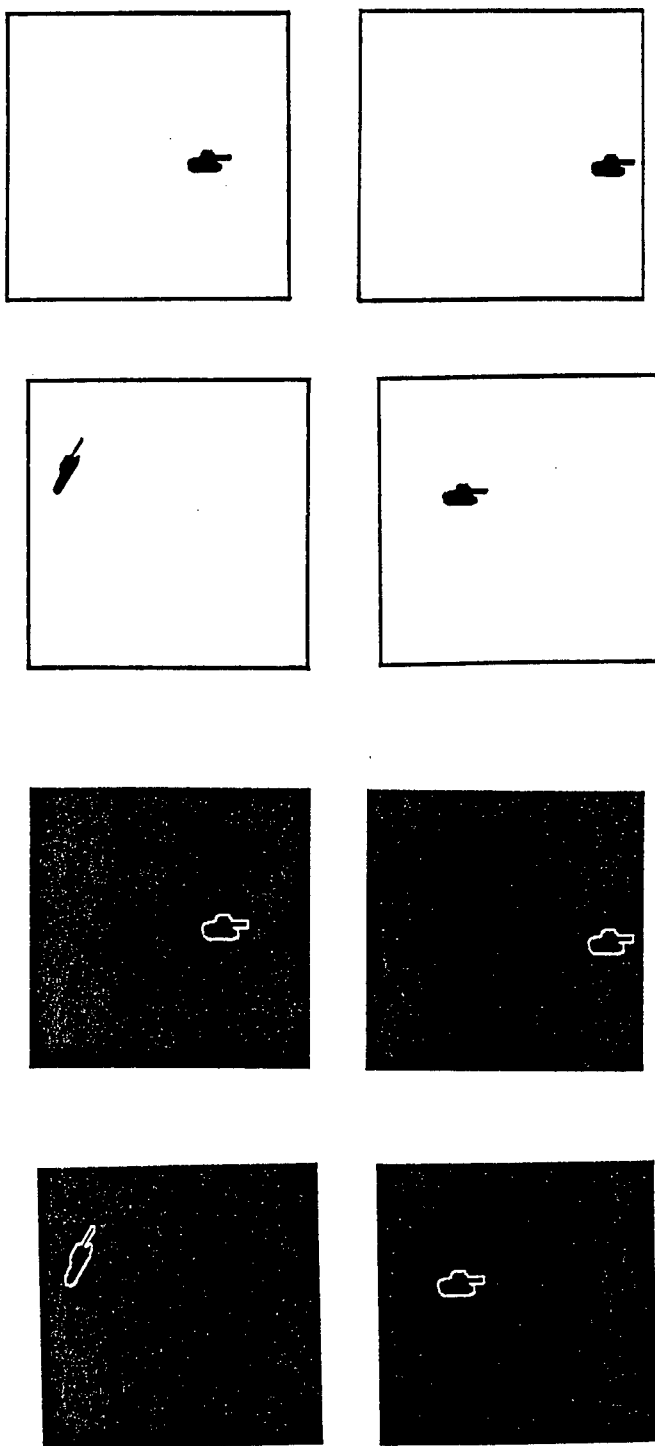
Total = 32.5 msec (without segmentation)

Simulated Results.

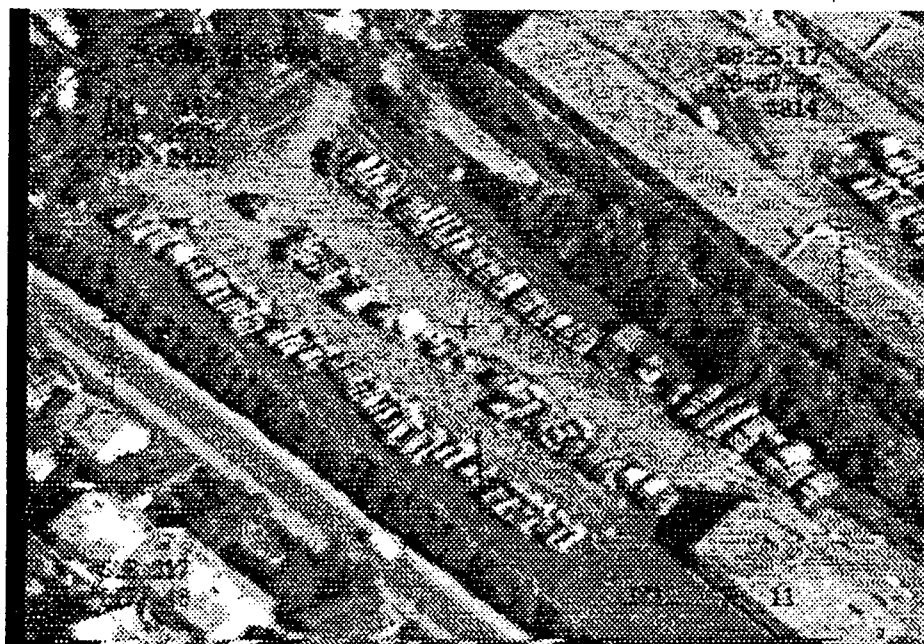
A. *Spiral-Diagonal Approach* Target moving-camera fixed



B. *Spiral-Spiral Approach* Target moving-camera moving



A Real Sequence of Images



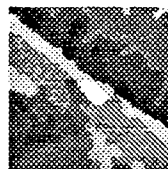
First Original Image



Window



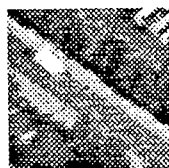
Smoothed



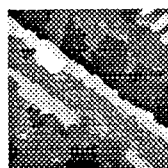
Segmented



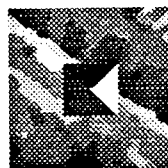
Target Shape



Window



Segmented



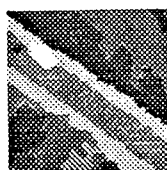
Spiral Search



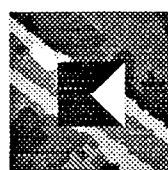
Target Shape



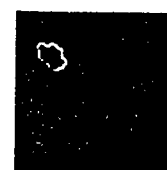
Window



Segmented



Spiral Search



Target Shape

4. Conclusion and Discussion

In this paper a near real-time methodology for visual tracking and extraction of targets from a sequence of images was presented. This methodology is based on a heuristic human like geometric approach by appropriately combining heuristic segmentation, edge detection, region growing, search (fractals), object extraction and tracking algorithms. The methodology applied on different scenario, such as moving camera-still target, moving target-still camera, and moving camera - moving target. For the implementation of the current status of this project 7K lines code was written.

Future work: real-time classification of targets under noisy condition, and fusion of different sensory data, such as IR, radar, thermal.

Acknowledgment

This work is partially supported by the IRR division , AFRL-Rome, 1997, and the authors wish to express many thanks to IRR personnel, especially to Andy Hall, Todd Howlett and Steven Farr for their continuous support .

References

- [1] S.Grossberg, H>Hawkins and A.Waxman "A special issue of ATR, Neural Network Journal, vol.8,7-8,1995
- [2] M.Brown and W.Swonger, "A prospectus for ATR", IEEE-T-AES, 25,3,1989
- [3] Min et. al., The second order neural nets for radar ship target recognition, NAE Conf. 1992, pp. 270-277
- [4] Songhua et al., "Target discrimination and recognition using high resolution range features", NAE Conf. 1992, pp. 280-286.
- [5] Theis, et. al., " Comparison of model based vision statistical based and neural net based ATRs", NAE Conf., 1989, pp. 1733-1739
- [6] J.Novak and N.Bourbakis, "A survey on ATR detection and recognition", TR-1993, MV Lab BU-CIS, pages 21.
- [7] N.Bourbakis et al., " A comparison among segmentation techniques for ATR", TR -1993, MV Lab, BU-CIS, pages 15
- [8] N.Bourbakis, " Knowledge extraction and representation during navigation in unknown environments, IJPRAI, 9,1,1995

- [9] A. Mogzadeh and N.Bourbakis, Region growing based segmentation of color images, IAPR Society Pattern Recognition Journal, 30,6,1997
- [10] N.Bourbakis and R.Andel, Fusion of color image and sensory data for 3-D space modeling, IEEE I&S-98, May. 1998 CA
- [11] N. Bourbakis, A family of SCAN languages, IAPR Society Pattern Recognition Journal to appear 1998
- [12] R.Chellapa et. al., Camera calibration, IEEE Symp. on Intelligent Vehicles, MI, 1995
- [13] E.Yfantis, J.Jeon, A.Sylakou and N.Bourbakis, An intelligent motion compensation algorithm, Int. Conf. on Intelligent Systems, Boston, MA, July 1997, pp.75-78.
- [14] L.Chan and N.Nasrabadi, An application of wavelet based vector quantization in target recognition, Int. IEEE Symp. on Intelligence and Systems, MD, Nov. 1997, pp.274-281
- [15] S.Ghosal and R.Mehtotra, "Detection of composite edges", IEEE T-IP, 3,1,1994

**RECONSTRUCTING THE INFORMATION WARFARE ATTACK SCENARIO
GUESSING WHAT ACTUALLY HAD HAPPENED BASED ON AVAILABLE
EVIDENCE**

Peter P. Chen
Associate Professor
Department of Computer Science

Louisiana State University
257 Coates Hall, Tower Road
Baton Rouge, LA70803

Final Report for:
Summer Research Program
Rome Laboratory

Sponsored by:
Air Force Office of Scientific Research
Bolling Air Force Base, Washington, DC

And

Rome Laboratory

September 1997

RECONSTRUCTING THE INFORMATION WARFARE ATTACK SCENARIO:
GUESSING WHAT ACTUALLY HAD HAPPENED BASED ON AVAILABLE EVIDENCE

Peter P. Chen

Foster Distinguished Chair Professor
Department of Computer Science
Louisiana State University

Abstract

A crucial component in the information warfare is to be able to identify the culprit and to take appropriate actions against the culprit such as to prosecute the culprit in courtroom or launch a counter attack. In order to do so, it will be extremely useful to be able to “reconstructing the information warfare attack scene”. In this paper, a specific approach in reconstructing the information warfare attack scenario is proposed. Future research directions in theory and computerized tools are discussed.

RECONSTRUCTING THE INFORMATION WARFARE ATTACK SCENARIO: GUESSING WHAT ACTUALLY HAD HAPPENED BASED ON AVAILABLE EVIDENCE

Peter P. Chen

I. Introduction

A crucial component in the information warfare (IW) is to be able to identify the culprit and to take appropriate actions against the culprit such as to prosecute the culprit in courtroom or launch a counter attack. In order to do so, it will be extremely useful to be able to “reconstructing the information warfare attack scenario”.

In this paper, we will discuss what has been done in the other fields such as murder crime scene reconstruction, what theories and techniques could be used as the foundation for developing the theory for IW attack scenario reconstruction. Then, we propose a specific approach in reconstruction of the IW attack. At the end, we discuss several future research directions and the potential benefits of such R&D efforts.

2. Methodology

Analogy

There are several analogies in our daily life very similar to the IW attack scenario reconstruction. One of the analogies is the crime and murder investigations and subsequent prosecutions of the culprits in which the reconstruction of the crime scene is a crucial component. A famous example is the O. J. trial. Another example is the Oklahoma bombing trial. Certainly, we can also relate what we intend to do with the various theories or hypotheses on how President Kennedy was assassinated.

In the murder crime scene investigations, are there any good procedures and practice can be borrowed by us in the IW attack scenario reconstruction? Let us take a closer look. The crime scene reconstruction techniques are used more and more often in the court rooms by both the prosecution and defense teams. Many attorneys have found that using the recreated crime scenarios, they can

convince the jury much easier than just using words. However, the current practice in the court rooms is not without its problems. For example, the attorneys tend to use a small set of "selected evidence" (usually, the evidence which is more favorable to their objectives) to support a particular crime scenario. Because each side emphasizes certain evidence in favor of their arguments and de-emphasizes the other evidence, the jury has a hard time to figure out which scenario (the one presented by the prosecution or the one presented by the defense) is the most likely one. It is like comparing apple from orange. Furthermore, because of more TV cameras getting into the courtrooms, the reconstruction of crime scene, more emphasis is placed on showmanship than science.

What Is Needed and Where Do We Start

What we need is a scientific theory and procedure to reconstruct the IW attack scenes from the evidence.

The current practice in the courtroom usually does not assess (and present to the jury) the precise probability of each piece of evidence. Because of this, it is very difficult for the jury to decide the likelihood of each possible crime scenario based on the existing evidence. We think it is very important and useful to have a scientific theory to accurately calculate the likelihood of each IW attack scenario so that we can compare them more accurately.

In the following, we will first studied the existing police crime scene reconstruction practice and discuss how we can learn from them. Next, we will look at several relevant cognitive theories or architectures to see whether they will be useful for our purpose.

Possible foundations for our theory

We have examined the following techniques for possible use for in the development of our IW attack reconstruction theory:

- cognitive architectures,
- Bayesian analysis,
- backward goal matching,
- neural network,
- deductive and inductive reasoning,
- Dempster-Shafer theory.

We will not get into the details of these techniques. Here, we only take one to show the range of techniques we have investigated. For example, there are many cognitive architectures:

- problem-space architecture (SOAR),
- subassumption architecture (Brooks)

- modular-integrated architecture (ICARUS)
- a basic integrated agent (Homer)
- situated action + planned action (Teton)
- planning and learning architecture (Prodigy).
- Heterogeneous asynchronous architecture (Gat)
- Others.

Each of these cognitive architecture provides a framework for the analysis of human cognition. For example, SOAR, which represents “State, Operator, and Result”, is a cognitive architecture based on deductive procedure. It uses an attribute-value representation knowledge representation technique, which is similar to the Entity-Relationship (ER) model [CH76] widely used in systems analysis and data modeling area.

After studying various techniques outlined above, we conclude that the Dempster-Shafer theory [De76, Sh76] can be used as the foundation for our approach for IW attack crime scene reconstruction.

Proposed Approach for Reconstruction of IW Attack Scenario

We propose the following approach for reconstruction of IW attack scenario:

1. Collect the IW attack evidence
2. Identify Possible culprits
3. For each culprit or group of culprits, identify possible attack scenarios.
4. Assess the probabilities of each piece of evidence based on the opinions of experts with the specific domain of knowledge
5. Derive the probabilities of each possible IW attack scenario using Dempster-Shafer theory.

Step 1: What information/evidence to collect

If your computer system (or network) encounter an IW attack, we recommend that you collect the following information:

- **What:** what is the size, extent, and shape of the damage?
- **Why:** why does your system get the IW attack? What are the possible causes?
- **When:** when did your system get the IW attack? What is the timeline for a series of events of the attack?
- **Who:** who has the access rights to your system? Who has accessed your systems based on your records and other evidence?
- **Where:** Where in the system did the IW attack first occur? Where did the IW attack agents propagate? Where are the possible origin places of the attackers?
- **How:** how did the IW attack occur? How did the IW attacker or its agents get inside your system?
How was the damage created?

You also need to collect the following information:

- Your computer system/network configuration and topology at the time of the IW attack
- The general physical environment of the computer system/network and the existing physical security system and procedures.
- The system personnel and users.

Where can we find the information for the above list of questions? The following is a list of possible sources:

- The data in the system and database logs
- The data collected via Common Intrusion Detection Framework (C.I.D.F.)
- The data collected by other sensors and monitors
- Examination and tour of the physical environment
- Documentation of the security mechanism and procedures
- Lists of system personnel and users
- Interview records with the system personnel, users, and security officers after the IW attacks.

Step 2: Identify Possible culprits

In this step, you need to identify the possible culprits responsible IW attacks. Here is a list of questions you need to ask:

- What individuals, groups, organizations, or countries are hostile to your organization/country?
- What individuals, groups, organizations, or countries are capable to launch this type of IW attacks?

Note that there two questions are not the same. Someone could attack you even though it may appear that he/she is not hostile to you. Also note that the “individuals” mentioned above include “hackers”.

Step 3: For each possible culprit or group of culprits, identify possible attack scenarios

For each possible culprit or group of culprits identified in Step 2, try to identify possible attack scenarios.

It is possible that there are several (or many) possible attack scenarios for each culprit (or group). It is also possible that the same (or very similar) attack scenario can be applied to each culprit (or group).

If there are too many possible attack scenarios for a particular culprit (or group), identify the top five most likely attack scenarios. This can be achieved by a careful assessment by domain and IW experts.

Step 4: Assess the probabilities of each piece of evidence based on the opinions of experts with the specific domain of knowledge

For each piece of evidence, you need to assign the probability that this evidence is 100% accurate. In other words, you need to assess the “confidence” of each piece of evidence. You can assign the probability of “1” if the evidence is without any doubts. Sometimes, it is difficult to pin down the exact value of the probability. In that case, a range of probability (such as from 0.3 to 0.5) should be identified. The assessment of these probabilities should be done by domain and IW experts.

Step 5: Derive the probabilities of each possible IW attack scenario using Dempster-Shafer theory

Dempster and Shafer developed a theory of evidence in 1976. Subsequently, many researchers have extended their theory. Based on the Dempster-Shafer theory, we can mathematically derive the probabilities of each possible IW attack scenario from the probabilities of the evidence.

The exact procedure of how to apply the Dempster-Shafer theory and an example will be documented in a research paper in the near future.

Future Research Areas

There are several directions for future research:

- To develop a procedure handbook for evidence collection: Many organizations got panic after they realized they had an IW attack. After the initial shock/panic was over, they tried to collect the evidence of the attack, but many of the crucial evidence were lost or contaminated during this shock/panic period. Furthermore, they did not know what information should be collected. We believe that it is very important to have a handbook of procedure for evidence collection available for the security officers of each organization. After the IW attack, these security officer should not get panic, and they can collect the valuable evidence immediately step-by-step based on the “handbook”.
- To modify the Dempster-Shafer Theory to fit the IW attack environment: Some researchers have pointed out some minor problems in applying the Dempster-shafer Theory in certain application domains. We think it will be useful to study further to see whether these weaknesses are also applicable in the IW attack environment. If so, research will be needed to modify the Dempster-Shafer theory to fit better.
- To study the linkage with C.I.D.F.: The common Intrusion Detection Framework provides a common interface for sources of information on intrusion detection. Research are needed to identify what information provided in C.I.D.F. will be used for our analysis and reconstruction of IW attack scenarios and how to apply the information in what stage of the process and in what sequence.
- To develop a pathology laboratory: If we have a pathology laboratory, we can study the IW attack and create the attack scenarios in a laboratory environment without interference with the actual recovery process and the daily normal operations of the computer system/network which were attacked. Furthermore, some of the experiments may not be able to perform in the actual system/network can be performed or simulated in the laboratory. Also, we can study the strengths of linkages between causes and effects in a laboratory environment.
- To develop a virtual reality simulator: It will be very useful to have a virtual reality simulator for reconstruction of the IW attack scenarios. It will be much easier to convict the culprit(s) if such a tool

is available. The virtual reality simulator can also be used for training purposes as well as for identification of system weaknesses.

- To develop a IW attack scenario estimator/evaluator: After we perfect the Dempster-Shafer theory to our needs, we can develop an estimator to dynamically rank each of the possible attack scenarios based on different sets of input values of probabilities for the evidence. This type of tools will be useful in the courtroom environment.

Conclusion

After investigating many techniques, we have develop a specific approach in IW attack scenario reconstruction based on murder crime scene reconstruction practice and Dempster-Shafer theory. We believe this research (with the extensions suggested) can become a very effective methodology and tool in identifying the culprits and successfully convict them in the courtroom. Certainly, it will be a very effect weapon and countermeasure in the Information warfare.

References

[Ch76] Chen, P. P. "Entity-Relationship Model: Toward a Unified View of Data," *ACM Transactions on Database Systems*, Vol. 1, No. 1 (March 1976).

[De76] Dempster, A.. "Upper and lower probabilities induced by a multivalued mapping," *Annals of Mathematical Statistics* 38: 325-339.

[Sh76] Shafer, G. *A Mathematical Theory of Evidence*, Princeton Univeristy presss, Princeton, New Jersey, 1976.

**A THREE-DIMENSIONAL, DIELECTRIC ANTENNA ARRAY
RE-CONFIGURABLE BY OPTICAL WAVELENGTH MULTIPLEXING**

Everett E. Crisman
Professor
Department of Physics

Brown University
Box 1843
Providence, Rhode Island 02912

Final Report for:
Summer Research Program
Rome Laboratory

Sponsored by:
Air Force Office of Scientific Research
Bolling Air Force Base, Washington, DC

And

Rome Laboratory

September 1997

A THREE-DIMENSIONAL, DIELECTRIC ANTENNA ARRAY RE-CONFIGURABLE BY OPTICAL WAVELENGTH MULTIPLEXING

Everett E. Crisman
Assoc. Professor (research)
Department of Physics
Brown University

ABSTRACT

Semiconductor antennae activated by fast laser pulses can serve as effective sources of broad-bandwidth electromagnetic radiation. The electromagnetic radiation is generated by accelerating optically stimulated carriers with a high voltage electric field within or along the surface of the semiconductor. If the photo-carrier lifetime is much longer than the laser temporal pulse width, the electromagnetic radiation waveform essentially emulates the optical pulse profile. We report here a three dimensional (3-D), reconfigurable, semiconductor based, phased array antenna which is activated by multiple wavelength, picosecond laser pulses (optical wavelength multiplexing). Based upon the nonlinear characteristics of the radiated field as well as dielectric nature of the semiconductor antenna elements, a 3-*dimensional* array can be implemented with minimum cross-talk among the elements. The antenna is reconfigurable by varying combinations of the applied voltages, optical beam geometry, and laser wavelengths. As suggested by theory, we have demonstrated experimentally that the radiation pattern of such an antenna is sensitive to the 3-D geometry of the radiation source. This, in turn, can be varied in a continuous manner by optical wavelength multiplexing.

A THREE-DIMENSIONAL, DIELECTRIC ANTENNA ARRAY RE-CONFIGURABLE BY OPTICAL WAVELENGTH MULTIPLEXING

by
Everett E. Crisman

INTRODUCTION

The rapid advance in miniaturized electronics and computers has pushed the performance requirements for antennae beyond what current antenna suites can support. For military applications, the mission requirements have greatly increased the number of electromagnetic sensors placed on antenna platforms. As a result, already critical problems of weight and volume limitations have been exacerbated. Furthermore, unwanted platform radar signatures also increase with the number of sensors in the suite. The concept of reconfigurable photoconductive antenna arrays addresses the need to include more antenna elements using fewer exposure apertures¹. Replacing bulky feed-lines with optical fibers also contributes to compactness, weight reduction and speed. Still more size, weight and speed advantages can be realized by optical rather than electro mechanical implementation of beam steering and signal processing².

The semiconductor antenna arrays can be activated by lasers operating in either the pulsed³⁻⁵ or CW mode⁶. When the laser source excites photo carriers in the semiconductor element, the carriers are accelerated in an externally applied electric field thereby generating electromagnetic radiation. When un-illuminated, the semiconductor elements are essentially transparent to E-M fields at RF frequencies and so they offer no interference to nearby, active elements. By their very nature as dielectrics, semiconductor antenna elements are also immune to detection when not activated.

In this paper, we report the measurements which demonstrate the use of picosecond laser pulses to activate two photoconductive antenna elements in a serial configuration. Instead of activating the individual elements through separate optical beam paths, the coherent multiple wavelength sources are contained in a single optical path. As a result, the array can be reconfigured by varying the wavelength content of the sources. When combined with coplanar excitation of photoconductive elements (illustrated in Figure 1, three-dimensional E-M radiation sources can be envisioned.

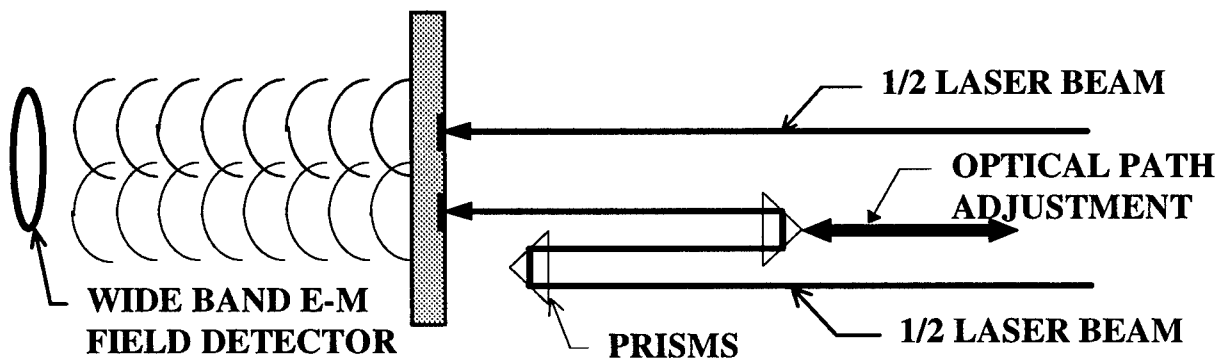


FIGURE 1: Experimental configuration for the co-planar excitation of two separate areas of a single semiconductor E-M source using a split laser beam.

The concept and general experimental setup of the laser induced, pulsed, picosecond, E-M sources (LIPPES) have been described in detail elsewhere⁵. Briefly, a mode-locked, Q-switched, YLF laser system provides 50uJ pulse energy with 80ps pulse duration at a wavelength of 1053nm and with a repetition rate of 378Hz. The laser pulses are selectively chosen by a Pockel cell and a KDP frequency doubler converts the pulses to a wavelength of 527.5nm. The doubling is accomplished in such a manner as to allow a significant amount of energy to radiate at 1053nm as well. An ultra fast photo detector is used to trigger a TEK11802 sampling scope. Pulses of 10ps duration are readily resolved with this setup. A 20kV, 5μs, bias pulse is synchronized with the laser pulse. Pulsed bias is used instead of dc bias to reduce problems with heating and surface flash over on the elements. Figure 2 illustrates the serial configuration of two semiconductor elements photo activated by such a dual wavelength laser source.

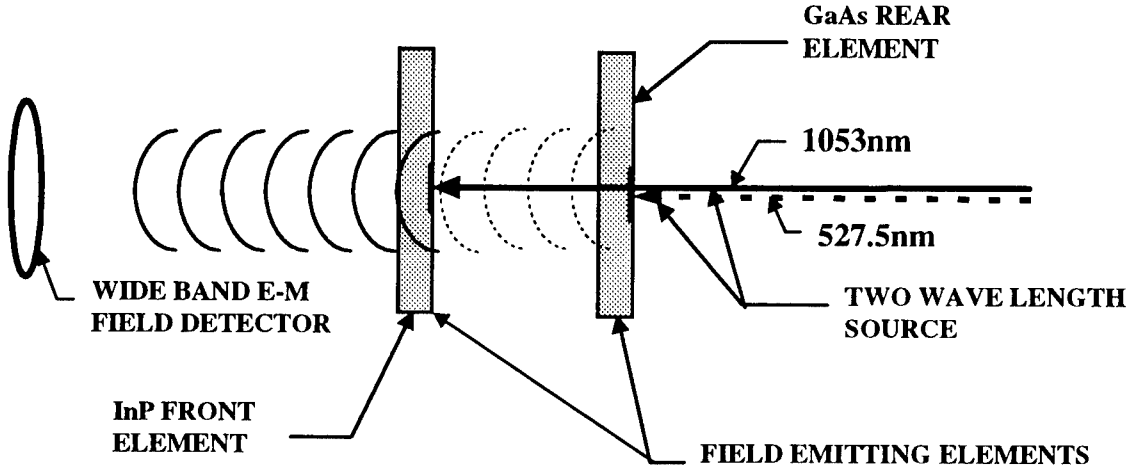


FIGURE 2: LIPPES series configuration for a two ‘color’ laser source exciting two E-M radiating element in series configuration.

The two antenna element system consists of GaAs wafer in the rear and InP wafer in front. Undoped, GaAs ($E_g=1.43\text{eV}$ @RT) strongly absorbs the 527.5nm but is transparent at 1053nm wavelength while the InP, with Fe impurities ($E_g=1.32\text{eV}$ @RT), absorbs strongly at 1053nm. As a result, the array elements are activated with a single optical path. For optimization, the absorption edge and thus the wavelength sensitivities of the semiconductors can be adjusted by varying the density and species of the impurities.

BACKGROUND

The nonlinear characteristic of the radiated field versus the bias field, generated by a gigahertz photoconducting antenna, have been reported⁷. The concept, as described above, is that the photo induced carriers in a semiconductor will be accelerated in a quasi-dc bias field and will radiate electromagnetic fields. The amplitude of such fields, $E(t)$, is proportional to their final velocity (v), as described in the following equation:

$$E(t) \propto \frac{ev(1-R)}{\hbar\omega} \int_{-\infty}^t dt' I_{op}(t') \exp\left[-\frac{(t-t')}{\tau_r}\right] \quad (1)$$

where e is the unit charge quantity, v is the carrier velocity, R is the optical reflectivity of the semiconductor at frequency ω , $\hbar\omega$ is the photon energy, I_{op} is the optical intensity, and τ_r is the photo carrier lifetime.

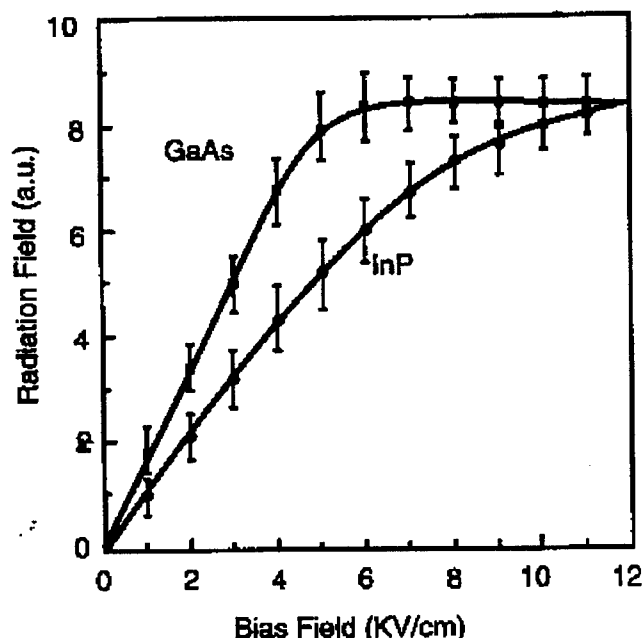


FIGURE 3: E-M field amplitude as a function of the bias field for GaAs, and InP with the optical fluence at $0.3\mu\text{J}/\text{cm}^2$. Two curves are scaled to have a same radiation field magnitude at the bias field of 12 kV/cm (after ref. 7).

Typically, the accelerated carriers (usually electrons) in the semiconductor can reach their final velocity within a few picoseconds or less, i.e. much shorter than the optical pulse duration of about 80ps. Consequently, the waveform of the generated microwave pulse emulates the profile of the optical pulse. Since the final velocity of the carrier is not linear with the bias electric field, some threshold value exists at which a saturated plateau is observed⁷. This relationship is shown in Figure 3 above.

As a consequence, with the bias field set in the plateau region, the photo induced, E-M radiated fields will become insensitive to variations of the bias field. Taking advantage of this property, the bias field of the front (InP) element was established above that threshold value ($\sim 6\text{kV}/\text{cm}$ for GaAs, and $\sim 12\text{kV}/\text{cm}$ for InP). Therefore, the arriving E-M field from the rear (GaAs) element does not affect the generation of E-M field in the front (InP) element (see Figure 2). Furthermore the E-M pulse and the optical pulse will arrive essentially simultaneously at the front element thus ensuring that the combined (front and rear elements) E-M field will be in phase. In this configuration, the couplings between the elements are expected to be minimal, and the total radiation signal at far field is given as the superposition of the individual E-M fields. Higher gain and beam width narrowing of the far field E-M radiation is thus expected. This was confirmed experimentally as shown in Figure 4.

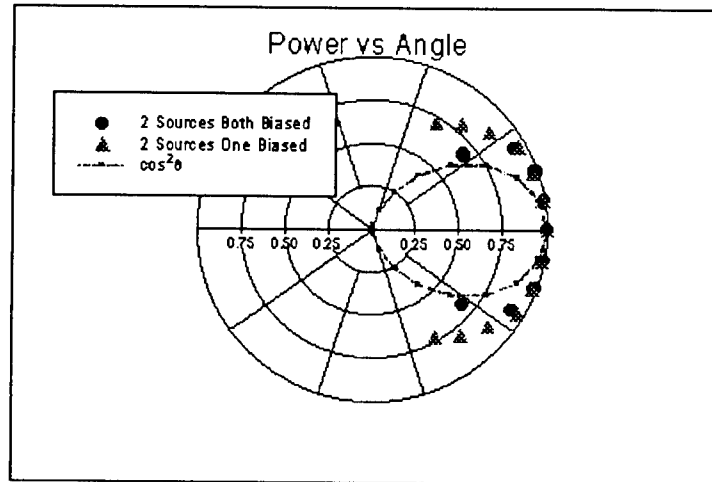


Figure 4: Polar Plot of electromagnetic radiation pattern by single optical path, double wavelength, laser source showing E-M radiation beam width narrowing. (The $\cos^2\theta$ plot is provided for comparison.)

SUMMARY

It is well known that the final velocity of free carriers in III-V semiconductor materials will decrease as the accelerating field is increased above some threshold due to inter-sub band transitions⁸. Such “negative differential conductivity”, is also applicable to optically generated carriers⁹ as well. This suggests that it should be possible, to further reduce the interaction of the element fields as follows. Since the optically generated E-M radiation has opposite polarity from the bias field¹⁰, the arrived electromagnetic pulse at the front element will *decrease* the bias field there, thus results in a higher final carrier velocity, when biasing in the plateau region of Figure 3, or in the negative differential conductivity region if that can be achieved. According to equation (1), the introduction of a higher carrier velocity implies an amplification for the E-M field generation. More significantly, the direction of far field maximum amplitude aligns with the optical beam direction permitting the E-M pulse to be steered optically.

We have demonstrated that multiple (two) photoconductive antenna elements can be optically excited in a serial configuration using a single optical path. The array elements are controlled and reconfigured by optical wavelength multiplexing. Mutual couplings or cross-talk among the elements is reduced to insignificance by using semiconductor elements and directionality can be manipulated via the optical beam direction. Finally, beam strength can be maximized by suitable choice of biasing voltage

ACKNOWLEDGMENTS

I thank Dr. David Liu (Lockeed/Sanders) for the valuable discussions on the laser setups and implementations and Dr. John Derov (Rome Laboratory, Hanscom) for substantial encouragement and help with the experimental data acquisition and analysis. Final particular thanks to Dr. Steven Mittenman for suggesting this project and accepting me into his section for the summer. I also express my appreciation to the Air Force Office of Scientific Research for making this program available to academic faculty in general and me in particular.

REFERENCE

- 1) Roland A. Gilbert, and Gerald T. Pirrung, "Structurally-embedded reconfigurable antenna technology", in Proceedings of the Sixth Annual ARPA Symposium on Photonic System for Antenna Applications (1996),
- 2) H. Zmuda and E. N. Toughlian, Photonic Aspects of Modern Radar, Boston: Artech House (1994).
- 3) Ch. Fattinger, and D. Grischkowsky, "Terahertz beams", *Appl. Phys. Lett.*, Vol. 54, pp. 490-492 (1989).
- 4) X.-C. Zhang, and D. H. Auston, "Generation of steerable sub millimeter waves from semiconductor surfaces by spatial light modulators", *Appl. Phys. Lett.*, Vol. 59, pp. 768-770 (1991).
- 5) D. W. Liu, J. B. Thaxter, and D. F. Bliss, "Gigahertz planar photoconducting antenna activated by picosecond optical pulses", *Opt. Lett.*, Vol. 20, pp. 1544-1546 (1995).
- 6) David Liu, Dave Charette, Marcel Bergeron, Henry Karwacki, Stephen Adams, and Bruce Lanning, "Structurally- embedded photoconductive silicon bow tie antenna", *IEEE Photonics Tech. Lett.* Vol. 9, no. 12 (1997).
- 7) D. W. Liu, P. H. Carr, and J. B. Thaxter, "Nonlinear photoconductivity characteristics of antenna activated by 80-picosecond optical pulses", *IEEE Photonics Tech. Lett.* Vol. 8, 815-817 (1996).
- 8) S. M. Sze, Physics of Semiconductor Devices, 2nd ed. (Wiley, New York, 1981), pp. 638-651.
- 9) G. M. Wysin, D. L. Smith, and A. Redondo, "Picosecond response of photo excited GaAs in a uniform electric field by Monte Carlo dynamics", *Phys. Rev. B*, Vol. 38, pp. 12514-12524 (1988).
- 10) J. T. Darrow, X.-C. Zhang, D. H. Auston, and J. D. Morse, "Saturation properties of large-aperture photoconducting antennas, *IEEE J. Quantum Electron.* Vol. 28, pp. 1607-1616 (1992).

A STUDY OF THE EMERGING DIAGNOSTIC TECHNIQUES IN AVIONICS

Digendra K. Das
Associate Professor
Department of Mechanical Engineering

SUNY Institute of Technology at Utica/Rome
Marcy Campus
P.O. Box 3050
Utica, NY 13504-3050

Final Report for:
Summer Research Program
Rome Laboratory

Sponsored by:
Air Force Office of Scientific Research
Bolling Air Force Base, Washington, DC

And

Rome Laboratory

September 1997

A STUDY OF THE EMERGING DIAGNOSTIC TECHNIQUES IN AVIONICS

Digendra K. Das
Associate Professor
Department of Mechanical Engineering Technology
SUNY Institute of Technology at Utica/Rome

Abstract

An in-depth study of the Emerging Diagnostic Techniques and their applicability to avionic and non-avionic systems was undertaken. The transfer function method model developed by Popyack and Skormin (Ref 1) was studied in detail and a Complementary Model using The Finite Element techniques was developed. An experimental set up using The Time Stress Measurement Device (TSMD) Technology was developed to generate experimental data to validate the model results.

A STUDY OF THE EMERGING DIAGNOSTIC TECHNIQUES IN AVIONICS

Digendra K. Das

INTRODUCTION

The performance of modern aircraft is highly dependent upon the built in sophisticated avionics systems. The reliability of these avionics systems, critical for the safe and reliable operation of an aircraft, can be ensured by means of quality manufacturing, on-line monitoring, diagnostics, and timely maintenance. Since the manufacturing aspects are beyond the scope of the current research, attention is focused on the development of modern monitoring technology and diagnostic methods. The development of these Emerging Diagnostic techniques is closely in track with the areas of research the US Air Force is interested in pursuing for advanced weapon systems such as the F-22 Fighter and the Joint Strike Fighter (JSF) planes. Advanced real-time diagnostic methods and tools for critical systems (such as aircraft avionics) are evolving into an increasingly important technology termed "System Health Monitoring." System health monitoring includes the monitoring of physical and electrical environments which affect electronic system reliability.

Recently a number of scientific papers have been published on this topic of interest (Ref 1 - 3). The Diagnostics Techniques may be categorized as off-line and on-line techniques. The off-line nondestructive diagnostic procedures include visual, ultrasonic and x-ray inspection, mechanical and electrical testing. The procedures are typically performed at regularly scheduled intervals. Off-line Destructive Techniques are "autopsies" of a system to gather statistical data and other information that can be utilized for the design of new systems and the validation of nondestructive diagnostic techniques.

The on-line diagnostic techniques are intended for the detection of abnormal operation of a system and classification of these abnormalities as failures of particular types. Another important feature of the on-line diagnostics techniques is the ability to predict rather than detect an imminent failure. The development of computer based models for these techniques is widely reflected in the published literature. Skormin and Popyack (Ref 1, 3) recently studied these techniques and developed mathematical models to address the problems associated with those. For

practical validation of the results from these computer models, a relatively new device called the Time Stress Measurement Device (TSMD) is available. A brief description of this new tool for diagnostics is given in the following section.

Time Stress Measurement Device (TSMD)

The development of the Time Stress Measurement Device (TSMD) was initiated in 1986 by the Rome Air Development Center (RADC, now Rome Lab) and the project contractor was Honeywell, Inc. The device is packaged into a 1" x 2" x 0.2" hybrid flat pack configuration (Ref 5, 6, 7). It is designed to be capable of measuring and digitally storing in nonvolatile memory, vibration, shock, temperature, dc voltage levels, and voltage transients. Data compression algorithms are used in order to obtain maximum utilization of memory space. The device operates from a 5V supply, consumes 100 mW of power and has provisions for an external battery if it is desired to maintain the system's real time clock as well as accumulate transportation shock data while the remaining system is silent. The data accumulated in the device is debriefed through a RS-232, 9600 baud output port to a terminal or personal computer. Debriefing requires no special external software.

The latest generation of the TSMD, usually referred to as the Advanced TSMD is based on a Motorola 32 bit microprocessor, the MC68333. The sensors are external to the hybrid circuit. This device is built specifically to monitor host system faults and record the operational environment before, during, and after a built-in-test (BIT) detected event. These TSMDs were used on operational B-1B aircraft to monitor the environment inside the aircraft's forward looking terrain following radar system. When the radar detected a fault with itself (BIT event), the TSMD recorded the past 40 seconds and the next 20 seconds of environment data. This "fault window" indicated what conditions were present when the fault occurred. The Advanced TSMD monitors vibration, mechanical shock, internal avionics temperature, cooling air pressure, cooling air temperature, and power supply conditions. In addition, high resolution recent stress data (past 1.8 hours), histogram data, fault type, time at stress levels, and depot failure resolution information are stored and the data sets are periodically downloaded to a database.

Summer Faculty Research Program

Objective

The objective of the Summer Faculty Research Program was to study in-depth the Emerging Diagnostic Techniques and their applicability to avionic systems and to explore the possibility of applying these new techniques to other non-aerospace systems.

Tasks

The following tasks were identified for the Summer Research program:

1. To familiarize with the current TSMD technology and review the relevant literature.
2. To review the transfer function method model developed by Popyack and Skormin (Ref 1) and explore the possibility of applying this model to an F-15 avionics card system.
3. To develop an FEM (Finite Element Method) model using MSC/PAL and EMRC's NISAI/DISPLAYIII softwares to complement the modeling effort indicated above in Item 2. Results from the FEM model should provide the guide lines necessary for the development of an experimental set up for obtaining experimental data for the validation of the results from the Transfer function and FEM models.
4. To develop the experimental set up and the related data logging system using the TSMD technology.
5. To explore the possibility of applying these new diagnostic techniques to other non-aerospace systems such as bridge integrity monitoring.

The accomplishments of the Summer Research Program are described briefly in the following sections of this report.

The specific work of Popyack, Skormin, and Plaskon published in the paper entitled "Transfer Function Method For Diagnostics of Electronic Circuit Boards Exposed to Mechanical Vibrations" (Ref 1) was used in this investigation. The model is briefly described in the following section.

The Transfer Function Model for a Plate (Ref 1)

The frequency spectrum of a vibrating structure usually contains a vast amount of information about the integrity of that structure. It is highly dependent on the spectrum of the external forcing function causing the vibration. If the frequency spectrum is known at two or more distinct points on the structure, this information can be used for the characterization of the propagation of vibrations, which exclusively

depends on the mechanical properties of the structure. Transfer functions may be used for relating vibration spectra of two adjacent locations of a vibrating structure. The configuration of such a transfer function typically reflects inertia (m), viscous friction (f), and stiffness (s) of the structure and does not change with time. Mechanical deterioration of a structure results only in the change of the transfer function parameters, primarily the ones associated with stiffness (Ref 9).

The differential equation of a vibrating mechanical structure can be expressed as:

$$F_K(t) = m_{Ki} \frac{d^2 x_i(t)}{dt^2} + f_{Ki} \frac{dx_i(t)}{dt} + s_{Ki} x_i(t) \quad (1)$$

where: $F_K(t)$ - is the forcing function applied at the K^{th} point of the structure, $x_i(t)$ - is the deflection of the i^{th} point of the structure, m_{Ki} , f_{Ki} , and s_{Ki} are inertia, viscous friction, and stiffness parameters representing propagation of vibrations along the K, i^{th} channel of the structure.

Since the vibrations are usually monitored by means of accelerometers, it is appropriate to rewrite (1) in the form:

$$c a_K(t) = m_{Ki} a_i(t) + f_{Ki} \int a_i(t) dt + s_{Ki} \iint a_i(t) dt^2 \quad (2)$$

where: $a_i(t)$, $a_K(t)$ are accelerations recorded at the i^{th} and k^{th} locations of the structure and c is a proportionality coefficient. Performing a Fast Fourier Transform (FFT) on (2).

$$A_K(j\omega) = m_{Ki} A_i(j\omega) + \frac{f_{Ki} A_i(j\omega)}{j\omega} + \frac{s_{Ki} A_i(j\omega)}{(j\omega)^2} \quad (3)$$

or,

$$\frac{\omega^2 A_K(j\omega)}{A_i(j\omega)} = \omega^2 m_{Ki} + s_{Ki} + j\omega f_{Ki} \quad (4)$$

where: $A_i(j\omega)$, $\omega = \omega_\zeta$, $\zeta = 1, 2, \dots, N$ is the FFT of the signal $a_i(t)$.

Taking the squared absolute value of (4) for particular frequencies ω_ζ , results in the system of equations:

$$\frac{|A_K(j\omega_\zeta)|^2}{|A_i(j\omega_\zeta)|^2} = \frac{[\omega_\zeta^2 m_{Ki} + s_{Ki}]^2 + f_{Ki}^2}{\omega_\zeta^2} \quad (5)$$

where $\zeta = 1, 2, \dots N$.

Subtracting (5) evaluated at its first frequency from (5) evaluated at each of the other frequencies yields:

$$\omega_{\zeta} \frac{[P_K(\omega_{\zeta}) - P_K(\omega_1)]}{[P_i(\omega_{\zeta}) - P_i(\omega_1)]} = \omega_{\zeta}^2 m_{Ki} - s_{Ki} \quad (6)$$

Where $P_i(\omega_{\zeta}) = |A_i(j\omega_{\zeta})|^2$ is the power spectral density of the signal $a_i(t)$
 $\zeta = 2, 3, \dots N$.

The LHS of equation (6) is numerically defined for each frequency ω_{ζ} and therefore equation (6) provides a reliable means for extraction of the stiffness parameter s_{Ki} .

According to equation (6), particular equations correspond to predefined frequencies ω_{ζ} . While the signal and noise are separated in the frequency domain, rational selection of the frequencies ω_{ζ} , $\zeta = 1, 2, \dots N$ allow for the reliable extraction of stiffness estimates with the minimum number of frequency points. Actually, in order to evaluate the unknown s_{Ki} , the vibration spectra can be defined at only three points which allows for significant reduction of the amount of computations and hardware complexity.

It should be noted that the obtained estimates for s_{Ki} are just proportional to the stiffness coefficients. The procedure described is not capable of delivering the exact values of these coefficients. Instead, it just provides the means for detection of changes in stiffness, which is consistent with the purpose of diagnostics.

An FEM model using the MSC/PAL and EMRCs NISAI/DISPLAY III Softwares was developed as a part of the Summer Research Project. A brief description of the model is given in the following section.

The FEM Model for the F-15 Avionics Card

An FEM model was developed for an F-15 Avionics Card to study its vibrational response as an additional complementary effort to validate the results of the Transfer function model and the experimental investigation.

A two step approach was adopted for the development of the FEM model. An initial preliminary model was developed using the software

MSC/PAL. The final version of the model was then developed using the software NISAI/DISPLAYIII.

The preliminary model was built using quadrilateral plate elements with a limited number of elements and nodes. The boundary conditions for the clamped ends were all set to zero (x, y, z translations and rotations). The following solutions were obtained:

1. Static solution
2. Dynamic solutions

The static solution output included (a) static deflection levels, (b) element internal forces and moments, (c) element stress levels, and (d) applied displacement force levels.

The dynamic solution was comprised of the following: (i) Normal mode solution, (ii) Frequency response solution, and (iii) Transient response solution. The normal mode solution outputs included the normal mode shapes and the corresponding natural frequencies. The steady-state response of the model to a sinusoidal displacement of 0.254 mm amplitude was obtained by using the frequency response solution. Here, though the procedure did not make use of the normal modes to form a solution, its results were used to guide the frequency response calculations. The dampings used for these calculations were 5% of the critical damping to Mode 1 and 2.5% to Mode 2.

In the transient response solution, a time varying Z-displacement was applied to a node at the center of the Avionics Card. The displacement rose linearly to 0.254 mm in 0.05 millisecond, remained constant for 0.45 millisecond, and then linearly decreased to zero amplitude over 1.5 milliseconds. Only the first four modes were used in the solution process and 10% of the critical damping was assigned to each mode.

A successful development of this preliminary model using the software MSC/PAL led to the next logical step of development of the final version of the model using the software NISAI/DISPLAYIII. This form of the model was developed with 3-D general shell elements (NKTP = 20). The Avionics Card was divided into 512 shell elements and the total number of nodes used was 561. The boundary conditions for the clamped ends were the same as those in the preliminary model (all x, y, z translations and rotations were set equal to zero). The types of analysis performed were: (1) Static analysis, and (2) Dynamic analysis. In the static analysis, instead of a displacement, a force of 178N was applied to a node at the center of the card. The outputs from this analysis included

the Z-displacements, element principal stresses, Von Mises equivalent stresses for the top, middle, and bottom surfaces.

The dynamic analysis included the following: (i) Linear Dynamic Analysis (LTRANSIENT), (ii) Eigen Value Analysis (EIGENVALUE), (iii) Frequency Response Analysis (FREQUENCY), (iv) Transient Dynamic Analysis (TRANSIENT), and (v) Shock Spectrum Analysis (SHOCK). The Linear Dynamic Analysis (LTRANSIENT) did not require the Eigen Value Analysis and the solutions are obtained by a direct integration of the equations of motion. As indicated earlier, a time varying force function was applied at a centrally placed node. The force rose linearly to 178N in 0.5 sec, remained constant for 0.5 sec, and then linearly decreased to zero amplitude over 1.5 sec. In this analysis 10% of the critical damping was applied at all nodes.

The Transient Dynamic, Frequency Response, and Shock Spectrum Analyses required an Eigen Value Analysis before the start of the computations. The consistent mass formulation and conventional subspace iteration techniques were used to extract the first five symmetric modes. The natural frequencies for these modes are shown in Table 1.

TABLE 1

<u>MODE NUMBER</u>	<u>FREQUENCY (HERTZ)</u>
1	196.70
2	462.00
3	788.97
4	1133.28
5	1241.82

The Frequency Response Analysis was performed by subjecting the Avionics Card to a steady state harmonic load of maximum amplitude 178N. Viscous damping of 2.5% of the critical was applied to all nodes.

The time varying force function used in the modal Transient Dynamic Analysis (TRANSIENT) was exactly the same as that of the Linear Dynamic Analysis (LTRANSIENT). A viscous damping of 2.5% of the critical was applied to all nodes, similar to the Frequency Response Analysis.

The Shock Spectrum Analysis (SHOCK) was performed by subjecting the Avionics Card to a shock displacement of 0.9249 mm applied at the supports (GROUND).

The model outputs from these dynamic analyses included all stresses, transient time histories, mode diagrams, etc.

The Experimental Set-Up

The objective of this task of the Summer Research Program was to develop an experimental set-up capable of generating enough experimental data for the validation of the Transfer Function Method model and the FEM model.

An F-15 aircraft Avionics Card was selected as the structure to be tested. A custom built fixture was used to mount the F-15 Avionics Card on a shaker (Bruel and Kjaer, B&K Vibration Exciter, Type 4809). The shaker was connected to a B&K Power Amplifier Type 2706 and a signal generator, Wavetek VCG/Noise Generator, Model 132.

Three (3) accelerometers (Type 501M501) made by Vibrometer Corp, were used as the monitoring sensors for this experimental set-up. These were mounted at three specifically selected locations on the F-15 card. Each of the accelerometers was connected to a Vibrometer Corp signal amplifier (Model P18) which had a 8V DC HP Precision Power Supply, Model 6114A. The output from the signal amplifier (10 mV/g) was fed to a Tektronix Oscilloscope, Model 2246, 100 MHz and a Burr Brown's Isolated Voltage Amplifier, Type SCM5B40-02, range -50 mV to +50 mV and -5V to +5V. The Isolated Voltage Amplifier was housed on an expansion board, Computer Boards, Inc, Model ISO-RACK08.

The output from the Isolated Voltage Amplifier was fed to a computer board mounted in an Insight 486 PC. The specification of the computer board was CIO-DAS801, 8 channels, 12 bit A/D, I/O board, sample rate 5000 Hz per channel. The Insight 486 PC was equipped with National Instrument's Lab View Software (Version 3.0.1) with CIO extension and universal library.

The experimental set-up described above was extensively tested for consistent operation. The results obtained from the preliminary tests using the rig were very encouraging and consistent.

Due to the limited duration of the Summer Research Program (12 weeks), all the necessary tests, both related to the model and the experiment could not be completed. Therefore, detailed results are not presented in this report. However, it is the intention of the author to continue this research project as a Summer Research Extension Program, for which a research proposal has been submitted to the Research & Development Laboratories (RDL).

Other Possible Applications of the New Diagnostic Techniques

one of the tasks of the current Summer Research Program was to explore other possible applications of the new diagnostic techniques

described in this report. A critical review of this task indicated that these techniques might be useful for monitoring the structural integrity of bridges, aircraft wings, and other structures.

Because of the limited duration of the summer program, only the bridge integrity monitoring was explored. This investigation revealed that the techniques presented in this report and another new technique known as MIR (Micro-Power Impulse Radar) technology (Ref 8) might be the suitable candidates for bridge integrity monitoring. Consequently, the author and Mr Leonard Popyack, Jr, the focal point of this Summer Research Project and another staff member from the ER/SR branch of Rome Lab, participated in a formal inspection of a bridge on Route 5, near Utica NY. The inspection was conducted by a certified bridge inspector from the NY State Department of Transportation.

Further, two laboratory bridge models available at the SUNY Institute of Technology at Utica/Rome NY, were identified for this investigation. It is the intention of the author to carry on this effort in the near future.

Conclusions

All the tasks identified for the Summer Research Project were completed within the specified time of 12 weeks. The research efforts conducted during the summer program clearly indicated the future research work necessary in this important area of the development of diagnostic techniques.

Recommendations for Follow On Research

It is recommended that the following research tasks be pursued to validate the diagnostics techniques described in this report:

1. The developed FEM model be tested by applying various forms of distortions (such as holes, notches, cracks (Ref 4), etc) for the failure of the Avionics Card.
2. The mode shapes for the Avionics Card be obtained with various forms of distortions and the strategic nodes, where the accelerometers should be mounted for experimental data be identified.
3. A series of experiments be conducted using the experimental set-up for the distortion configurations. The experimental data be transformed into proper formats for the Transfer Function Method model using the signal analysis modules of the software Lab view.
4. The experimental data then be used to validate the model results from the Transfer Function Method model and the FEM model.

5. An experimental investigation be conducted on the lab models for the bridge to validate the application of the diagnostics models described in this report.

Acknowledgment

The author would like to thank Mr Leonard J. Popyack, Jr, the focal point of the project and Mr James Collins, Chief, ERSR Branch, Rome Lab, Rome NY, for their encouragement, technical help and hospitality during this summer project. Thanks are also extended to Ms Lucy Burgard for typing this report.

REFERENCES

1. Popyack, L.J., Skormin, V.A., and Plaskon, S.L. "Transfer Function Method For Diagnostics of Electronic Circuit Boards Exposed to Mechanical Vibrations." Proceedings - IEEE National Aerospace and Electronics Conference (NAECON), 24 - 27 May 93.
2. Skormin, V.A. and Popyack, L.J. "Methods of Diagnostics in Technical Systems." International Proceedings of the Conference "Modern Problems of the Information Theory, Control, and Information Networks," Almaty, Republic of Kazakhstan, Jan 97.
3. Skormin, V.A. and Popyack, L.J. "Reliability of Avionics and Its 'History of Abuse' A Prognostic Technique." Proceedings of the International Conference on Informatics and Control, St Petersburg, Russia, Jun 97.
4. Wilson, S.P. and Taylor, D. "Reliability Assessment from Fatigue Micro-Crack Data," IEEE Transactions on Reliability, Vol 46, No 2, Jun 97.
5. McCallum, M., Popyack, L.J., and Collins, J.A. "Environmental Measurement and Recording Techniques Utilizing a Time Stress Measurement Device (TSMD)." Proceedings - Institute of Environmental Sciences, 1990.
6. Havey, G., Louis, S., and Buska, S. "Micro-Time Stress Measurement Device Development," RL Technical Report. RL-TR-94-196, Nov 94.
7. Broadwater, S.P. "Advanced Built-in-Test and Reliability Assessment Technology." (Unpublished).
8. Warhus, J., Mast, J., and Nelson, S. "Imaging Radar for Bridge Deck Inspection," SPIE Paper, Jun 97.
9. Skormin, V.A. "A Frequency Approach to Mathematical Modeling of a Nuclear Power Plant." Transactions of the ASME - Journal of Vibration, Acoustics, Stress, and Reliability in Design, Vol 107, p 106-111, Jan 85.

INFORMATION FUSION FOR TEXT CLASSIFICATION AN
EXPERIMENTAL COMPARISON

Venu Dasigi
Associate Professor
Department of Computer Science and Information Engineering

Sacred Heart University
Fairfield, CT 06432

Final Report for:
Summer Faculty Research Program
Rome Laboratory

Sponsored by:
Air Force Office of Scientific Research
Bolling Air Force Base, DC

And

Rome Laboratory

September, 1997

INFORMATION FUSION FOR TEXT CLASSIFICATION - AN EXPERIMENTAL COMPARISON

Venu Dasigi

**Associate Professor and Graduate Program Director
Department of Computer Science and Information Technology
Sacred Heart University**

Abstract

This report is on our recent software development, experiments, and results on automatic classification of free text documents into a given number of categories. Text classification has applications in information filtering and routing, automatic indexing, retrieval, etc. We use different kinds of feature extractors and integrate neural net learning into the method. We then compare their performance and that of different interesting combinations of them using different metrics.

The feature extractors are based on the “latent semantics” of a *reference library*. Intuitively, the technique of latent semantic indexing (LSI) [Deerwester, et al., 90] projects any document into a dimensionally reduced space of concepts from the reference library. Different sets and sizes are used for the reference library to form different features. Terms, noun-phrases, and simple category profile matching are used in the features. Neural nets are used to incorporate a learning component, as well as to fuse information from different combinations. Metrics such as micro and macro averaged precision, recall and correctness are used to compare the performance of the different feature extractors and effectiveness of their fusion.

The results indicate that a larger reference library is not necessarily more effective. However, information fusion almost always performs better than information from the individual feature extractors, and certain combinations seem to do better than the others. Additional parameters can have varying degrees of effectiveness, and remain to be investigated.

INFORMATION FUSION FOR TEXT CLASSIFICATION - AN EXPERIMENTAL COMPARISON

Venu Dasigi

1. Introduction

Information *retrieval* and *classification* refer to automated retrieval in response to a query and automated classification into various categories of what may be thought of as *unstructured* information. This endeavor, therefore, is to be contrasted specifically with database retrieval, where the data are *structured*. In this age of information explosion, information retrieval and classification have become more critical research areas than ever. In this work, our focus is on automated classification of unstructured text. Such automated classification has many applications, such as information filtering based on user profiles, personalized information delivery, etc. For the problem of information retrieval itself, classification of information can help in automatic indexing, as well as in other ways. Other related applications include classification and routing electronic message traffic (e.g., in military aircraft operations), e-mail filtering (very useful when a department receives thousands of e-mail messages a day), etc.

The goal of this work is to evaluate the effectiveness of different sensors² that extract important features from text, and also to evaluate the effectiveness of information fusion from multiple sensors in automatically classifying free text documents into a given number of categories. Neural net learning is incorporated into the approach so that information derived by a feature extractor from training documents, along with the correct classification, are used to train the neural network. The neural network is also used as an information fusion mechanism when multiple information sensors are used. This general approach itself was motivated in part by the Gene Recognition and Analysis Internet Link (GRAIL) system developed at the Oak Ridge National Laboratory, because of the similarity in problem characteristics [Uberbacher and Mural, 91] [Xu, et al., 94]. GRAIL is a very successful pattern recognition system for identifying rarely occurring protein-encoding segments of DNA sequence in higher eukaryotes, which may span tens to hundreds of sparse kilobases, in which a multi-layer feed-forward neural network assigns an input pattern (formed by different sensors) to a given number of classes.

Similarly, in classifying large amounts of text, multiple clues are often needed to give enough confidence for proper classification. Synthesizing different feature extractors, and choosing appropriate parameters in them is in itself an interesting problem. Further, it is not always clear how to best integrate them into a decision. Our focus here is entirely on *information* rather than *decision* fusion. Although the latter is a very interesting problem and

² The terms *sensor* and *feature extractor* are used synonymously in this report. Sometimes, the terms *algorithmic sensor* and *logical sensor* are also used.

some work has been done by others [Belkin, et al., 94] [Dumais, 96] [Towell, et al., 95], we focus here only on issues with information fusion.

We start with different standard features, such as term frequency and noun-phrase frequency. We then project a document vector of the original features into the space of semantic concepts from a *reference library* using Latent Semantic Indexing (LSI) [Deerwester, et al., 90]. A term-document (or a phrase-document) *reference matrix* represents the frequencies of terms (or phrases, respectively) from a collection of documents from the reference library. In LSI, this large and sparse term-document matrix is reduced into three smaller matrices, one of which is simply a diagonal matrix, by singular value decomposition (SVD). The diagonal matrix yields the singular values from which the dominant ones are selected. Thus, instead of representing documents by thousands of possible terms or phrases, LSI allows for a document to be represented by a substantially smaller number of *factors* that intuitively capture the significant “latent semantics.”

Thus, a reference matrix is the term-document matrix of a reference library / collection of documents. A reference library is the collection of documents that adequately represents all concepts of interest. The SVD computations are performed on such a reference library only once, and the linear transformations mentioned above essentially project *any* new document into the concept space represented by the reference library. One of the parameters we experimented with in this work is the size of the reference library.

Section 2 describes background material and the general approach. It also discusses the metrics we use. Section 3 deals with the experimental set up. Section 4 summarizes and discusses the results. Section 5 concludes the paper by putting this work in the context of other related work and also the work that still remains to be done. Appendix A includes several tables that show details of performance for each experiment. Appendix B describes the programs written to facilitate experimentation.

2. Background

Our hypothesis in this work has been that a neural network, as in GRAIL [Uberbacher and Mural, 91] [Xu, et al., 94], would not only incorporate a learning component into a classification method, but would also be capable of integrating information from different features in a systematic way, thereby improving performance over previous approaches. To this end, our specific goal in this work has been to develop a few different feature extractors, measure their individual performance, and then measure the performance after carrying out fusion of information from different sets of them. In order to make training the neural net practical, the dimensionality of the pattern recognition problem had to be contained, and Latent Semantic Indexing (LSI) [Deerwester, et al., 90] is used for this purpose. Thus, there are two ways to view the approach: either as a neural net method, made practical by LSI,

or as an LSI-based approach augmented with neural net learning. We first present a quick overview of how LSI is used in this work and then briefly describe the metrics used to measure performance.

2.1. Dimensionality Reduction with LSI

The developers of LSI indicate that a query may be viewed as a pseudo-document and may be represented as a vector of a chosen number of factors, so it may be placed in the same vector space as regular document vectors [Deerwester, et al., 90]. This technique is used in here to reduce the dimensionality of a regular document, so it can be input to a neural network. This is done as follows. First, as pointed out in the introduction, a reference term-document sparse matrix X is derived from the library of documents that are of interest. This matrix is split into three matrices by Singular Value Decomposition (SVD) [Forsythe, et al., 77], so that

$$X = T.S.D'$$

Here, X is a $t \times d$ matrix, where t is the numbers of distinct terms (word roots) and d is the number of documents in the reference collection. The order of T is $t \times k$, that of S , which is a *diagonal* matrix, is $k \times k$, and that of D is $d \times k$, where k is the chosen number of factors. (LSI research indicates that a choice of k near 100 is good.) Now, the pseudo-document vector D_Q corresponding to a $1 \times t$ query vector Q may be derived simply as:

$$D_Q = Q.T.S^{-1}$$

In this work, we use this same idea to squash any $1 \times t$ document vector into a $1 \times k$ vector that serves as input to the neural network. The dimensionality reduction is substantial: t is generally a few thousand to a few tens of thousands, and k is near one hundred. *The only care that must be exercised is to make sure that the reference term-document matrix that is used as the starting point is one that "adequately" represents all concepts of interest.* (We return to address the adequacy issue in Section 4 on Experiments and Results.) This requirement is no more stringent than would be required in the standard LSI approach.

2.2. Performance Metrics

Precision and *recall* are very commonly used as measures of performance in information *retrieval*. Precision is defined as the fraction of retrieved items that are actually relevant (the rest are *false positives*), and recall is defined as the fraction of relevant items that are actually retrieved (the rest are *false negatives*). Thus, precision is inversely related to false positives and recall is inversely related to false negatives during retrieval.

Lewis is perhaps the first to define these metrics in the context of information *classification* [Lewis, 92]. In classification, there are multiple classes, zero or more of which are to be assigned to each document. If each class were viewed as a retrieval query, the definitions fall into place. That is, for any class, precision is the fraction of items assigned to the class that actually belong to the class, and recall is the fraction of items that belong to the class that are actually assigned to the class. We further define *correctness* of classification as the fraction of all documents that are classified correctly with respect to the class, namely, the ratio of the sum of the numbers of *true positives* and *true negatives* to the total number of documents. That is, for the *i*-th class, if tp_i , fp_i , tn_i and fn_i stand respectively for the numbers of true positives, false positives, true negative and false negatives, we have:

$$\begin{aligned} \text{precision}_i &= tp_i / (tp_i + fp_i) \\ \text{recall}_i &= tp_i / (tp_i + fn_i) \\ \text{correctness}_i &= (tp_i + tn_i) / (tp_i + tn_i + fp_i + fn_i) \end{aligned}$$

The picture gets a little more complex. With these metrics distributed over all the classes, to get global performance measures, some kind of averaging is needed. There are two ways to do the averaging. In *macro-averaging*, the individual measures for each class are taken and an overall average is computed simply by adding them and dividing the grand total by the number of classes. In *micro-averaging*, the grand total aggregates of the individual numbers for true/false positives and true/false negatives are computed and the appropriate ratios give the metrics. Thus, assuming below that *i* ranges over all classes in the summation, with the scope of Σ being the single term or parenthesized expression following it, and *N* is the number of classes, we have:

$$\begin{aligned} \text{macro-precision} &= \Sigma_i \text{precision}_i / N \\ \text{macro-recall} &= \Sigma_i \text{recall}_i / N \\ \text{macro-correctness} &= \Sigma_i \text{correctness}_i / N \\ \\ \text{micro-precision} &= \Sigma_i tp_i / \Sigma_i (tp_i + fp_i) \\ \text{micro-recall} &= \Sigma_i tp_i / \Sigma_i (tp_i + fn_i) \\ \text{micro-correctness} &= \Sigma_i (tp_i + tn_i) / \Sigma_i (tp_i + tn_i + fp_i + fn_i) \end{aligned}$$

A simple analysis reveals that macro-averaging and micro-averaging always result in the same value for correctness. Another point to note is that the correctness measure can increase just by increasing true negatives, without directly affecting the other measures. Since generally the number of true negatives is very high, a high correctness measure can give a false / misleading sense of good performance.

Generally, in any retrieval / classification experiment, a single parameter is varied to get a precision-recall pair at each parameter value. Together, they form a precision-recall curve. Generally, in such experiments, when the parameter is changed so as to increase precision, the recall figure decreases and vice versa. In the extreme case,

when the parameter is such that there are no false positives (100% precision), very likely we recall very little by being conservative. On the other hand, if the parameter is such that there are no false negatives (100% recall), we are so permissive that we retrieve everything, decreasing precision substantially.

Due to this inverse relationship between precision and recall, it is hard to compare the performance of different approaches by looking at isolated figures. The entire precision-recall curves need to be compared. Alternatively, a single measure called the *break-even point* is sometimes used for comparison. The break-even point is the point on the precision recall curve that has the same value for precision and recall. A higher break-even precision (recall) indicates better performance. The break-even point may be linearly interpolated from the two points closest to it on either side on the precision-recall curve. If the two points on either side of the break even point are $\langle p_1, r_1 \rangle$ and $\langle p_2, r_2 \rangle$ such that $p_1 > r_1$ and $p_2 < r_2$, the break-even point $\langle b, b \rangle$ is given by:

$$b = (r_2 * p_1 - r_1 * p_2) / (r_2 - r_1 + p_1 - p_2)$$

3. Experimental Set Up

In order to train the neural network, we turn to a collection of data made available by the Reuters news agency, and prepared by Dr. David Lewis³. The Reuters data are described in [Dasigi et al., 97] and [Lewis, 92]. The advantage of this collection is that the Reuters stories are already manually classified, and include a sufficiently high number of stories per category. The Reuters stories have anywhere from zero to five categories assigned to each of them. Since there are too many fine categories for the Reuters data, we combine several of them into single higher level categories, as suggested by the data developers. We use eight such high level categories:

1. *money / foreign exchange*
2. *shipping*
3. *interest rates*
4. *economic indicators*
5. *currency*
6. *corporate*
7. *commodities*
8. *energy*

The size of the Reuters corpus is about 25 MB, representing 22,173 Reuters news wire stories. The stories are pre-classified and pre-analyzed. Thus, in addition to the 25 MB of raw text, many additional files are provided that

³ The Reuters-22173 text categorization collection is copyrighted by Reuters, Ltd., and is distributed freely for research purposes only. Copyright for additional annotations and a number of auxiliary files resides with David D. Lewis and the Information Retrieval Laboratory at University of Massachusetts. The authors thank the footnote continued on next page

contain information such as what categories, if any, have been assigned to each document, what words are present in each document (story) with what frequency, what multi-word noun-phrases occur in each document with what frequency, etc. Many details about the collection can be found in [Lewis, 92], and also in the *README* file associated with the collection. Details of distribution of the documents among the various categories may be found in [Dasigi, et al., 97].

The collection contains 22,791 different words and 29,496 different noun-phrases indexed to the documents. These numbers are rather high, and part of the reason is “words” corresponding to the different numeric values that occur in the documents, special symbols, etc. have all been treated as genuine words. It is up to the system that processes this information to use them appropriately. (In our work, we do not do anything special in this regard.) The documents come with pre-assigned classification, with about 135 topic categories and another 539 other kinds of categories. The 135 categories may further be grouped into 8 higher level categories as already mentioned, which we use in this work.

As mentioned before, the feature extractors used in this work are based on LSI applied to words or noun-phrases. The choice of the reference library can be important in LSI, because documents are represented in the space defined exclusively by the concepts from the reference library. So, three of our feature extractors are based on terms from three different reference libraries. The first reference library consists of the first 1,500 documents from the Reuters collection, and the second library consists of the next 1,500 documents. The third reference library comprises the first 3,000 documents, that is, it includes all the documents from the first two reference libraries.

We do know, however, that the utility of LSI is limited by the reference library of documents. Thus, there is an important need to complement or at least supplement this information with other feature extractors. The additional sensors should be sensitive to *new* words and patterns in the input or otherwise relate to the output categories. For this purpose, we use a feature extractor based on the noun-phrases in the documents. LSI is applied to the noun-phrase-document matrix, projecting all document vectors (that would otherwise be in the noun-phrase space) into the space created by the factors chosen from the SVD of this matrix. Since the Reuters-22173 collection came pre-analyzed for all the noun-phrases contained in the collection, this feature extractor could be programmed quickly.

In our past work, we used another feature extractor based on simple category profiles, where each category profile is simply a set of keywords characterizing that particular category. There is one input per category to the neural network from this logical sensor, where each input simply represents what fraction of the terms in the given document match the corresponding category profile. Although this sensor is somewhat simple-minded, it can still

providers of the Reuters-22173 collection for making it available. It can be obtained at the URL <ftp://ciir-fjp.cs.umass.edu/pub/reuters1>.

complement the information provided by the LSI-based sensor, since, to paraphrase a point made by [Schütze, et al., 95], LSI is much more sensitive to the latent semantics (theme) rather than the exact terms. To summarize, the following feature extractors are used:

- 1a. *Term*-based, from the *first 1,500* document reference library
- 1b. *Term*-based, from the *second 1,500* document reference library
- 1c. *Term*-based, from the *first 3,000* document reference library
- 1d. *Noun-phrase*-based, from the *first 1,500* document reference library
- 1e. Simple, *category profile*-based (no LSI)

For the purposes of information fusion, our old results from combining information from the first term-based feature and the simple, category profile-based one are reproduced for consistency and reinterpreted in terms of the metrics we have chosen to use. We also performed information fusion for the noun-phrase-based feature with either of the first two term-based features (dealing with the 1,500 document reference libraries). Finally, information from the first two term-based features themselves is fused together, as well. To summarize, the following combinations are used in the information fusion experiments:

- 2a. 1a and 1e
- 2b. 1a and 1d
- 2c. 1b and 1d
- 2d. 1a and 1b

4. Experiments and Results

We start off by pointing out the precision and recall values when straight LSI-based retrieval is adopted to perform classification. This is done by first using LSI to retrieve the document from the reference library that best matches the document to be classified. In other words, the document to be classified is used as if it were a query, as explained in [Deerwester, et al., 90]. Then the categories assigned to the best-matching document from the reference library are assigned to the “query document”, completing the classification task. No learning is incorporated into this method. In this experiment, there are no parameters to vary as in the other experiments, and so there is a single set of macro- and micro- averaged precision and recall figures, and correctness. The results are as follows:

Macro-Precision	Macro-Recall	Micro-Precision	Micro-Recall	Correctness
9.55%	5.60%	20.86%	13.56%	89.76%

It may be noted that although the correctness figure is good, the precision-recall figures are not very high. One reason for this behavior might be that the number of true negatives is perhaps very dominating, pushing the correctness percentage very high. Since true negatives have no bearing on precision and recall, those figures are

small. In particular, it may be noted that in either kind of averaging, both the precision and recall figures are rather low, a behavior that may be contrasted with the results in the remaining experiments that incorporate learning.

The number of output units in all neural net experiments is 8, one for each class. In all the single sensor experiments that used LSI, 112 factors are used⁴. The neural nets therefore also have 112 input units. The number of hidden units used is 9 in experiments 1a-1d. The simple, category profile-based sensor input (1e) is not transformed using LSI because it had given very poor results on another set of data when LSI was applied to it, as discussed in [Dasigi, et al., 97]. The neural net in experiment 1e has 8 input units and 5 hidden units. When two different features are combined in 2a-2d above, the number of input units is equal to the total number of inputs (120 for 2a, and 224 for 2b-2d). The number of hidden units is 10 for 2a, and 9 for 2b-2d. The specific architecture, namely the number of hidden layers (always one in our experiments) and the number of hidden units, is chosen after some experimentation, based on performance after initial training. (Several meaningful choices have been experimented with for this purpose.)

Of the 22,173 documents, the first 4,000 documents are used for training in all the experiments, and the remaining 18,173 are used for testing. The neural network is trained for 16,000 iterations at a time (each training document presented four times), all the way up to 80,000 iterations. After each step of 16,000 iterations, the network is tested with all the training documents and then with all the test documents, separately, and the outputs saved in files. These raw output files are interpreted with the threshold value (that distinguishes the binary decision) as the parameter and macro- and micro-averaged precision and recall, as well as correctness are calculated at each parameter value. Break-even points are also calculated for the macro-averaged precision-recall curve as well as the micro-averaged precision-recall curve. The performance measures presented here are those for the test data set that correspond to the same point of training that results in the best break-even points in the training data.

The results are distributed over several tables, which are included in Appendix A. For convenience, the table numbers are made to correspond to the different experiments identified in the previous section. Tables 1a through 1e summarize the results from our single-sensor experiments. Tables 2a through 2d summarize the results of our information fusion experiments. We also compiled all the break-even points into a single table, since the break-even points may be thought of as giving a single global measure of performance. Thus, Table 0 below lists the macro-averaged and micro-averaged break-even points for each of the five single-sensor experiments and the four information fusion experiments for a quick and easy comparison. (All figures are percentages except, of course, the threshold figures in Tables 1a-1e and 2b-2d in Appendix A.)

⁴ The exact choice of this number is arbitrary; a number of about 100 is recommended by the developers of LSI.

Table 0: Summary of Breakeven Points		
Experiment	Macro	Micro
1a	52.70	68.09
1b	55.29	66.98
1c	53.43	67.09
1d	37.17	54.24
1e	33.35	42.44
2a	54.82	68.86
2b	51.99	68.36
2c	54.19	67.31
2d	57.41	70.36

The big picture emerges from Table 0. The individual term-based feature extractors 1a, 1b and 1c show performances that are comparable to each other. All of them have their macro-averaged break-even points between 52.70 and 55.29, and micro-averaged break-even points between 66.98 and 68.09. The macro and micro break-even points seem to vary inversely with each other within this group. A noteworthy point is that a larger reference library of 3000 documents, used in sensor 1c, which happens to be the union of the reference libraries used in sensors 1a and 1b, does not seem to have any bearing on performance. It is, therefore, reasonable to conclude that a reference library of the first 1,500 documents is “adequate” from the perspective of the *thematic space* that latent semantic indexing creates (from the chosen number of factors), and an additional 1,500 documents do not substantially add to the richness of that space. It should, however, be recalled that although the reference libraries themselves and their sizes are different between the sensors of this group, the number of SVD factors used is the same in all three of them.

The other two individual feature extractors, 1d and 1e, are a little different in that they are not simply term-based. It is obvious that their performance is substantially inferior to that of sensors 1a-1c, as evidenced by lower values for *both* macro and micro break-even points. For the noun-phrase-based feature extractor (1d), the break-even points are a little higher than for the simple category profile-based one (1e). For sensor 1d, the macro break-even point is 15-18% smaller and the micro break-even point is 12-14% smaller than for any of the term-based sensors. For sensor 1e, the differences are 19-22% and 24-26%, respectively. It is perhaps not unreasonable to expect that these two sensors are valuable only in the context of information fusion, but not individually.

The fusion results on the next three lines of Table 0 appear to be mixed. In spite of its simple-mindedness, when information from the category profile sensor (1e) is fused with that from sensor 1a, the performance does seem to get better, albeit only by a small amount. The point to note is that break-even points are higher with either kind of averaging, compared to those of either of the constituent sensors. When information from either of the term-based sensors 1a or 1b is combined with that from the noun-phrase-based sensor 1d (in fusion experiments 2b and 2c, respectively), there does not appear to be any marked change in performance, compared to that of the individual

term-based sensors. This is somewhat surprising, although consistent with what other researchers noted in other contexts [Lewis, 92]. This lack of improvement may be explained by the fact that although noun phrases capture more context in the text, there are still two problems: (i) the information they provide is not substantially different (in terms of concepts) from the term-based information (since they are still combinations of the same words which are already used in the term-based sensors), and (ii) they are not only much fewer in number but are also substantially less frequent to be of good statistical significance.

We *did* expect fusion experiment 2c to show a better performance than 2b, because of the substantial independence between the constituent sensors in 2c. Note that 2c performs information fusion between 1b and 1d, and that sensors 1b and 1d are not only of different kinds, but are also based on complementary reference libraries. In contrast, the reference library underlying sensors 1a and 1d, information from which is fused in experiment 2b, is the same! However, the actual performance is not exactly consistent with our expectation. While the performance improved by over 2% in the macro break-even point, it went down about 1% in the micro-averaged version (see below). *It is interesting to note that although the individual performance of the simple-minded sensor 1e is clearly inferior to that of the noun-phrase sensor 1d, when combined with a term-based sensor, the combination with 1e is clearly better. Although this behavior might appear anomalous at first, it can be explained by the relative dependence or lack thereof between the information sensors.*

The performance of information fusion experiment 2d, which combines information from the first two individual term-based sensors stands out somewhat. Although the improvement is only within 5%, it is important to observe that *both* the macro and micro averaged performances have improved. It may be noted that a higher break-even point indicates an improvement in *both* precision *and* recall. Further, often there appears to be a friction between the macro-averaged performance and the micro-averaged performance. In macro-averaging, all categories used in the classification are viewed equally important, and in micro-averaging, the more *populous* categories (those with more documents assigned to them) dominate. Considering that many learning algorithms, including neural networks, have a tendency toward being over-trained, or biased toward the more populous categories, it might be important focus on the macro-averaged performance. A better performance both ways indicates that precision and recall are better in *most* categories, not just some specific ones or just the populous ones.

Full details of the test results are summarized in Tables 1a-1e and 2a-2d in Appendix A. All the tables display an interesting behavior. As one scans each table top down, one observes that break-even occurs first between macro-averaged precision and recall, followed quickly by break-even between micro-averaged precision and recall, and soon followed by the correctness value reaching its peak. A meaningful interpretation, if any, of this behavior and identification of its significance, if any, are not obvious.

5. Conclusion

Several other researchers are working on similar issues. The Reuters data have been very popular in experimentation on classification work because they come pre-classified and pre-analyzed. Our results do appear to compare very favorably with those of [Lewis, 92]. The results are not entirely comparable because, although the same data are used in both works, we combined the low level categories into a few high level ones.

Our results are consistent with the observations made by several other researchers. For instance, [Hull, et al., 96] claim that complex fusion strategies are not always effective, especially when there is much correlation between the methods being combined. There is some evidence that context-sensitive feature extractors can add value in information fusion [Cohen and Singer, 96]. Our results, as well as those of [Lewis, 92] indicate, however, that syntactic context as captured in noun phrases is not very valuable.

To compare our approach itself with other similar methods, we believe our approach makes for a synergy between LSI and neural network learning. The dimensionality reduction by LSI limits the size of the neural network making it practical, and the neural network augments LSI with learning. Using a reference library with a one time SVD computation makes the approach practical. [Schütze, et al., 95] also employ an LSI-based approach in conjunction with neural network learning. Our approach differs from theirs in using a reference library and in employing multiple sensors. In their work, they seem to have used the set of all tested documents together as the reference library, obviating the need for a hidden layer in the neural network. We believe our approach is more practical since the SVD computations are made just once.

Many issues are still to be explored, and much work remains to be done in this area. Plans for future work include:

- *Synthesis of other sensors:* Other sensors could be based on Bayesian network approach, context vectors [Qing, et al., 95], n-grams, clustering, natural language analyses, etc. It should be kept in mind that a sensor that performs comparable to LSI would be needed in order to expect significant improvement.
- *Automatic synthesis of category profiles:* [Zhou and Dapkus, 95] came up with a method to identify the significant terms for given pre-defined topics. If the categories are thought of as pre-defined topics, their method could be turned into a method to synthesize the profiles automatically.
- *Evaluation of the impact of the number of factors used in LSI computations:* Intuitively, the LSI factors are ordered in terms of their decreasing ability to capture significant associations. Since the last few / several / many factors are the smaller and less significant values, it is expected that the usefulness of the factors would be limited after a certain number. It would be very interesting to compare the performance in an experiment that fuses information from two sensors using m and n factors each against that in an experiment that uses a

single sensor with $m+n$ factors. It is worth noting that the SVD computations take a longer time as the number of factors goes up.

- *Application:* The quantitative results in the tables do not give an intuitive picture, but they compare very well with the best results in classification. To get an intuitive feel for the effectiveness of the approach, it would be very interesting to use it in an application that is frequently used.
- *Evaluation of the impact of the training set size:* Although, the Reuters data came pre-classified for the purpose of training, it is generally hard to find or build large amounts of training data. It would be useful to find out a threshold training set size, if any, beyond which the improvement is negligible.
- *More systematic experimentation to analyze the impact of uneven distribution of categories among the documents:* An uneven distribution of categories in the training data tends to bias the network. The categories occurring more often influence the weights in the network more, resulting in a bias that favors them (minimizing false negatives for those categories). One possible consequence of this bias is that documents belonging to other less frequent categories might get incorrectly classified into one of the frequent categories (false positives).
- *Data combination (Decision fusion) from different networks using single sensor each:* Other IR researchers have worked on data combination methods that fuse the results from different approaches [Towell, et al., 95]. It would be worth comparing the effectiveness of query combination (sensor fusion) and data combination (decision fusion).

Acknowledgments

The author thanks the Air Force Office of Scientific Research (AFOSR) for the summer fellowship that made this work possible. Dr. Heather Dussault has been a great mentor; her invaluable support is gratefully acknowledged. Thanks are also due to Prof. Mike Berry of the Computer Science Department at the University of Tennessee, Knoxville and his students for distributing the SVDPACKC software. Help from Mr. Paul Yaworsky and Mr. Dale Richards of the Air Force Rome Laboratory in establishing access to NeuralWorks⁵ and emacs is particularly appreciated. Mr. Christopher Harrison's help with computer and network problems has been very valuable.

References

1. Belkin, et al., 94: Belkin, N. J., P. Kantor, C. Cool, and R. Quatrain, Combining Evidence for Information Retrieval. In Harman, D. (Ed.), *The Second TREC Conference*, NIST Special Publication 500-215, pp. 35-44, 1994.

⁵ NeuralWorks is the name of the neural net tool we used, and is a trademark of NeuralWare, Inc.

2. Cohen and Singer, 96: Cohen, W. and Y. Singer: Context-Sensitive Learning Methods for Text Categorization, *SIGIR-96*, pp. 307-315, 1996.
3. Dasigi, et al., 97: Dasigi, V., R. C. Mann, and V. Protopopescu, Multi-Sensor Text Classification Experiments - A Comparison, Oak Ridge National Laboratory Technical Memorandum ORNL/TM-13354, Oak Ridge, TN 37831, January, 1997.
4. Deerwester, et al., 90: Deerwester, S., S. Dumais, G. Furnas, T. Landauer, and R. Harshman, Indexing by Latent Semantic Analysis *Journal of the American Society for Information Science*, 41(6), pp. 391-407, 1990.
5. Dumais, 96: Dumais, S., Combining Evidence for Effective Information Retrieval, *Working Notes of AAAI Spring Symposium of Machine Learning in Information Access*, pp. 26-30, March, 1996.
6. Forsythe, et al., 77: Forsythe, G., M. Malcolm, and C. Moler, *Computer Methods for Mathematical Computations* (Chapter 9: Least Squares and the Singular Value Decomposition), Prentice Hall, Englewood Cliffs, NJ, 1977.
7. Hull, et al., 96: Hull, D., J. Pedersen, and H. Schütze, Method Combination for Document Filtering, *SIGIR-96*, pp. 279-287, 1996.
8. Lewis, 92: Lewis, D., Representation and Learning in Information Retrieval, Ph.D. dissertation, University of Massachusetts, Amherst, February, 1992.
9. Qing, et al., 95: Qing, K., W. Caid, and C. Ren: Image / Text Automatic Indexing and Retrieval System using Context Vector Approach, *Proc. SPIE Digital Image Storage and Archiving Systems Conference*, pp. 372-379, 1995.
10. Schütze, et al., 95: Schütze, H., D. Hull, and J. Pedersen, A Comparison of Classifiers and Document Representations for the Routing Problem, *SIGIR-95*, pp. 229-237, 1995.
11. Towell, et al., 95: Towell, G., E. M. Voorhees, N. K. Gupta, and B. Johnson-Laird, Learning Collection Fusion Strategies for Information Retrieval, *Proc. Twelfth Annual Machine Learning Conference*, Lake Tahoe, July, 1995.
12. Uberbacher and Mural, 91: Uberbacher, E. and R. Mural, Locating Protein-Coding Regions in Human DNA Sequences by a Multiple Sensor-Neural Network Approach, *Proc. Natl. Acad. Sci. USA*, 88, pp. 11261-11265, 1991.
13. Xu, et al., 94: Xu, Y., R. Mural, M. Shah, and E. Uberbacher, Recognizing Exons in Genomic Sequence using GRAIL II, *Genetic Engineering, Principles and Methods*, Plenum Press, 15, June, 1994.
14. Zhou and Dapkus, 95: Zhou, J. and P. Dapkus, Automatic Suggestion of Significant Terms for a Pre-defined Topic, *Third ACL Workshop on Very Large Corpora*, MIT, Cambridge, June 1995.

Appendix A: Performance Tables

Starts on the next page. All figures, except Threshold values, are percentages.

Table 1a: Performance with Sensor 1a					
Threshold	Macro		Micro		Correctness
	Precision	Recall	Precision	Recall	
-0.80	7.43	100.00	7.43	100.00	7.43
-0.70	7.43	100.00	7.43	100.00	7.44
-0.60	7.44	100.00	7.43	100.00	7.45
-0.50	7.44	100.00	7.43	100.00	7.48
-0.40	7.45	100.00	7.43	100.00	7.51
-0.30	7.49	100.00	7.44	99.99	7.63
-0.20	7.56	100.00	7.47	99.99	7.99
-0.10	7.78	100.00	7.58	99.99	9.43
0.00	9.64	98.96	10.53	99.56	37.15
0.10	35.51	71.82	41.43	89.43	89.82
0.20	52.43	53.19	60.40	77.41	94.55
0.30	60.65	38.57	71.82	63.56	95.44
0.40	67.70	27.83	79.52	51.98	95.44
0.50	70.60	20.13	83.27	42.63	95.10
0.60	71.00	14.00	86.24	33.03	94.63
0.70	73.75	9.51	91.82	25.45	94.29
0.80	93.42	5.88	93.91	18.41	93.85
0.90	95.37	3.47	96.05	12.38	93.45
Breakeven	52.70		68.09		

Table 1b: Performance with Sensor 1b					
Threshold	Macro		Micro		Correctness
	Precision	Recall	Precision	Recall	
-0.90	7.43	100.00	7.43	100.00	7.43
-0.80	7.43	100.00	7.43	100.00	7.43
-0.70	7.43	100.00	7.43	100.00	7.43
-0.60	7.43	100.00	7.43	100.00	7.44
-0.50	7.44	100.00	7.43	100.00	7.46
-0.40	7.45	99.99	7.43	99.99	7.50
-0.30	7.47	99.99	7.44	99.98	7.59
-0.20	7.53	99.99	7.46	99.98	7.89
-0.10	7.73	99.92	7.56	99.93	9.24
0.00	9.49	98.90	10.43	99.51	36.48
0.10	35.65	76.09	39.66	91.08	89.04
0.20	56.55	53.97	58.07	77.43	94.17
0.30	66.38	38.46	70.53	62.82	95.29
0.40	75.11	28.04	78.26	51.80	95.35
0.50	82.18	19.52	82.33	42.36	95.04
0.60	81.71	13.41	86.86	32.32	94.61
0.70	76.39	9.58	91.46	26.79	94.38
0.80	90.62	6.94	93.98	22.55	94.14
0.90	94.93	4.65	96.26	16.91	93.78
Breakeven	55.29		66.98		

Table 1c: Performance with Sensor 1c					
Threshold	Macro		Micro		Correctness
	Precision	Recall	Precision	Recall	
-0.90	7.43	100.00	7.43	100.00	7.43
-0.80	7.43	100.00	7.43	100.00	7.43
-0.70	7.43	100.00	7.43	100.00	7.43
-0.60	7.43	100.00	7.43	100.00	7.44
-0.50	7.44	100.00	7.43	100.00	7.46
-0.40	7.45	100.00	7.43	100.00	7.49
-0.30	7.47	100.00	7.44	99.99	7.57
-0.20	7.51	100.00	7.46	99.99	7.79
-0.10	7.68	99.98	7.54	99.97	8.95
0.00	9.15	99.31	10.07	99.70	33.80
0.10	36.51	73.75	39.00	90.78	88.77
0.20	54.98	51.57	56.24	78.20	93.86
0.30	64.28	36.40	71.12	62.94	95.35
0.40	78.90	24.96	79.26	49.33	95.28
0.50	80.47	17.26	83.79	39.44	94.93
0.60	79.03	11.59	88.27	28.70	94.42
0.70	91.85	7.84	92.17	22.88	94.13
0.80	90.76	4.77	94.02	15.87	93.68
0.90	95.87	2.84	96.07	10.19	93.30
Breakeven	53.43		67.09		

Table 1d: Performance with Sensor 1d					
Threshold	Macro		Micro		Correctness
	Precision	Recall	Precision	Recall	
-0.50	7.43	100.00	7.43	100.00	7.43
-0.40	7.43	100.00	7.43	100.00	7.43
-0.30	7.44	100.00	7.43	100.00	7.46
-0.20	7.45	100.00	7.44	100.00	7.53
-0.10	7.52	99.95	7.48	99.94	8.15
0.00	8.44	95.51	9.29	98.22	28.60
0.10	28.99	45.89	33.84	73.36	87.37
0.20	42.98	30.96	47.09	60.42	92.02
0.30	51.87	21.03	67.43	42.82	94.22
0.40	70.45	15.61	77.42	35.33	94.43
0.50	76.35	11.39	83.76	28.52	94.28
0.60	81.38	8.56	87.05	23.52	94.06
0.70	79.15	5.57	94.16	17.16	93.77
0.80	86.38	3.17	95.31	10.34	93.30
0.90	96.54	1.16	96.88	4.31	92.88
Breakeven	37.17		54.24		

Table 1e: Performance with Sensor 1e					
Threshold	Macro		Micro		Correctness
	Precision	Recall	Precision	Recall	
-0.40	7.43	100.00	7.43	100.00	7.43
-0.30	7.43	100.00	7.43	100.00	7.43
-0.20	7.43	100.00	7.43	100.00	7.44
-0.10	7.45	100.00	7.43	100.00	7.50
0.00	7.62	99.53	7.87	99.72	13.21
0.10	31.86	34.83	33.79	65.98	87.87
0.20	49.80	17.06	38.70	52.33	90.30
0.30	60.90	3.82	53.52	13.16	92.70
0.40	73.62	0.73	49.00	2.50	92.56
0.50	80.98	0.18	44.38	0.66	92.56
0.60	59.46	0.05	59.46	0.20	92.58
0.70	85.71	0.01	85.71	0.06	92.57
Breakeven	33.35		42.44		

Table 2a: Performance with Sensor Fusion on 1a and 1e					
Threshold	Macro		Micro		Correctness
	Precision	Recall	Precision	Recall	
-0.80	7.43	100.00	7.43	100.00	7.43
-0.70	7.43	100.00	7.43	100.00	7.44
-0.60	7.43	100.00	7.43	100.00	7.45
-0.50	7.44	100.00	7.43	100.00	7.48
-0.40	7.46	100.00	7.44	100.00	7.52
-0.30	7.49	100.00	7.44	99.99	7.64
-0.20	7.56	100.00	7.47	99.99	7.98
-0.10	7.79	99.99	7.59	99.98	9.52
0.00	10.17	99.09	11.12	99.49	40.88
0.10	37.18	76.59	41.42	90.61	89.78
0.20	54.53	55.46	59.33	78.96	94.42
0.30	61.85	39.78	71.34	66.23	95.52
0.40	68.19	28.55	79.43	54.23	95.56
0.50	70.83	20.39	83.56	44.16	95.21
0.60	67.73	14.37	85.74	34.95	94.74
0.70	76.90	9.75	91.45	26.43	94.35
0.80	92.67	6.28	94.08	19.43	93.92
0.90	96.27	3.71	95.90	13.01	93.50
Breakeven	54.82		68.86		

Table 2b: Performance with Sensor Fusion on 1a and 1d					
Threshold	Macro		Micro		Correctness
	Precision	Recall	Precision	Recall	
-0.80	7.43	100.00	7.43	100.00	7.43
-0.70	7.43	100.00	7.43	100.00	7.43
-0.60	7.43	100.00	7.43	100.00	7.44
-0.50	7.44	100.00	7.43	100.00	7.46
-0.40	7.45	100.00	7.43	99.99	7.49
-0.30	7.47	100.00	7.44	99.99	7.60
-0.20	7.53	100.00	7.46	99.99	7.92
-0.10	7.73	99.93	7.59	99.94	9.67
0.00	10.15	98.60	11.39	99.36	42.55
0.10	34.18	71.44	41.06	88.79	89.70
0.20	50.08	54.74	59.00	77.87	94.34
0.30	58.86	42.05	70.33	66.36	95.42
0.40	65.85	32.14	78.16	55.94	95.57
0.50	70.20	24.35	83.86	47.08	95.40
0.60	73.73	18.69	87.39	39.48	95.08
0.70	75.83	13.71	89.58	32.81	94.73
0.80	87.27	9.57	91.95	26.55	94.37
0.90	87.55	5.52	96.52	17.47	93.82
Breakeven	51.99		68.36		

Table 2c: Performance with Sensor Fusion on 1b and 1d					
Threshold	Macro		Micro		Correctness
	Precision	Recall	Precision	Recall	
-0.80	7.43	100.00	7.43	100.00	7.43
-0.70	7.43	100.00	7.43	100.00	7.43
-0.60	7.43	100.00	7.43	100.00	7.44
-0.50	7.43	99.99	7.43	99.99	7.45
-0.40	7.44	99.99	7.43	99.99	7.49
-0.30	7.47	99.99	7.44	99.99	7.60
-0.20	7.52	99.99	7.46	99.98	7.88
-0.10	7.72	99.89	7.59	99.93	9.56
0.00	9.90	98.85	10.81	99.48	39.00
0.10	34.73	77.52	39.86	90.85	89.14
0.20	52.65	56.18	56.46	78.29	93.90
0.30	63.70	41.87	69.32	65.28	95.27
0.40	71.51	32.02	76.93	55.00	95.43
0.50	81.88	23.86	82.04	46.22	95.25
0.60	85.14	18.11	86.38	39.29	95.03
0.70	84.48	13.24	89.02	33.24	94.74
0.80	84.14	9.82	91.45	28.12	94.47
0.90	90.35	6.20	96.61	20.33	94.03
Breakeven	54.19		67.31		

Table 2d: Performance with Sensor Fusion on 1a and 1b					
Threshold	Macro		Micro		Correctness
	Precision	Recall	Precision	Recall	
-0.80	7.43	100.00	7.43	100.00	7.43
-0.70	7.43	100.00	7.43	100.00	7.44
-0.60	7.43	100.00	7.43	100.00	7.45
-0.50	7.44	100.00	7.43	100.00	7.47
-0.40	7.45	100.00	7.43	99.99	7.51
-0.30	7.48	100.00	7.44	99.99	7.63
-0.20	7.55	100.00	7.47	99.99	8.00
-0.10	7.81	99.89	7.61	99.94	9.85
0.00	10.08	98.67	11.25	99.45	41.67
0.10	35.71	79.55	40.78	92.58	89.46
0.20	55.67	59.86	59.02	81.97	94.43
0.30	65.81	45.56	70.54	70.17	95.61
0.40	71.86	34.30	77.30	59.12	95.67
0.50	75.78	25.95	81.77	49.74	95.44
0.60	81.77	19.63	84.83	42.44	95.16
0.70	78.16	13.82	87.61	33.70	94.72
0.80	92.62	9.65	92.80	26.48	94.39
0.90	90.96	6.38	95.29	20.61	94.03
Breakeven	57.41		70.36		

Appendix B - Brief Description of Some Programs Written during this Work

These descriptions are best understood relative to the description of related programs in [Dasigi, et al., 97]. Two programs `ccsNP` and `RneuralNP` are written, which are analogous to `ccs` and `Rneural`, except that they work with the file `cd2/churchp1p1-docs/df2tk2-all/wdf.trn`, which contains the noun phrase-document associations.

A program named `Rresall` is written which expects to be given the number of categories, a step value to be used in different thresholds, an input and an output file. The input file is the raw output produced by NeuralWorks⁵ (the file with the `.nnr` extension), and a summary of the macro- and micro- averaged precision and recall, and correctness at each threshold value, as well as the break-even points are written out to the output file.

Other utilities, `combsens` to combine different sensor outputs, `sepsens` to separate combined sensor outputs, and `septrntst` to separate a single large neural net input file (with the `.nna` extension) into training and test inputs, are also written.

ENHANCING THE ROME LAB ADII VIRTUAL ENVIRONMENT SYSTEM

**Richard R. Eckert
Associate Professor
Department of Computer Science
Thomas J. Watson School of Engineering**

**Binghamton University
Vestal Parkway East
Binghamton, NY 13902**

**Final Report for:
Summer Faculty Research Program
Rome Laboratory
Griffiss Air Force Base
Rome, NY 13441**

**Sponsored by:
Air Force Office of Scientific Research
Bolling Air Force Base, DC**

and

Rome Laboratory

July, 1997

ENHANCING THE ROME LAB ADII VIRTUAL ENVIRONMENT SYSTEM

Richard R. Eckert
Associate Professor
Department of Computer Science
Thomas J. Watson School of Engineering
Binghamton University

Abstract

An effort to understand and enhance Rome Laboratory's virtual reality system was undertaken. The Cubeworld software system was modified to enable user-induced changes in the position of the observer and the center of projection—thereby producing changes in the binocular disparity of the stereoscopic image. Further additions to the program permit interactive scaling of the scene. Attempts were made to streamline the dual (stereoscopic) viewing/projection pipelines to enhance the performance of the system. A software "fix" to a damaged VPL Dataglove was implemented, and new voice commands for the HARK speech recognition system were instituted. The latter involved modifications of the grammar file and of the program running on the machine generating the Cubeworld virtual world simulation as well as on that running the speech recognizer. A major accomplishment was the incorporation of primitive three-dimensional sound into the simulation. An animated object was created with Designer's Workbench and added to Cubeworld's list of objects. On each iteration of the simulation's main event loop, the object updates its position on a circular trajectory and reports this position as well as the frequency and amplitude of the virtual sound it is emitting to the program running on the machine that will generate the sound. The communication is done via network sockets. Routines to handle this communication were implemented in the programs running on both machines. The receiver side program uses the information it receives to compute the interaural time difference and interaural intensity difference of the sound that would arrive at each ear of the observer. These have been shown to be the primary cues a human being uses to localize the source of a sound in three-dimensional space. The receiver program also computes the Doppler frequency shift. The results of these computations are used to fill the system's audio buffer, which, in turn is read by the audio hardware. The result is the generation of a sound to each earphone worn by the observer of the simulation. Thus the sound perceived by the observer is similar to that he would have heard if he had really been in the world in which the sound source was moving. This enhances the reality of the simulation.

ENHANCING THE ROME LAB ADII VIRTUAL ENVIRONMENT SYSTEM

Richard R. Eckert

Introduction

The Advanced Displays and Intelligent Interface (ADII) group of the Computer Systems (C3AB) Branch of the Rome Air Force Laboratory Command, Control, and Communications Directorate has implemented a virtual environment visualization system. This system enables the user to have the sensation of being immersed in a 3D virtual world that he or she can manipulate. A stereoscopic projection system consisting of two sets of RGB projectors, each with polarizers, generates two color images with opposite polarization onto a large screen. In addition a modified helicopter pilot helmet equipped with two monochrome CRTs with a 1280x1024 pixel resolution can present an image to each eye of the person wearing the helmet. A computer program called Cubeworld, originally created by the MITRE Corporation for a Silicon Graphics (SGI) platform, produces two separate images of a polygon-modeled "world" with binocular disparity. These images are sent to the projection system and/or helmet CRTs. Screen viewers wear polarized glasses, and each eye sees one of the screen images. This produces the effect of stereopsis, a very powerful depth cue.^{7,8} Standard 3D computer graphics techniques produce the other typical 3D depth cues. The result is the sensation that the user is immersed in the scene being generated by the system.

The user interacts with the "virtual world" generated by Cubeworld by using VPL Datagloves, a Logitech 3D mouse (each connected to a tracking system), a Spaceball, and/or a HARK speech recognition system. The helmet also has a Polhemus magnetic tracker mounted on top, which, when activated, permits the position and orientation of the head of the wearer to be fed back to the program. Cubeworld takes input from the Dataglove, 3D mouse, and/or helmet tracker and determines their positions and orientations in the virtual world. An image of a hand is projected into the world at that position. Pointing and grabbing gestures are used to manipulate objects in the world and/or to bring up and select actions or objects chosen from menus or catalogs. The six-degree-of-freedom Spaceball provides position and orientation input which is used to reposition the right and left eye viewpoints -- thus permitting interactive navigation through the virtual world. The HARK speech recognition system is programmed to provide a series of audio commands, thereby providing the user an alternative method of interacting with the virtual world. Objects and scenes for Cubeworld can be generated using the Coryphaeus Designer's Workbench 3D modeling program.

During my summer tour my main objective has been to try to understand the virtual world system and in particular the Cubeworld software. The hope was that this understanding would enable me to modify the system and add to it so that it is more efficient, easier to use, less fatiguing, more user friendly, and capable of providing a more realistic simulation. The following summarizes some of my efforts.

Deciphering how Cubeworld works

The Cubeworld program contains more than 75 essentially undocumented C++ program modules. A complex class inheritance structure makes it very difficult to understand how the program works. After several weeks of effort I was able to decipher a great deal about Cubeworld's inner workings. Some of the more important modules and their functions are shown in the following table.

Module (.cc)	Function
Catalogxxx	Several modules describing objects/scenes selectable from floating visible catalogs
DeviceDIS	Provides an interface to distributed interactive simulations (e.g., ModSAF) on other machines
DeviceHARK	The speech recognition module
DeviceNetwork	Controls communication over the network
DeviceSGI	Controls the Spaceball
Environment	Provides basic functionality such as getting a display, stopping execution, running objects, etc.
Fastrak	Controls the Polhemus tracking system
Fltxxx	Several modules that generate objects and animations
G_Device	Provides the parent class for controlling all devices
G_Object	Provides the parent class for controlling all objects in the scene
HostInfoRomeLab	Provides constants and other information specific to Rome Lab
Logitech	Controls the 3D mouse
Matrix3D	Provides all the mathematical matrix manipulation functionality
Menuxxx	Several modules that provide floating menus from which the user can select objects, scenes, etc.
ScreenDevice	Provides the 3D viewing/projection transformation pipeline for both eyes
SerialPort	Controls the SGI serial ports (serial communication with devices such as the glove)
VPLGlove	Controls the Data Glove
VRTime	Provides real-time information useful in animations
Vector3D	Provides vector definitions and mathematical operations
cubeworldRomeLab	Module that executes first, contains main()

A brief discussion is now given of what happens when Cubeworld executes.

When the program starts, the Environment class constructor invokes the ScreenDevice constructor, which, in turn, initiates the Rome Lab projection screen. The left and right viewports, the default centers of projection, the viewing transformation matrices, the projection transformation matrices, and the front/back clipping planes are all set up here. The viewing pipeline is exactly that described in Foley and VanDam¹, namely a five-step chain of 4x4 homogeneous matrix multiplications. The matrix operations are:

1. Translate the view reference point (VRP) to the origin.
2. Rotate the viewing-reference coordinate system (VRC) such that the view-plane normal (VPN) becomes the z axis.
3. Translate such that center of projection (COP) is at the origin.
4. Shear such that the center line of the view volume becomes the z axis.

5. Scale such that the view volume becomes a symmetrical truncated right pyramid

The authors of the Cubeworld program opted to go with separate viewing pipelines for each stereoscopic view.

After initialization the Environment class run() function is executed. This contains the program's main event loop. In simplest terms the basic structure is:

While (quit == 0)

 Run all the devices (get input)

 Run all the objects (get geometric/material/position/animation descriptions)

 Call the ScreenDevice class draw() member function (project and render all objects)

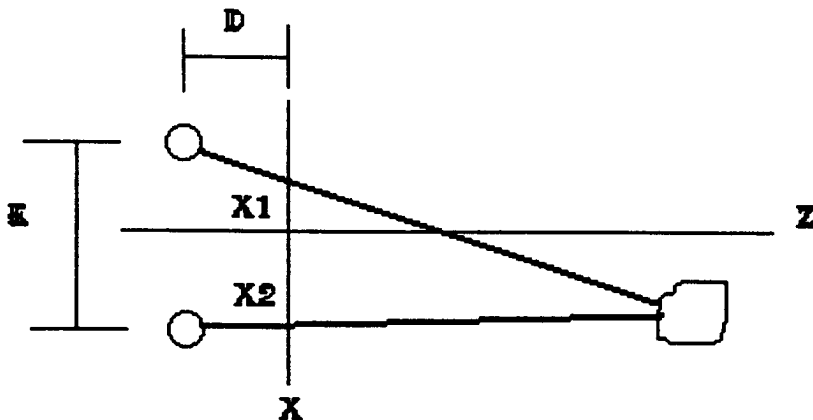
On each iteration of this loop all objects are redrawn in whatever new positions might be specified in each object's description. Input is received and acted upon. Viewpoints may be modified.

Building Models

I spent a couple of days familiarizing myself with the Designer's Workbench software package¹² which enables the user to build objects for Cubeworld. This is a powerful 3D modeling system. The resulting objects can be stored in the .flt format used by Cubeworld. I was able to design a Phong-shaded chess bishop and to incorporate it into the Cubeworld's C5I object catalog by modifying the CatalogC5I.cc file.

Binocular Disparity (Stereo Viewing)

I spent more than a week trying to find a way of streamlining the double viewing pipeline. As mentioned above, Cubeworld computes all points on all objects twice--once for each center of projection. The following figure shows the situation.



Here E is the interocular distance, D the distance of eyes from the projection plane, (x,z) the viewing coordinates of the object being observed, and x_1, x_2 the x coordinates of the images seen by each eye on the projection plane. Simple geometry gives the following results:

$$x_1 = \frac{x D - E z / 2}{z + D} \quad x_2 = \frac{x D + E z / 2}{z + D}$$

If we denote the binocular disparity $(x_2 - x_1)$ by dis , it is easy to show that $dis = E z / (z + D)$

Since $x_2 = x_1 + dis$, instead of sending each point through the five-step chain of transformations twice to get the projection point on the screen (as currently is done in Cubeworld), we could do it just once to obtain x_1 . Then with a multiply, a divide, and two adds, we could obtain the value of x_2 .

The situation becomes even more convenient for objects that are distant from the observer. For those cases, the disparity approaches the interocular distance, E . Therefore x_2 could be obtained from x_1 by a single add: $x_2 = x_1 + E$. Unfortunately, because of the way Cubeworld is written, there is no easy way to incorporate this performance-enhancing simplification without a complete redesign of the program.

In conjunction with the viewing pipeline, I noted the user was unable to alter the binocular disparity built into the current version of Cubeworld. It is well known that different people have different abilities to fuse images in a stereo system, so that the ability to change the binocular disparity is very important to increasing the comfort level and decreasing the fatigue level of the user. (It can also lead to interesting special effects such as a super depth of field.) I was able to add options to the main menu that enable the user to increase or decrease both the interocular distance and the z value of the center of projection. These changes can be found in the module MenuDef4.cc. To illustrate, given below is the code to install an "IncCOP" menu item that, when selected, increases the z distance of the center of projection (COP) by a factor of 1.5.

```
static struct Item_Inc_cop : public MenuItem
{
    Item_Inc_cop(): MenuItem("IncCOP"){ }
    void callback()           // function called when the user selects this menu item
    {
        vector3D cop;
        cop = ScreenDev::getCOP(); // get the old center of projection
        cop.z *= 1.5;             // scale the z value up
        ScreenDev::setCOP(cop);   // set the result to be the new center of projection
    }
}
```

VPL Dataglove

During my tour we began having trouble with the right-hand VPLglove's thumb flexing. With age, the fibre optic flex sensors along the digits of the glove become worn. In our case the extremity of the thumb's fiber optic cable came to the point that it no longer gave the correct flex signal. A simple "fix" was to tie the part of the thumb outside the joint to the part inside the joint in software. After considerable searching I found the code that does that is in the VPLGlove.cc module. I replaced the line: `static const char RIGHTMAP[] = {0,1,2,3,4,5,6,7,6,7};` with: `static const char RIGHTMAP[] = {0,0,2,3,4,5,6,7,6,7};` which effectively tied the two parts of the thumb together. After this modification the glove was again usable.

Spoken Commands

I spent a couple of weeks working with the HARK speech recognition system.⁶ The basic setup is that one SGI machine (Rajah) runs a program (cubeworld.c) that matches digitized input voice patterns with pre-programmed combinations of phonemes. These combinations are set up in a grammar file. When a match is found the program sends an appropriate identifier over a serial link to the machine (Ares) running the Cubeworld virtual world simulator. Cubeworld's DeviceHARK.cc module (in conjunction with SerialPort.cc) monitors the serial port and, when there is a HARK command there, responds to it. Adding new voice commands is done by modifying the grammar file (cubeworld.hg) and the the cubeworld.c program on the sender side as well as the DeviceHARK.cc module on the receiver side. I was able to add several new voice commands that move the observer, change the position of the center of projection, and scale the scene up or down. The relevant code additions are:

In the sender's grammar file (cubeworld.hg) I added:

\$commands:

...

| MOVE/M

(DOWN/L

 |LEFT/L

 |RIGHT/RT

| UP/U

| [CENTER OF] PROJECTION IN/CI

| [CENTER OF] PROJECTION OUT/CO

)

| SCALE

(UP/UP

 | DOWN/DN

)

| ZOOM/M

(IN/IN

 | OUT/OU

)

In the enum statement of the sender's cubeworld.h file, I added:

```
enum { QUIT = 'A'
...
    MOVELEFT,
    MOVERIGHT,
    MOVEUP,
    MOVEDOWN,
    MOVEIN,
    MOVEOUT,
    COPIN,
    COPOUT,
    COPDOWN,
    SCALEUP,
    SCALEDN,
```

In the sender's cubeworld.c file in the process_recognition() function's if statement, the new code for moving the center of projection in is as follows. (The other new voice command handling code is very similar.)

```
else if (strcmp(tags, "M CI") ) /* defined in the grammar file */
    { c = COPIN;
      if (write(ttyfds, &c, 1) == -1)          // send command to serial port
          printf("error while writing %c\n", c);
    }
```

Finally on the receiver side, in the DeviceHARK.cc module, the new HARK commands would be added to the large enum statement at the beginning of the file as in the sender's cubeworld.h file (see above). Then the if statement in the DeviceHARK::run() member function would be modified by making the following additions. (Only the code for the COPIN, MOVEDN, and SCALEUP commands are given; the others are handled in similar fashion.)

```
if (port.getData(command))
...
{
switch (command)
case COPIN:
    { Vector3D cop = ScreenDev::getCOP(); // reduce center of projection z value
      cop.z *= 0.9;
      ScreenDev::setCOP(cop);
      break;
    }
case MOVEDOWN:
    { location = Environment::getLocation(); // get current position of observer
      Matrix3D temp (0,0,00,
```

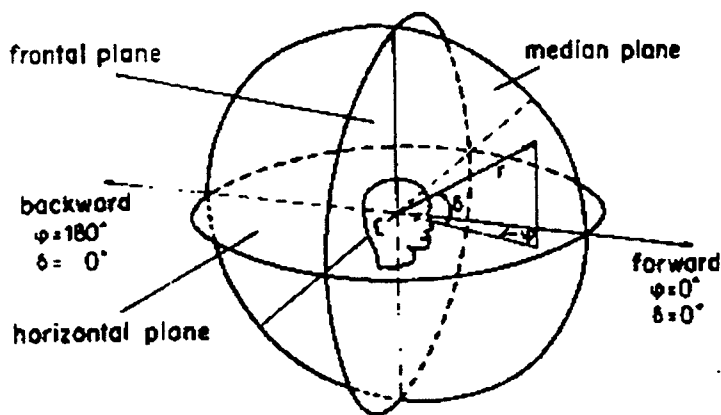
```

        0,0,0,0,
        0,0,0,0,
        0,0.5,0,0);      // last row contains x,y,z coordinates—want to add .5 to y
location += temp;        // add it in
Environment::setLocation(location); // set new position of observer
}
case SCALEUP:
{ ZoomKnob::setViewscale(2.0); // ZoomKnob class contains scaling functionality—scale by 2
break;
}

```

Three-Dimensional Sound

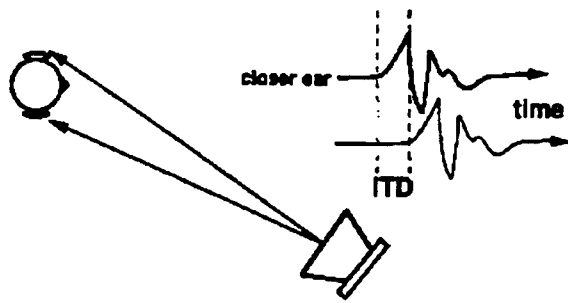
The major portion of my tour (the last four weeks) was spent on trying to incorporate three-dimensional sound into the Cubeworld virtual reality system. The basic idea is to incorporate sound-emitting objects into Cubeworld (e.g., an airplane emitting the sound of a jet engine). The system should attempt to reproduce the sound digitally and output it to earphones worn by the user. If this is done properly, it will seem to the user that the sound is coming from the image of the object as it moves in the virtual world. The figure below shows the situation. We assume the sound source is at a position relative to the user specified by an azimuthal angle (ϕ) and elevation angle (δ). The objective is to produce waveforms that go to each earphone speaker such that the sound perceived by the user is as close as possible to that he would hear if a real sound source were located at that position.



(2)

Researchers have discovered that there are several important cues that indicate where a sound is coming from.^{2,4}

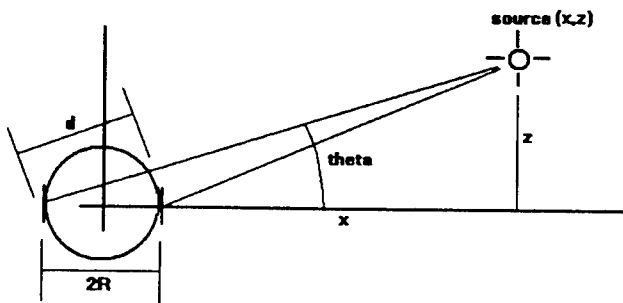
The most important of these is the interaural time difference (itd). A sound that comes from an azimuth not equal to 0 or 180 degrees will arrive at one ear before it arrives at the other. The human auditory system picks up the resulting phase difference and is able to use this a cue to determine the azimuth of the source. The following figure shows the situation.



(3)

The itd effect is especially important at low frequencies where the wavelength of the sound is of the order of magnitude or larger than the size of the head.

Quantitatively we may derive an equation that will determine how much the time difference is for a source located at a given point (x,z) with respect to the observer. The following figure shows the situation. Here R is the radius of the listener's head.



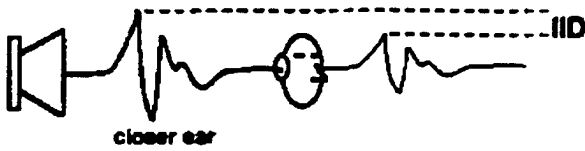
The path difference for sound traveling to each ear (d) is given approximately by

$$d = 2R \cos(\theta) = \frac{2R}{\sqrt{x^2 + z^2}}$$

The interaural time difference is then given by $\text{itd} = d/u$, where u is the velocity of sound.

The second important three-dimensional sound cue is the difference in the intensity (pressure) of the sound that arrives at each ear.^{2,4} In part this is a consequence of the fact that sound intensity (proportional to the square of the amplitude) falls off in an inverse square law with distance. If the listener is not looking directly toward or away from the source, one ear will be farther and receive a reduced intensity. More important is the effect of shading due to the fact that the head blocks part of the sound arriving at the far ear. This effect is most pronounced at high frequencies, since at low frequencies the wavelength of the sound is of the same order of magnitude of the size of the head, implying that the sound is diffracted around the head,¹⁰ thereby reducing significantly the shadowing. The combined effect is known as the interaural intensity difference (iid).

The following figure shows the situation.



(3)

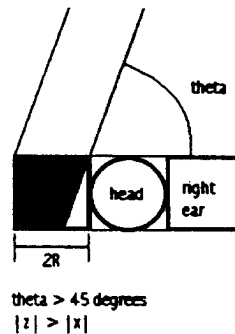
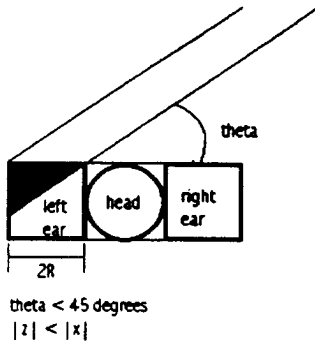
The intensities I_1 (near ear) and I_2 (far ear) are given by:

$$I_1 = \frac{I_0}{(x - R)^2 + z^2} \quad \text{and} \quad I_2 = \frac{I_0}{(x + R)^2 + z^2}$$

After some algebra, we get the following approximation (for far-away listeners):

$$\frac{I_1}{I_2} = \frac{1 + \epsilon}{1 - \epsilon}, \quad \epsilon = \frac{2Rx}{x^2 + z^2}$$

In order to take into account the head shadowing effect for high frequency sound waves, I came up with an approximation in which the ears are considered to be squares on either side of the head, which is also approximated by a square. The situation is shown in the following two diagrams—one for $\theta < 45$ degrees and the second for $\theta > 45$ degrees. As can be seen in the diagrams, in the first case the non-shadowed (black) area of the far ear is a triangle and in the second it is a trapezoid. Assuming that only the black area receives sound (which would be the case if there were no diffraction¹¹—i.e. at high frequencies), The result for each case is:



$$I_1/I_2 = (0.5 * zz/xx) f / f_{max}$$

$$I_1/I_2 = (1 - 0.5 * xx/zz) f / f_{max}$$

Here I_1 refers to the sound intensity received at head-shadowed left ear and I_2 to that received at the non-shadowed ear. XX and ZZ are the absolute values of the x and z distances to the source.

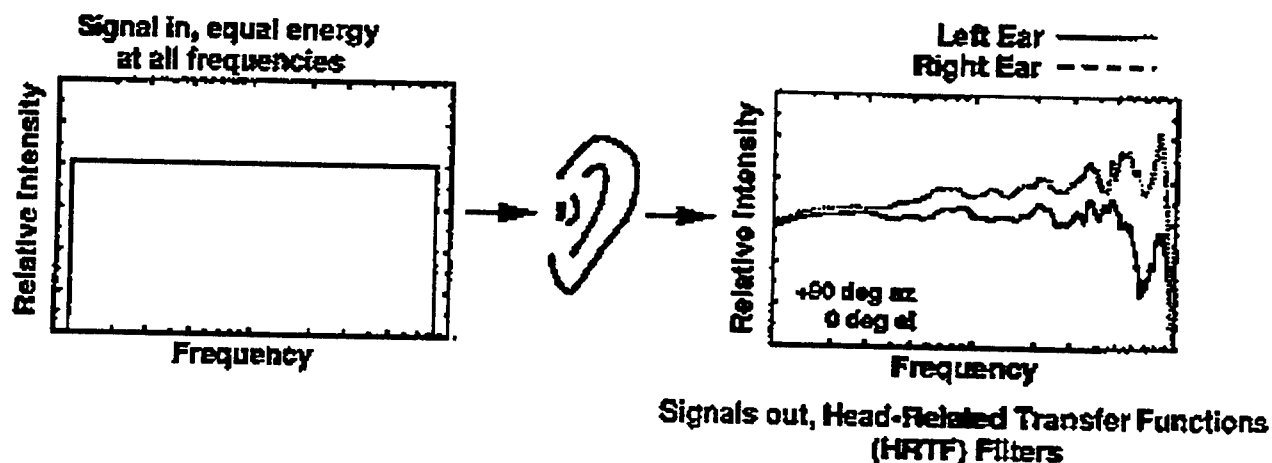
I have taken f_{\max} to be about 10,000 Hz, since above 5,000 Hz diffraction effects become less important.

A third effect that determines what the listener hears is the Doppler effect which produces a change in frequency when there is relative motion along the line that joins the sound source and the observer. From elementary physics, the result is:¹⁰

$$f = f_0 \frac{u}{u + \mathbf{r} \cdot \mathbf{v}}$$

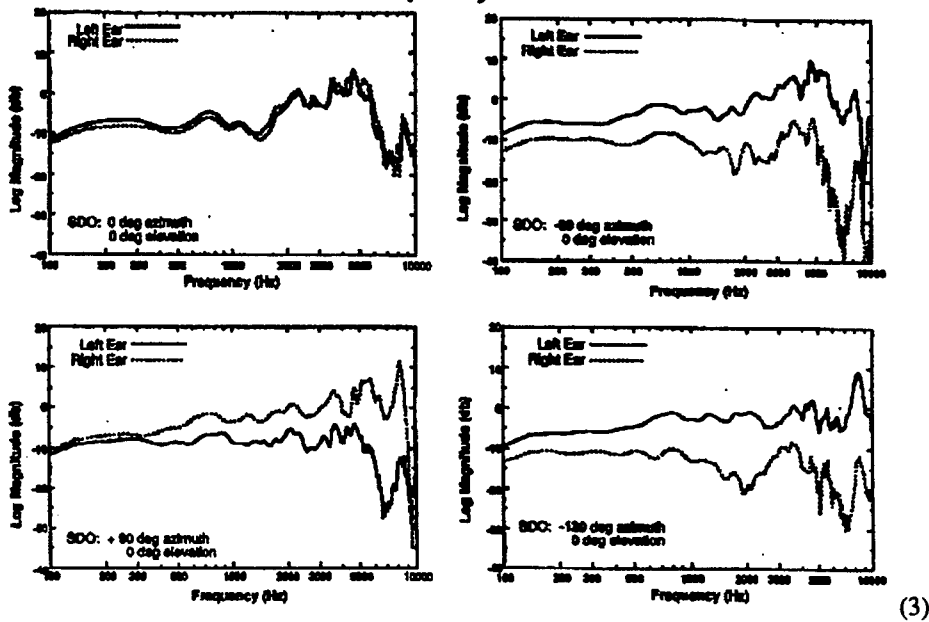
where u is the speed of sound, \mathbf{r} a unit vector from the observer to the sound source, and \mathbf{v} the velocity vector of the source. (If the observer is moving also, the result is more complex.) Here f_0 is the frequency of the emitted sound, and f is that perceived by the listener.

Notice that none of these 3D sound cues provides any information on the elevation angle of the sound source. Most auditory scientists feel that the pinnae (outer ear structures) modify the sound spectrum that arrives at the ear in a way that depends on frequency, azimuth, and elevation. (See the figures below.) This may be taken into account by calculating a "head-related transfer function" (HRTF) and convolving this with the sound arriving at the ear^{2,4}. The resulting sound is fed into the earphones and should reproduce what the listener would actually hear. Unfortunately, to be able to do this, we would need digital signal processing equipment that our group at Rome Lab currently does not possess.



(3)

Head-Related Transfer Functions (HRTFs) Frequency Domain



Practical Considerations

In order to put into practice the theoretical concepts described above, I wanted to produce an animation of a sound-emitting object (my chess bishop) in Cubeworld. Unfortunately the machine running Cubeworld (Ares) does not have a sound card. So I decided to use the machine running the HARK system (Rajah), which does have sound capability. This meant that Cubeworld would have to send a signal containing information on the position of the object after each iteration of the main event loop. It would be possible to do this using another serial port, but unfortunately there were no more serial ports available on Ares. At the suggestion of several associates, I decided to look into using network sockets to provide the communication. This is something I had never done before, and it took me a week or so to figure out how to do it.⁹

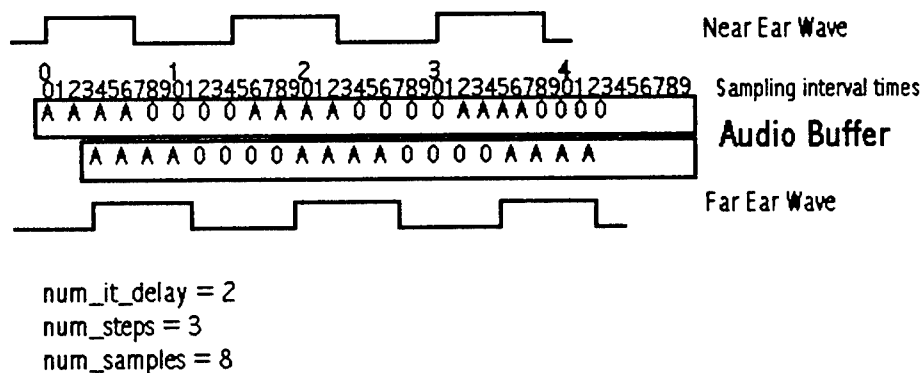
For the sender (Cubeworld on Ares) I wrote a C++ program (Sound7.cc) that has a Sound class with member functions that can open a socket connection, write an integer to a socket, and close a socket. The write_sock() routine extracts the ASCII code of each digit of the integer provided in the function's argument and writes them one at a time using the stream I/O function putc(). The last character sent for each integer is a blank which serves as a sentinel to the receiver indicating there are no more digits.

For the receiver (on Rajah) I wrote a C program (sound7.c) that has functions that open a socket, read an integer from a socket, and close a socket. The read_sock() routine uses getc() to retrieve the incoming characters, and assembles them into an integer. The trailing blank sentinel causes the function to terminate. The main() function in this program expects the integers to come in the following order: first the intrinsic frequency of the sound source, then its intrinsic amplitude, and finally pairs of integers representing the (x,z) coordinates of the position of the

sound source. Reading continues until a 9999 is received, which causes a call to be made to `close_sock()`. After each pair of integers is received, a call is made to the function `square_wave()`, which takes the information received and computes the amplitude, frequency, and interaural time difference (itd) of the sound to be sent to each earphone.

The actual sound output is done using the audio library built into the SGI sound system. In my very simple test case, the sound that is output is a square wave, but it would be straightforward to take, for example, a WAVE file, extract the amplitude samples, modify them according to the computed itd and iid factors, and fill the audio system's sound buffer with that information.

The way the SGI sound library works is that a buffer is filled with amplitudes corresponding to each sample time. (The sampling interval (SamplingRate) can be obtained by invoking the library function `GetAudioOutputRate()`.) If the system is in stereo mode, the amplitudes stored in even positions in the buffer go to the left speaker and odd ones to the right speaker. The following figure shows how this buffer would be filled if a square wave with an given itd is to be produced.



Once the buffer is filled, calls can be made to audio library routines that actually send the information to the audio hardware.

Notice that in order to fill the buffer correctly, we need to compute three loop iteration counts, each of which, in turn, is determined by a time interval. The frequency of the wave determines the length of each wave pulse. The number of sampling intervals (`num_samples`) is given by the length of the pulse divided by the sampling interval. But the length of the pulse is one-half the wave's period, which, in turn, is the inverse of the wave's frequency. Thus

$$\text{num_samples} = \text{SamplingRate} / (2 * \text{frequency})$$

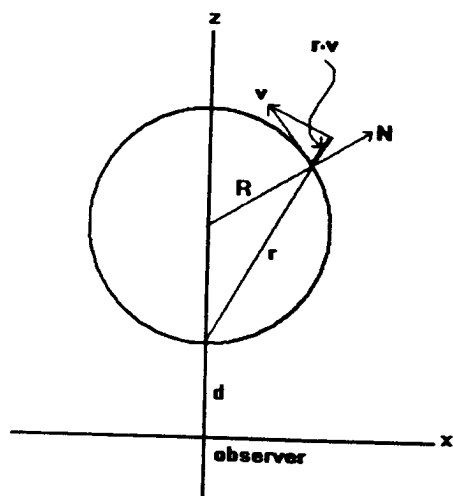
The number of pulses output will be the amount of time the sound is to last (duration) divided by the time one complete wave lasts. This latter time is nothing more than the period of the wave. Thus the number of pulses (`num_steps`) is given by:

$$\text{num_steps} = \text{duration} * \text{frequency}$$

The number of sample times that must pass between the moment the wave is sent to the near ear and that in which it goes to the far ear is determined by the interaural delay time (itd) computed from the position of the sound source. Again this is nothing more than the ratio of the itd to the sampling interval, which, of course is the inverse of the sampling frequency. Thus:

$$\text{num_it_delay} = \text{itd} * \text{SamplingRate}$$

The final programming task required is on the sender side. I needed to modify and add to the code that generates the bishop object to animate it and send the appropriate (x,z) coordinates over the socket. This meant digging into the CatalogC5I.cc module in Cubeworld. The animation I wanted was for the bishop to traverse a circular orbit in the x-z plane. Assuming that the observer is at the origin in the x-z plane as in the following diagram, we would have a situation where we should be able to observe the three 3D sound effects—interaural time difference, interaural intensity difference, and Doppler effect.



In the Miscellaneous Objects section of Cubeworld's CatalogC5I.cc module the code I added defines a Bishop_C5I() class constructor that reads in the model I created with Designer's Workbench ("Bishop.flt"), sets the intrinsic frequency and amplitude of the sound to be emitted by the bishop to 440 Hz and 10 units, respectively. Then it sets the observer's location so that it is slightly above the x-z plane at the origin and sets the initial position of the bishop object to the bottom of the circle shown in the above figure. Finally the object's constructor opens a socket and sends out the frequency and amplitude.

The Bishop_C5I class run() function (which will be executed each time Cubeworld's event loop repeats) uses the equation of the circular orbit to determine the new (x,z) coordinates of the object and updates the internal position coordinates that are read in the program's event loop (and used to display the new position) with these new values. It then makes calls to write_socket() to send the new coordinates to the Rajah machine so that the program running there can compute the information necessary to produce the 3D sound. After one orbit is completed, the Bishop_C5I

destructor is invoked, and this, in turn, sends the 9999 receiver termination sentinel, closes the socket connection, and invokes the Environment::stop() function which sets the variable quit equal to 1 (true), thereby causing Cubeworld to terminate execution.

Perhaps a comment should be made about the Doppler effect computation. First of all, if we factor out u , the speed of sound, the equation may be rewritten as follows:

$$f = f_0 \frac{1}{1 + (r \cdot v / u)}$$

Referring to the previous figure, we can see that

$$\mathbf{r} = \frac{(x, z)}{(x^2 + z^2)^{0.5}} \quad \text{and} \quad \mathbf{v} = \frac{v_0(z-d-R, x)}{[x^2 + (z-d-R)^2]^{0.5}}$$

Here v_0 is the magnitude of the velocity of the object. To a good approximation, the scalar product $\mathbf{r} \cdot \mathbf{v}$ is given by:

$$\mathbf{r} \cdot \mathbf{v} = \frac{v_0 * [(z-d-R) * x + z * x]}{x^2 + z^2}$$

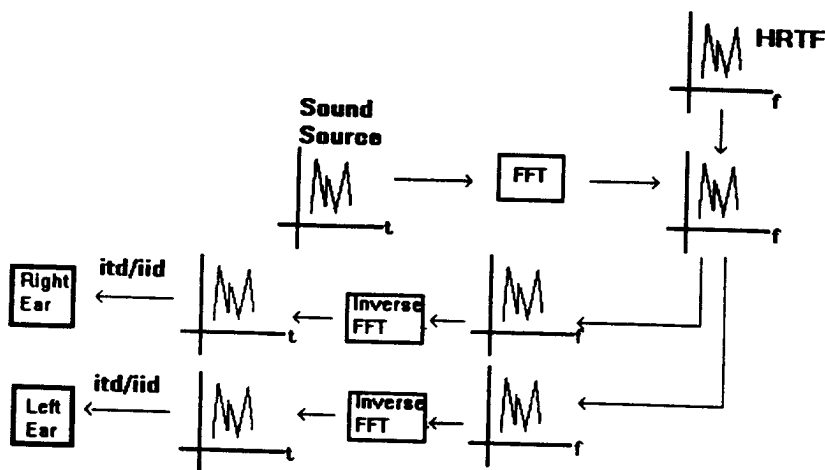
Substituting this result into the Doppler effect equation and simplifying gives the following result:

$$f = \frac{f_0}{1 + \text{del}} \quad \text{where } \text{del} = (v_0/u) * \frac{x}{(x^2 + z^2)}$$

The + (-) sign is used when the object is receding from (approaching) the observer.

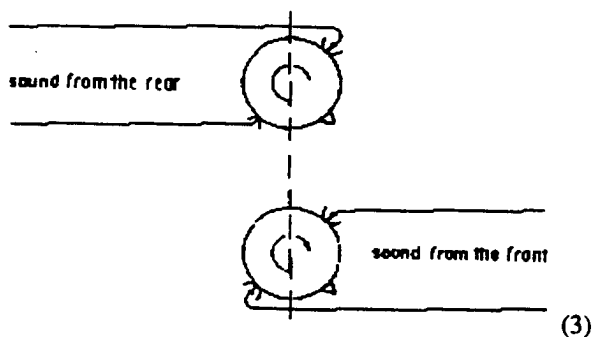
Possible Future work

These very preliminary tests with 3D sound on the Cubeworld system indicate what can be done. What is needed is to add the head related transfer function (HRTF) so that the sound that arrives at the ear drum of the user is very close to what he would hear if he were in the real scene. Then all the pertinent 3D cues will be there. The system I visualize is something like that shown in the following figure.



In this figure a complex sound (perhaps from a WAVE file) is convolved with the head related transfer function (HRTF) associated with the ear of the listener. Depending on the relative position and velocity of the source with respect to the observer, the interaural time difference, interaural intensity difference, and Doppler effect are computed and the resulting wave forms are sent to each ear. This will require digital signal processing in the form of a discrete Fourier transform (FFT) of the original waveform to give the frequency spectrum.⁵ This is then combined with the HRTF spectrum and the reverse Fourier transform of the result is taken to give the waveform that would arrive at the eardrum of the listener. Finally the itd and iid described in this paper are applied and the resulting sounds are output to each ear. We note that in order to be able to do these operations a fast digital signal processor will be required.

I would also like to take into account movement of the observer and make the 3D sound generation less specific to individual objects. Obviously when the listener turns his head, the sound he hears is quite different. (See following figure.) This technique is used by humans to disambiguate whether the sound comes from the front or rear. Notice that neither the itd nor the iid factors distinguish between sources at the same azimuth in front or in back of the observer.



Since Cubeworld can output to a head-mounted display with a Polhemus tracker and the software to do the orientation tracking is already in place, it should be quite straightforward to incorporate these observer location/orientation effects into the sound generation.

At present all of the 3D sound I have implemented is hard-coded for a specific kind of source trajectory and source sound spectrum (a square wave). It would be nice to write a 3D sound class for Cubeworld that will handle the generation of 3D sound in a completely general way.

Closing Thoughts

I have very much enjoyed my summer tour at Rome Lab. It has provided me the opportunity to work with very sophisticated hardware and software and to learn a great deal. In closing I would like to thank the people I have worked with. My supervisor, Dick Slavinski was an encouraging facilitator and gave me the freedom to look into research areas of interest to me. He also gave me the freedom to follow my ideas. My associates in the lab—Lieutenant Mark Brykowytch, Captain Steve McCown, Peter Jedrysik, Jason Moore, and Rich Evans were always helpful and understanding of my relatively low position on the learning curve. Without their assistance this summer would have been much more difficult. I would also like to thank secretaries Martha Kraeger and Patty Froio for their understanding and help.

Bibliography

1. Foley, J.D., VanDam, A., Feiner, S.K., Hughes, J.F., Computer Graphics: Principles and Practice, Second Edition, Addison-Wesley, 1990.
2. Blauert, Jens, Spatial Hearing, MIT Press, 1997.
3. Wenzel, Elizabeth, Foster, Scott, Virtual Reality: Principles and Applications, Psychophysics and Technology of Virtual Acoustic Displays, The Institute of Electrical and Electronics Engineers, Inc., 1993.
4. Begault, Durand R., 3-D Sound for Virtual Reality and Multimedia, AP Professional, 1994.
5. Moore, F.R., "An Introduction to the Mathematics of Digital Signal Processing," Computer Music Journal, (II:2), 1978.
6. HARK Recognizer Programmer's Guide and Writing Applications Course Guide, Bolt, Beranek and Newman, Inc., 1994.
7. Fisher, S.S., Merrit, J.O., Bolas, M.T., editors, "Stereoscopic Displays and Virtual Reality Systems II," Proceedings of the International Society for Optical Engineering, Volume 2409, 1995.
8. Bolas, T.B., Fisher, S.S. Merritt, J.O. editors, "Stereoscopic Displays and Virtual Reality Systems III," Proceedings of the International Society for Optical Engineering, Volume 2653, 1996.
9. Horspool, R.N., The Berkeley UNIX Environment, Second Edition, Prentice-Hall Canada, 1991.
10. Bueche, F.J., Introduction to Physics for Scientists and Engineers, Third Edition, McGraw-Hill, 1980.
11. Crawford, Jr., F.S., Waves: Berkeley Physics Course, Volume 3, McGraw-Hill, 1968.
12. Designer's Workbench 3.1 Reference, Second Edition, Coryphaeus Software, Inc., 1995.

**TARGET IDENTIFICATION FROM LIMITED BACKSCATTERED FIELD
DATA**

Michael A. Fiddy
Professor
Department of Electrical Engineering

University of Massachusetts
Lowell, MA 01854

Final Report for:
Summer Research Program
Rome Laboratory

Sponsored by:
Air Force Office of Scientific Research
Bolling Air Force Base, Washington, DC

And

Rome Laboratory

September 1997

TARGET IDENTIFICATION FROM LIMITED BACKSCATTERED FIELD DATA

Michael A. Fiddy
Professor and Department Head
Department of Electrical Engineering
University of Massachusetts

Abstract

The problem of determining the nature of a target from limited backscatter data contains two difficult features. The first is the problem of inverting scattered field data when multiple scattering arises. There are few proposed theoretical methodologies do this and even fewer computationally feasible algorithms. The second problem lies in the fact that one would normally hope to have scattering data taken all around a target for all possible illumination directions. This is a luxury that rarely exists. We have adopted a simple signal processing-based approach to solving the inverse scattering problem when only limited incident and backscatter angles are available. We have applied these techniques to real data measured at Rome Laboratory using microwaves and model targets whose structure is known *a priori*. Some of these data have been made available to the imaging community at large but without revealing the structure of the target. This has proved to be a very important exercise when it comes to comparing different inversion techniques and their claimed success. During this summer internship, recently provided data were processed using an inversion method we refer to as cepstral filtering. All of the so-called mystery targets were imaged although their resolution was poor. These results were presented at a special session at the URSI Meeting held in Montreal in July. The poor resolution results in part from the limited number of data points used in the inversion step. During this summer new work was carried out on a spectral estimation technique that can make use of prior knowledge about the target to improve resolution. It transpired that this approach was particularly effective at identifying support bounds on the actual target. These support bounds provided a better indicator of what the target was than the image derived from the same scattering data. This leads one to conclude that with a certain number of data points and a certain degree of detail in one's prior knowledge of a target set, one can determine whether the best course of action is to "shape" the target using a dynamic prior function, or to form an image. These latter observations were carried out using real data acquired from a model of a cruise missile. Being a metallic target, there was little multiple scattering and the inverse scattering aspect of the identification step was not demanding. Future work will focus on folding the spectral estimation step into the cepstral filtering algorithm in order to identify penetrable targets using very little backscatter data.

TARGET IDENTIFICATION FROM LIMITED BACKSCATTERED FIELD DATA

Michael A. Fiddy

Introduction

Methods for inverse scattering, directed toward imaging a permittivity from scattered field data, typically require that the object be weakly scattering or have a permittivity which varies spatially only slowly on the scale of the illuminating wavelength. Under these assumptions, inversion methods, also collectively referred to as diffraction tomography techniques, can be formulated as straightforward Fourier inversion procedures.¹ The scattered field data under these conditions, based on adopting the first-order Born and the Rytov approximations, are mapped onto the Ewald sphere in k -space and inverse transformed. There have been many developments which extend the domain of validity of the Born and Rytov approximations.¹⁻³ These methods, sometimes iterative in nature, either assume sufficiently weak scattering that the Born series or a modified form of it converges or they assume that some *a priori* information about the scattering object is available. In the case of the latter, this can provide a (strongly scattering) background against which small fluctuations in permittivity can be imaged by applying distorted-wave Born and Rytov methods. The distorted-wave approach has been developed recently and reported,¹ but does not provide a sufficiently general approach to solve this inverse problem. In all of these cases, additional difficulties arising from the availability of limited sampled measured data, necessitate that an image estimation or restoration technique be included in the inversion algorithm. This is readily done when the algorithm remains essentially Fourier-based in form.

More general methods or "exact" inversion procedures have proved extremely difficult to implement, sometimes relying on embedding the object in a medium whose permittivity is close to that of the mean of the object's permittivity, or are limited to recovering shape or surface profile information⁴⁻⁶. A potentially "exact" method based on a nonlinear filtering method has been reported by us previously and is based on homomorphic filtering. This method extends the range of validity of the existing techniques to arbitrary scatterers, i.e. without the need to specify an upper bound on the permittivity of the object. Consider a scattering object having a permittivity ϵ which is embedded in a medium of permittivity ϵ_0 , where $\epsilon(\mathbf{r}) = \epsilon_0 [1 + V(\mathbf{r})]$. The object is assumed to be bounded by a compact support D , and assume that ϵ_0 is the free-space permittivity; we refer to $V(\mathbf{r})$ as the so-called scattering function, i.e. it represents $\epsilon/\epsilon_0 - 1$. If the scattering object possesses cylindrical symmetry and the polarization of the

incident time-harmonic electromagnetic wave is along the symmetric axis of the scattering object. the depolarization term in the vector wave equation can be neglected.¹

For the case of an incident plane wave $\Psi_0(\mathbf{r}, \hat{\mathbf{k}}_0) = e^{ik\hat{\mathbf{r}}_0 \cdot \mathbf{r}}$, then from the scalar Helmholtz equation we can express the total field $\Psi(\mathbf{r}, \hat{\mathbf{k}}_0)$ in terms of the inhomogeneous Fredholm integral equation of first kind, namely,

$$\begin{aligned}\Psi(\mathbf{r}, \hat{\mathbf{k}}_0) &= \Psi_0(\mathbf{r}, \hat{\mathbf{k}}_0) - k^2 \int_D d\mathbf{r}' G_0(\mathbf{r}, \mathbf{r}') V(\mathbf{r}') \Psi(\mathbf{r}', \hat{\mathbf{k}}_0) \\ &= \Psi_0(\mathbf{r}, \hat{\mathbf{k}}_0) + \Psi_s(\mathbf{r}, \hat{\mathbf{k}}_0),\end{aligned}\quad (1)$$

where $\Psi_s(\mathbf{r}, \hat{\mathbf{k}}_0)$ is the scattered field resulting from the interaction of the incident wave $\Psi_0(\mathbf{r}, \hat{\mathbf{k}}_0)$ with the scattering function $V(\mathbf{r})$, $G_0(\mathbf{r}, \mathbf{r}')$ is the free-space Green's function, k is the wavenumber in free space, and $\hat{\mathbf{r}}_0$ denotes the direction of illumination. The integration in Eq. (1) is over the support of $V(\mathbf{r})$ defined by D . Using the far-field approximation for the outgoing spherical wave $G_0(\mathbf{r}, \mathbf{r}')$, we obtain

$$\Psi_s(\mathbf{r}, \hat{\mathbf{k}}_0) = k^2 \frac{e^{ikr}}{4\pi r} \int_D d\mathbf{r}' e^{-ik\hat{\mathbf{r}} \cdot \mathbf{r}'} V(\mathbf{r}') \Psi(\mathbf{r}', \hat{\mathbf{k}}_0) \quad (2)$$

When adopting the first Born approximation, the total field (or internal field) $\Psi(\mathbf{r}, \hat{\mathbf{k}}_0)$ is replaced with the known incident field $\Psi_0(\mathbf{r}, \hat{\mathbf{k}}_0)$ in the integral above.⁷ This approximation is valid when $k|\epsilon_T - 1|a < \pi/2$, which is not typically appropriate for most imaging problems we would be interested in. The parameter a is the characteristic dimension of the object, and as the extent of the object increases or the magnitude of the permittivity fluctuations increases, the first Born approximation becomes increasingly poor. We do note however that these effects can be ameliorated by increasing the illuminating wavelength, which in turn degrades the resolution of the resulting image. Equation (2) may be written

$$\Psi_s(\mathbf{r}, \hat{\mathbf{k}}_0) = k^2 \frac{e^{ikr}}{4\pi r} f(\hat{\mathbf{k}}, \hat{\mathbf{k}}_0), \quad (3)$$

where $f(\hat{\mathbf{k}}, \hat{\mathbf{k}}_0)$ is the scattering amplitude and defined as

$$f(\hat{\mathbf{k}}, \hat{\mathbf{k}}_0) \equiv \int_D d\mathbf{r}' e^{-i\hat{\mathbf{k}} \cdot \mathbf{r}'} V(\mathbf{r}') \Psi(\mathbf{r}', \hat{\mathbf{k}}_0). \quad (4)$$

In the first Born approximation, the relationship between the scattering amplitude and the scattering function $V(\mathbf{r})$ becomes a Fourier transformation, namely,

$$f^{BA}(\hat{\mathbf{k}}, \hat{\mathbf{k}}_0) = \int_D d\mathbf{r}' e^{-i\hat{\mathbf{k}} \cdot \mathbf{r}'} V(\mathbf{r}') e^{i\hat{\mathbf{k}}_0 \cdot \mathbf{r}'} . \quad (5)$$

One can recover $V(\mathbf{r})$ by performing inverse Fourier transformation on the measured data for $f^{BA}(\hat{\mathbf{k}}, \hat{\mathbf{k}}_0)$ and this procedure is formally equivalent to backpropagating the scattered field into the object domain from the measurement space. When the Born approximation is not valid, this Fourier relationship can still be exploited and this is the key to the nonlinear approach we implement. One can readily see that inverting the scattering amplitude data determines not $V(\mathbf{r})$ but rather the function $V_B(\mathbf{r}, \hat{\mathbf{k}}_0)$ ⁸ which is given by

$$V_B(\mathbf{r}, \hat{\mathbf{k}}_0) = V(\mathbf{r}) \frac{\Psi(\mathbf{r}, \hat{\mathbf{k}}_0)}{\Psi_0(\mathbf{r}, \hat{\mathbf{k}}_0)}. \quad (6)$$

The symbol $\hat{\mathbf{A}}$ in the above equation recognizes the fact that the reconstruction is approximate since Fourier transformation is only appropriate for $\hat{\mathbf{r}}_0 = \text{constant}$. As the total field can be expressed by

$$\Psi(\mathbf{r}, \hat{\mathbf{k}}_0) = \Psi_0(\mathbf{r}, \hat{\mathbf{k}}_0) - k^2 \int_D d\mathbf{r}' G_0(\mathbf{r}, \mathbf{r}') V(\mathbf{r}') \frac{\Psi(\mathbf{r}', \hat{\mathbf{k}}_0)}{\Psi_0(\mathbf{r}', \hat{\mathbf{k}}_0)} \Psi_0(\mathbf{r}', \hat{\mathbf{k}}_0), \quad (7)$$

for the case of a general scattering object, one can write the Fourier relation

$$f(\hat{\mathbf{k}}, \hat{\mathbf{k}}_0) = \int_D d\mathbf{r}' e^{-i\hat{\mathbf{k}} \cdot \mathbf{r}'} V(\mathbf{r}') \frac{\Psi(\mathbf{r}', \hat{\mathbf{k}}_0)}{\Psi_0(\mathbf{r}', \hat{\mathbf{k}}_0)} \quad (8)$$

Consequently, a first Born inversion of the scattered field data for $\hat{\mathbf{r}}_0 = \text{constant}$ provides a filtered version of $V(\mathbf{r}) \Psi(\mathbf{r}, \hat{\mathbf{k}}_0) / \Psi_0(\mathbf{r}, \hat{\mathbf{k}}_0)$. In most circumstances, the field $\Psi(\mathbf{r}, \hat{\mathbf{k}}_0)$ which is the field within the scattering volume D , cannot be assumed to be equal to the incident field. It is explicitly dependent on the direction of the incident plane wave which is known. Consequently, for each illumination direction used, one obtains an "image" of the function $V(\mathbf{r}) \Psi(\mathbf{r}, \hat{\mathbf{k}}_0)$. Given data from

many illumination directions, a set of these “images” can be generated, one for each illumination direction, and in which V is common to all of them but Ψ is different. The recovery of an image of V can therefore be formulated as a problem in which an ensemble of noisy images of V require processing, the “noise” being multiplicative in nature.

Cepstral filtering

For each different incident direction, the product $V(\mathbf{r})\Psi(\mathbf{r}, \mathbf{k}\hat{\mathbf{r}}_0)$ will change and a set of these single view reconstructions can be generated. We regard the term $\Psi(\mathbf{r}, \mathbf{k}\hat{\mathbf{r}}_0)$ as an unwanted factor or multiplicative noise term, which contains a certain range of spatial frequencies determined by the distribution of energy of the radiation field and its effective wavelength within the object. With respect to the spatial frequency content of the scattering object, this *multiplicative* factor can be removed by homomorphic filtering techniques⁹⁻¹⁶. Direct Fourier filtering is not appropriate for multiplied signals of this kind since their spectra are convolved.

For a weakly scattering object, the internal field approximately equals the incident field. Since illumination is assumed a plane wave, this field will have a characteristic spatial frequency in the direction of propagation. As the degree of scattering increases, the internal field will become increasingly complex, however, it will retain a characteristic correlation length (i.e. a minimum scale) determined by the wavelength of the radiation in the medium $V(\mathbf{r})$. As the permittivity increases, the effective wavelength of the radiation in the scattering volume decreases. The idea to be conveyed here is that there will likely be some characteristic set of spatial frequencies associated with the internal field $\Psi(\mathbf{r}, \mathbf{k}\hat{\mathbf{r}}_0)$ inside the scatterer. This information is evident following backpropagation, and can be removed by filtering in the cepstral domain. Since the spatial frequency content of $\Psi(\mathbf{r}, \mathbf{k}\hat{\mathbf{r}}_0)$ should be concentrated around some limited range of spatial frequencies, one can expect that the energy associated with these components is located in an annular region in the spatial frequency domain, determined by the mean effective wavelength of the radiation in D .

The cepstral filtering inversion approach is as follows. When the Born approximation is violated, one recovers the function given by equation (6). For each different incident direction, the product $V(\mathbf{r})\Psi(\mathbf{r}, \mathbf{k}\hat{\mathbf{r}}_0)$ will change and the set of these single view reconstructions is generated and stored. Taking the logarithm of $V(\mathbf{r})\Psi(\mathbf{r}, \mathbf{k}\hat{\mathbf{r}}_0)$ changes the multiplicative relationship between V and Ψ into an additive one. This then permits linear filtering techniques to be applied to the spectrum of $\log[V(\mathbf{r})\Psi(\mathbf{r}, \mathbf{k}\hat{\mathbf{r}}_0)]$ to remove, or at least minimize, the effect of Ψ . The spectrum of $\log[V(\mathbf{r})\Psi(\mathbf{r}, \mathbf{k}\hat{\mathbf{r}}_0)]$ is referred to as the cepstrum of $V(\mathbf{r})\Psi(\mathbf{r}, \mathbf{k}\hat{\mathbf{r}}_0)$. This operation will modify the spatial frequency content of

V over the same spectral region as that of the removed Ψ , but a second experiment at a different illumination wavelength should rectify this.

In practice there are difficulties associated with taking the logarithm of the product $V(\mathbf{r})\Psi(\mathbf{r}, \mathbf{k}\hat{\mathbf{r}}_0)$ because the phase of $\log[V(\mathbf{r})\Psi(\mathbf{r}, \mathbf{k}\hat{\mathbf{r}}_0)]$ can be highly discontinuous if the phase delay incurred on propagation through the object exceeds 2π radians. The first Born approximation assumes that this phase delay is much less than π . The phase function will therefore be wrapped into $[-\pi, \pi]$ and abrupt discontinuities in this phase function generate unwanted harmonics in the cepstrum, making it difficult to correctly filter. A solution to this problem that avoids phase wrapping difficulties, is to make use of the differential cepstrum.¹³ During the summer internship, and following discussions with Prof. Oppenheim at MIT, it was decided to focus on filtering $\log[1 + |V(\mathbf{r})\Psi(\mathbf{r}, \mathbf{k}\hat{\mathbf{r}}_0)|]$. This proved very successful despite the fact that only low pass filtering was employed. An example is given in figures 1 and 2 which show the 1996-97 mystery target data imaged using the Born approximation (figure 1) and then using a low-pass cepstral filter to minimize the presence of the internal field. As can be seen, reconstructions were obtained of a conducting wedge (data set ips009), a dielectric wedge (ips010), and conducting cylinder with a sector of the perimeter missing (ips011) and finally the same cylinder with the penetrable wedge (ips010) inserted into the cylinder, with its apex protruding from the cylinder (ips012).

This cepstral filtering approach deals directly with the nonlinear nature of the integral equation of scattering and does not rely on linearizing methods based on the Born, Rytov, or their associated distorted-wave approximations. However, being a nonlinear method, one has to separate the spatial frequency components of the internal field from those of the scattering object in the cepstral domain. This filtering step has not been optimized and will necessarily result in some loss of information about the target at those spatial frequencies that are filtered out. An important area of investigation to pursue is the design of an optimal cepstral filter, one that exploits the directivity of the internal field, evident in each backpropagated field arising from a given incident field direction.

The problem of limited data

With only a few exceptions, most previously developed imaging methods, based on inverting scattered field data, assume scattered field data are collected all around the target for each incident field direction. The methods we have developed have been designed to recover images of strongly scattering targets while remaining computationally efficient, i.e. Fourier based. In many radar applications, as well as medical imaging, remote sensing, and non-destructive testing requirements, only a limited amount of measured data are typically available for a limited range of incident field directions.

ips009

ips010

ips011

ips012

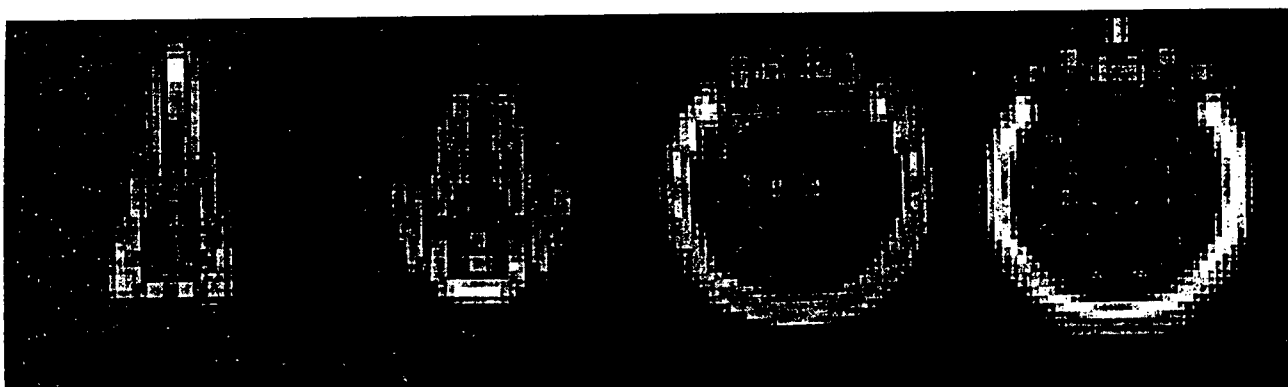


figure 1



figure 2

We have developed Fourier-based methods for image restoration, phase estimation and superresolution^{17,18,19}. These techniques can be directly applied to our methods for inversion of scattered field data, thereby compensating for limited and noisy measurements. We have considered these techniques for an imaging system designed to study millimeter wave technologies (also providing a scaled-down imaging method for longer wavelength (e.g. radar) -related problems). The data collection procedure which has been developed, makes measurements only in a small solid angle around the backscattering direction at a single wavelength. Given that the object is known to be located in a specific region of space and is precessed²⁰ relative to the transmitter and receiver positions, we determine the k-space coverage associated with these data. With these data defined, k-space data extrapolation and filtering is presented to recover the object permittivity profile. Further advances to this imaging system will employ wavelength diversity, bringing the capacity of 3-dimensional resolution and increasing the k-space data coverage. Though this is very limited data to obtain an image from, the measurement technique can provide stable estimates of the phase of the scattered field from the target. The imaging method works particularly well for single scattering or point targets within the object. The objective of this technique is to extract a maximum amount of radar information on complex conducting targets, just from backscattered signals. Common to these methods is a stationary radar and a target whose radar aspect is varied in some specified way. In this case, an arbitrary target axis intersects the radar beam axis making an angle θ with it. As the target axis precesses around the beam axis its motion is similar to a precessing top. Varying θ between 0 and values of the order of 10 degrees yields k-space data on a spherical cap with nearly constant polarization illumination and nearly aspect independent return levels from specular scatterers. These data are processed into 2D images. Larger values of θ introduce polarization and return level variability but yield information in the third dimension as well. The resulting k-space coverage is that of a truncated cone. Reconstruction of a target from such a limited k-space coverage can result in considerable distortion of the image. The available data comprise a truncated conical region in k-space of angular extent 2θ with co- and cross polarization information over the full angular range of 2π . The imaging apparatus operates 584GHz or in the sub-mm regime. It makes use of mechanical frequency shifting to achieve the high short term and long term phase stability required for coherent imaging²¹. Since the instrumentation radar range is short, transmit and local oscillator signals of the radar are derived from a single unstabilized signal source. One of the signals is mechanically Doppler shifted since heterodyning in the radar receiver virtually eliminates frequency and phase instabilities on both signals by the source. Both co- and cross polarized receive signals can be determined. More recently, a wideband (12 to 18 GHz) imaging system was constructed, implicitly using the target precessional motion. This wavelength diversity adds 3D resolution capability to a small angle system, effectively filling a truncated cone in k-space.

The imaging provided by this kind of approach, i.e. from precessional data, can be applied to many different remote sensing/non destructive evaluation applications, for which this data collection scheme is ideally suited. When applying inversion methods, there is frequently a prior estimate of the scattering target. We describe here a spectral estimation procedure that exploits prior knowledge about the scattering object. It takes a prior estimate, $P(r)$, of the broad features of $V(r)$, e.g., $V_I(r)$, and a set of equations of the form, expressed in 1D for convenience, is solved:¹⁸⁻¹⁹

$$f(m) = \sum_{n=-N}^N a_n p(m-n) ; \quad m = -N, \dots, N. \quad (9)$$

The values $p(m)$ ($m = -N, \dots, N$) are taken from the discretized Fourier transform of $P(r)$ and the backscattered field data, or more precisely here, the scattering amplitude data are represented by $f(m)$ ($m = -N, \dots, N$). Inversion of a matrix with elements derived from $p(m)$ allows one to solve for the coefficients a_n ($n = -N, \dots, N$). In principle, the data, $f(m)$, need not be uniformly sampled, which means that this approach can be used to interpolate and extrapolate both nonuniformly sampled and incomplete data sets. Obtaining the coefficients, a_n allows one to define an estimator that minimizes the approximation error given by:

$$\int_{-\pi}^{\pi} dr \frac{1}{P(r)} \left| V_I(r) - P(r) \sum_{n=-N}^N a_n e^{inr} \right|^2 \quad (10)$$

The resulting estimator of $V(r)$ is termed the PDFT estimator because of its form, namely, $\text{PDFT}(r) = P(r)A(r)$, where $A(r)$ is the trigonometric polynomial with coefficients, a_n , i.e. we have

$$\text{PDFT}(r) = P(r) \sum_{n=-N}^N a_n e^{inr}. \quad (11)$$

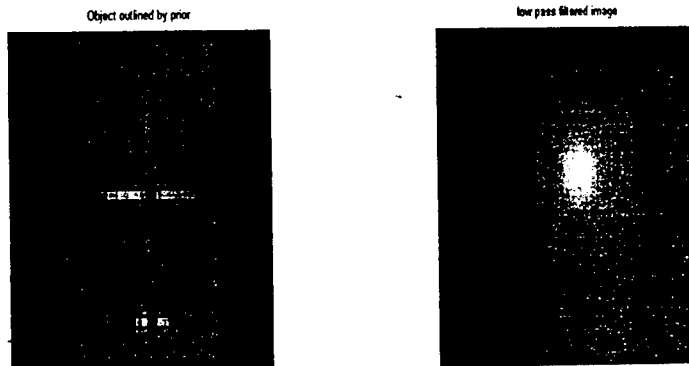
If no prior knowledge is available, $P(r)$ is a constant and the estimator reduces to the DFT of the available Fourier data. In other words, if the prior estimate, $P(r)$, is a constant for all r , then $a_n = f(n)$ and the PDFT reduces to the discrete Fourier transform (DFT) estimator, that is usually calculated. This PDFT

estimator is both continuous and data consistent, and the algorithm is easily extended to the two- or higher-dimensional case. An important and useful attribute of this estimator is that if the prior estimate is smaller than the actual target, the energy of the PDFT estimate becomes very large. This provides a convenient way in which one can "size" a target by dynamically varying the prior estimate of the target's shape while monitoring the energy of the associated PDFT estimate. This property is a consequence of the behavior of the eigenvalues of P which mimic p (including any internal structure one might know about the target and include in p). The PDFT coefficients, a_n are the projections of the eigenfunctions of P onto the target divided by the corresponding eigenvalue. When the prior is chosen to be smaller than the actual object, its eigenvalues become small where a projection component exists. This results in unstable and very large a_n coefficients.

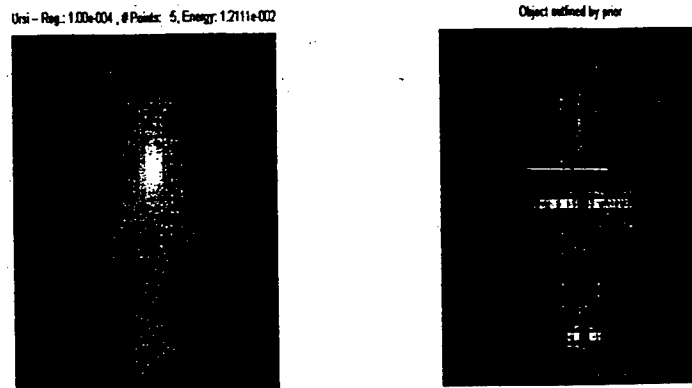
This estimation technique is easily regularized in the presence of noise. One can either modify the prior estimate, $P(r)$, to take a small value outside the anticipated support of the scatterer, $V(r)$, or one can add a small positive constant to the diagonal of the matrix, p . These can be shown to be equivalent to a Miller-Tikhonov regularization process¹⁸. This had proved to be a computationally intensive algorithm because it requires the solution of a large set of linear equations. For $2M$ by $2M$ uniformly sampled scattered field data, one must invert a $2M$ by $2M$ matrix if the prior estimate, $P(r)$, can be expressed as a separable function, otherwise a $(2M)^2$ by $(2M)^2$ matrix must be inverted. The algorithm had not been written until this summer to perform the PDFT with a non-separable prior. This was successfully done allowing us to work with arbitrarily shaped prior functions. Moreover, we were able to develop the algorithm in such a way that the prior function could be systematically "shaped" in order to contour the perimeter of a target shape thereby converging to an optimal prior estimate from what might initially have been only a poor guess.

We have applied the PDFT to data collected from a model of the missile, and this is shown on the left in figure 3 below. On retaining only a few of the k -space data (specifically 25 data points) the DFT estimate of the missile is shown in figure 3a below. From this DFT image, which corresponds to the Born approximation estimate, one cannot deduce anything useful about the target. Reconstructions of the missile target are shown in figure 3b below. The important point here is to recognize that with so few k -space data, one can still obtain an image, but that the reconstruction that results from progressively shrinking the prior estimate in all directions until the energy of the PDFT estimate starts to increase, provides a useful means for identifying the target from this shape function, even when the associated image is of poor quality due to the lack of data points.

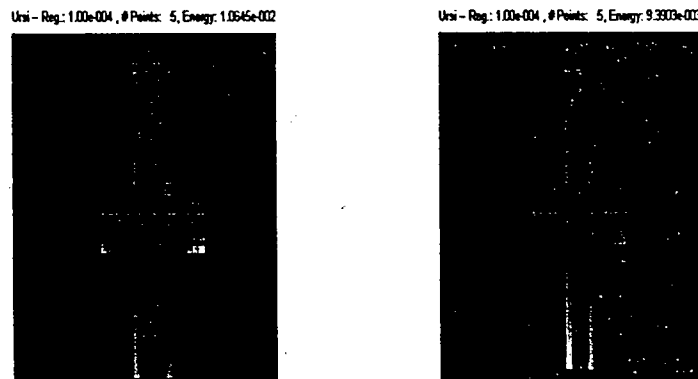
It should be noted that the energies calculated are a function of the regularization parameter chosen. For example, in the cases shown, the regularization parameter was applied by multiplying the diagonal



The image of the missile in figure a is that obtained using 128 by 128 k-space data points, the data being taken down to baseband to provide low-spatial frequency information in this projection or 2D projected view of the 3D missile. The image on the right above illustrates (figure b) the DFT estimate of this missile based on only the lowest 5 by 5 spatial frequency or k-space data present in the data used to generate the image on the left. As is evident, all of the features about the missile are lost due to severe low pass filtering.



Using the same 5 by 5 low pass data, figure c shows the improvement in the reconstruction of the image of the missile that is possible using the grey shaded rectangle in figure a as the prior estimate for the target shape, $p(\omega)$. The rectangular prior is then systematically shrunk until the energy of the associated PDFFT estimate no longer decreases, but increases. An example of an improved prior estimate is shown by the grey shaded region in figure d. The corresponding PDFFT estimate using this $p(\omega)$ is shown below in figure e.



There are now some recognizable features of the missile appearing, although with so few data there is little chance of obtaining a much better image than this. With more data points in k-space being used, the quality of the PDFFT estimate improves dramatically. However, in many cases where one wishes to identify the target rather than generate a high quality image, a more interesting question is how little data does one need to collect in order to make an unambiguous classification of a target. Figure f shows the result of further contracting the support function, $p(\omega)$ until no further width or height reduction is possible without an increase in the associated PDFFT estimate's energy. It should be noted that this minimization of the prior estimate $p(\omega)$ is very useful information about the target, since the actual high resolution image of the target must lie within the perimeter of this $p(\omega)$. However, it is debatable whether the image obtained in f is better than that in figure e. One has to choose between reconstructing a visually useful rendition of the target as compared to determining a minimal shape in which the image lies. For the purposes of target recognition, it is often sufficient to know as quickly as possible whether the measurements are indicative of target I, target II etc. It is possible to set up prior estimates $p(\omega)$ for each anticipated target and calculate the inverse of the associated P matrices ahead of time, making the PDFFT energy calculations very fast. The prior estimate with the minimum energy will correspond to the most likely target descriptor.

figure 3

elements of the P matrix by $1 + \nu$ where ν has the value 0.0001. The PDFT energies reduced from approximately 0.1 to 0.001 (arbitrary units) as p was contracted. As ϵ is reduced, the PDFT estimate deviates increasingly from the DFT estimate and more features with higher resolution are revealed. For each choice of ϵ there is a minimum shape function p . If it is allowed to get too small the coefficients become ill-conditioned and the PDFT estimate maintains a high energy. Fortunately, there is a large range of regularization parameter values one can choose and it is usually obvious whether that parameter is too small or too large.

Conclusions

In many imaging applications, it is either convenient or only possible to measure scattered field data in the backscatter direction. Whether the object is a weak or strong scatterer, inversion techniques exist which can be formulated in terms of a Fourier inversion of limited data in k-space. If data are collected for multiple illumination directions, surrounding the target, these data map into fairly uniform coverage of k-space and a reasonably artefact-free reconstruction of the target or of $V\Psi$ can be expected. If prior knowledge of the target is known, a procedure has been developed that extrapolates these data in k-space thereby improving the estimate of the target. It was shown however, that even in the absence of a prior estimate, one can use the PDFT estimation technique with a variable prior estimate in order to determine an optimal prior. This optimal prior is found by monitoring the energy of the PDFT estimate as the prior function is modified. This modification can be of the support of the target and/or of information about the target itself that lies within its boundaries. Examples were shown of how to use this method to infer information about the target when very little backscatter data were available (5 by 5 data points only), insufficient to be able to deduce anything from a simple DFT inversion of the same data. The point is further made that the PDFT estimate may not provide a particularly clear image if the number of data points and the detail of the prior estimate are limited. However, by varying the prior, its eventual optimal shape can provide a good indicator of the true target even if the corresponding image is unclear. Thus the use of the PDFT to generate a target signature or identifier was proposed for cases in which very low levels of data are measured.

In summary, new advances have been made in the recovery of strongly scattering targets from scattered field data measured assuming plane wave illumination incoming on the target from different directions^{22,23}. The approach is based on a nonlinear filtering technique (cepstral or homomorphic filtering) which is currently being applied using a simple low-pass filter in the cepstral domain (spectrum of logarithm of function). On going work is focusing on three further problems: i) refinement of the shape and selectivity of the cepstral filter, ii) recovery of target information (e.g. a signature) when only limited (and noisy) backscatter data are measured and iii) recovery of target information when only the intensity

of scattered fields can be measured. Progress was made in each of these areas during the summer of 1997 and reported on at the PIERS, IEEE AP/URSI and SPIE conference²⁴.

Acknowledgements

MAF acknowledges the partial support of ONR Grant N00014-89-J-1158 and Department of the Air Force contract F19628-95-C-0035 for some of the work presented here. MAF is especially grateful to AFOSR for the summer faculty position and to the many staff at Rome Laboratory who made his stay so productive.

References

1. F. C. Lin and M. A. Fiddy, "Image estimation from scattered field data," *Int. J. Imaging Systems and Technology*, 2, 76-95, 1990.
2. F. C. Lin, A. Alavi, R. McGahan, and M. A. Fiddy, "Diffraction tomography in the distorted-wave Born approximation," *Optical Society of America Annual Meeting, ThY29*, November 4-8, 1990, Boston, MA.
3. M. A. Fiddy, A. Alavi, F. C. Lin, and R. McGahan, "Inversion of 10GHz scattered field data using distorted-wave Born approximations," *Proc. SPIE*, Vol. 1351, 200-211, 1990.
4. N. Joachimowicz, Ch. Pichot and J.P. Hugonin, "Inverse scattering: an iterative numerical method for electromagnetic imaging", *IEEE Trans Ant. Propag.* Vol 29, Dec 1991, pp.
5. R.E. Kleinman and P.M. Van den Berg, "An extended range modified gradient technique for profile inversion", *Proc. 1992 URSI International Symposium on Electromagnetic Theory*, Sydney, Australia, August 1992.
6. G.P.Otto, W.Chew, "Microwave scattering - local shape function imaging for improved resolution of strong scatterers", *IEEE Trans. microwave Th. and Tech.*, Vol 42, Jan 1994, pp. .
7. E. Wolf, "Three-dimensional structure determination of semi-transparent objects from holographic data," *Optics Comm.*, 1, 153, 1969.
8. M. Slaney, A.C. Kak and L.E. Larsen, "Limitations of imaging with first-order diffraction tomography", *IEEE Trans Microwave Theory and Techniques MTT-32*, 860, 1984.
9. D. Raghuramireddy and R. Unbehauen, "The two-dimensional differential cepstrum", *IEEE Trans. Acoustics, Speech and signal Processing. ASSP-33*, 1335, 1985.
10. W. K. Pratt, *Digital Image Processing*, John Wiley & Sons, New York, 1978.
11. R. C. Gonzalez and P. Wintz, *Digital Image Processing*, Addison-Wesley Publishing Co., Reading, Massachusetts, 1977.

12. A. V. Oppenheim and R. W. Schaffer, Digital Signal Processing, Prentice Hall, Englewood Cliffs, New Jersey, 1975.
13. H. Rossmanith and R. Unbehauen, "Formulas for computation of 2-D logarithmic and 2-D differential cepstrum," Signal Processing, 16, 209-217, 1989.
14. J. B. Morris, R.V. McGahan, F.C. Lin and M. A. Fiddy, "Imaging of strongly scattering objects using cepstral filtering", Inverse Optics III, Ed. M. A. Fiddy, Proc. SPIE 2241, pp69-77, 1994.
15. J. B. Morris, and M. A. Fiddy, "Nonlinear filtering applied to single view backpropagated images of strongly scattering objects", Proc. O.S.A. Topical Meeting on Signal Recovery and Synthesis V, March 1995.
16. J. B. Morris, M. A. Fiddy and D. A. Pommet, "Nonlinear filtering applied to single-view backpropagated images of strong scatterers" J. O. S. A. A 13, pp1506-1515, 1996.
17. C.L. Byrne and M. A. Fiddy, "Estimation of Continuous Object Distribution from Limited Fourier Magnitude Data." Journal of the Optical Society of America, A4, pp. 112-117, 1987.
18. C. L. Byrne, R. L. Fitzgerald, M. A. Fiddy, T. J. Hall, and A. M. Darling, "Image restoration and resolution enhancement," J. Opt. Soc. Am. 73, 1481-1487, 1983.
19. C. L. Byrne and M. A. Fiddy, "Images as power spectra; reconstruction as a Wiener filter approximation," Inverse Problems, 4, 399-409, 1988.
20. U.H.W. Lammers, R. A. Marr, "Doppler imaging based on radar target precession", IEEE Trans AES, 29, pp166-173, 1993.
21. U.H.W. Lammers, R. A. Marr and J. B. Morris, "Narrowband heterodyne reception using unstabilized sources", Int. J. of Infrared and Millimeter Waves, 11, pp701-716, 1990.
22. J. B. Morris, R.V. McGahan, J. L. Schmitz, R.M. Wing, D.A. Pommet and M.A. Fiddy, "Imaging of strongly scattering targets from real data", IEEE AP Magazine, 39, pp22-26, 1997.
23. D.A. Pommet, Marr, R. A., Lammers, U.H.W., McGahan, R.V., Morris, J.B. and M. A. Fiddy, "Imaging using limited-angle backscattered data from real targets", IEEE AP Magazine, 39, pp 19 - 22, 1997.
24. M. A. Fiddy, R.V. McGahan and D. A. Pommet, "Minimal data collection: imaging from limited angle data using prior knowledge", in Proc. Solving ill-posed inverse imaging problems: medical and nonmedical applications; Ed R.L. Barbour, M. J. Carvlin and M. A. Fiddy, July 1997.

THE STUDY OF ELECTRICAL CHARACTERISTICS OF CdS PASSIVATION ON INP

Lili He
Associate Professor
Department of Electrical Engineering

Northern Illinois University
590 Garden Road
DeKalb, IL 60115

Final Report for:
Summer Research Program
Rome Laboratory

Sponsored by:
Air Force Office of Scientific Research
Bolling Air Force Base, Washington, DC

And

Rome Laboratory

September 1997

The Study of Electrical Characteristics of CdS Passivation on InP

Lili He
Associate Professor
Department of Electrical Engineering
Northern Illinois University

Abstract

InP surface passivation has been realized by a convenient chemical bath deposition (CBD) of a thin CdS layer. For comparison, samples without any treatment and with only a thin SiO₂ layer were also prepared. Also studied was the effect of a thin layer of SiO₂ deposited immediately after the CdS deposition. Schottky contacts were made on the CdS-passivated InP by electron-beam deposition of Ti/Au. Electrical characterization was conducted by current-voltage (I-V) and capacitance-voltage (C-V) measurements. Atomic force microscopy was used for surface morphology studies. It was found that the electrical performance of the Schottky contacts of the CdS-passivated samples was improved significantly. The thickness (deposition time) of the CdS strongly affects the device electrical performance. The additional SiO₂-on-CdS layer plays an important role in the process of InP surface passivation. Post-treatment in the CdS deposition process also significantly improves the surface morphology and electrical properties.

The Study of Electrical Characteristics of CdS Passivation on InP

Lili He

Introduction

In recent years, more and more semiconductor devices researchers have focused on opto-electronic devices[1]. The advent and use of optoelectronic devices has been primarily due to the development of advanced semiconductor materials technology and low-loss optical fibers. Optoelectronics, which combines the properties of light with the capabilities of microelectronics, is an essential enabling technology for the information age. It is known that optical fibers have their lowest loss at $1.55\mu\text{m}$. The lowest dispersion and optical amplification in fibers have been demonstrated at $1.3\mu\text{m}$ [1]. Since their bandgaps are compatible with the region of low loss and low dispersion in optical fibers, InP and related ternary (GaInAs, AlInAs), and quaternary (InGaAlAs, InGaAsP) semiconductor compounds are important in optoelectronic device applications at long wavelengths for optical fiber communications. A large amount of effort has been put into the study of the metal/InP interface due to its complex interface phenomena and poor electrical performance. Phosphorus vacancies at the InP surface and native oxides are always difficult to avoid. Therefore surface passivation of InP has been a continuing topic of research for device applications. The passivation of the InP surface by use of chemical bath deposition (CDB) of CdS has been proven successful in recent studies[2-6]. Various analysis techniques include XPS, Auger, PL, RHEED, TEM, and C-V

measurements, which have been used for surface and interface characterization. The CBD CdS passivation greatly reduces the density of interface states, as well as native oxides. The technique has been implemented in the fabrication of InAlAs/InGaAs high electron mobility transistors (HEMTs) and metal-semiconductor-metal (MSM) photodetectors, both of which showed significant improvement in device characteristics[6].

Experimental

Bulk n-type InP samples used in this work were from Sumitomo, with free carrier concentration of $\sim 4 \times 10^{15}/\text{cm}^3$. The samples were divided into several groups. In the first group, CdS with different thicknesses were directly deposited by standard CBD. The second group of samples were post-treated (which will be described later) after CdS deposition. An additional thin SiO₂ layer was deposited on the third group but with no post-treatment. In the fourth group, samples were post-treated after CdS deposition and then covered by an SiO₂ layer. For comparison, the samples without any additional treatment and SiO₂ only were also studied. The standard CBD deposition includes a pre-treatment in 0.033M thiourea [CS(NH₂)₂] and 12.8M NH₃ at 85°C for 15 minutes. Then, a 0.028M thiourea, 11M NH₃, and 0.014 M Cd(C₂H₃O₂)₂ solution was used at 85°C for 1, 3, 5, 7, and 9 minutes for CdS deposition at different thicknesses. The post-treatment used the identical solution and conditions as for the pre-treatment. For the SiO₂ deposition, a low-temperature (260°C), low-pressure (1.5Torr) technique was used. The thickness of the SiO₂ is about 50Å. Ohmic contacts were deposited on the back of the

samples by thermal evaporation of indium with thickness about 1000-2000Å. Rapid thermal annealing (RTA) by an HEATPULSE 210 at 250°C for 60s was immediately performed for ohmic contact formation.

Table 1. Sample List and Preparation Conditions*

Sample	CdS Deposition	SiO ₂	Post-treatment
A-1(805)	1 min.	no	no
A-2(806)	3 min.	no	no
A-3(807)	5 min.	no	no
A-4(808)	7 min.	no	no
A-5(809)	9 min.	no	no
A-6(810)	9 min.	no	yes
B-1(812)	0 min.	no	yes
B-2(814)	1 min.	no	yes
B-3(816)	3 min.	no	yes
B-4(818)	5 min.	no	yes
B-5(820)	7 min.	no	yes
C-1(813)	0 min.	yes	no
C-2(815)	1 min.	yes	no
C-3(817)	3 min.	yes	no
C-4(819)	5 min.	yes	no
C-5(821)	7 min.	yes	no
D-1(848)	none	no	no
D-2(849)	none	yes	no
D-3(850)	1 min.	yes	yes
D-4(851)	3 min.	yes	yes
D-5(852)	5 min.	yes	yes
D-6(853)	6 min.	yes	yes
E-1(871)	none	yes	no
E-2(872)	3 min.	yes	yes
E-3(873)	5 min.	yes	yes

* Pre-treatment was done on every sample except "none", including "0 min." CdS deposition samples.

Schottky metal Ti/Au was deposited by electron-beam evaporation through a shadow mask with a Ti layer of thickness $\sim 500\text{\AA}$ deposited first, followed a Au layer about $1500\text{-}2000\text{\AA}$. The I-V characteristics were measured with an HP4142A system. C-V measurements were conducted with an HP4275A multi-frequency LCR meter at 1 MHz. RTA anneals were carried out at 300°C , and 400°C , for 30s in nitrogen.

Results and Discussions

I. I-V Characteristics

Schottky contacts were initially made on all samples listed on Table 1. Current-voltage measurements were conducted immediately on each sample. All group-A samples showed very poor electrical properties. The I-V plots from the group-A samples are shown in Figure 1. A very high reverse leakage current appeared in this group of samples. The rectification characteristic was almost absent. Even after 300°C and 400°C annealing no obvious improvement was observed. Since group-A consists of samples with different CdS thicknesses (deposition times), it is obvious that the CdS layer alone could not generate the effect to enhance Schottky characteristics of InP. Sample A-6 was prepared the same as A-5, except a post-treatment was added after CdS deposition. It was observed with a microscope the sample surface was smoothed by the post-treatment, since after 9 min. CdS deposition, as seen in A-5, the sample surface was very rough. The post-treatment also improved I-V characteristics somewhat. Group-B are the samples with the same deposition conditions as group A, but with an additional post-treatment after the

CdS deposition. No obvious improvement was observed. For a sample with only pre- and post-treatment, B-1, the I-V performance was also very poor.

With SiO_2 deposition, group-C samples showed greatly enhanced I-V characteristics. Group-C samples corresponded to samples in group-B, except a thin SiO_2 layer was added after CdS deposition. The thickness of CdS itself, i.e., the CdS deposition time, now could be an important factor in device performance. Figure 2 shows the I-V characteristics of group-C samples, with CdS deposition time changed from 1 min. to 7 min. The best Schottky contact obtained in group-C was C-2 (1 min. CdS deposition), with barrier height, Φ_b , of 0.656eV, and ideality factor, n , of 1.35. Sample C-3 (3 min.) also showed very good performance with a Φ_b of 0.598eV and an ideality factor, n , of 1.52. With further increases in CdS thickness, the I-V performance deteriorated. It was noted, sample C-1, that pre-treatment (0 min. CdS) alone, showed very poor I-V results. Rapid thermal annealing at 300°C for 30s did not show any improvement; instead, it deteriorated the results slightly. A subsequent 400°C, 30s RTA showed significant improvement for sample group-C. For sample C-2, 400°C annealing resulted in a barrier height, Φ_b , of 0.845eV, and ideality factor, n , of 1.36; while for sample C-3, a Φ_b of 0.759eV, and n of 1.27 were obtained. For the rest of the samples in group-C, annealing did not show significant improvement in their poor performance.

In group-D, in addition to one bare InP reference sample (D-1) and one bare InP with SiO_2 (D-2) for comparison, an additional post-treatment was added to compare with group-C. The reference sample D-1 was dipped in a H_3PO_4 based solution to remove its

native oxide before load for Schottky deposition. As expected, the sample showed very poor I-V characteristics. The barrier height was about 0.48eV, and the ideality factor could not be extracted due to the poor I-V response. It was noted sample D-4 (3 min CdS deposition) showed very good I-V performance with a barrier height, Φ_b , of 0.716 eV, and ideality factor, n , of 1.62. This sample also showed further enhanced characteristics after a 300°C RTA. However, a annealing temperature of 400°C deteriorated the device performance. For comparison, sample D-2 (with SiO₂ only) had a barrier height of 0.725eV, however, the ideality factor $n > 2$ makes the calculation questionable. Annealing at 300°C and 400°C did not improve this sample. Figure 3 shows the I-V plots from group D samples.

Group-E samples were prepared to confirm some results from group-D. Therefore samples E-1 and D-1, E-2 and D-4, and E-3 and D-5, were prepared under the same conditions. All samples in group-E showed extremely low leakage current and, therefore, very high barrier height. However, the large (usually $n > 2$) ideality factor n again make the calculation questionable. Since the group-D samples were from a freshly opened package, while group-E samples were from the same package exposed to air for several days, the results from group-D may be more reliable. It was noted, sample E-2 showed the same response to annealing as D-4. The as-deposited sample E-2 had a barrier height of 0.879eV. After 300°C RTA, the barrier height increased to 0.883eV; it decreased after 400°C RTA to 0.774eV. This behavior was the same as observed in D-4. It was also observed all the samples became very non-uniform after 400°C RTA. Figure 4

shows I-V plots from sample E-2. Table 2 gives a partial list of I-V data for comparison study.

All I-V calculations mentioned above were based on the thermionic emission theory by which the current-voltage (I-V) characteristics of a Schottky diode can be described by[7]

$$J = J_0 \exp(qV/nkT) \quad \text{for } V > 3kT/q \quad (1)$$

where V is the voltage drop across the rectifying barrier, n the ideality factor, and J_0 is the reverse leakage current density given by

$$J_0 = A^* T^2 \exp(-q\Phi_b/kT) \quad (2)$$

where A^* is the effective Richardson constant, and Φ_b the barrier height. So the barrier height can be obtained by

$$\Phi_b = (kT/q) \ln(A^* T^2/J_0) \quad (3)$$

The ideality factor, n , is defined as

$$n = (q/kT) \partial V / \partial [\ln(J)] \quad (4)$$

According to the thermionic emission theory, which is most often used in metal-semiconductor contacts, the ideality factor should be close to unity. An ideality factor larger than unity may due to current mechanisms more than thermionic emission or other poor performance. In CdS-passivated InP, more complex mechanisms may be involved in the current transport since a heterojunction could exist between the metal and

semiconductor. CdS itself, as a wide-gap semiconductor, may result in another junction. Therefore, the ideality factor given above needs adjustment. The conduction mechanism needs to be modified from simple thermionic emission. More interpretation for the above experimental data will be given later.

Table 2. Partial list of I-V Results Summary

Sample	Annealing (°C)	Barrier Height Φ_b (eV)	Ideality Factor n	I_R at 1 V (A)
C-2	no	0.656	1.35	5×10^{-7}
C-2	300	0.556	>2	2×10^{-5}
C-2	400	0.845	1.36	5×10^{-9}
C-3	no	0.598	1.52	4×10^{-6}
C-3	300	0.514	>2	1×10^{-5}
C-3	400	0.759	1.27	3×10^{-8}
D-2	no	0.725	>2	2×10^{-7}
D-2	300	0.651	>2	6×10^{-6}
D-2	400	0.658	>2	4×10^{-6}
D-4	no	0.716	1.61	2×10^{-7}
D-4	300	0.768	1.73	3×10^{-8}
D-4	400	0.629	1.77	2×10^{-6}
E-1	no	0.810	1.67	4×10^{-8}
E-1	300	0.953	>2	2×10^{-10}
E-1	400	0.680	~2	6×10^{-8}
E-2	no	0.879	2.00	4×10^{-8}
E-2	300	0.883	~2	7×10^{-10}
E-2	400	0.774	~2	5×10^{-8}
E-3	no	0.740	~2	5×10^{-9}
E-3	300	0.924	>2	5×10^{-10}
E-3	400	0.774	~2	3×10^{-8}

II. C-V Characteristics

Capacitance-voltage (C-V) measurements were conducted on the Schottky contacts at 1MHz. Typical comparison was between the samples with and without CdS deposition. Figure 5 and Figure 6 show the C-V characteristics of sample E-1 (bare InP with SiO₂), and sample E-3 (CdS plus SiO₂). The annealing at 300°C effectively removed surface and interface mobile charges. Further annealing at 400 °C seems unnecessary, which agrees with the I-V results. A $1/C^2$ vs. V plot was used for sample uniformity and barrier height extraction as shown in Figure 7 [8]. It was found for the CdS passivated samples, E-2 and E-3, the plot showed very good linearity, which indicate the uniformity of the carrier concentration in the depletion region. The linear $1/C^2$ vs. V plot also extracts barrier height for the CdS-passivated samples which corresponds to the I-V calculation well. For the sample with SiO₂ only, the $1/C^2$ vs. V plot shows irregular curve, which may indicate certain surface interactions. Further study for C-V tests at different temperatures, the C-V-T study, may yield more information.

Atomic force microscopy (AFM) is being performed for samples with different treatments and processing. By the time of this report, only part of the AFM results was obtained. For samples without post-treatment after CdS deposition, the surface showed very rough morphology. Post-treatment could effectively eliminate such roughness. This is consistent with the aforementioned I-V results. More detailed AFM results will be used to explore the effect of annealing on surface morphology and microstructure.

Conclusion

Electrical characteristics of CdS passivated InP were studied by current-voltage (I-V) measurements on Schottky contacts of Au/Ti-InP. Capacitance-voltage (C-V) measurements were also carried out at high frequency (1MHz) on some samples. It was found that the CdS effectively enhanced electrical performance of metal/InP Schottky contacts. The most appropriate CdS deposition time range from 1 to 5 minutes. Post-treatment after CdS deposition improved sample surface morphology and the electrical properties. A thin SiO₂ layer on the CdS is essential for optimum device performance. Post-annealing is necessary for CdS-passivated devices; 300°C RTA is appropriate for most cases, 400°C could deteriorate device performance. The sample with only SiO₂ for passivation also showed very low reverse leakage current and high barrier height. However the large ideality factor (>2) is not satisfactory for a high performance device. C-V characteristics showed that there is a high density of surface state charges in samples before post-annealing. Post-annealing effectively removes these charges.

Acknowledgment

The author would like to thanks AFOSR and Rome Laboratory for providing her with this wonderful opportunity, her focal point, J. P. Lorenzo, for his guidance, and laboratory arrangement. The author also wishes to express her appreciation to her laboratory co-workers, H. Dauplaise, A. Davis, E. Martin, S. Spaziani, K. Vaccaro, and W. Waters for all of their help.

References

1. P. Bhattacharya, Semiconductor Optoelectronic Devices, 2nd edition, Printice Hall, 1997
2. K. Vaccaro, H. M. Dauplaise, A. Davis, S. M. Spaziani, and J. P. Lorenzo, Appl. Phys. Lett., 67, 527 (1995)
3. H. Dauplaise, K. Vaccaro, A. Davis, G. O. Ramseyer, S. M. Spaziani, J. V. Beasock, E. A. Martin, and J. P. Lorenzo, SPIE Proc. Vol. 2481, Orlando, FL (1995)
4. A. Davis, H. M. Dauplaise, K. Vaccaro, J. P. Lorenzo, MRS Symposium Proceedings, Vol. 421, Compound Semiconductor Electronics and Photonics, pp. 99-104 (1996)
5. H. Dauplaise, K. Vaccaro, A. Davis, G.O.Ramseyer, J. P. Lorenzo, J. Appl. Phys., 80, 2873 (1996)
6. K. Vaccaro, A. Davis, H. M. Dauplaise, S. M. Spaziani, E. A. Martin, and, J. P. Lorenzo, J. Electron. Mater., 25, 603 (1996)
7. S. M. Sze, Physics of Semiconductor Devices, 2nd edition, John Wiley and Sons, 1981
8. D. K. Schroder, Semiconductor Material and Device Characterization, John Wiley and Sons, 1990

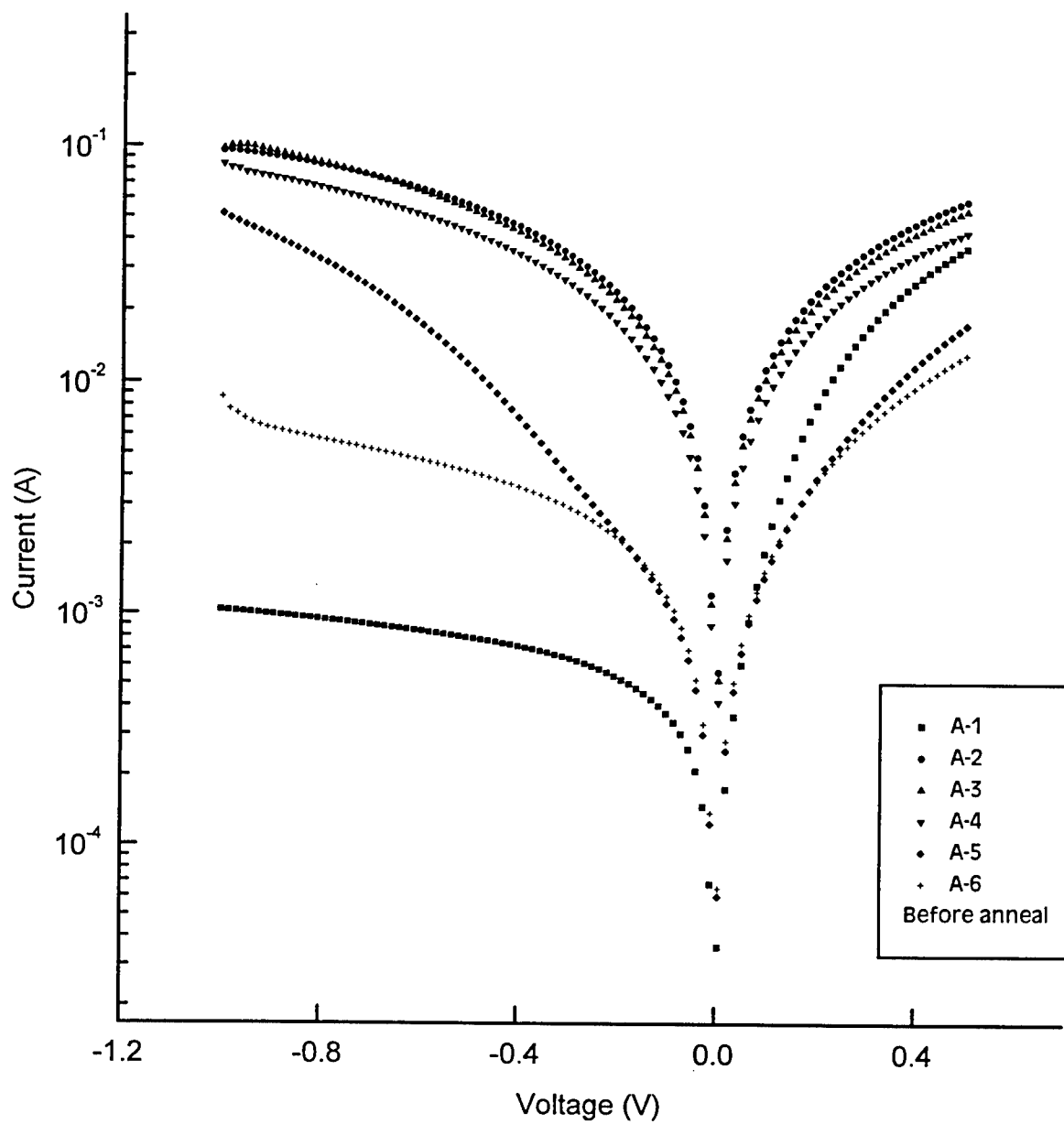


Figure 1. The I-V characteristics of group-A samples.

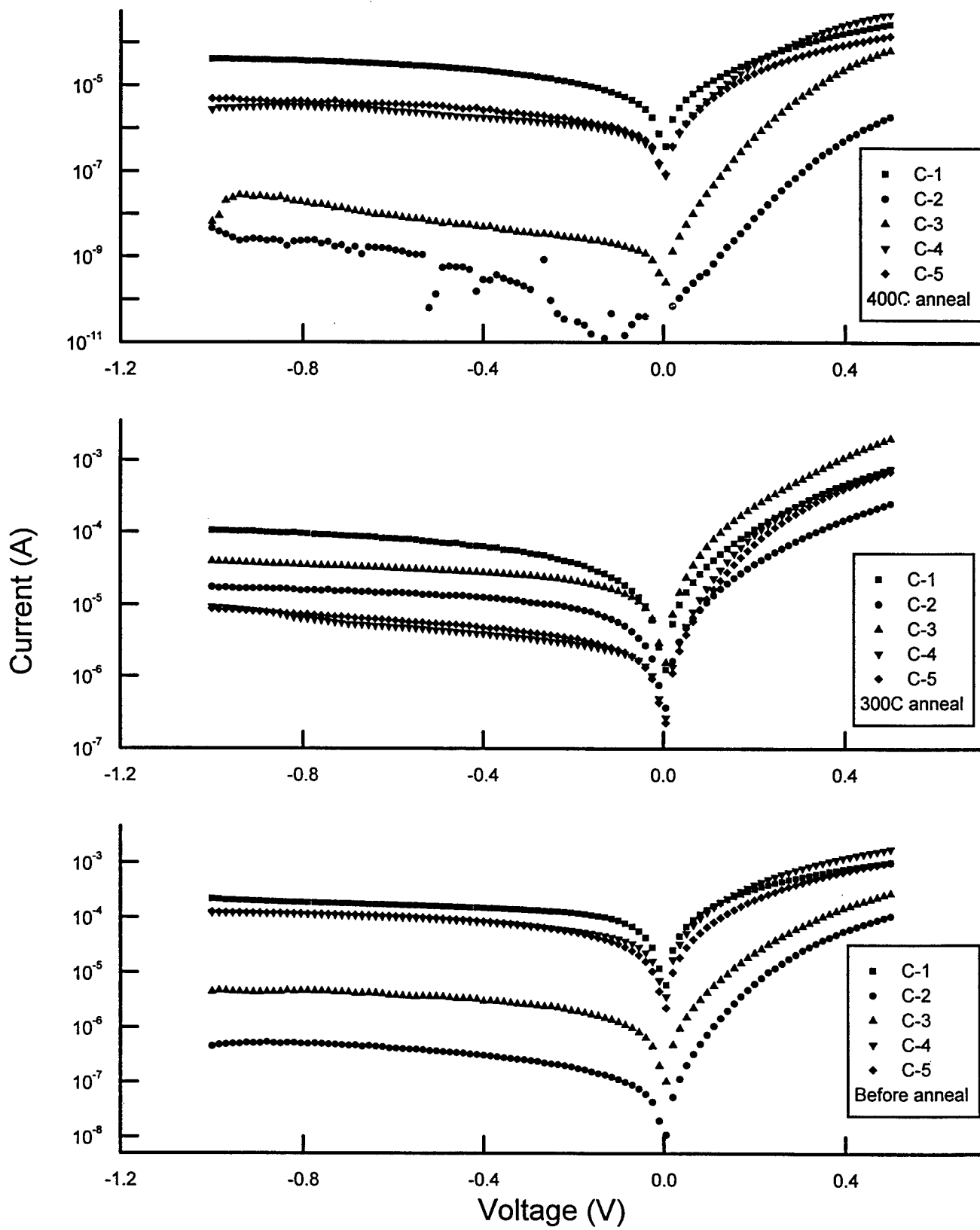


Figure 2. The I-V characteristics of group-C samples.

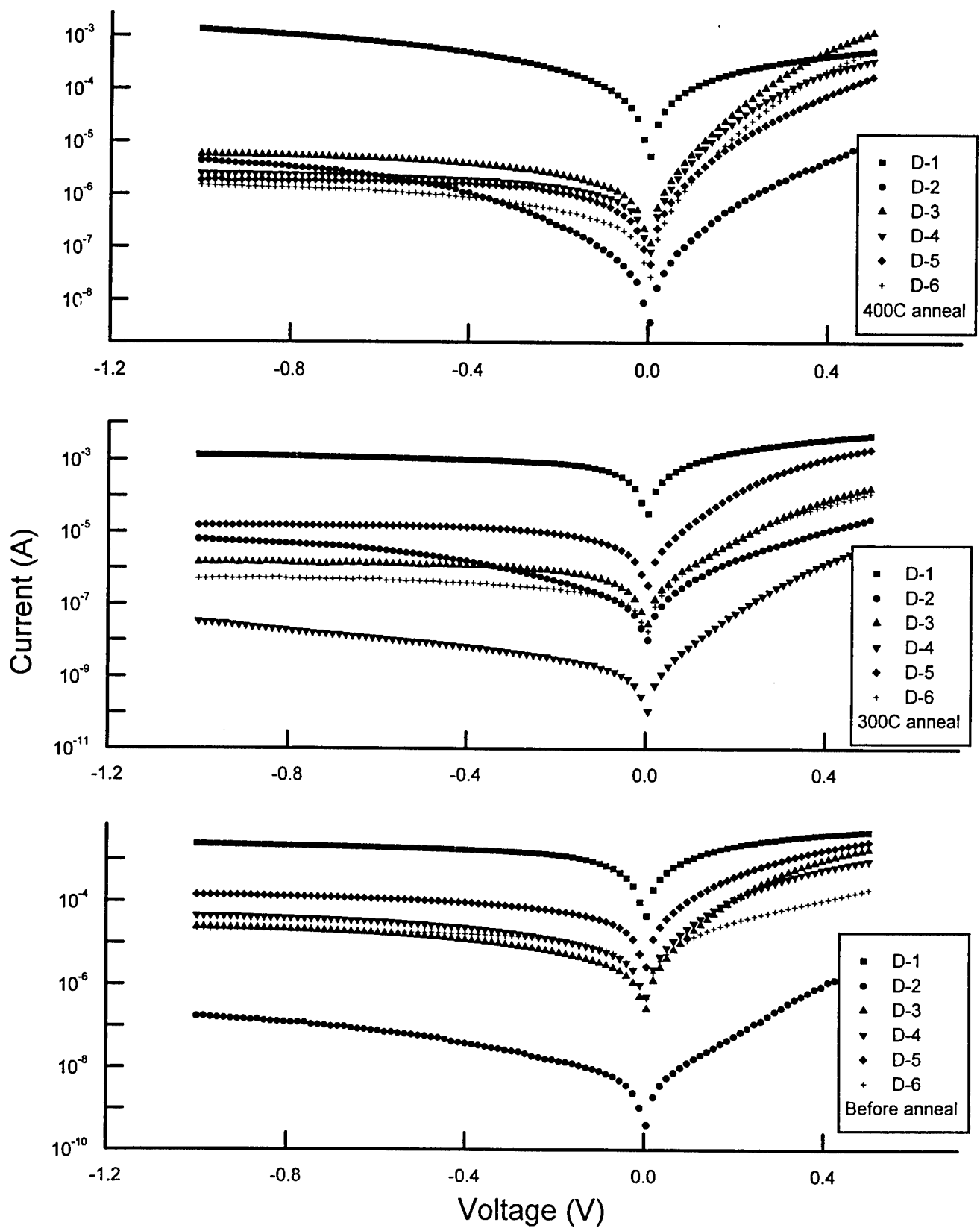


Figure 3. The I-V characteristics of group-D samples.

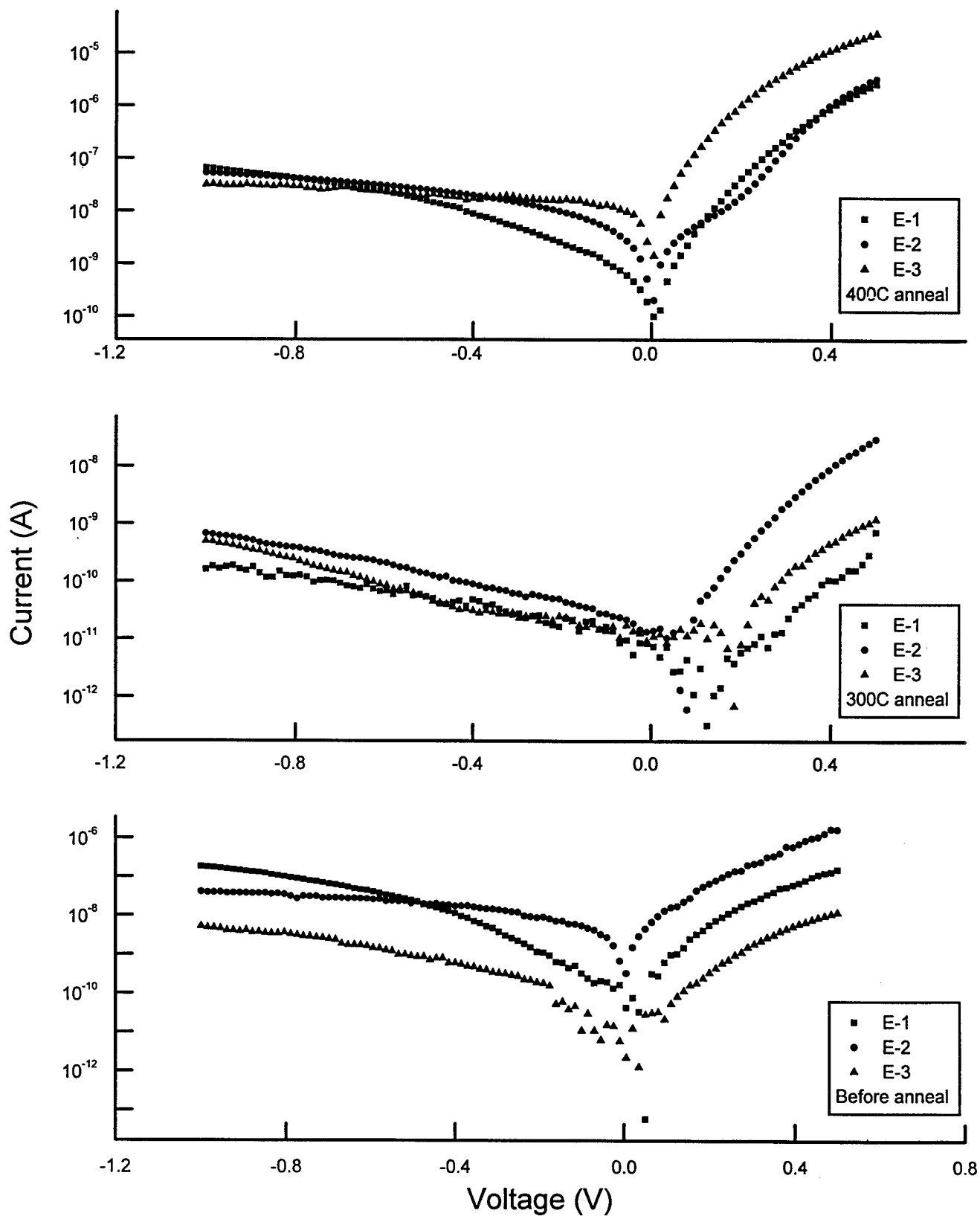


Figure 4. The I-V characteristics of group-E samples.

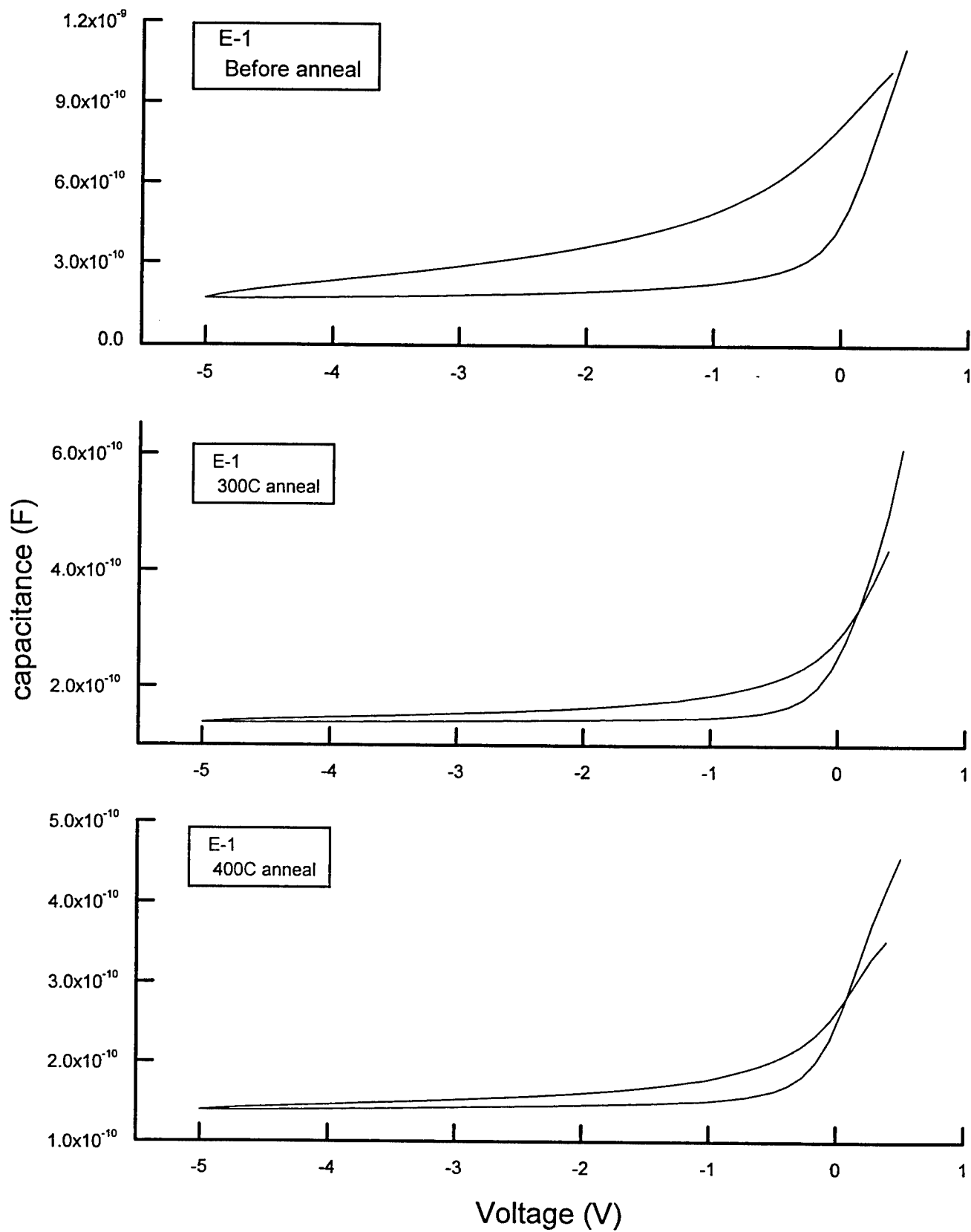


Figure 5. The C-V characteristics of sample E-1.

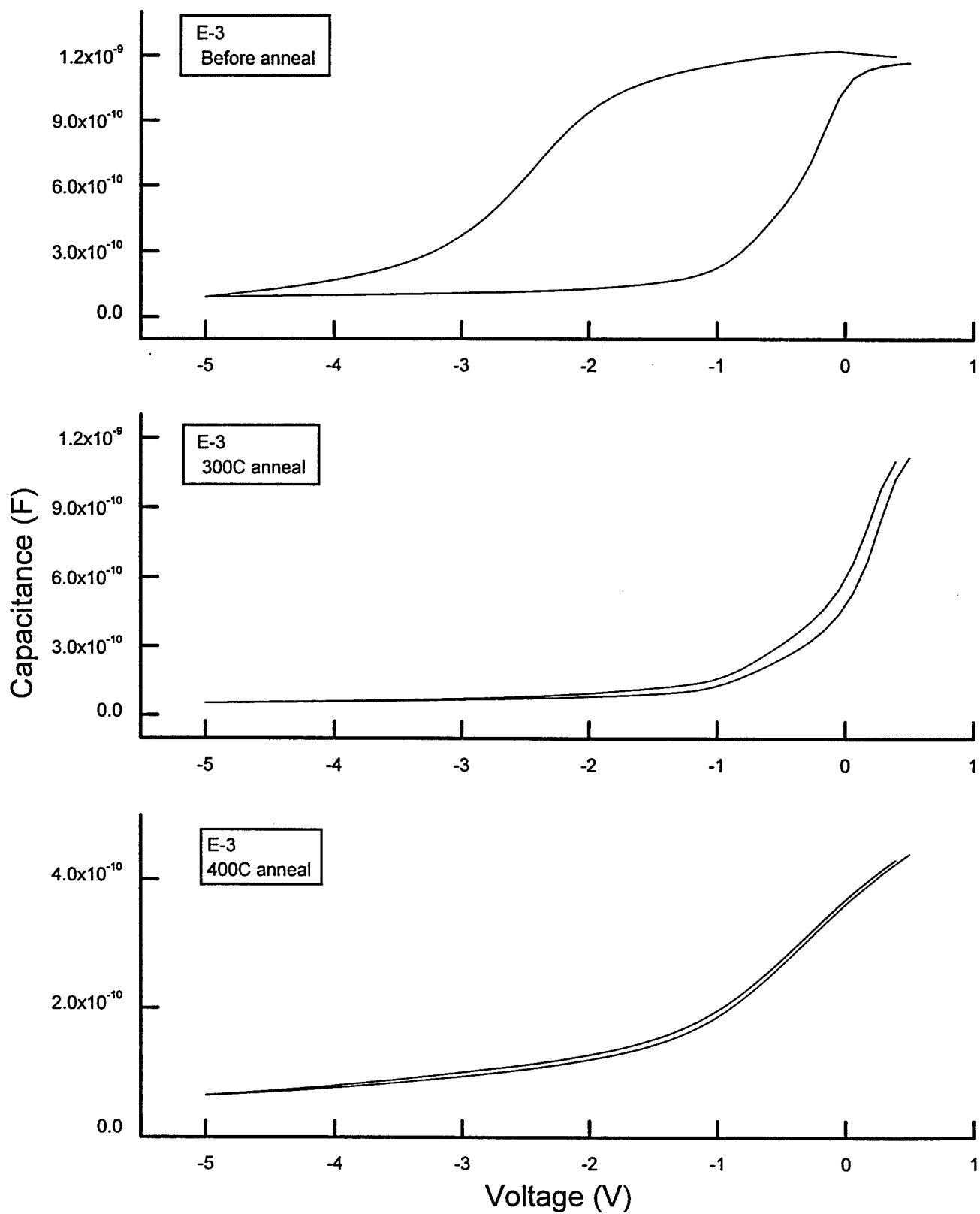


Figure 6. The C-V characteristics of sample E-3.

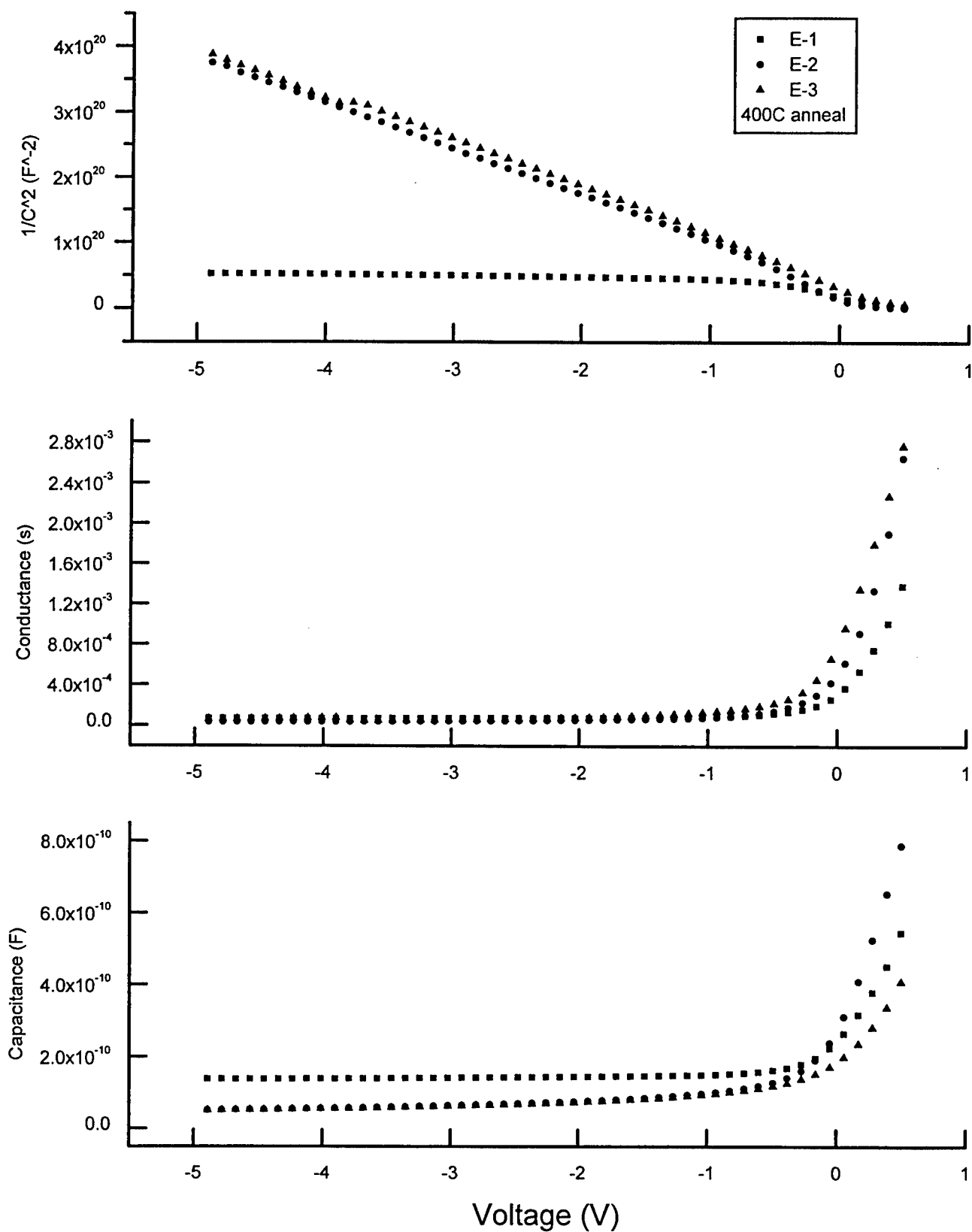


Figure 7. The C-V characteristics of group-E samples.

EFFECTS OF SURFACE SCATTERING IN 3-D OPTICAL MASS STORAGE

Edem Ibragimov
Associate Professor
Department of Mathematical Sciences

Michigan Technological University
Houghton, MI

Final Report for:
Summer Research Program
Rome Laboratory

Sponsored by:
Air Force Office of Scientific Research
Bolling Air Force Base, Washington, DC

And

Rome Laboratory

August 1997

Effects of Surface Scattering in 3-D Optical Mass Storage

Edem Ibragimov

Department of Mathematical Sciences, Michigan Technological University,
Houghton, Michigan, U.S.A. 49931-1295. edibragi@mtu.edu

August 28, 1997

Abstract

In this work a problem of surface scattering of the light during 3-D optical recording is investigated on the basis of analytical solutions obtained using spectral approach. Results of analysis show that such effects become considerable if the averaged peak-to-peak surface error becomes greater than the half of the wavelength of the recording light. Both bit and binary image types of storage are considered.

Edem Ibragimov

1 Introduction

Computer 3-D memories is a new and inevitable step in the development of high capacity and fast data transfer storage systems for the computing demands. Despite of ultra high storage densities of the current state of art two-dimensional optical memories, a long-term expansion projects for these systems are limited since they recorded data on only one or two planes and read/write operations are serial in nature. It is clear that introduction of one more dimension will allow to increase the capacity of data storage devices by a factor of $10^3 - 10^4$ without increasing a volume of the recording medium. One of the most promising technologies is 3-D optical memories based on two-photon absorption. In the last five years a feasibility of two-photon optical memories was demonstrated on the examples of devices utilizing both cube and disk shapes of the recording media [1, 2]. However, the data capacity of such systems is still far below the theoretical limits. One of the reasons limiting 3-D data density is a scattering of the information and recording beams on the surface of the recording medium. Recent investigation [3] has revealed that even smallest surface inhomogeneities can lead to considerable reading and writing errors. Attempts to reduce the amount of errors by manual polishing did not improve the quality of the images. The analysis of the problem of scattering provided in [3] is based on a numerical calculations and does not provide a general picture of the process. The primary goal of the present research is to provide a comprehensive picture of the process and to answer major questions associated with the problem of surface scattering: 1. When the effects of surface scattering are important? 2. Which spatial frequencies are most important? and 3. What needs to be done to completely eliminate surface scattering? The answer to these questions is obtained on the basis of analytical theory, which allows to predict the behavior of the reading/recording system for the wide range of the parameters.

2 Basic Equations

The current Read Only Memory (ROM) architecture uses picosecond pulses of the first and second harmonics of neodymium laser. A schematic of the optical system is shown in Fig 1. Digital information recorded in the two-photon material as pages of digital data, the data pages separated in the axial direction. (Here only a cubic shape of the recording material will be considered. However with little changes all the results can be used for geometries with any shape of a recording material). As can be seen from the picture, the surface of the recording material can be thought as an object placed between the focusing lens and the focal plane. Such a problem is well-known in optics and has an analytical solution [4, 5]. To solve the propagation

problem one has to propagate the beam from the focusing lens to the front face of the cube, account for the surface inhomogeneities, and then propagate the beam to the focal point or to the image plane depending whether bit, vector or binary image geometry is considered.

The amplitude distribution of the light after the focusing lens can be described by the following formula:

$$U(x, y) = A_0 P\left(\frac{x}{L}, \frac{y}{L}\right) \exp\left[-i \frac{k}{2f} (x^2 + y^2)\right] \quad (1)$$

where f is a focal distance of the lens, A_0 is the amplitude of the electric field, k is the wave number, L is the aperture of the beam, x and y are the coordinates in the lens plane, and $P(x, y)$ is the pupil function:

$$P(x, y) = \begin{cases} 1 & \text{if } x, y \leq \frac{1}{2} \\ 0 & \text{if } x, y > \frac{1}{2} \end{cases} \quad (2)$$

If the numerical aperture of the lens is high ($N = f/a \gg 1$) and the image is not located close to the edge of the recording material, the light distribution immediately after passing the front face of the recording material can be written as:

$$U(x_s, y_s) = \frac{A_0 f}{d} P\left(\frac{x_s f}{L d}, \frac{y_s f}{L d}\right) \exp\left[-i \frac{k}{2d} (x_s^2 + y_s^2)\right] t(x_s, y_s) \quad (3)$$

where x_s and y_s are the spatial coordinates in the plane parallel to the surface of the cube, and $t(x, y)$ is the surface transmittance function and d is the distance from the surface of the cube to the focal plane.

The last step is to propagate the light from the surface of the cube to the focal point of the lens. For this the Fresnel approximation can be used. Using (3) as an initial function in the Fresnel integral after cancellation of quadratic phase factors yields:

$$U_f(x_f, y_f) = \frac{A_0 f}{i \lambda d^2} \iint_{-\infty}^{\infty} P\left(\frac{x f}{L d}, \frac{y f}{L d}\right) t(x, y) \exp\left\{-i \frac{2\pi n}{\lambda d} (x_f x + y_f y)\right\} dx dy \quad (4)$$

where x_f and y_f are the coordinates in the focal plane, λ is the wavelength and n is the refractive index of the recording material.

The equation 4 shows that the field distribution U_f is proportional to the two-dimensional Fourier transform of the surface transmittance function multiplied by the pupil function $t(x, y)$.

Further it will be supposed that light experience no reflection on the surface of the recording material. Therefore the surface scattering affects only a phase distribution of the beam. Therefore the surface transmittance function can be written in the form:

$$t(x, y) = \exp\{i\gamma(x, y)\} \quad (5)$$

For the sake of simplicity below only a one-dimensional case will be considered: it will be supposed that the function $t(x, y)$ does not depend on the y coordinate. (The extension on the case of two variables is straightforward.) In general $\phi(x, y)$ is a pure real random function determined by the surface qualities. Let the function $h(x, y)$ be a function describing the surface of the recording material and the $c(\alpha)$ represent a spatial spectrum of the function $h(x, y)$. Keeping only one coordinate we obtain:

$$h(x_s) = \frac{1}{\sqrt{N}} \sum_{k=1}^N c_n \sin[2\pi(f_n x_s - \phi_n)] d\alpha \quad (6)$$

where ϕ_n is the random number between 0 and 2π . For the further analysis it is convenient first to consider the effects of scattering on one single frequency. The results of such an analysis then will be generalized to the case with an arbitrary spectral distribution.

3 Spectral approach

Let us consider the case when the spectrum c_n has only one spatial frequency: $c_n \neq 0$ only if $n = 0$ and $c = 0$ for all $n \neq 0$. Then the instead of the integral 6 we have a simple sinusoidal function:

$$h(x) = \frac{\Delta z}{2} \sin[2\pi(f_0 x + \phi_0)] \quad (7)$$

where ϕ is a random number. In this case the surface can be thought as a sinusoidal phase grating with the spatial frequency f_0 and amplitude $\Delta z/2$ where Δz represents the peak-to-peak modulation of the surface. Schematically the surface profile is depicted in Fig 2 where the vertical axis corresponds to the direction of the beam propagation z . The light which passes through the hills will be delayed with respect to the light passed through the valleys. Therefore after the passing through the surface boundary the light will have a phase modulation. For the light with the wave number k and the medium with the refractive index n such a phase modulation is given by the function:

$$\gamma(x) = \pi \frac{\Delta z}{\lambda} (n-1) \sin[2\pi(f_0 x + \phi_0)] \quad (8)$$

and the transmittance function can be written as:

$$t(x) = \exp \left\{ i \frac{\pi \Delta z}{\lambda} (n-1) \sin[2\pi(f_0 x + \phi_0)] \right\} \quad (9)$$

For most optical materials $n \approx 1.5$, therefore further we will assume that $n-1 = 0.5$. As it follows from the expression (4) the light distribution in the focal plane is proportional to the Fourier transform of the surface transmittance function $t(x)$ multiplied by the pupil function $P(xf/d)$. To find this Fourier transform let us represent the function $t(x)$ as a superposition of the exponential functions using the following relationship [4]:

$$\exp \left\{ i \frac{\pi \Delta z}{2\lambda} \sin[2\pi(f_0 x - \phi_0)] \right\} = \sum_{q=-\infty}^{\infty} J_q \left(\frac{\pi \Delta z}{2\lambda} \right) \exp[i2\pi(qf_0 x + \phi_0)] \quad (10)$$

where $J_p(x)$ is a Bessel function of the order q . Considering that the Fourier transform of the product of two functions is equal to the convolution of these functions, we can find the expression for the light distribution in the focal plane:

$$\begin{aligned} U_f(x_f, y_f) &= \frac{A_0 f}{i \lambda d^2} \left[\sum_{q=-\infty}^{\infty} J_q \left(\frac{\pi \Delta z}{2\lambda} \right) \delta \left(\frac{nx_f}{d\lambda} - qf_0, \frac{ny_f}{d\lambda} \right) e^{i2\pi q \phi_0} \right] * \\ &\quad \left[\left(\frac{Ld}{f} \right)^2 \text{sinc} \left(L \frac{nx_f}{f\lambda} \right) \text{sinc} \left(L \frac{ny_f}{f\lambda} \right) \right] = \\ &= \frac{A_0 L^2}{i \lambda f} \sum_{q=-\infty}^{\infty} J_q \left(\frac{\pi \Delta z}{2\lambda} \right) e^{i2\pi q \phi_0} \text{sinc} \left[\frac{nL}{f\lambda} \left(x_f - \frac{qf_0 \lambda d}{n} \right) \right] \text{sinc} \left(\frac{nL}{f\lambda} y_f \right) \end{aligned} \quad (11)$$

The sign '*' here denotes a convolution and $\text{sinc}(x)$ is a commonly used in Fourier analysis function determined as $\sin(x)/x$.

The expression (11) gives the diffraction pattern in the focal plane when the surface of the recording material is described by a simple sinusoidal function (7). Below effects of a surface scattering are analyzed on the bases of the expression (11).

4 Discussion of the results

The expression (11) is a sum of an infinite number of sinc functions with the coefficients $J_p(\pi \Delta z / 2\lambda)$. However if Δz is not very large only a few terms in this series

have appreciable amplitudes. If the surface is absolutely flat and orthogonal to the direction of the beam propagation than $\Delta z = 0$. For the absolutely flat surface only one of the coefficients is not equal to zero: $J_0(0) = 1$. In this case the expression (11) reduces to:

$$U_f(x_f, y_f) = \frac{A_0 L^2}{i \lambda f} \text{sinc} \left(\frac{L n}{f \lambda} x_f \right) \text{sinc} \left(\frac{L n}{f \lambda} y_f \right) \quad (12)$$

which is a Fraunhofer diffraction pattern describing a focal distribution which the beam would have in an absence of the recording material. When $\Delta z/2$ is increasing the picture changes. The sinusoidal phase variation across the surface of the recording material deflects some of the energy out of the central diffractive pattern into additional side-patterns. The central diffraction pattern (called zero-order component) remains the same radius, but its amplitude is reducing. High-order components of the pattern will have exactly the same radii as the central lobe but will be displaced from the center of the diffraction pattern on the distance $q f_0 \lambda d / n$. Figure 3 shows a cross section of the intensity pattern when the peak-to-peak surface excursion Δz is equal to zero (solid curve), half wavelength (dot-dashed curve) and to one wavelength (dotted curve). As can be seen from the pictures, the diffraction pattern has substantial sidelobes of the first order when $\Delta z = \lambda/2$, and when $\Delta z = \lambda$ first-order component becomes even larger than the central lobe. Therefore for such a situation effects of surface scattering will be very large.

The expression (11) provides an easy estimation of the influence of the surface scattering on the focusing process. The dependence of the amplitude of q -th component on the spatial peak-to-peak modulation Δz is given in Fig 4. The amplitude of each component is determined by the Bessel function of an order q with the argument $\pi \Delta z / 2 \lambda$. Fig 4 shows the amplitudes of the zero, first and second orders. For simple estimations we need to know only amplitudes of the components of zero and the first order. Let us assume that the effects of the surface scattering become considerably large when the component of the first order becomes half as large as the zero order component. For this Δz has to satisfy the following equation:

$$J_1(\pi \Delta z / 2 \lambda) = \frac{1}{2} J_0(\pi \Delta z / 2 \lambda) \quad (13)$$

which yields:

$$\frac{\Delta z}{\lambda} \approx \frac{1.8}{\pi} \approx \frac{1}{2} \quad (14)$$

Therefore, when the the peak-to-peak surface modulation is greater than $\lambda/2$ the effects of the surface scattering should be considerable. Surface scattering becomes

more pronounced for the beams with smaller wavelengths. Therefore for the beam with $\lambda = 0.53 \mu k$ the scattering will be twice as large as for the beam with $\lambda = 1.06 \mu k$. Expression 14 shows that one can expect considerable deviations from the ideal diffraction pattern if $\lambda = 0.53 \mu k$ and $\Delta z \geq 0.25 \mu k$. This exactly matches the expected roughness of the surfaces produced using injection techniques.

As it follows from (11) the first-order component in the diffraction pattern will be spaced $f_0 \lambda d / n$ cm away from the central lobe. This means that spatial frequencies higher than $f_{max} = nL / \lambda d$ are not important for the consideration. Such frequencies will have their first order components outside the cube. For $n = 1.5$, $\lambda = 1 \mu k$, and $l = d$ we obtain $f_{max} = 1.5 \cdot 10^4$. Let us denote the width of the central component as $\Delta x = 2f\lambda / nL$. Then the first-order component will be spaced from the center on the distance $Ldf_0 / 2f$ times the width of the central lobe Δx . Thus, the position of the first maximum measured in the numbers of the width of the central lobe depend only on the spatial frequency f_0 and the aperture of the beam on the front face of the cube $a = Ld/f$. (At the same time this distance does not depend on the wavelength of the beam). If $f_0 > 2/a$ the corresponding spatial frequency will not affect the shape of the central lobe. Therefore most important for the consideration are the low frequency components of the spatial spectrum with the frequencies $f_0 < 2/a$ when the period of the spatial modulation is less than 2 times greater than the size of the beam. Such low frequencies can substantially alter the focal pattern. Fig 5 shows focal distribution of the focused beam in the case when $\Delta z = 0.6 \lambda$ and $f_0 = 1$ (three broken curves). The phase ϕ_0 for each case was chosen randomly. The solid curve in this picture shows the ideal situation with no surface inhomogeneities. Similar results were obtained in [3] on the basis of numerical simulations of the process. However the fact that such patterns are produced by the extremely low frequency components was not noticed. High sensitivity of the focal picture to the low spatial frequencies explains a lack of success to eliminate surface scattering by a manual polishing of the surfaces: the high frequency components can be removed by manual polishing, but the errors associated with the low frequencies remained.

For the extremely low frequencies ($f_0 \ll 1$) the function $h(x)$ describing the surface roughness becomes a straight line. Therefore the equation (11) in the case $f_0 \ll 1$ corresponds to the situation when the axis of the beam is slightly deviated from the proper direction and does not make a right angle with the surface of the recording cube. Consideration of this case provides a good verification for the used method. From simple geometrical consideration it is obvious that the amplitude distribution in the focal plane should not change when the beam is slightly tilted with respect to the proper direction, but the entire picture will be shifted from the center. Fig 6 shows the results of calculations of (11) for the case with a tilt ($f_0 \ll 1$). As can be seen, the theory gives expected results: each curve in Fig 6 is a *sinc* function

shifted from the central position on the distance proportional to the tilt of the beam toward the surface. These calculations show very strong dependence of the position of the image on the error in the beam's direction.

A consideration of the surface scattering for a single frequency allows better understanding of the process. However, a real surface does not usually have a simple sinusoidal shape, but can only be represented as a superposition of a large (or infinite) number of spatial frequencies (6). Further we shall show that the main conclusions for a single frequency analysis can be extended to the multi-frequency case.

To obtain an expression for a randomly varied surface we make all the amplitudes c_k in (6) to be equal: $c_k = \Delta z/2 = c$. In this case amplitudes of all spatial frequencies are equal and the expression 6 represents so-called *white noise* - a completely random surface. The phase transmittance function will look like:

$$\exp\{it(x)\} = \exp \left\{ i \sum_{k=1}^N \frac{\pi \Delta z}{2\lambda \sqrt{N}} \sin(2\pi f_k x + \phi_k) \right\} = \prod_{k=1}^N \exp \left\{ i \frac{\pi \Delta z}{2\lambda \sqrt{N}} \sin(2\pi f_k x + \phi_k) \right\} \quad (15)$$

Using 10 we obtain:

$$\exp\{it(x)\} = \prod_{k=1}^N \sum_{q=-\infty}^{\infty} J_q \left(\frac{\pi \Delta z}{2\lambda \sqrt{N}} \right) \exp(i2\pi q f_k x + iq\phi_k) \quad (16)$$

When Δz is small only the terms of the zero and the first order in the sum 16 will be important. Let us first consider the terms of the zero order.

$$T_0 = \prod_{k=1}^N J_0 \left(\frac{\pi \Delta z}{2\lambda \sqrt{N}} \right) \approx J_0 \left(\frac{\pi \Delta z}{2\lambda} \right) \quad (17)$$

Therefore the height of the central lobe in the diffraction pattern for a single frequency and in the multi-frequency case will be the same. In other words, in the case of completely random surface the amplitude of the central maximum of the diffraction pattern is given by the function $J_0(\pi \Delta z_{av}/2\lambda)$ where Δz_{av} is the average peak-to-peak error on the surface.

4.1 Binary image storage

In the previous discussion only the case when the beam is focused as a whole to one point was considered. Such an analysis can be applied for the consideration of the

addressing beam, or both addressing and information beams in the case of the single bit image storage when the addressing and the information beam intersect in a single point. Considerable interest for the practical needs represents binary image storage. In this case the beams intersection is a two-dimensional plane. Such architecture allows a reading an information in the entire plane in a single operation. Schematic of the binary image data storage is depicted in Fig 7. The input image is placed in the front of the focusing lens and is reproduced in the image plane inside the recording material. Due to the more complicated geometry, the horizontal dimensions in this case will be slightly larger than for the single bit storage. As it is well known [4], when diffraction effects are included, the image of the object will be a convolution of the impulse response h with the image predicted by geometrical optics:

$$U(x, y) = \iint_{-\infty}^{\infty} h(x - x_0, y - y_0) \left[\frac{1}{M} U_0 \left(-\frac{x_0}{M}, -\frac{y_0}{M} \right) \right] dx_0 dy_0 \quad (18)$$

where the function $U_0(x, y)$ represents the geometrical optics prediction, that is the original object function reduced M times. The impulse response function for this case is given by the expression (11): $h(x, y) = U_f(x, y)$. Results of numerical calculations on the basis of the expression 18 are represented in the Fig 8-10. For the binary image storage the final image is determined by the interplay between diffraction effects and the effects of the surface scattering. For the simplicity only one spatial dimension was taken into account. The input image was chosen as a combination of so-called supergaussian functions: $\exp[-(x/a)^n]$ where n is a degree of the supergaussian function. Such a function approximates the shape of an single mark in the input image. For the numerical simulations the parameter n was chosen to be equal 20 and the distance between two neighboring marks was taken to be $0.23 a$, where $2a$ is the size of a mark. Numerics show that when the diameter of the focusing lens $L = 1 \text{ cm}$, $f = 1 \text{ cm}$, and $\lambda = 0.53 \text{ } \mu\text{k}$ the size of the bit in the image plane is limited by the diffraction and can not be smaller then $4 \text{ } \mu\text{k}$. When the focal distance increases or the diameter of the lens decreases the diffraction becomes more and more important. The pictures of the images produced by the lenses of different sizes are given in Fig 8 (a,b,c). As can be seen from Fig 8, when the diameter of a lens is 6 cm the shape of each mark is very close to its original shape. However because of the surface scattering ($\Delta z = 0.5\lambda$ in both figures) some additional peaks appear and in some cases the height of extra peaks is comparable to the hight of the original peaks which will lead to reading errors. When the diameter of the lens decreases the diffraction changes the shapes of the marks in the image. Each mark does not have a supergaussian shape any more. However without surface scattering such marks would still be readable. Surface scattering leads to the redistribution of the energy in the image plane and to an appearance of the additional maximums.

5 Conclusions

An investigation of the effects of the surface scattering has shown that even small surface inhomogeneities can seriously alter the light distribution in the focal and image planes. Specifically, when the peak-to-peak surface error Δz is greater than a half of the wavelength of the recording beam, the effects of surface scattering may lead to considerable recording errors. Consideration on the basis of spatial spectrum approach shows that the surface errors with the periods greater than 100 nm will not affect the focusing. In the case of single bit image recording only very small spatial frequencies (with periods not larger than one quarter of the length of the recording material) are important. In the case of binary image storage surface scattering leads to the appearance of false maxima and to the redistribution of the light in the image plane. For the binary data storage the surface scattering appears to be more pronounced and all spatial frequencies with the periods between 1 and 10^{-3} cm become important. All the numerical calculations used in this work were performed on the basis of Matlab program.

Dr. Ibragimov greatly appreciates the support that he received from Rome Laboratory personnel during the project. Also, he is thankful for the opportunities extended to him by the Air Force Summer Faculty Research Program.

References

- [1] A.A. Jamberdino, F.N. Haritatos, and B.W. Canfield, *Optical Database Storage*, Rome Laboratory Technical Journal, **1**, 81-96, (1995).
- [2] J.L. Kann, B.W. Canfield, Capt. USAF, A. Jamberdino, B.J. Clarke, E. Daniszewski, and Gary Sunada, Lt., USAF, *Optical Mass Storage and Retrieval at Rome Laboratory*, Proceedings of Fifth NASA Goddard Conference on Mass Storage Systems and Technologies, Maryland, September, 1996, Volume II, p. 389.
- [3] J.L. Kann, F.B. McCormick, *Numerical Simulations of Scattering in a Two-photon Optical Data Storage System*, Applied Optics, to be published.
- [4] J.W Goodman, *Introduction to Fourier Optics*, McGraw-Hill, (1968).
- [5] K. Iizuka, *Engineering Optics*, Springer-Verlag, (1985).

Figure Captions

Figure 1. A schematic of the optical system. The magnification of the surface of the recording material is given inside the circles.

Figure 2. An illustration of light scattering on the sinusoidal phase grating

Figure 3. The picture of intensity distribution in the focal plane of the light scattered off a sinusoidal surface with $f_0 = 6 \text{ cm}^{-1}$. $\lambda = 0.5 \text{ } \mu\text{k}$, $\Delta z = 0, \lambda/2$, and λ for the solid, dot-dashed and dotted lines correspondingly.

Figure 4. Dependence of the amplitudes of the components of the zero, first and second order on the parameter Δz .

Figure 5. A picture of the intensity distribution in the focal plane when the spatial frequency of the surface is small. $f_0 = 1 \text{ cm}^{-1}$, $\Delta z = 0.6\lambda$, $\lambda = 5 \cdot 10^{-5}$

Figure 6. A shift of the focal pattern from the central position caused by the tilting of the beam. $\theta = 0, 1.5 \cdot 10^{-4}$, and $3 \cdot 10^{-4} \text{ rad}$

Figure 7. A schematic of the optical system for the binary image storage.

Figure 8. The intensity distribution in the image plane formed by 6 datamarks. The ideal image is given by the dashed line. $f_0 = 11$, $\Delta z = 0.5 \lambda$, $L = 6 \text{ cm}$ (a), $L = 3 \text{ cm}$ (b), and $L = 1 \text{ cm}$ (c). L is the lens's diameter.

Figure 9. The intensity distribution in the image plane formed by 6 datamarks. The ideal image is given by the dashed line. $f_0 = 5$, $\Delta z = 0.5 \lambda$, $L = 6 \text{ cm}$ (a), $L = 3 \text{ cm}$ (b), and $L = 1 \text{ cm}$ (c). L is the lens's diameter.

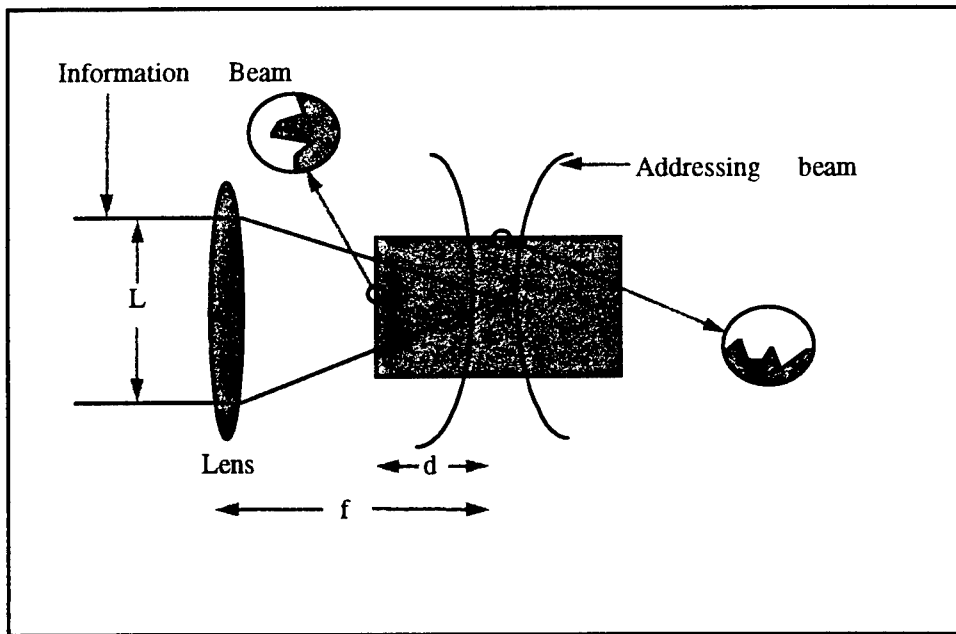


Figure 1

Figure 2

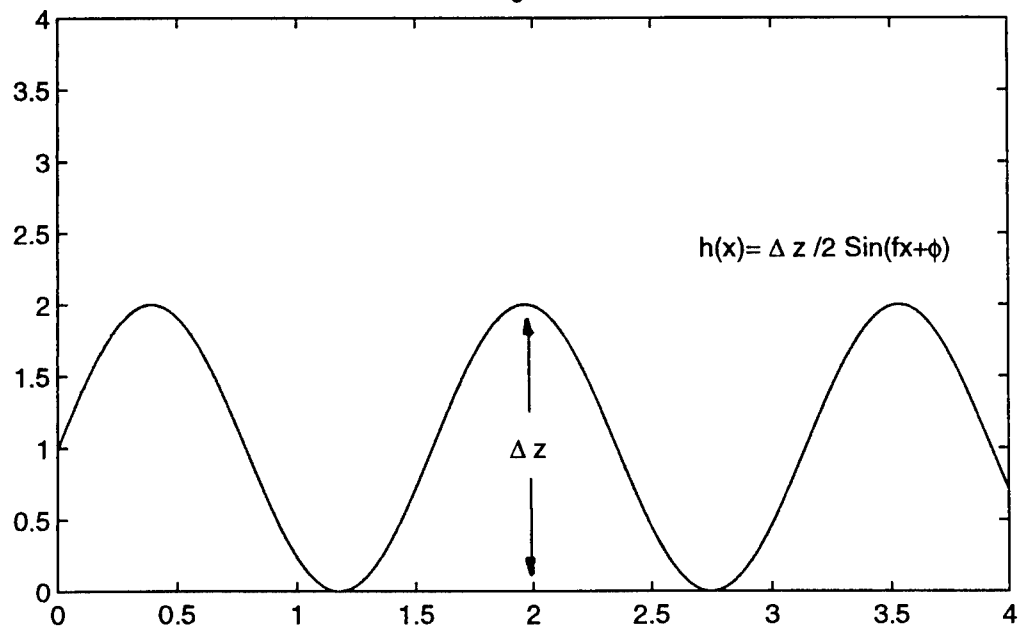


Figure 3

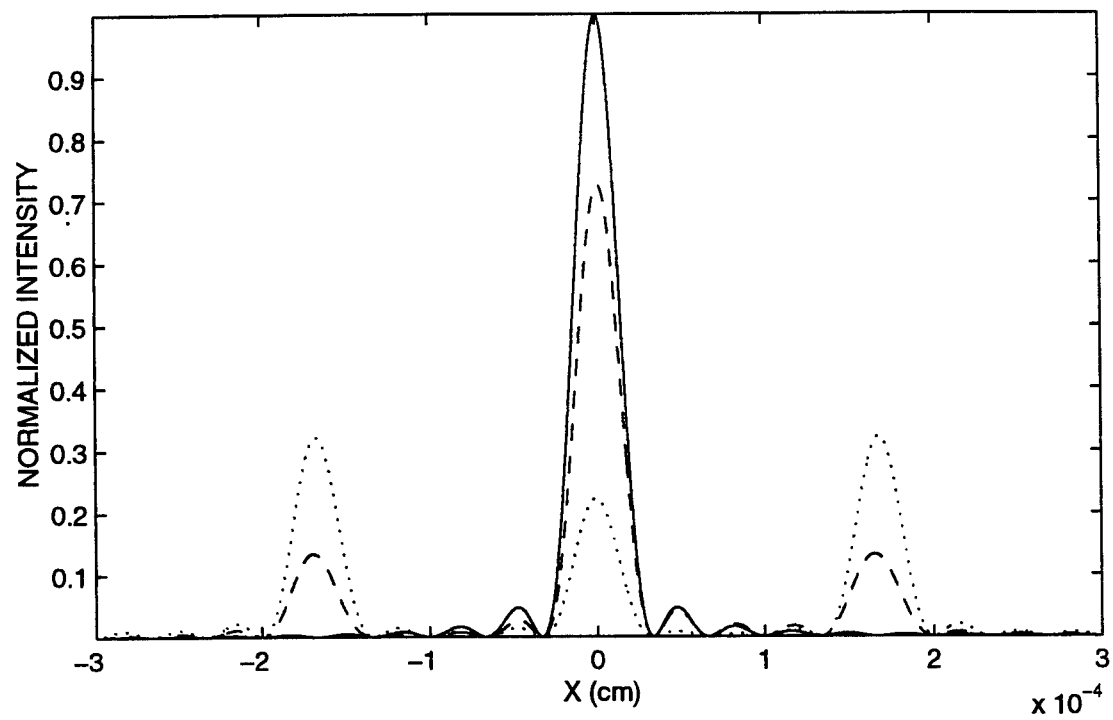


Figure 4

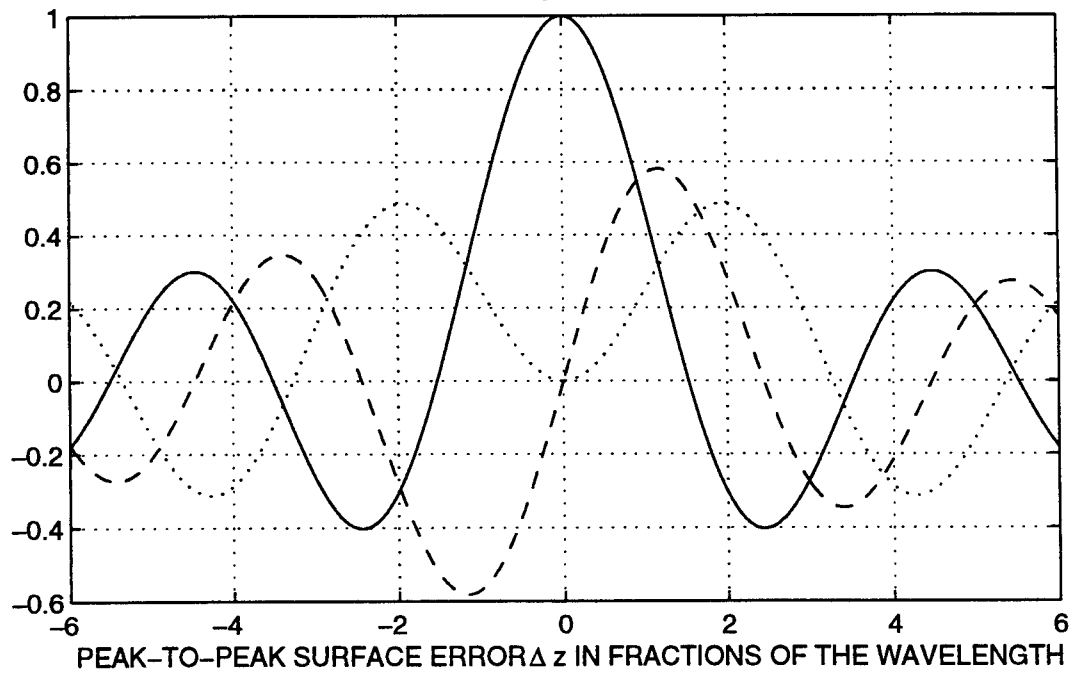


Figure 5

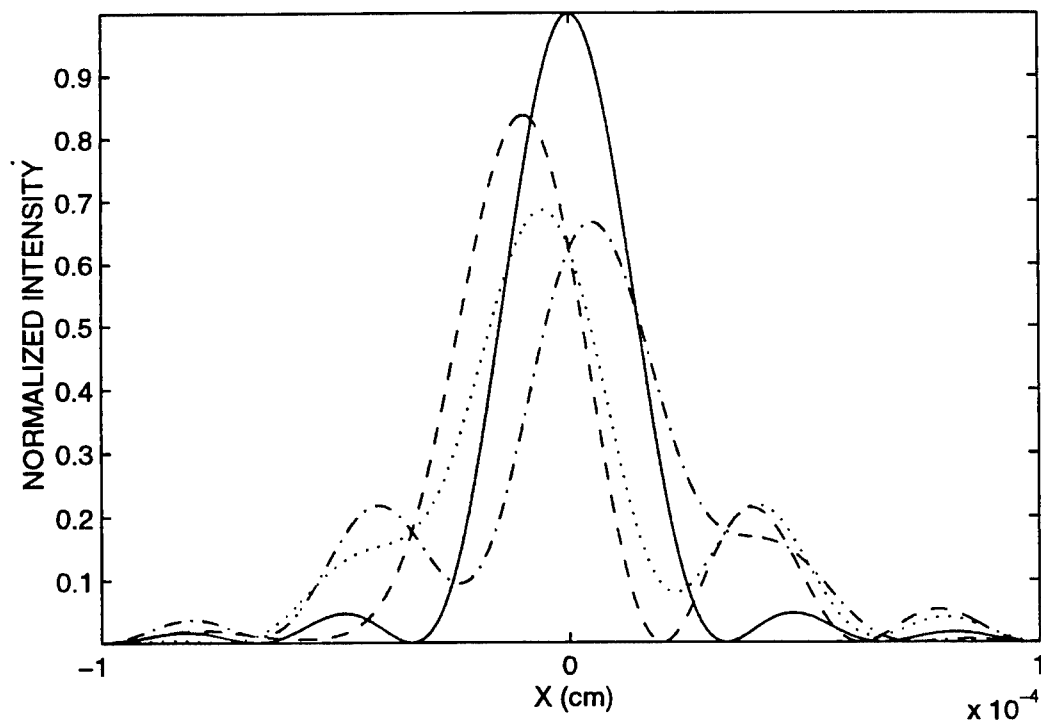
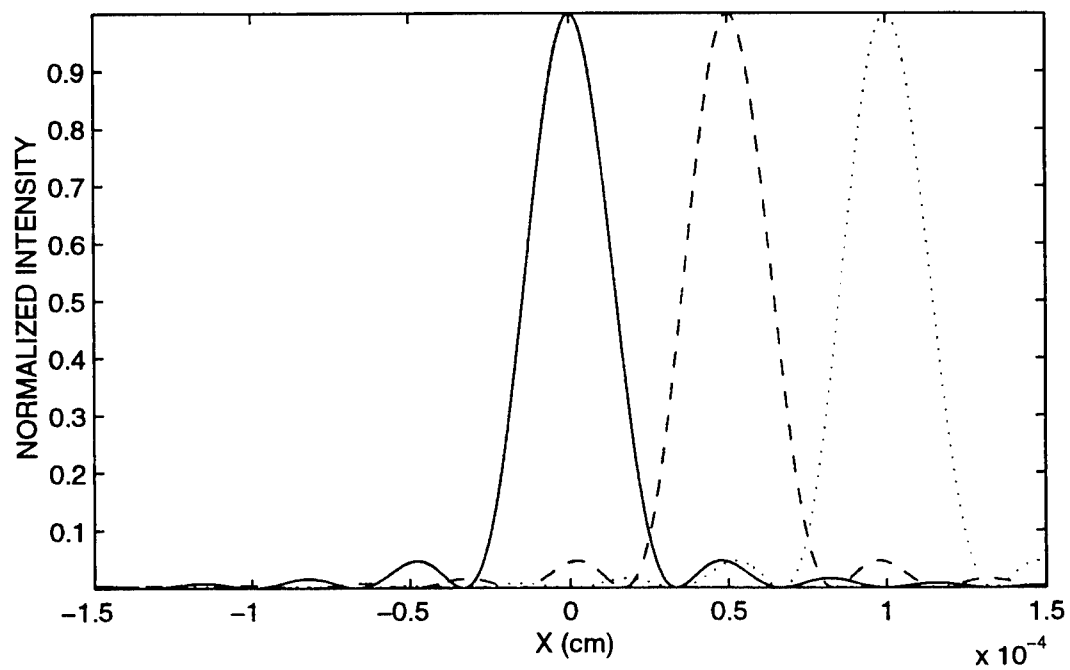


Figure 6



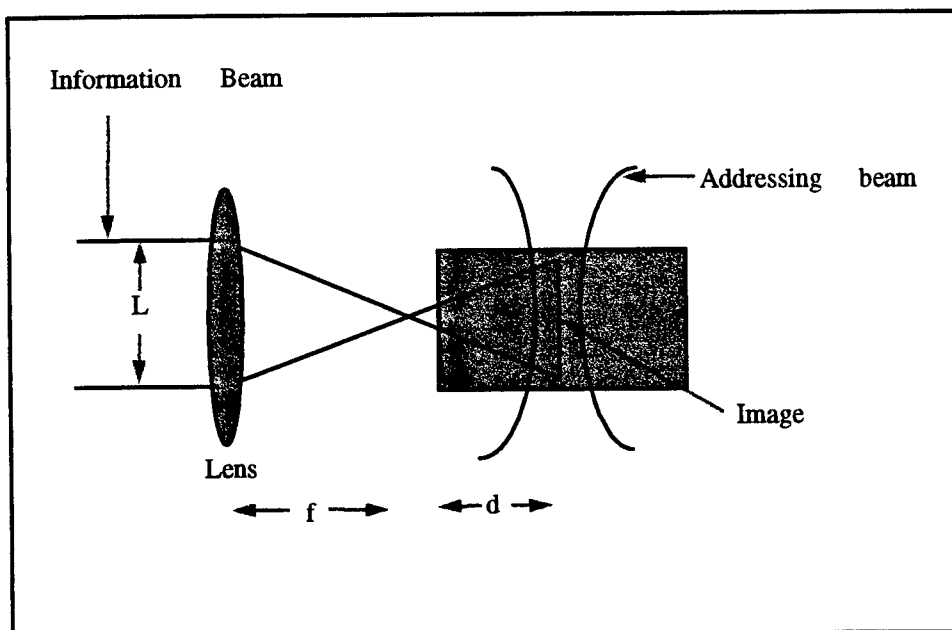


Figure 7
Figure 8a

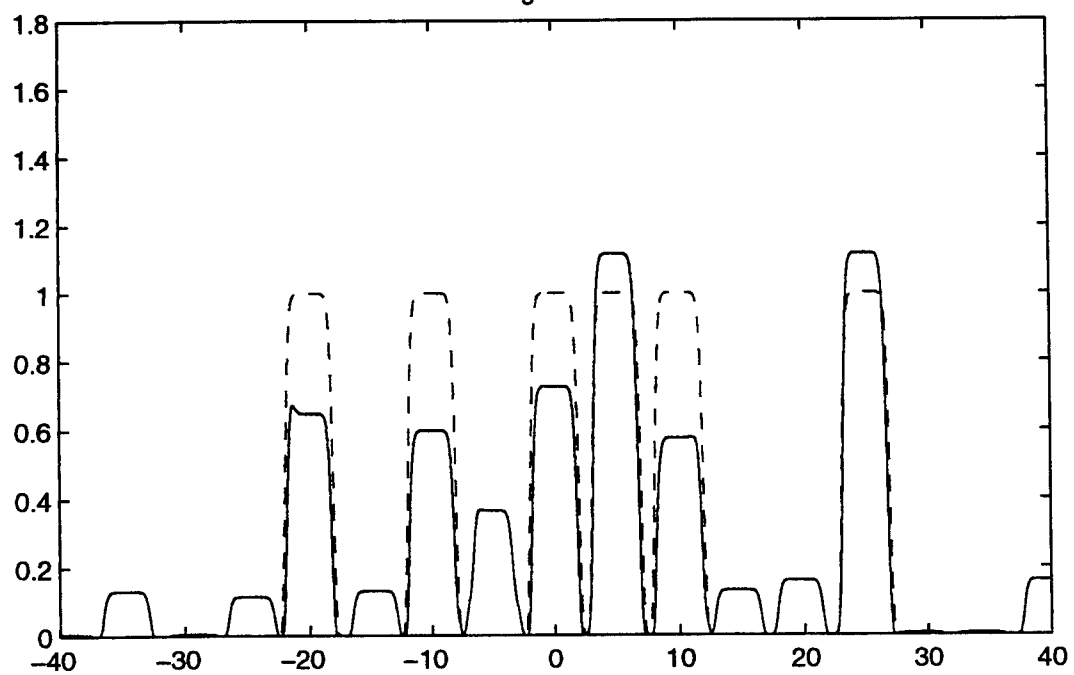


Figure 8b

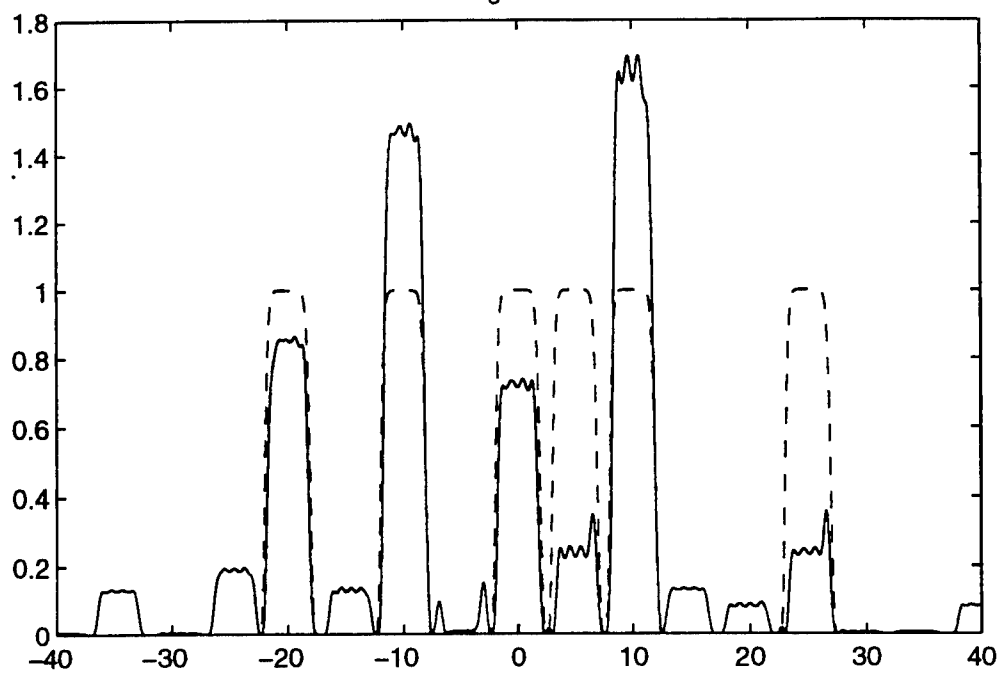


Figure 8c

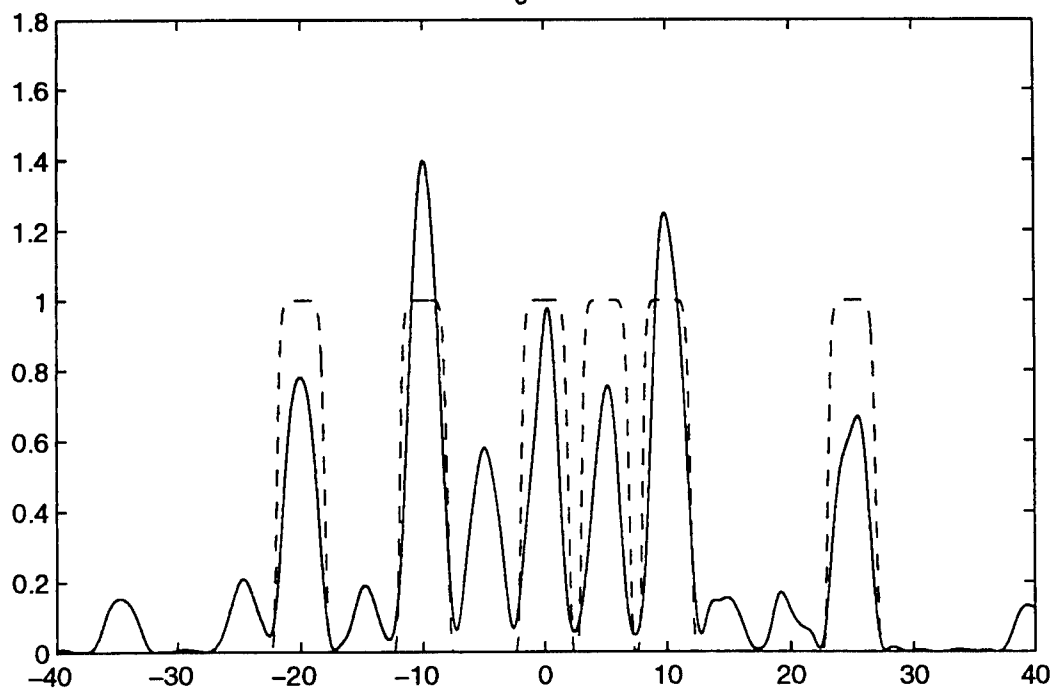


Figure 9a

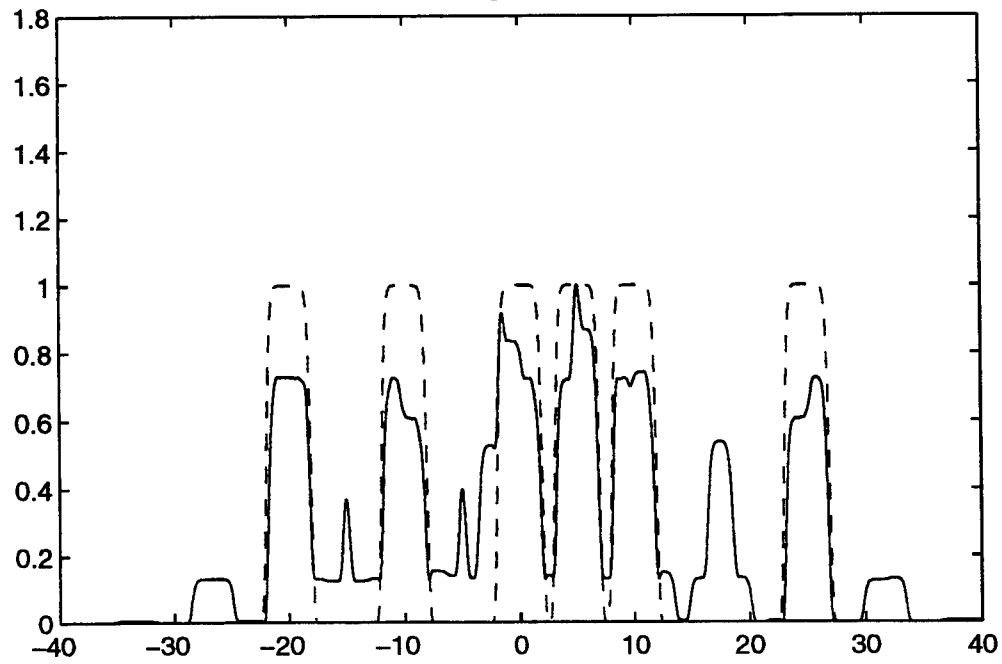


Figure 9b

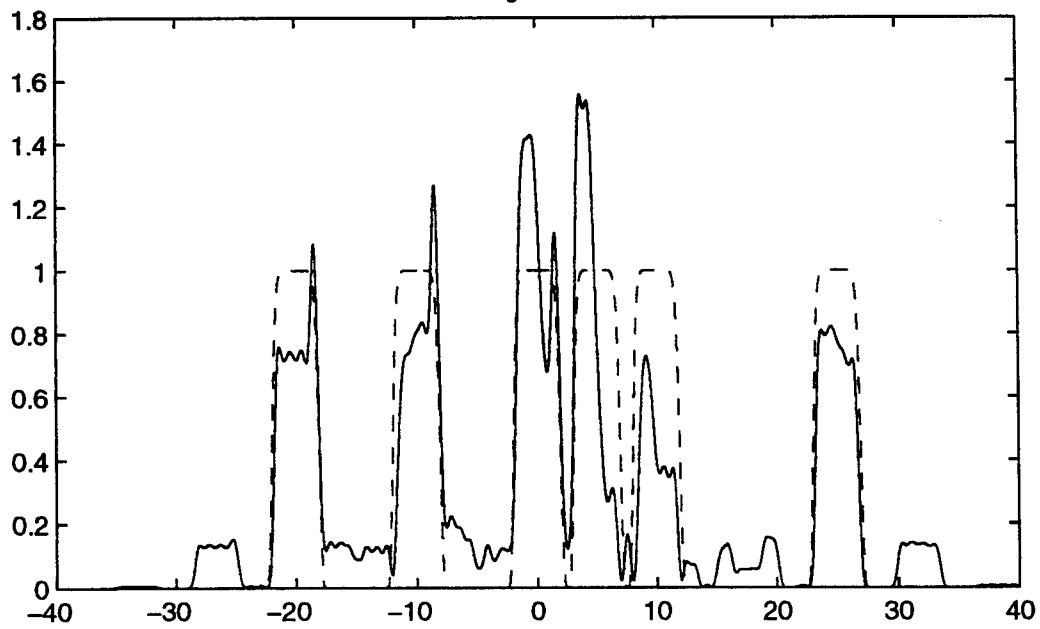
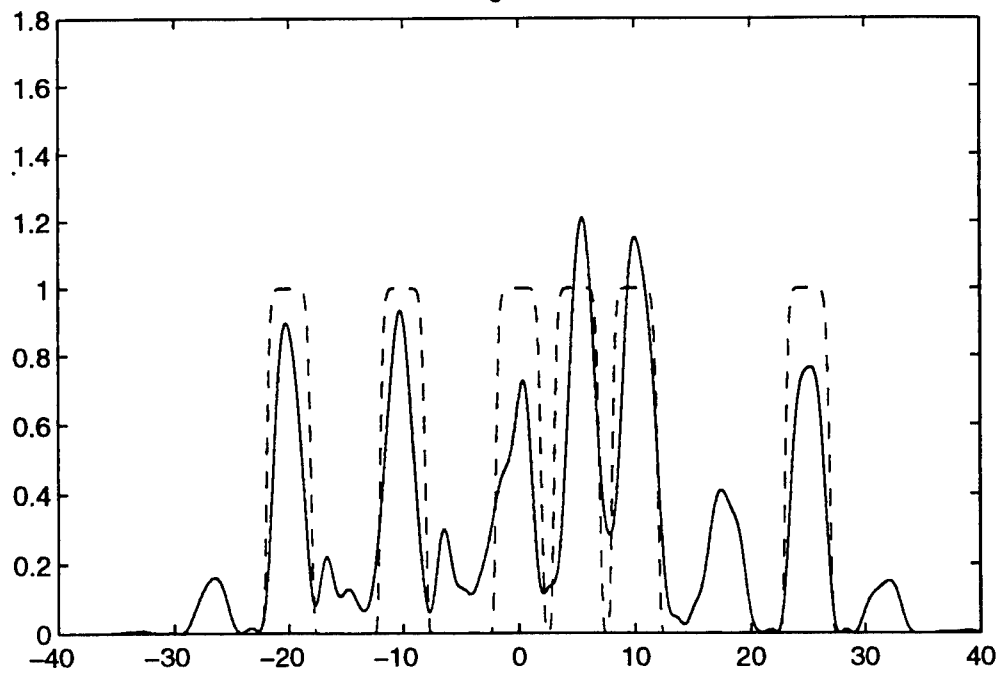


Figure 9c



ANALYSIS OF OPTICALLY ACTIVE MATERIAL LAYER FIBERS

Philipp Kornreich

Professor

DEPARTMENT OF ELECTRICAL ENGINEERING AND COMPUTER SCIENCE

Syracuse University

Syracuse, N. Y. 13244

Final Report for:

Summer Faculty Research Program

Rome Laboratory

Sponsored by:

Air Force Office of Scientific Research

Bolling Air Force Base, DC

and

Rome Laboratory

September 1997

ANALYSIS OF OPTICALLY ACTIVE MATERIAL LAYER FIBERS

Philipp Kornreich

Professor

DEPARTMENT OF ELECTRICAL ENGINEERING AND COMPUTER SCIENCE

Syracuse University

Syracuse, N. Y. 13244

Abstract

We have analyzed both fibers having a thin AlCu alloy layer strip that covers about 15 degrees of arc at the core cladding boundary and fibers having a thin CdTe semiconductor layer cylinder at the core cladding boundary of the fiber. Both the AlCu alloy strip and the CdTe cylinder are about 5 nm thick. The AlCu alloy strip fibers have absorption resonance at 449 nm, 935 nm, and 1140 nm in the transmission spectrum and exhibit both a polarization sensitive absorption at 1140 nm and birefringence at 1320 nm. The CdTe fibers exhibit a step at a wavelength of 795 nm in the transmission spectrum. This step is shifted towards shorter wavelength from its value of 827 nm in the bulk material in the fiber preform.

ANALYSIS OF OPTICALLY ACTIVE MATERIAL LAYER FIBERS

Philipp Kornreich

1. Introduction

We have analyzed both fibers having a thin AlCu alloy layer strip that covers about 15 degrees of arc at the core cladding boundary and fibers having a thin CdTe semiconductor layer cylinder at the core cladding boundary of the fiber. Both the AlCu alloy strip and the CdTe cylinder are about 5 nm thick. The fibers were fabricated in the Syracuse University Fiber Fabrication Research Laboratory. We measured the transmission spectrum of the AlCu alloy strip fibers. These fibers exhibit absorption resonance at 449 nm, 935 nm, and 1140 nm. The absorption at 1240 nm is polarization dependent. Light polarized parallel and light polarized perpendicular to the strip is absorbed at a different rates. The fiber is nearly single mode at 1140 nm. The absorption at 935 nm is somewhat polarization dependent and the absorption at 449 nm is less polarization dependent since the fiber is multi mode at these wavelength. The interaction of the light with the metal is only strong in single mode fiber. The AlCu alloy strip fibers exhibit birefringence at 1320 nm where the fibers do not absorb light. All measurements were performed at room temperature.

We measured the transmission spectrum of the CdTe semiconductor cylinder fibers. The CdTe fibers exhibit a step at a wavelength of 795 nm in the transmission spectrum. They absorb light with wavelength shorter than 795 nm and transmit light with wavelength longer than 780 nm. This step is shifted towards shorter wavelength from its value of 827 nm in the bulk material. We, also, measured the transmission spectrum of the fiber preform. The fiber preform exhibits a step at a wavelength of 827 nm in the transmission spectrum. This is in agreement with its value in bulk crystalline CdTe. The step is relatively sharp having a width of only 1.7 kT. Again, all measurements were performed at room temperature.

2. AlCu Alloy Strip Fiber

We measured the transmission spectrum of the AlCu alloy strip fibers at room temperature using an unpolarized white light source. The data is shown in Fig. 1. Fiber samples about 30 cm long were used. Note the resonances at 449 nm, 935 nm, and 1140 nm. These resonances correspond to optical frequencies of 6.677×10^{14} Hz, of 3.206×10^{14} Hz, and of 2.630×10^{14} Hz

respectively. These frequencies are much too low to be plasma resonance frequencies. Plasma resonances are of the order of 10^{16} Hz. Perhaps, the resonances that we observe correspond, approximately, to etalon resonances in the approximately 5 nm thick metal film. We assume that the fundamental mode, where the metal film thickness of 5 nm corresponds to one half wavelength occurs at a wavelength of 935 nm. Thus the wavelength

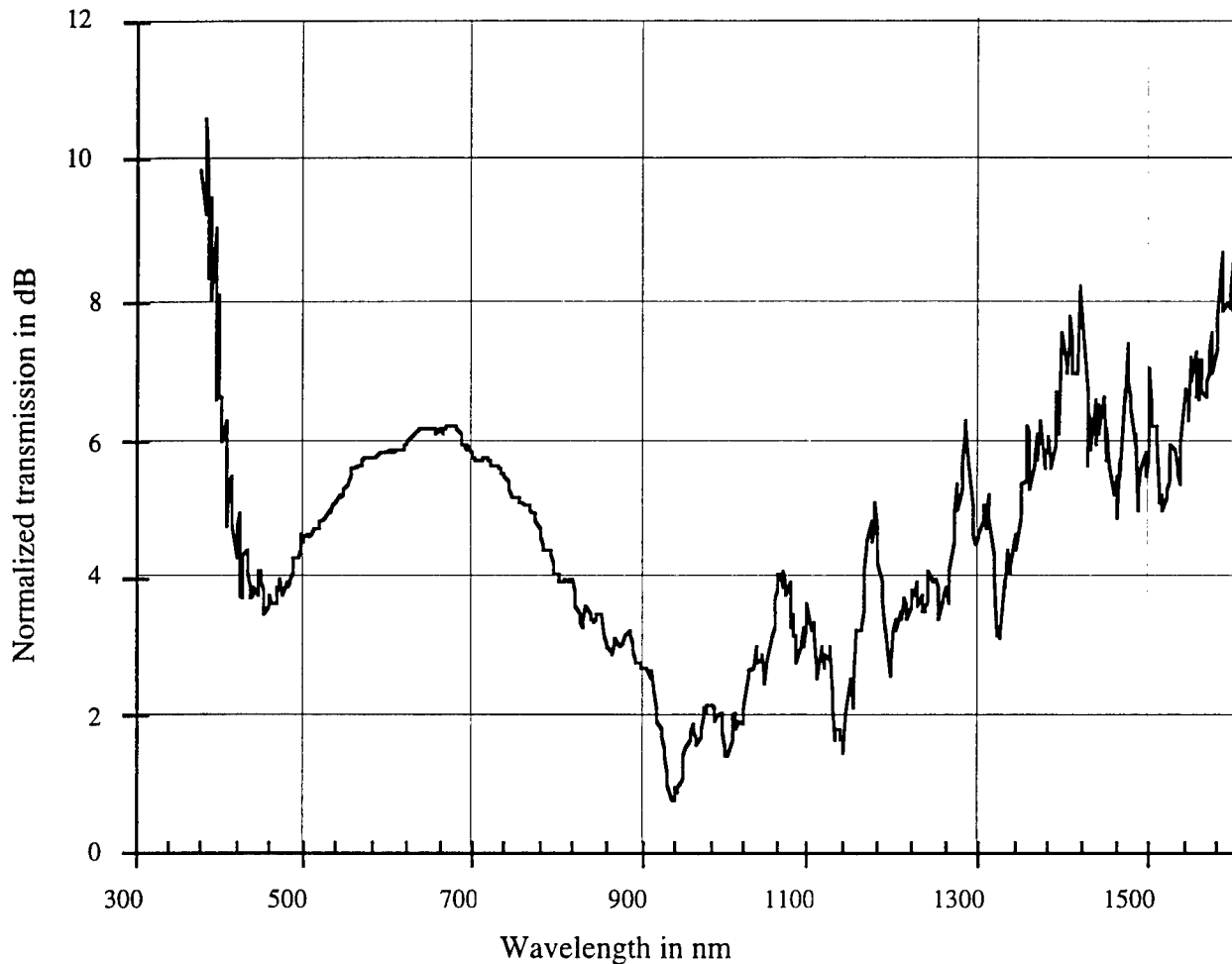


Fig. 1. The transmission spectrum of the AlCu alloy strip fibers. Note the absorption resonances at 449 nm, 935, nm and 1140 nm. Fiber samples about 30 cm long were used.

in the metal is 10 nm at this frequency. The wavelength in the metal is equal to the wavelength in vacuum, 1140 nm, divided by the index of refraction n in the metal at this wavelength. This gives an index of refraction $n_o = 93.5$ at a light frequency f_o of 3.206×10^{14} Hz. We assume that the

resonance at 449 nm is the next higher mode where the metal thickness corresponds to a complete wavelength. This yields an index of refraction n_1 of 89.8 at a light frequency of 6.677×10^{14} Hz.

The index refraction at a light frequency f and a plasma frequency f_p is given by:

$$n^2 = 1 + \frac{f_p^2}{f^2} \quad (1)$$

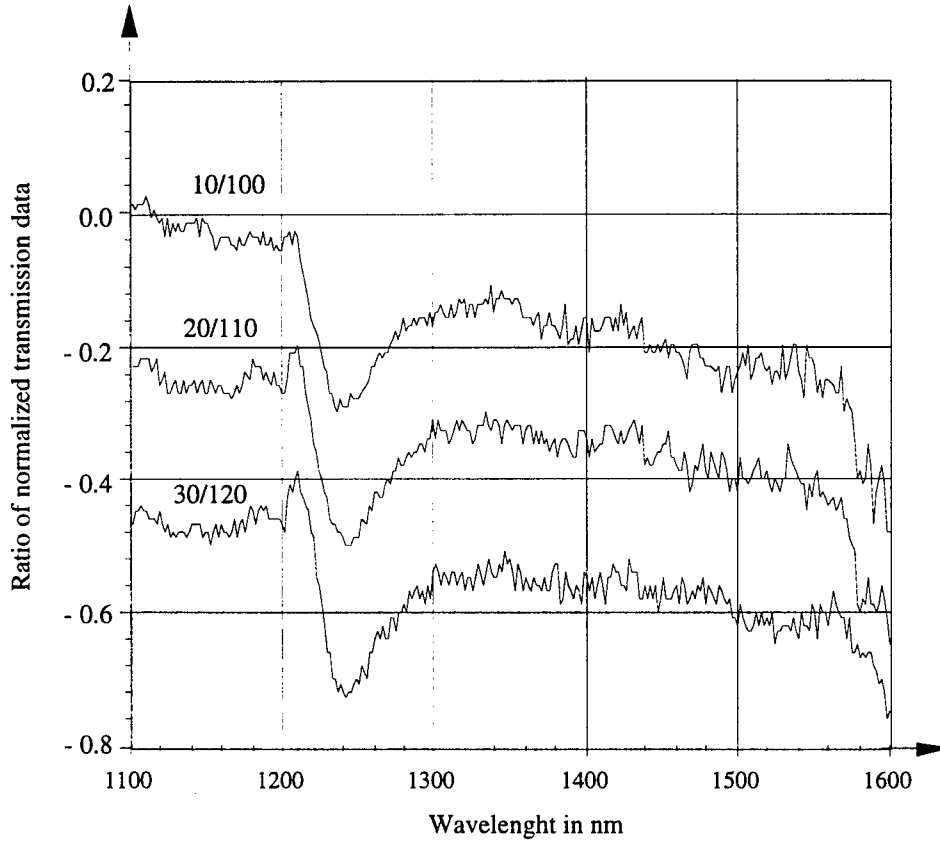


Fig. 2. The ratio of the transmission spectrum of the AlCu alloy strip fibers with polarizations that differ by 90 degrees. The first curve is the ratio of the transmission spectrum at a polarization of 10° to the transmission spectrum at 100° . The second curve is the ratio of the transmission spectrum at a polarization of 20° to the transmission spectrum at 110° , and the third curve is the ratio of the transmission spectrum at a polarization of 30° to the transmission spectrum at 120° .

This gives a plasma frequency f_p of 2.998×10^{16} Hz for the fundamental mode has the right order of magnitude. The plasma frequency of the next higher mode with a resonance at 449 nm is f_{p1} of 5.995×10^{16} Hz.

The metal strip fiber should absorb light polarized parallel to the metal strip and light polarized perpendicular to the metal stripe differently. In order to illustrate the polarization properties of the metal strip fibers we divided the transmission spectrum taken at polarizations that differ by 90° and plotted the results.. This is shown in Fig. 2, 3, and 4.

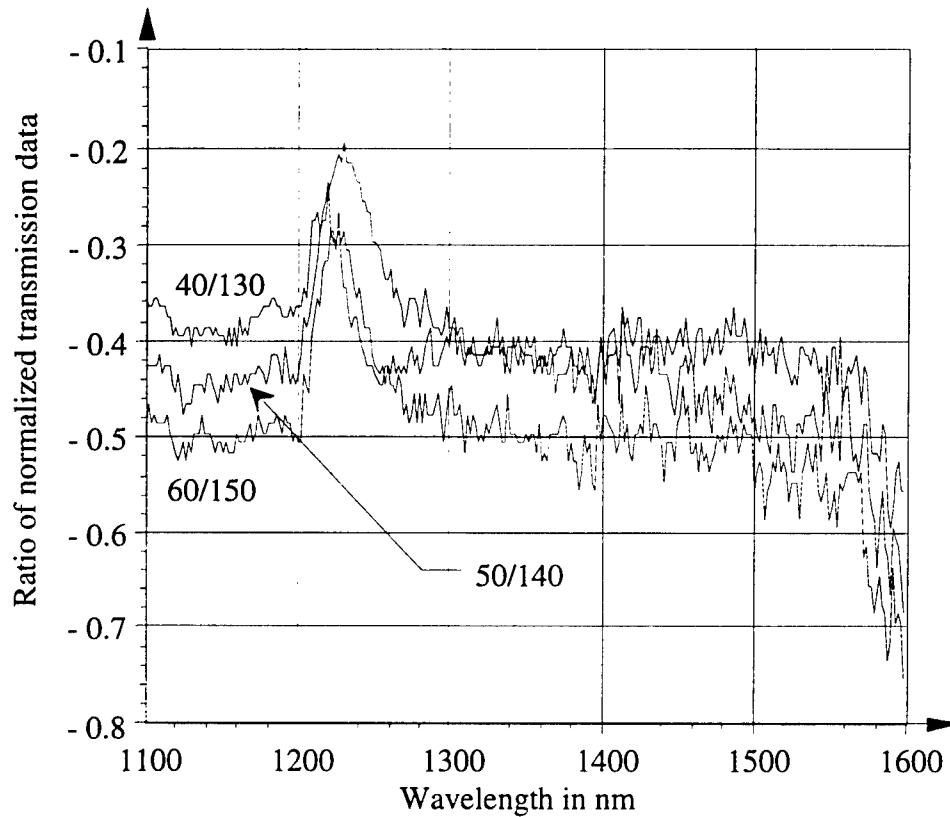


Fig. 3. The ratio of the transmission spectrum of the AlCu alloy strip fibers with polarizations that differ by 90 degrees. The first curve is the ratio of the transmission spectrum at a polarization of 40° to the transmission spectrum at 130° . The second curve is the ratio of the transmission spectrum at a polarization of 50° to the transmission spectrum at 140° , and the third curve is the ratio of the transmission spectrum at a polarization of 60° to the transmission spectrum at 150° .

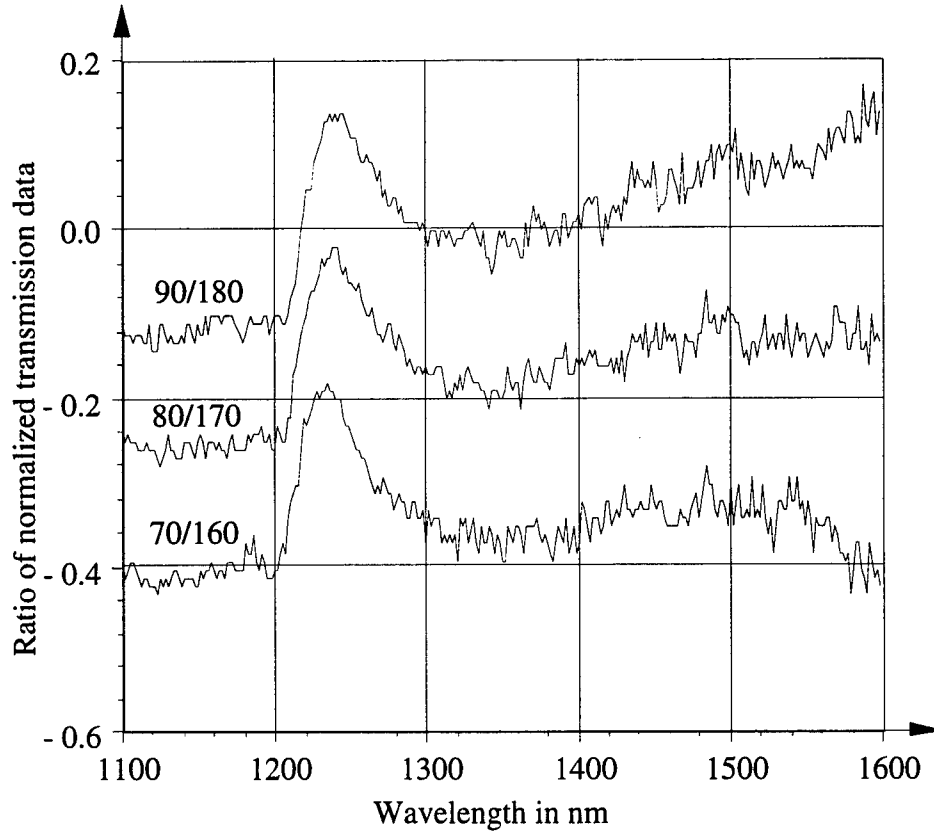


Fig. 4. The ratio of the transmission spectrum of the AlCu alloy strip fibers with polarizations that differ by 90 degrees. The first curve is the ratio of the transmission spectrum at a polarization of 70° to the transmission spectrum at 160°. The second curve is the ratio of the transmission spectrum at a polarization of 80° to the transmission spectrum at 170°, and the third curve is the ratio of the transmission spectrum at a polarization of 90° to the transmission spectrum at 180°.

The metal strip fibers have yet another application. They can be used as very high dispersion fibers for “True Time Delay” optical processors for Phased Array Antenna applications. Near the resonances exceedingly high dispersions can be achieved in relatively short pieces of fiber of about 15 cm. A light Frequency Dependent Delay can be generated by using a fiber where the light propagating through it has a phase $\phi(\omega)$ that depends on the square of the frequency for some frequency range:

$$\phi(\omega) = \phi(\omega_p) + b(\omega - \omega_p)^2 + \dots \quad (2)$$

where ω_p is the frequency about which the Taylor series expansion is performed. For an angular frequency consisting of the sum two frequencies $\omega_o + \omega_{RF}$ where ω_o is the frequency of the light and ω_{RF} is a “Radio Frequency” at which, say, a phased array antenna would operate. The light, in this case, has a single side band modulation as is conventional in “True Time Delay” heterodyne optical phased array antenna processors. By substituting into equation 1 we obtain:

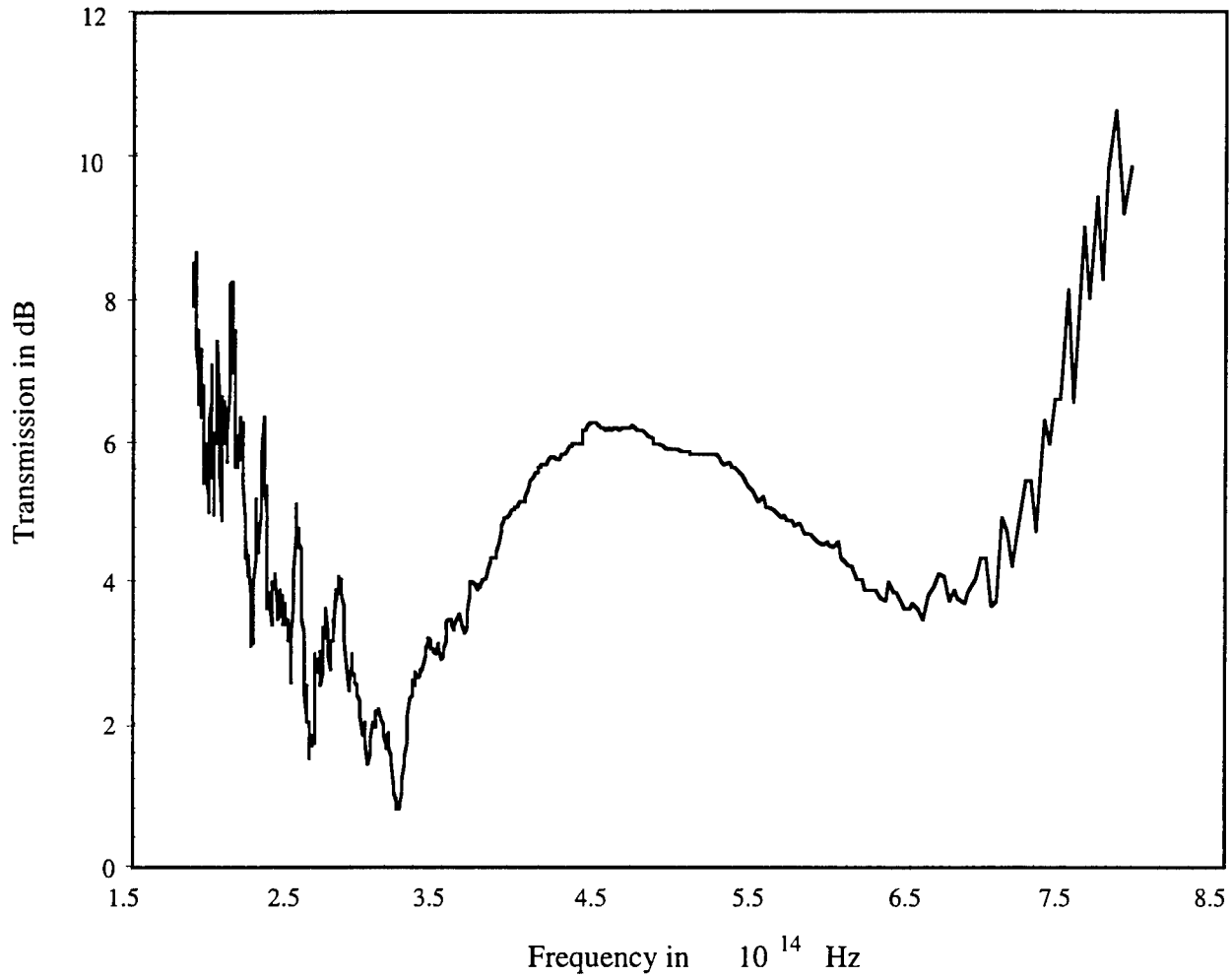


Fig. 5. The logarithmic transmission spectrum of the AlCu alloy strip fibers as a function of the radial frequency ω of the light.

$$\phi(\omega) = \phi(\omega_p) + b(\omega_o - \omega_p)^2 + 2b\omega_{RF}(\omega_o - \omega_p) + b\omega_{RF}^2 + \dots \quad (3)$$

Indeed, there is a phase term $2b\omega_{\text{RF}}(\omega_o - \omega_p)$ that depends both on the radio frequency and the light frequency. The linear radio frequency dependence is necessary for a true time delay. This phase delay can be changed by varying the optical frequency ω_o with a variable wavelength laser.

In Fig. 5 we replotted the logarithm of the spectral response as a function of light frequency. The phase $\phi(\omega)$ can be calculated from the logarithm of the spectral response by the use of the Hilbert transform. Values for the expansion coefficient b can be obtained for values of the light frequency where the first derivative of the phase $\phi(\omega)$ with respect to the light frequency ω is equal to zero. We obtain for b of the order of 10^{-24} radians-seconds² per meter (1000 radians-psec.² per km).

3 Semiconductor Cylinder Fibers

We have tested new CdTe semiconductor cylinder fiber. Some three years ago we tested at Rome Laboratory a CdTe cylinder fiber that was made by Syracuse University. This fiber had a core diameter of 70 μm and a non uniform semiconductor cylinder. Even though the interaction between the light and the semiconductor in this multi mode fiber was very weak we obtained the transmission spectrum of the fiber. The fiber pieces tested were about 8 mm long. The transmission spectrum of the fiber was similar to the transmission spectrum of bulk CdTe. This result demonstrated that at least CdTe survived the fiber fabricating process. This led us to the initiation of a research project to develop fibers with Optically Active Material layers at the core cladding boundary. The process of fabricating such fibers is, now, well understood. We have developed a process for fabricating develop fibers with Optically Active Material layers at the core cladding boundary.

We have recently tested fibers with a CdTe semiconductor at the core cladding boundary. These fibers had a core diameter of 10 μm and a smooth uniform semiconductor layer. Since the core diameter is near single mode the interaction is much stronger. Also this time the transmission spectrum does exhibit a blue shift due to the quantum size effect of the very thin, approximately 5 nm thick, semiconductor layer.

We, first, measured the transmission spectrum of the fiber preform. The fiber preform exhibits a step at a wavelength of 827 nm in the transmission spectrum as shown in Fig. 6. This is in agreement with its value in bulk crystalline CdTe. The step is relatively sharp having a width of only 1.7 kT. A measurements were performed at room temperature.

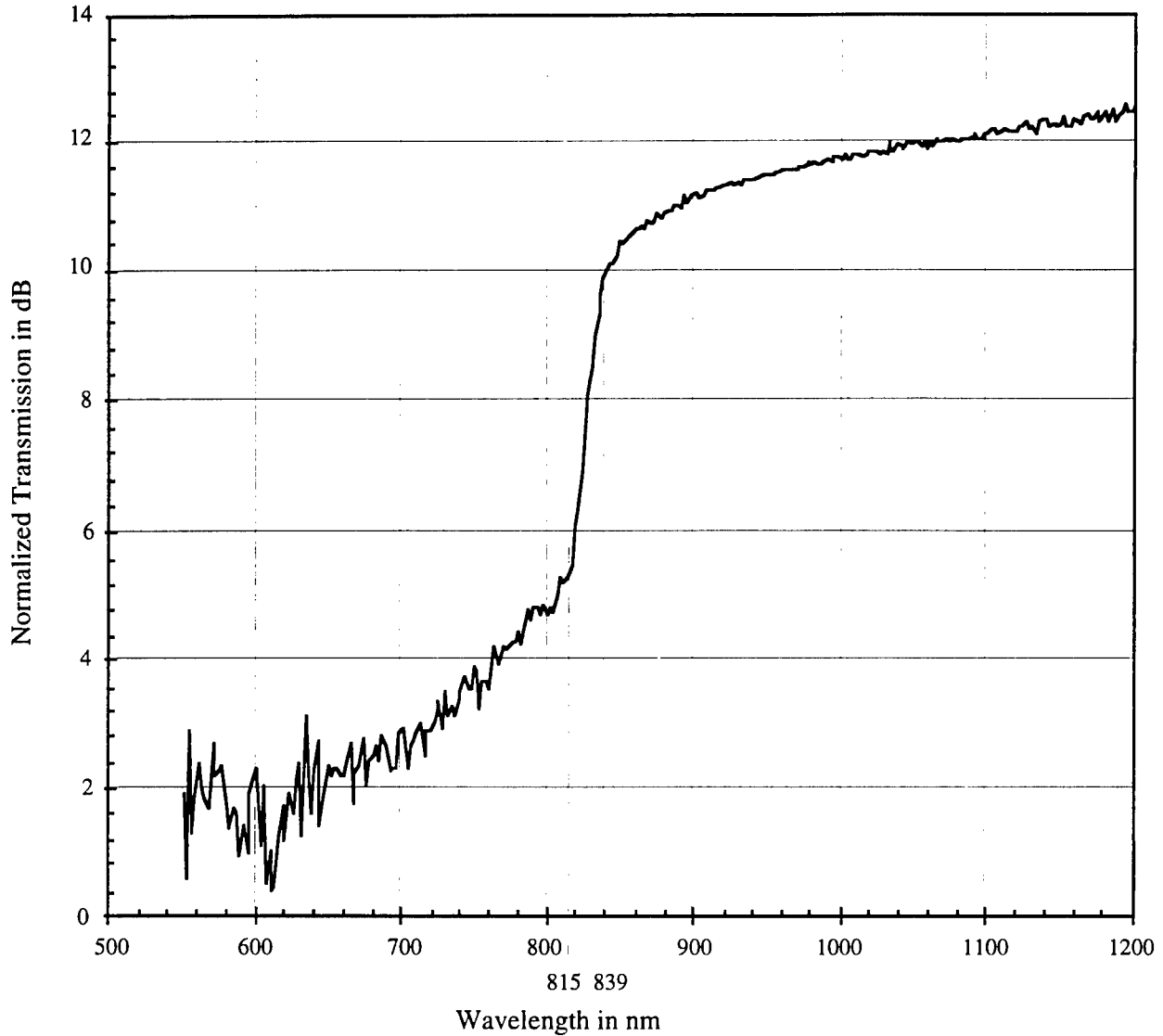


Fig. 6. The transmission spectrum of CdTe cylinder fiber preform.

We pulled a fiber from this preform. The fiber exhibits a step at 795 nm. That is the step is shifted, as expected, towards the blue in the spectrum by about 32 nm. This corresponds to a blue shift of 60 meV. The observation of a blue shift is encouraging since no such phenomenon was observed in the original CdTe Cylinder Fibers. The measurements were performed on 10 mm long pieces of fiber. It would be necessary to pump these fibers with light having a wavelength shorter than, say, 770 nm.

The theoretical shift in energy ΔE in eV due to a confinement of electrons with an electron effective mass ratio $m_e^* = 0.411$ and a holes with a hole effective mass ratio $m_h^* = 0.644$ in a semiconductor layer of thickness a is:

$$\Delta E = \frac{\hbar^2 \pi^2}{2m_0 e a^2} \left[\frac{1}{m_e^*} + \frac{1}{m_h^*} \right] \quad (4)$$

Since we know the shift in energy $\Delta E = 0.06$ eV we can use equation 4 to calculate the thickness a of the semiconductor layer. We obtain a thickness a of 4.998 nm in good agreement with the predicted values.

A STUDY ON THE CROWDED AIRSPACE
—SELF ORGANIZED CRITICALITY

Kuo-Chi Lin
Associate Professor
Institute for Simulation and Training

University of Central Florida
3280 Progress Drive
Orlando, FL 32826-0544

Final Report for:
Summer Faculty Research Program
Rome Laboratory

Sponsored by:
Air Force Office of Scientific Research
Bolling Air Force Base, DC

and

Rome Laboratory

August 1997

A STUDY ON THE CROWDED AIRSPACE —SELF ORGANIZED CRITICALITY

Kuo-Chi Lin
Associate Professor
Institute for Simulation and Training
University of Central Florida

Abstract

A crowded airspace involves large numbers of airplanes interacting with each other. In general, the dynamic behavior of the system is quite complex and conventional mathematical modeling is difficult. Here, a generic air traffic model is used to investigate the application of the notion of “self-organized criticality”. The results show that a crowded air traffic system exhibits the characteristics of self-organized criticality.

A STUDY ON THE CROWDED AIRSPACE —SELF ORGANIZED CRITICALITY

Kuo-Chi Lin

Introduction

With the rapid increase of air traffic going into the 21st century, the airspace near major airports will become more and more crowded. There is an urgent need to understand the dynamics of the air traffic system at or near its saturated state.

Current approaches in the analysis of air traffic systems are mainly based on simulation.¹⁻⁴ The lack of an analytical approach is due to the difficulty in modeling the complicated interactions among a large number of airplanes. However, there exist some new ideas which have been used successfully in other fields to model complex dynamic systems. One of them is the self-organized criticality (SOC).

The concept of SOC was developed by Bak, Tang, and Wiesenfeld⁵ in 1987, to explain the behavior of complex systems', those containing millions and millions of elements that interact over a short range. Typical examples of such systems are earthquakes, avalanches, stock markets, and ecosystems.⁶ Those dynamic systems with many interacting degrees of freedom may organize themselves into a marginally stable "critical" state. At this SOC state, the system is able to produce a wide range of fluctuations or "avalanches". In other words, it can spontaneously generate structures or events of many different sizes. A metaphor for the idea of SOC is a sandpile, which will be described in the next Section.

Bak, et. al., used a simple computer model to simulate the sandpile and concluded that it is SOC. Many other scientists have since conducted experiments on real sandpiles⁷⁻¹¹ and other similar systems, such as rice piles¹². Bak has used one chapter in his book "How Nature Works"¹³ to compare all the experiments. Other authors have applied the SOC concept to various fields. A list of references can be found in Bak's book.¹³ However, the SOC concept has not been applied to air traffic problems.

In 1976 Musha and Higuchi¹⁴ conducted measurements on Japanese highway traffic. The results showed an " $1/f$ " spectrum in the Fourier transformed density fluctuations. " $1/f$ " noise, which has been detected in many physical phenomena, such as earthquakes and avalanches, is a classic problem in physics. The original motivation of Bak, et. al., to develop the SOC model is to explain the widespread occurrence

of “ $1/f$ ” noise. In recent years, Kai Nagel, et. al., successfully showed that the engineering problems in large, urban highway systems can be explained by self-organized criticality.¹⁵⁻¹⁷

However, the air traffic problem is different from the highway traffic problem in many essential ways. The most significant one is that an airplane cannot stop-and-go nor change its speed as quickly as a car. Therefore, the model used in Nagel’s papers cannot be applied to the air traffic problem. Another major difference between the two systems is that a car is confined by the highway, while an airplane is free to move in space.

In this paper the concept of SOC is first reviewed using the sandpile model. The dynamic behavior of the air traffic system is discussed next. An air traffic model is examined for the features of SOC. A near-airport simulation is then conducted to demonstrate the model.

Self-Organized Criticality—Sandpile Model

A pile of sand is a deceptively simple model which serves as a paradigm for self-organized criticality. Imagine that a sandpile is built by a device which can place one grain of sand at a time on a flat, horizontal platform. At the beginning, the sand particle just rests where it lands. It is stable. If the sand grains are continuously added to the platform, eventually one particle will land on top of one already there. In this case, it is unstable and the sand grain will fall off to one side. This is a microscopic avalanche¹¹.

As sand particles are continuously added to the platform, a sandpile will start to form. When the slope of the pile is small, it is stable and the sand grains will stay where they are sprinkled. As more sand grains are added and the slope of the sandpile increases, it is more likely that the newly added particle will be unstable and start to move after it lands. When one particle moves and hits another particle, it may start a chain-reaction, i.e., an avalanche. The avalanche may be small (affects less particles) or large (affects more particles). The larger the slope of the sandpile is, the possibility of triggering a large avalanche is higher. The slope of the sandpile will decrease after the avalanche. Since the sand grains are continuously added to it, the slope of the sandpile will be gradually reinstalled.

This process will persist until the steady-state angle is reached where, for every particle that is added to the pile, on average one particle will fall off the edge of the platform¹¹. In reality, sand grains do not leave the platform one at a time, but rather do so in avalanches. Therefore, the size of the sandpile

fluctuates. This phenomenon implies that the sandpile slope has a critical value¹¹. If the slope of the pile is smaller than the critical value, the possibility of avalanche is small, and the addition of sand grains will increase the slope. On the other hand, if the slope of the pile is larger than the critical value, addition of sand grains will likely trigger large avalanches which will bring the slope back to the critical value. The critical point is self-organized; hence the name “self-organized criticality”.

There are three major features in an SOC system, argued by Bak, et. al.^{5,6}. First, the critical state is robust with respect to any small change in the rules of the system. In the sandpile example, whether the particles are dry sand, wet sand, even snow flakes, the dynamics are similar. Second, the system exhibits fractal structure. In other words, the sandpile has all-length and self-similar avalanches. Third, the system generates “ $1/f^B$ ” noise. If the weight of the sandpile is measured with respect to time, its low-frequency power spectral density displays a power-law behavior over vastly different time scales.

Dynamic Behavior of Air Traffic System

In Nagel’s highway traffic jam model¹⁵⁻¹⁷, a car changes its speed reacting to the distance of the car in front of it. When there is a large number of cars in a traffic jam, the complicated interactions among cars can be explained using self-organized criticality. The air traffic system is essentially different from the highway traffic system, in that airplanes cannot stop-and-go nor change their speed as fast as cars. They usually follow the preset flying profiles (courses and speeds). The major interaction between two airplanes is collision avoidance. The maneuver involved is mainly the change of direction. Based on this feature, the air traffic system behavior is analyzed below.

When one airplane is flying too close to another airplane, there is a possibility of collision. Both airplanes will receive alarms from their own devices and/or from the air traffic controller. Both pilots have to change their airplane’s direction or altitude to avoid collision. To simplify the analysis, we only use direction change so that the problem is reduced to a two-dimensional one. Also, we only consider the sudden encounter of the colliding airplanes. Predicting the colliding possibility from a long distance and changing the course to avoid it is not considered.

If an airplane is moving without any collision possibility, it can maintain its course and is therefore in an “undisturbed” state, which is analogous to the stable state in the sandpile model. When another airplane appears nearby, the original airplane needs to react to this collision threat, and its state is changed to a “disturbed” state. As a matter of fact, both involved airplanes are disturbed. If the disturbance moves one of the disturbed airplanes to the vicinity of a third airplane, the third airplane also becomes disturbed. It may start a chain reaction. This process is analogous to the avalanche in the sandpile model. The propagation of disturbance dies down when all airplanes have maneuvered out of collision possibilities and return to their courses.

How far the disturbance can propagate, or how many airplanes will be disturbed, depends on the local crowdedness of the airplanes. If the airspace is over-crowded, the possibility of large disturbances will be high. Once disturbance starts, it will persist until some airplanes are driven “away”. After the crowdedness of the airspace is reduced to certain level, the disturbance can die down. If the airspace is under-crowded, the disturbance, if any, will be minor and die down quickly. New airplanes can enter the airspace until the number reaches a critical value.

From the above analysis, the air traffic system suggests some basic characteristics of self organization. Next, a generic model will be used to examine the applicability of self-organization criticality to the air traffic system.

Air Traffic Model

We have developed a simple, generic model for this purpose. The airplanes in the model must have the ability to (1) avoid collision, (2) stay in a certain region, and (3) move toward a target (e.g. airport), or a certain direction.

The model is described as follows. It is a discrete event model. The field is a two-dimensional rectangular grid system. At each step of time, the airplane moves from one grid point to the next one along the grid line (no diagonal motion). When two (or more) airplanes enter the same grid point at the same time, or two entities move over the same grid line at the same time, there is a collision. The possible “collision threat positions” are shown with “x” marks in Figure 1. When at least one other airplane occupies one of those positions, the airplane at the center of Figure 1 is said to be “under collision

threat(s)". The rules which decide how the airplanes move have the following priorities: 1) Avoiding collision; 2) Staying in the field; 3) Moving toward a preset target or a preset direction. The rules to avoid collision are listed in the Appendix.

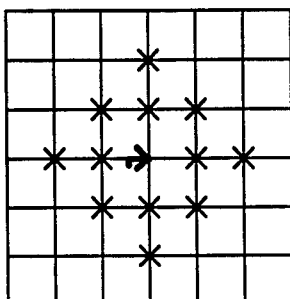


Figure 1. Possible collision threat positions.

The following example is used to illustrate the system behavior of the airspace model described in the previous Section. The field and airplanes are shown in Figure 2. The dotted-line diamond in the figure represents the collision threat positions of airplane #11. Since no other airplane is within that diamond, airplane #11 is undisturbed. As a matter of fact, all airplanes in the field are undisturbed. All airplanes are flying from the left edge of the field to the right edge of the field. After reaching the right edge, the lifetime of the airplane is over. However, new airplanes appear on the left edge. The field has a stable number of airplanes.

If one airplane, airplane #2 (circled by dotted line), is out of place, as shown in Figure 3 (a), airplanes #4 and #8 are disturbed and have to react to the collision threat. As those three airplanes start to change courses, other airplanes are disturbed, triggering an avalanche. After a period of time, the field eventually will return to the undisturbed state. Figure 3 (b) shows the positions of the airplanes that are disturbed by the avalanche.

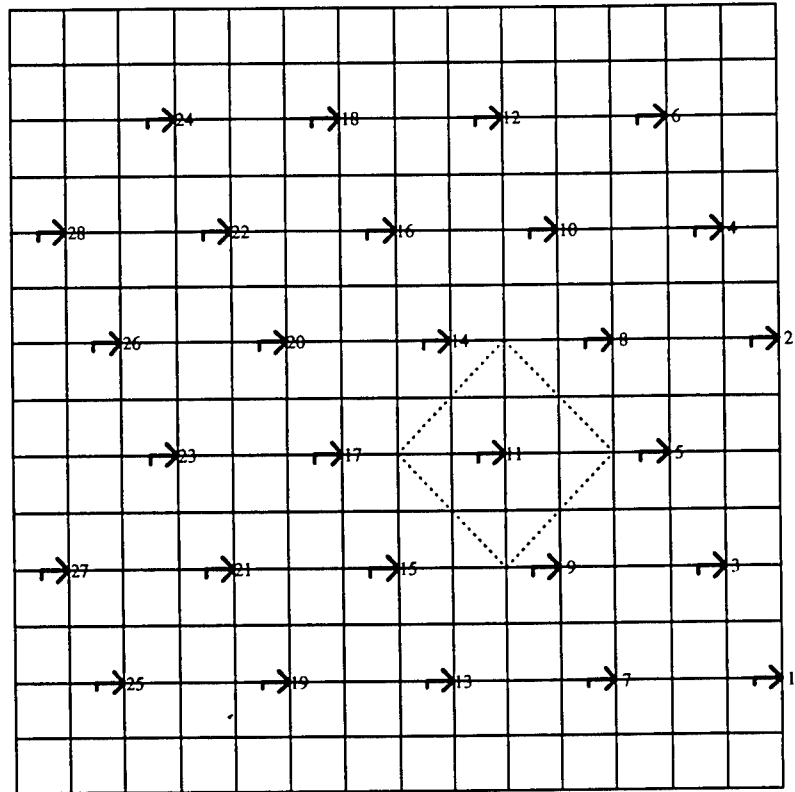
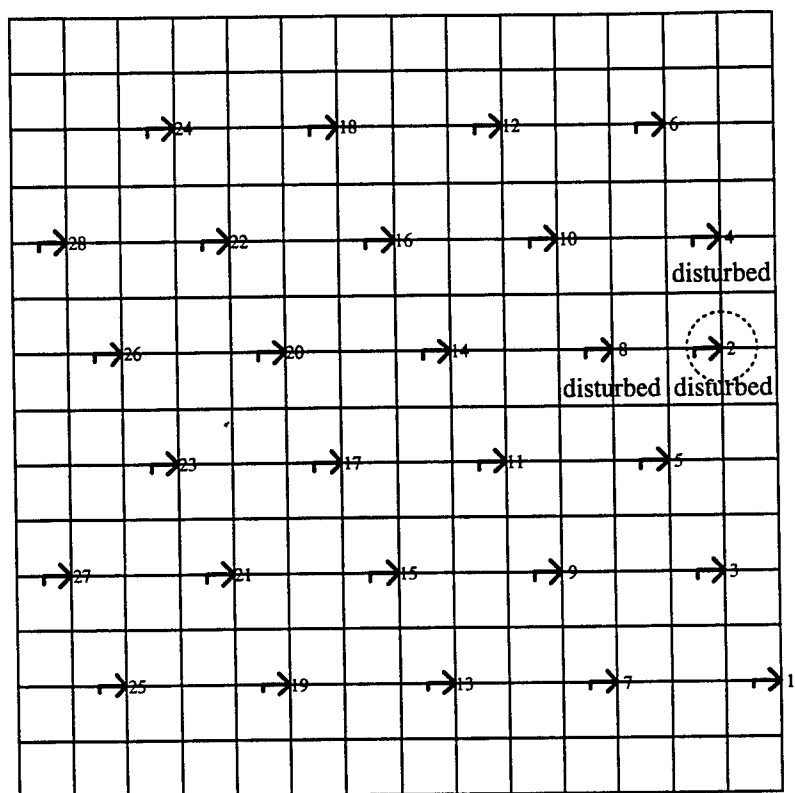


Figure 2. Example of the undisturbed field. The possible collision threat positions for airplane #11 are enclosed by the dotted-line diamond.



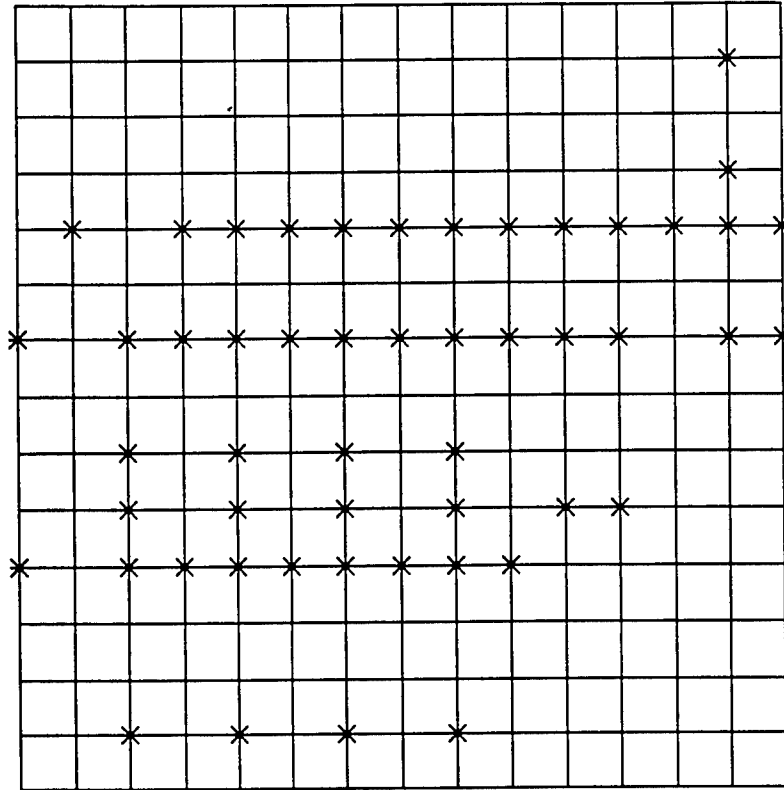


Figure 3 (b). The positions (marked by x) that are disturbed before the disturbance dies down.

Figure 4 (a) and (b) shows another example of field disturbance. In Figure 4 (a) the airplanes are in a pattern similar to the pattern in Figure 3 (a) except that there is a wider gap between the upper and lower groups. The same airplane (#2) is out of place. Figure 4 (b) shows the positions that are disturbed before the disturbance dies down. Comparing Figure 4(b) with Figure 3 (b), it is easy to see that the lower group is completely undisturbed. Apparently, the gap prevents the disturbance to propagate from the upper group to the lower group. Therefore, it is evident that local crowdedness decides the size of the avalanche, which is analogous to the role of the slope in the sandpile model.

If the above examples are repeated with different levels of local crowdedness, the number of airplanes disturbed will vary, and the final patterns (Figures 3(b) and 4 (b)) will be different. Simulation results show that the sizes of avalanches cover a wide range.

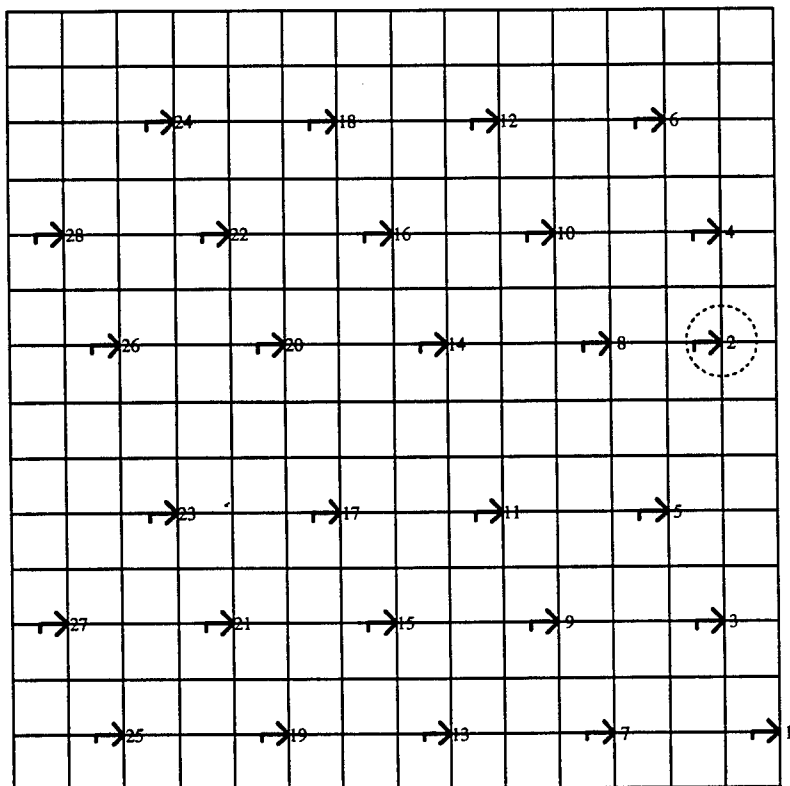


Figure 4. (a) The field is initially disturbed by airplane #2.

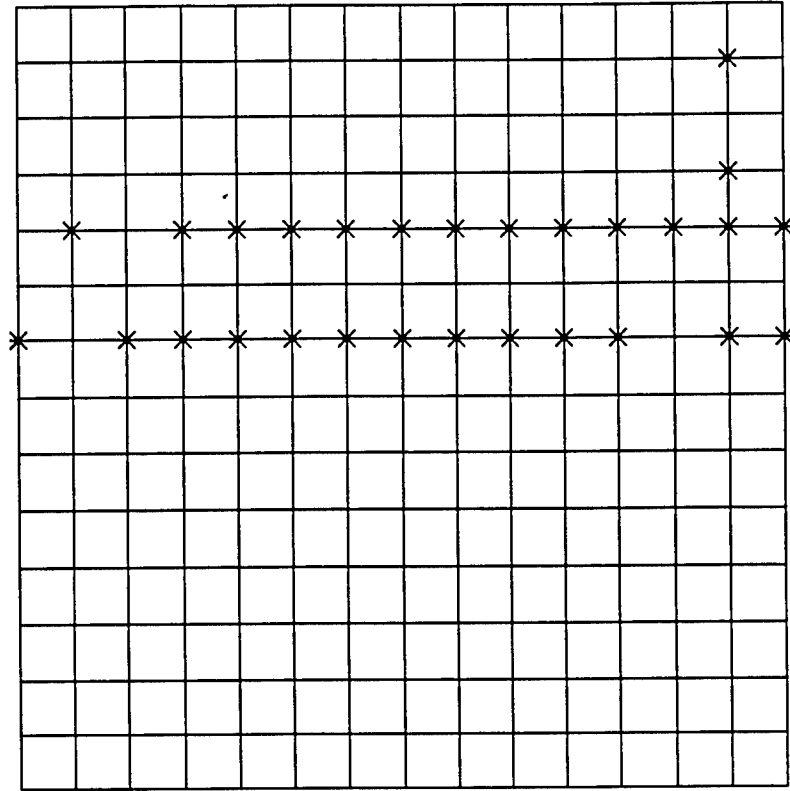


Figure 4 (b) The positions that are disturbed before the disturbance dies down.

Another consequence of the disturbance is that the number of airplanes in the field will fluctuate. The mechanism of the fluctuation is explained as follows. Once an airplane is disturbed and change its course, the “lifetime” of the airplane increases; that is, it stays in the field longer due to the detour. The number of airplanes in the field will increase. However, if the disturbance propagates to the left side of the field, new airplanes cannot enter the field because of the collision threats from those disturbed (out-of-place) airplanes. The number of airplanes in the field will decrease. Another possible reason for decreasing numbers, although it did not happen in the examples shown in Figure 2, 3, and 4, is some airplanes may be driven out of the field in the wake of disturbance.

Example: Crowded Airspace near an Airport

Figure 5 shows the field of the airspace near an airport. The field is a 21×21 square. The position of the airport is represented by a circle. After every unit time step (1 second is arbitrarily picked as the time step)

one new airplane enters the field from one of the edges. The entering position is randomly picked. All airplanes are flying toward the airport unless they are disturbed. Once an airplane reaches the airport, or it is forced out of bounds in disturbance, its lifetime is over. The airplanes which are still in the field are called "active".

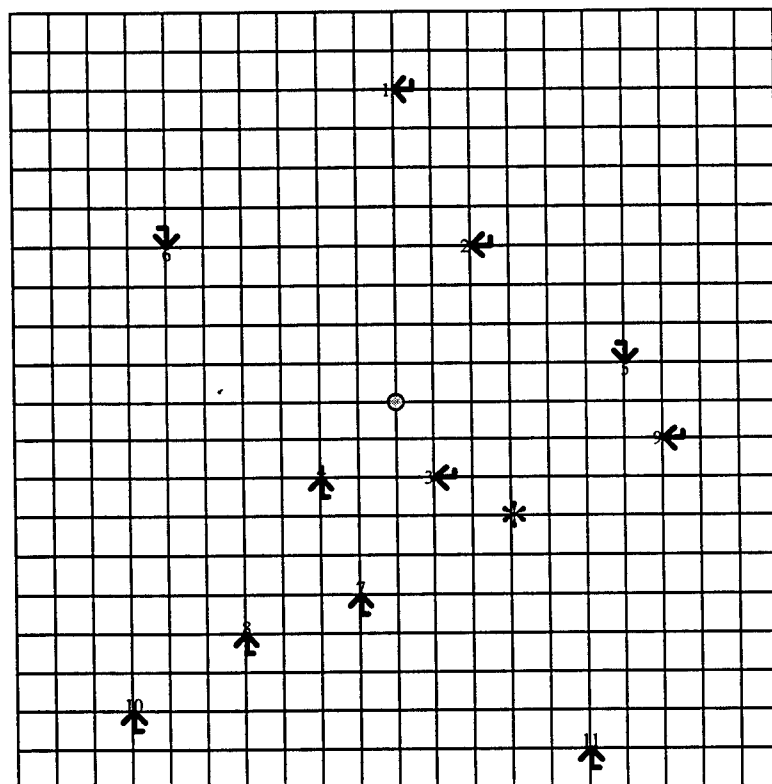


Figure 5. The field of airspace near an airport.

The main difference between this example and the example in Figure 2 is that as the airplanes approach the airport, the local crowdedness around the airport increases. After a minor disturbance far away from the airport dies down, the airplanes may again be involved in another disturbance as they fly closer to the airport. As the field is very crowded, there may be many disturbances all over the field. The influence regions of the disturbances overlap each other. It is very difficult to analyze each individual disturbance alone. This is also the major difference between this model and the sandpile model. In the sandpile model, once the avalanche is over, all sand grains will remain at their position until a new sand grain triggers a new avalanche.

Because of the difficulty in analyzing each individual disturbance, a global approach is used. The total number of active airplanes is recorded at each time step (1 second). This is analogous to the sandpile model, where the weight of the sand on the platform is measured with respect to time. Figure 6 shows the results for the first 400 seconds. At the beginning, airplanes enter the field at a constant rate and all stay in the field. The number of active airplanes increases linearly. After a while, some airplanes reach the airport, while some are forced out of the field. The number of active airplanes starts to level off. Since the landing rate is less than the rate of new airplanes entering the field, the field becomes more and more crowded. The scale of disturbance increases and many airplanes are driven off the field. After the crowdedness of the field is reduced, the scale of disturbance is small. The number of airplanes in the field starts to increase again. Therefore, the "steady state" value fluctuates. Figure 7 shows the steady-state number of active airplanes for a long period of time. The noise-like fluctuation is evident. Figure 8 shows the power spectral density of the steady-state fluctuation in a log-log diagram. It can be approximated by a straight line with a -1.9 slope. It fits in the model of $f^{-\beta}$ noise. This is another characteristic of self-organized criticality.

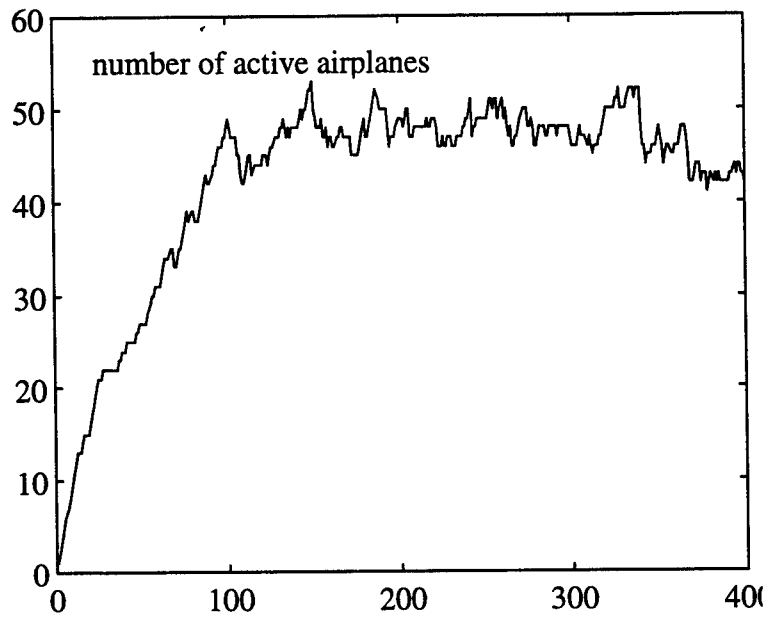


Figure 6. No. Of active airplanes vs. time.

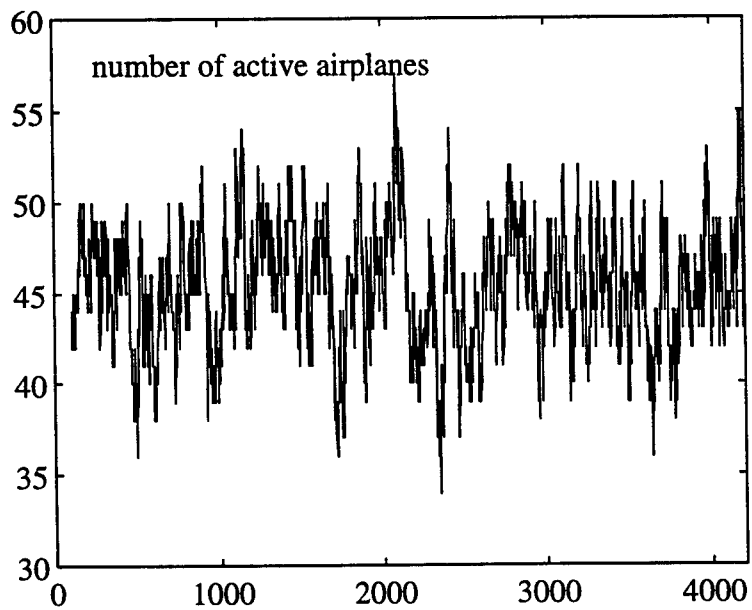


Figure 7. The steady-state number of active airplanes.

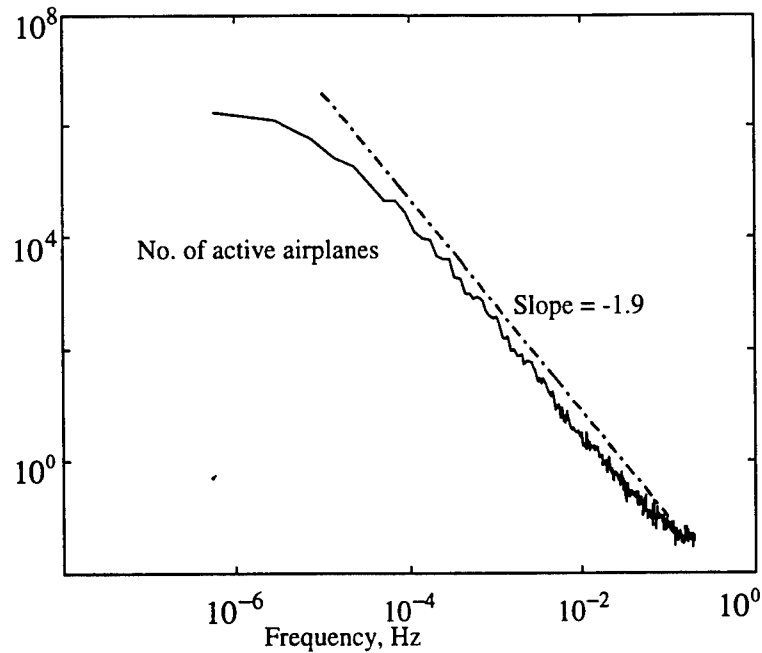


Figure 8. Power spectral density (128 averages) of steady-state number of active airplanes, airport open.

To examine the robustness of the criticality, the system is changed as follows. The airport in Figure 5 is closed due to bad weather. The airplanes still fly toward the airport, but are not allowed to land. Other conditions remain the same. Figure 9 shows the power spectral density of the steady-state fluctuation in a log-log diagram. The numbers may not be identical, but the fact that it satisfies a power law $f^{-1.9}$ noise profile remains the same.

Conclusion

This paper has established that the dynamic behavior of a crowded airspace can be explained by a self-organized criticality model. The air traffic system looks very much different from a sandpile. The sand grains in a sandpile rest at their respective stable positions after a disturbance. In the air traffic system, however, the airplanes keep moving. Despite the difference, they are analogous, as has been shown again and again in this paper.

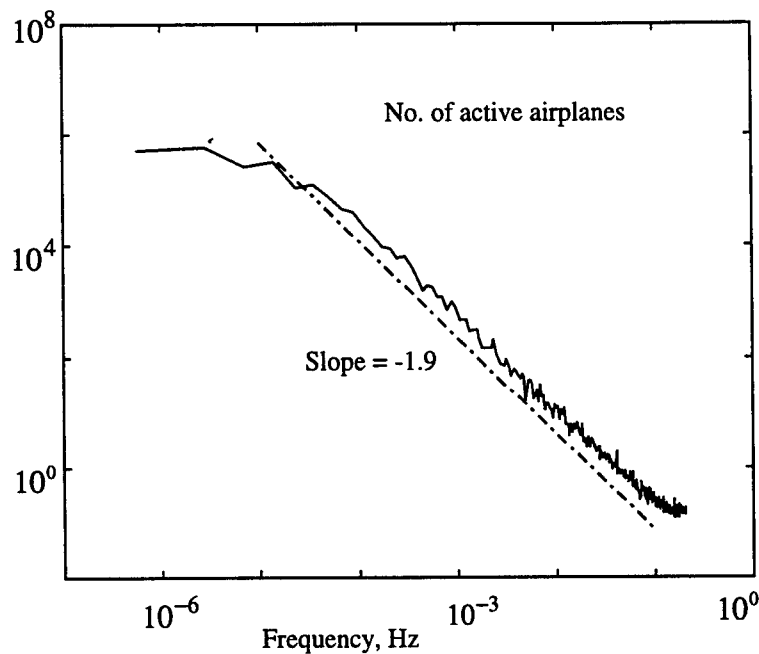


Figure 9. Power spectral density (128 averages) of steady-state number of active airplanes, airport closed.

The parameter that decides the critical state in an air traffic system is its local crowdedness. In this paper, the author did not establish a numerical value of the critical local crowdedness. The actual value will depend on the rules of collision avoidance. In the generic model used in this paper, the pattern shown in Figure 2 is very close to the critical local crowdedness.

The importance of realizing that an air traffic system exhibits the behavior of self-organized criticality is that it sets an absolute upper limit for the airspace crowdedness close to an airport. Below this value, the possibility of large disturbance is very low. The actual upper limit used should be lower than this critical value. How much lower will be decided by the tolerance of the disturbance.

References:

- 1 Uffelman, K.E., "Flying 800 Planes Simultaneously via Simulation. A powerful traffic simulator for FAA upgrade of air-traffic control", *Photonics spectra*, APR 1991, v 25 n 4, pp. 108-110.
- 2 Blair, E. L., et. al., "Distributed simulation model of air traffic in the national airspace system", *Proceedings of the 1995 Winter Simulation Conference*, Arlington, VA, 1995, pp. 1203-1206.
- 3 Tofukuji, N., "An Airspace Design and evaluation of Enroute Sector by Air Traffic Control Simulation Experiments", *Electronics & communications in Japan*, part 1, AUG 1996 v 79 n 8, pp. 103-113.

- 4 Tofukuji, N., "Air Traffic Flow Management Methods: Development and Testing by Real-Time Dynamic Simulation Experiments", *Electronics & communications in Japan*, part 1, MAY 1997 v 80 n 5, pp. 35-44.
- 5 Bak, P., Tang, C., and Wiesenfeld, K., "Self-Organized Criticality: An Explanation of $1/f$ Noise", *Physical Review Letters*, JUL 1987, v 59 n 4, pp. 381-384.
- 6 Bak, P., Chen, K., "Self-Organized Criticality", *Scientific American*, JAN 1991, pp. 46-53.
- 7 Bretz, M., et. al., "Imaging of Avalanches in Granular Materials", *Physical Review Letters*, 1992, v 69, pp. 2431.
- 8 Held, G., et. al., "Experimental Study of Critical Mass Fluctuations in an Evolving Sandpile", *Physical Review Letters*, 1990, v 65, pp. 1120.
- 9 Jaeger, H., Liu, C., and Nagel, S., "Relaxation of the Angle of Repos", *Physical Review Letters*, 1989, v 62, pp. 40.
- 10 Jaeger, H., and Nagel, S., "Physics of Granular State", *Science*, 1992, v 255, pp. 1523.
- 11 Nagel, S. R., "Instability in a Sandpile", *Reviews of Modern Physics*, January 1992, v 61 n 1, pp. 321-325.
- 12 Frette, V., et. al., "Avalanche Dynamics in a pile of rice", *Nature*, 1995, v 379, pp. 49.
- 13 Bak, P., "How Nature Works : The Science of Self-Organized Criticality", Springer Verlag, NY, 1996.
- 14 Musha, T., Higuchi, H., "The $1/f$ fluctuation of traffic current on an expressway", *Japanese Journal of Applied Physics*, 1976, v 15, pp. 1271-1275.
- 15 Nagel, K., Herrmann, H. J., "Deterministic models for traffic jams" *Physica A*, OCT 1993, v 199 n 2, pp. 254-269.
- 16 Nagel, K., Paczuski, M., "Emergent Traffic Jams", *Physical Review E*, 1995, v 51, pp. 2909.
- 17 Nagel, K., Rasmussen, S., Barrett, C. L., "Network Traffic as a Self-Organized Critical Phenomena", in *Self-organization of complex structures: From individual to collective dynamics*, edited by Schweitzer, F., Gordon and Breach, London, 1997, pp. 579-592.

Appendix

When there is another airplane in one of the collision threat positions, the allowed maneuvers are as follows. Figure A1 shows the disturbance coming from one of the x-marked positions. The arrows show the three allowed maneuvers. The rules encourage, but do not require, the airplane to move “away” from the threat (to the right in the figure). Sometimes, if one of the other two directions takes the airplane closer to the airport, it may be chosen. A weighting factor is put in to make the decision.

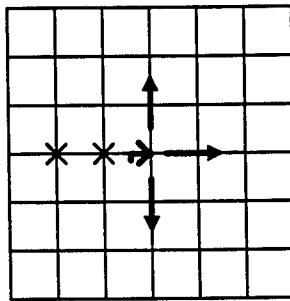


Figure A1. Disturbance positions and the allowed moves.

Figure A2 shows another possible collision threat position and the allowed maneuvers. There is no preference between these two moves. Other factors, such as which move brings the airplane closer to the airport, will decide the maneuver.

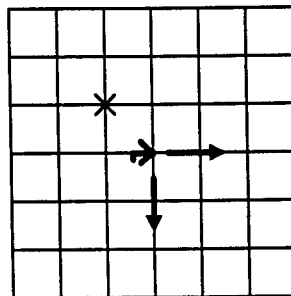


Figure A2. Disturbance positions and the allowed moves.

**THE MIAMI CORPUSLATIN AMERICAN DIALECT DATABASE:
CONTINUED RESEARCH AND DOCUMENTATION**

Beth L. Losiewicz
Associate Professor
Department of Psychology and Natural Sciences

The Colorado College
14 E. Cache La Poudre
Colorado Springs, CO 80901

Final Report for:
Summer Research Program
Rome Laboratory

Sponsored by:
Air Force Office of Scientific Research
Bolling Air Force Base, Washington, DC

And

Rome Laboratory

August 1997

**THE MIAMI CORPUS LATIN AMERICAN DIALECT DATABASE:
CONTINUED RESEARCH AND DEVELOPMENT**

**Beth L. Losiewicz
Assistant Professor
Psychology Department
Division of Natural Sciences
The Colorado College**

ABSTRACT

The work reported herein is a continuation of the research and development being carried out on the Latin American Spanish Dialect database collected in Miami in 1995 by Drs. Rekart and Losiewicz with a Rome Laboratory and Analytical Systems Engineering Corporation (ASEC) collection team: a digitally recorded database containing 228 speakers from 10 different Latin American countries, developed by the Speech Processing Group at Rome Laboratory to aid in continued research on the feasibility of automatic machine dialect recognition. This report summarizes the development of an extensive PC-based database documenting the detailed information about each speaker in the corpus, including: language background, dialect features and technical recording details for each speaker. It also summarizes the research that has been conducted with the database thus far, and the documentation and research issues that still need to be addressed in order to make maximum use of the information contained in the database, towards the eventual goal of developing automatic dialect recognition algorithms.

THE MIAMI CORPUS LATIN AMERICAN DIALECT DATABASE: CONTINUED RESEARCH AND DEVELOPMENT¹

Beth L. Losiewicz

Overview of Past Work: Collection and Description of the Database

In January 1995, Rome Laboratory sent a team of linguists and lab personnel to Miami Florida to begin collection of a Latin American Dialect Database to be used in developing machine speech recognition algorithms for Spanish (Zissman, Gleason, Rekart and Losiewicz, 1996). Participants were recruited via posters, newspaper advertisements and word of mouth, recorded at a university campus, and were paid \$10 each for their participation. Recordings were made using a Sennheiser Close Talking Microphone, a Shure FP11 pre-amp and a Sony TCD-D7 DAT digital recorder. Twenty to 45 minutes of Spanish and English, read and spontaneous speech, was collected from each of 228 speakers from a variety of dialect regions in Latin America. Extensive biographical background information relevant to language use was documented for each speaker - including places lived, extent of exposure to English, region of origin of parents, languages spoken at home in childhood, other languages, extent of exposure to and use of English, etc.

¹ The author would like to acknowledge the assistance of Jim Cupples of Rome Laboratory, and Roy Ratley of ASEC, in the planning stages of database development; and Gail Libent-Smith, of ASEC, for assistance in data analysis.

Both read and spontaneous Spanish speech was collected from each speaker, with read and spontaneous English also collected from those speakers with sufficient skills in that language. Each elicitation session began with the elicitation of spontaneous Spanish, in the form of an interview in which the speaker was encouraged to do as much of the talking as they were willing to do. The main goal of the Spontaneous Speech question set was to elicit a flow of uninterrupted, relaxed speech from the participant (e.g., What surprised you most when you came to the US? What did you like best? Tell me about your family. Tell me about your favorite movie. What was the happiest day of your life? etc.). Questions were also asked about language or dialect-relevant biographical information (e.g., Where were you born? How long did you live there? Where else have you lived? At what ages did you move? Where were your parents born? What language was spoken at home? When did you come to the US?, etc.). The purpose of these questions was to verify and expand on the information elicited from each participant prior to the recording session, on a written biographical data sheet . A third type of question nominated topics encouraging the use of dialect cue-bearing words (e.g., What is the climate like in your native region? (*lluvia*). What kinds of food are common there? (*arroz*). The fourth type of question was designed to elicit words relating to US place names, modes of transportation, and numbers, dates and time in general (e.g., Where have you visited? Where would you like to visit? How would you get there? How do you get to work every day? What year were you born? What year did you come to the US? Tell me about your daily schedule, etc.).

After 10-20 minutes of spontaneous speech was elicited, each speaker was asked to read a series of Spanish sentences designed to contain dialect-cue-bearing words (e.g., *puerto, pan, leche, ajo, fuerte, en frente, polvo, verde, bello, dolor, gente, plaza, callo, cayo, hielo, curvas*). This was followed by a reading of a phonetically balanced paragraph in Spanish and a Cloze (fill-in-the-blank) passage eliciting first name, gender, date, time, area code and a telephone greeting word (usually *Alo?* or *Hola*). Last of all, each speaker read aloud the digits 0 through 10, twice each, in a different random order for each speaker. Participants also read aloud 2 additional texts (one from a Mexican newspaper and one from a Spanish culture textbook; designated as “variable” texts, as each speaker read a different text). After the Spanish speech was elicited, speakers were asked to read the same digits (in a different random order) in English, and, if they were able, to read a translation of the Cloze text aloud in English; followed by a series of English sentences designed to elicit particular phonemes, a variable (newspaper) text in English, and a phonetically balanced English paragraph. If the speaker was capable of dialogue in English, they also completed a short section of spontaneous English using translations of the question set used in the Spanish elicitation. (For further details about the Elicitation Instrument, see Rekart and Losiewicz, 1995. For further details about the collection effort, see Losiewicz, 1997)

After collection each speaker was categorized according to country of origin, based on a weighting of: how they identified themselves; where their parents were born and

raised; where they were raised, especially between ages 2 and 18; and the dialect they identified themselves as speaking

Although the decisions to label speakers by country of origin did not seem difficult (there were few or no “borderline cases” where a determination wavered between two choices) it is currently unknown how much dialect variation/lack of purity may exist in the speech of those speakers who have lived in more than one place, and/or have had contact with a variety of different dialects. The few speakers who identified themselves as atypical or “contaminated” speakers of their native dialect, were noted, and their speech has not been used in any subsequent analysis.

Overview of Past Work: Analysis of Performance of Human Experts

In 1996 Losiewicz used the database to investigate the accuracy with which expert humans (Latin-American Spanish dialectologists) could identify the region of origin of a subset of (90) speakers from the database, after listening to 3, 6, or 30 seconds of speech. The segments were taken from the middle portion of the spontaneous elicited speech for each speaker, and were edited only to ensure that no explicit clues (names of cities, mountains, typical foods, etc.) would give a cue to the dialect region. The human experts were asked to choose the country of origin of the speaker from a list of 11 countries, (all of which appeared on the test tape at least once)² and were also asked to specify and rank order the cues they used in the identification. The expert performance

² The countries were: Argentina, Chile, Colombia, Mexico, Ecuador, Peru, Costa Rica, Puerto Rico, Cuba, Venezuela and Nicaragua. Discovery of a clerical error after the tapes were distributed reduced the number of countries actually represented on the tape to 10: the one speaker originally identified as Costa Rican was discovered to have been mislabeled. Although born in Costa Rica, this speaker had Cuban parents and spent his critical language years (from age 2-18) in a Cuban community.

was quite variable, with the best dialectologists correctly identifying 49% of the speakers, and the worst performing below chance (< 9 %). There was a significant correlation between each dialectologists' confidence in their decisions and their accuracy, with this correlation being somewhat greater for those dialectologists who performed the best in the identification task. The dialectologists reported relying most on intonation cues, followed closely by phonetic cues, followed (in decreasing order) by: lexical, rhythm, speech and pitch cues. Overall, performance was the same across segments of all lengths, although there was a trend for intonation cues to be reported as being important more frequently for the shorter segments. A confusion matrix was also developed to study which dialects were being confused with which others. The most common misidentification was a mutual confusion between Cuba and Puerto Rico, (21% of the time) followed by a mutual confusion between Venezuela and Puerto Rico (approximately 12% of the time). A striking feature of the confusion matrix was its occasional asymmetry (e.g., even though Cuban speakers were misidentified as Venezuelans 12% of the time, Venezuelans were only misidentified as Cubans 2% of the time). It was also noted that speakers from a Caribbean country were much more likely to be misidentified as being from another Caribbean country, while non-Carribeans were most likely to be confused with other non-Carribeans.

Overview of Past Work: Machine Analysis

The MIT Lincoln Laboratory Speech Group under contract with Rome Laboratory, tested off-the-shelf machine language identification algorithms with 3 minute

spontaneous speech segments from 143 Cuban and Peruvian speakers from the Miami Corpus database. (See, Zissman, Gleason, Rekart and Losiewicz, 1996.) After training, the Lincoln Laboratory algorithm could make a correct identification (in a binary forced choice task) 84% of the time (chance = 50%).

ITT Aerospace Communications Speech Group, also under contract with Rome Laboratory, in a three-way decision task (Peru, Cuba or Other), found that their language identification algorithm chose accurately 45% - 50 on segments ranging in length from 5 to 60 seconds in duration (chance = 33%) (Li, 1997).

Delectability and identifiability of Spanish-accented English speech was also investigated in a recent Ph.D. dissertation completed by Rene Arechiga at the University of New Mexico, using speech from this corpus.

Current Work

The preliminary studies reviewed above all reached the same conclusion: that identification of region of origin of an unknown speaker based on dialect cues is a promising avenue for further research and perhaps eventual development. The Miami Corpus speech provided an excellent starting point for these early studies, and should continue to provide a rich data source in the future. However, up to the present, studies have been hampered by the fact that the extensive information collected about each speaker was not yet available in a format conducive to easy analysis. The need for a carefully-planned, flexible and comprehensive information database became apparent: to facilitate analyses of the multiple factors that may influence dialect characteristics and the

ability of machines to detect them. Thus, the goal of the summer project work reported herein was to document and develop such a database as the essential next step towards further testing and analysis.

The first task was the development of a PC-based information database with a record for each speaker, containing all information about that speaker from a variety of sources. This database has been developed, with data fields recording the unique Speaker Number for each speaker; information about country and city of origin; places lived between age 2 and 5, between ages 6 and 18, and during adulthood; parents' region of origin; length of time in US; extent of foreign travels; and knowledge of other languages. The record for each speaker also holds technical recording information documenting when and where each speaker was recorded, with details about the equipment used, the equipment settings and microphone placement. Data fields were also designed to hold details of the dialect analysis done on each speaker by Dr. Rekart (ASEC consultant for Rome Laboratory) along with documentation of the segmentation and storage work done on each type of speech for each speaker. Fields were created to identify the variable texts read by each speaker, as well as details from the Human Expert Identification Study (Losiewicz, 1995). The Master Plan also provides for entry of information about the results of various Machine Dialect Identification tests, to be entered into the record for each speaker. This central, complete database was the first step towards facilitating further research, as it allows diverse, quickly executed, flexible sorts to be done on the

data to expedite future analyses and tests.³ A sample record for single speaker in the database is included in this report as Appendix A.

The second task accomplished this summer was the writing of a detailed follow-up documentation of the original elicitation efforts based on extensive notes made by Dr. Losiewicz during the original collection (Losiewicz, 1997). Although the term of the summer research program was insufficient to complete this document it is approximately 85% complete, and includes details about the Elicitation Procedures, technical details about the recording equipment and procedures, analyses of the efficacy of various recruitment and collection approaches, suggestions for ongoing collection, etc.

The third task was the development of a Master Plan for completing, verifying, managing, and disseminating the PC-based information database. Slightly less than half of the required information has been entered into the database to date, and a separate PC-based database was required to document the tasks that still need to be completed (the "Document and Management Plan" or "DMP"). Further, since multiple entities need access to the database in connection with Air Force initiatives,⁴ it is critical that clear, centrally controlled documentation exists both about the speakers in the database and the various disseminations and uses of the database. Thus the DMP database not only maps out future database management needs, but documents data disseminations, and past management tasks completed (with detailed notes) - thus serving as a historical record of

³ Some of the useful sorts to date have been: developing a list of speakers who identified their dialect as atypical; a sort that will eventually allow a correlation to be computed between details of biographical background with dialect identifiability; a sort allowing comparison of machine and human identification results for any given speaker, etc.

⁴ E.g., MIT LL Speech Group, and ITT Aerospace Communications Division: and the number is expected to grow in the future.

what has been done and by whom, with the goal of maintaining current, accurate, centralized information to ensure continuity of effort and avoid inadvertent task duplication.

Future Work

With the Miami Corpus Speaker Information Database design 90% complete, and with data entry currently in progress(30% complete), the next task is to gather clues as to what sorts of features are being used by humans and machine to identify dialects, and what characteristics of the speech of any given individual contributes to his dialect identifiability.

Although humans have some success identifying dialects, no controlled psycholinguistic study has ever attempted to systematically discover how they do so. By analyzing similarities and differences between dialects in terms of the acoustic features available to humans and to machines (phonemes, prosody, Cepstra, Spectra, etc.), and by correlating the presence or absence of these factors to human and machine performance, we should be able to develop hypotheses about which features are most useful in distinguishing between dialects, which features are used by humans, and whether machines are capable of using the same cues. As reviewed above, Losiewicz (1996) began investigation of the cues used by human experts, but many more questions remain to be asked.

For example: can we find confirmatory evidence that human experts actually do use the cues they claim to be using in dialect identification? How long does it take for a

human to develop expertise in dialect identification? Presumably, if even non-experts can be trained quickly to distinguish between dialects, this increases the likelihood that machine identification algorithms are feasible. However, if long training from childhood (as in the case of a well-traveled native speaker) is necessary to achieve satisfactory human performance, it is more likely that unknown human “hard-wiring” or developmental factors are involved, which in turn reduces the likelihood that machines would ever outperform humans.

Further investigation is also needed to determine whether there are identifiable differences between those human experts with excellent performance and those with poorer performance? Can we exploit the knowledge of this difference in our machine algorithms? Work this summer began to address this question, and, although the summer time-frame did not allow completion of the analysis, certain trends are becoming apparent: identification is weakly (if at all) correlated with a dialectologist’s self-declared area of expertise; and native speakers of a Latin American dialect uniformly outperform non-native Speakers, regardless of other indicators of expertise. This may result from any one of (or a combination of) factors: that some special sort of speech processing is going on in native speakers that cannot be matched by those who learned the language as adults; that an “ear” for the language is more important to accurate identification than any amount of “book” knowledge; that prosody may be one of the critical elements in dialect identification, etc.

In short, investigation of differences in the performance of human experts may begin to give us cues that would allow us to develop a workable model of how humans identify dialect, which in turn should help us develop and fine tune a workable machine algorithm.

Another variable that needs to be investigated more thoroughly is the amount of variability that exists between speakers of a given dialect, and whether that variability affects dialect identifiability. The database developed this summer will, for the first time, make feasible an investigation into which of many biographical and language background factors are predictive of dialect strength and consistency, and how those factors interact (e.g., language of parents, or peers, age of learning a second language, etc.). This in turn will provide us with a framework within which to interpret the results of various machine algorithms.

We also need more extensive knowledge about the performance parameters of machines, and of humans. How complex can the task become before machine and human performance deteriorates? Obviously a binary forced choice is a much simpler task than choosing between 11 possible countries. What does the complexity/accuracy curve look like for humans? For machines? What is the optimum level of complexity (i.e. how complex of a classification can we eventually ask machines to do without sacrificing accuracy?); is this level different than the optimum complexity level for humans?

Once we know the performance parameters of the machines we also need to develop and test Expert System classification schemata for categorizing speakers. It is

envisioned that a complex “family resemblance” sort of classification system will be eventually needed to efficaciously sort dialects, but before this can be even attempted, more base-line analysis needs to be completed.

A comparison of machine and human performance is sorely needed at this stage as well. Are the cues used by the machine algorithms the same, or different, than those used by humans? If different, would a change in algorithm substantially increase the accuracy of identification?

In short, analysis of the Miami Corpus database, and related studies and tests has begun, but a great many more questions need to be asked, and many more tasks need to be completed before machine dialect identification can become a reality.

REFERENCES

- Arechiga, Rene. (1997). Detection and Recognition of Spanish Accented English. Ph.D. Dissertation, University of New Mexico, Dept. of Engineering.
- Li, K. P. (1997). Dialect Identification. ITT Project Presentation, Contract No. F30602-94-C-0289. Presented at Rome Laboratory May, 1997.
- Losiewicz, B. (1997). Miami Corpus Latin American Dialect Database Elicitation Narrative. Unfinished report. Speech Processing Group, IRAA, Rome Laboratory, Rome, NY.
- Losiewicz, B. (1995). Human expert identification of Latin American Dialects. Summer Research Program Follow-on Grant Final Report. AFOSR; Bolling AFB, Washington, DC.
- Rekart, R. and B. Losiewicz. (1995). Elicitation Instrument and Elicitation Procedures: Air Force Dialect ID Database. MIT Lincoln Laboratory Project Report.
- Zissman, Marc, T. Gleason, D. Rekart and B. Losiewicz. (1996). Automatic dialect identification of extemporaneous, conversational, Latin American Spanish speech. In ICASSP Proceedings May, 1996.

APPENDIX A: SAMPLE DATA RECORD FOR A SINGLE SPEAKER

MIAMI CORPUS: ALL DATABASE FIELDS HUMAN ID TESTED? ☒

Speaker Number: 2039 Origin (country) CUBA
Sex M (city) MATANZAS

Original DAT tape # 1020

Date recorded 1/23/95

Location: MIAMI

I. BIOGRAPHICAL DATA

Room: FIU 521A

Age 47

Equipment: BL

Education: UNIV 5

Mic Placement LEVEL WITH LIPS, 3 "
AWAY

Years in U.S: 3

Born (country, city): CUBA, MATANZAS

Lived (age 2-5): CUBA, MATANZAS

Lived (age 6-18): CUBA, MATANZAS

After 18 also lived: US, MIAMI
(at least 1 year)

Father from: CUBA, HAVANA

Mother From: CUBA, HAVANA

Comments:

II. COMMENTS ON DIALECT, SPEECH AND RECORDING QUALITY

This Section may need to be modified to accommodate Dr. Rekart's data.)

SPANISH IS: (Check One) ☐ MOSTLY STANDARD (Few or no dialect features) INITIALS
☐ SOMEWHAT NON-STANDARD (Some dialect features) OF JUDGE:
☐ DEFINITELY NON-STANDARD (Many dialect features)

Comments on Spanish:

DIALECT
FEATURES (Check One) ☐ Mostly TYPICAL of region of origin INITIALS
☐ Somewhat ATYPICAL of region of origin OF JUDGE:
☐ Definitely ATYPICAL of region of origin

Comments on Dialect:

Comments on English: NO SPONTANEOUS ENGLISH; NO ENGLISH SENTENCES

APPENDIX A (CONTINUED)

Other Languages? ENGLISH

Comments on Speech:

Speech or Hearing Problems?

Comments on Recording:

III. SPANISH TEXT SEGMENTATION

<u>Spanish Spontaneous Speech</u>	SAMPLE	
	BEGIN #	END #
Spanish Spontaneous		

OTHER LOCATIONS
DAT B0011

Spanish Spontaneous Place Names

Spanish Spontaneous Digits

Spanish Read Text

Fixed Text

Spanish Sentences

Spanish Shibboleths

F. Vanero
(phonetically)

Spanish Cloze

Spanish Read Digits

Variable Text

Paragraph #

III.22 Span. Newspaper

2-10 Spanish Civ. y Cul.

APPENDIX A (CONTINUED)

IV. ENGLISH TEXT SEGMENTATION

English Spontaneous Speech

English Spontaneous

English Spontaneous Place Names

English Spontaneous Digits

ENGLISH READ TEXT

Fixed Text

Rainbow (phonetically balanced)

English Sentences

English Cloze

English Read Digits

Variable Text

Paragraph #

VII.49 English Newspaper

V. HUMAN DIALECT IDENTIFICATION RESULTS

(14 Dialectologist choosing between 11 countries)

Dialectologists who correctly ID'd Country 4 Who correctly ID'd City 0

Cues Reported by successful Dialectologists

Weighted % LIST

Intonation

Phonemes

Other Cues

Comments on Cues

APPENDIX A (CONTINUED)

		<u>Number of times this mistake was made</u>
Most often Mistaken as (country)	PUERTO RICO	4
Second Most often mistaken as	CHILE	2
Third Most often mistaken as		
Comments	Mistaken ID	MISTAKEN ONCE EACH AS: ECUADOR, COLOMBIA

WHICH DIALECTOLOGIST CORRECTLY IDENTIFIED THIS SPEAKER (1= CORRECTLY IDENTIFIED)

(See Human Dialect ID Folder for Identity of Dialectologists BL)

O	J	Q	S	N	T	L	B	G	K	W	H	R	D	F
	1	1		1			1							

MICROWAVE HOLOGRAPHY USING INFARED THERMOGRAMS OF ELECTROMAGNETIC FIELDS

**John D. Norgard
Professor
Department of Electrical and Computer Engineering**

**University of Colorado
1420 Austin Bluffs Parkway
Colorado Springs, CO 80917-7150**

**Final Report for:
Summer Research Program
Rome Laboratory**

**Sponsored by:
Air Force Office of Scientific Research
Bolling Air Force Base, Washington, DC**

And

Rome Laboratory

August 1997

MICROWAVE HOLOGRAPHY USING INFRARED THERMOGRAMS OF ELECTROMAGNETIC FIELDS

John D. Norgard
Professor/ECE
Department of Electrical & Computer Engineering
University of Colorado

Abstract

An infrared (IR) imaging technique for measuring electromagnetic (EM) fields is being developed to map two-dimensional EM field distributions near a radiating antenna or a scattering object. The magnitude of the field is determined by measuring the temperature distribution (due to Joule heating) developed in a thin lossy 2D detector screen placed in the region over which the field distribution is to be measured. The measured temperature distribution is presented as an IR thermogram, i.e. as an equi-temperature contour plot, which can be interpreted to yield the value of the field intensity incident on the screen. The phase of the electric or magnetic field can also be determined with this technique using holographic interference techniques.

The measured phase, in conjunction with the measured magnitude of the field, is being used to determine the radiation pattern of an antenna-under-test (AUT). The phase is measured in the near field of the AUT. Two different techniques for phase-retrieval from magnitude only data are being developed. One technique extracts the phase from the IR thermogram using an iterative "Plane-to-Plane" (PTP) 2D Fourier Transformation convergence method. The other technique extracts the phase from the magnitude only data based on holographic interference patterns developed between the AUT and a known microwave reference antenna standard. The reference standard is being supplied and calibrated by the National Institute of Standards & Technology (NIST/Boulder) through a cooperative partnership with the University of Colorado at Colorado Springs (UCCS). The advantages and disadvantages of these two holographic techniques, viz. their inherent accuracies, are being determined and compared.

Numerical algorithms are being developed to collect and process the holographic data. The original numerical algorithms were developed at and in conjunction with NIST/Boulder. Calibrated magnitude and phase data on the reference antenna also were measured at NIST/Boulder. The codes were further refined and enhanced at RL.

In the PTP method, two IR thermograms are made several wavelengths apart in the radiating near-field of the AUT. In the holographic interference technique, four holograms are made at one near-field location, one for the magnitude of the AUT only, one for the magnitude of the reference antenna alone, and two interference patterns with different phase shifts between the reference antenna and the AUT. These data can be processed to determine the complex intensity (magnitude and phase) of the field at any distance in front of the AUT (including the aperture plane).

Numerical simulations of the PTP holographic technique were performed (using data collected on another project) to predict the accuracy of the PTP technique. Numerical simulations of the holographic interference technique were not attempted at this time.

Initial tests to prove the validity, accuracy and sensitivity of these techniques were not performed this summer due to the non availability of the anechoic chamber at the Electromagnetic Vulnerability Analysis Facility (EMVAF) at Rome Laboratory (RL). Experimental tests will be performed at RL at a later time. Numerical simulations of the holographic interference technique also will be completed at a later time.

Six papers were presented at international IR and EM conferences. One paper was published in an IR journal. Several papers are being planned for presentation at several IR conferences next year.

**MICROWAVE HOLOGRAPHY
USING INFRARED THERMOGRAMS OF ELECTROMAGNETIC FIELDS**

John D. Norgard

Table of Contents

1.	Introduction
2.	PTP Technique
3.	Magnitude Measurements
3.1	Thermal Convection
3.2	Thermal Conduction
3.3	Thermal Radiation
3.4	Thermal Equilibrium
4.	Magnitude Results
5.	Phase Measurements
6.	Phase Results
6.1	Simulation
6.2.	Experiments
7.	Conclusions
8.	Future Work
9.	Publications
	Acknowledgments
	References

MICROWAVE HOLOGRAPHY

USING INFRARED THERMOGRAMS OF ELECTROMAGNETIC FIELDS

John D. Norgard

An infrared (IR) measurement technique is being developed to measure electromagnetic (EM) fields. This technique uses a minimally perturbing, thin, planar IR detection screen to produce a thermal map (IR Thermogram) of the intensity of the EM energy over a two-dimensional region. EM fields near radiating microwave sources and scattering objects can be measured with this technique. The electric and magnetic fields can be measured separately. Electric fields can be measured with a lossy conductive screen; magnetic fields can be measured with a lossy ferrite screen. Numerical simulations of the holographic technique were performed using data collected on another project to predict the accuracy of the different techniques. The magnitude and phase of the field can be determined. The magnitude of the field is determined at each point (each pixel) in the thermogram by measuring the difference in the temperature in the detector screen when illuminated by the field and when no incident field is present (background ambient temperature). The phase of the field is determined by holographic interference techniques.

1. Introduction

In this study, numerical algorithms were developed to retrieve phase information from the measured IR magnitude-only data. This phase information can be used to develop a near-field to far-field measurement capability.

Two different phase-retrieval techniques are being developed. One technique extracts the phase from the IR thermogram using a "Plane-to-Plane" (PTP) 2D Fourier Transformation convergence method. The other technique extracts the phase from the magnitude only data based on the holographic interference pattern developed between the AUT and a known microwave reference antenna standard. The reference standard is being supplied and calibrated by the National Institute of Standards & Technology (NIST/Boulder) through a cooperative partnership with the University of Colorado at Colorado Springs (UCCS). The advantages and disadvantages of these two holographic techniques will be compared.

The results of the PTP simulation study are given below.

2. PTP Technique

The purpose of this study is to develop and evaluate a technique for obtaining magnitude and phase information from thermographic measurements of microwave field intensity patterns. This work is

described in more detail in [1,2]. The process of determining the field magnitude data from Infrared (IR) thermograms is first described; then, based on magnitude only measurements, a phase retrieval technique is presented.

3. Magnitude Measurements

The basic principle involved in IR measurements of the magnitude of a radiating field is that a lossy material positioned in the field will heat as it absorbs power from the field. Since the absorbed power is related to the strength of the field, the temperature rise in the material can be measured and then related to the field strength.

For a thin, low-loss material, the field in the material can be approximated as constant; thus, the power absorbed per square meter in the material is adequately described by [3, 4]:

$$P_{abs} = \frac{1}{2} \int_0^d [(\sigma' + \omega \varepsilon'')(E_t^2) + \omega \mu''(H_t^2)] dn \quad (1)$$

where \hat{n} is a vector normal to the surface of the lossy material, d is the thickness of the lossy material, ω is the radian frequency, σ' is the real part of the material conductivity, ε'' and μ'' are the imaginary parts of the complex permittivity and permeability of the material, respectively, and the t subscripts on the field quantities imply the tangential components.

In this work, Teledeltos resistive paper was used as the lossy material. The material properties of this paper are $d = 80 \mu\text{m}$, $\sigma' = 8 \text{ S/m}$, $\varepsilon'' \cong 0$, and $\mu'' \cong 0$. Thus, for the Teledeltos paper, the absorbed power can be described by:

$$P_{abs} = \frac{\sigma'}{2} \int_0^d [E_t^2] dn \quad (2)$$

Consider the illustration of a propagating electric field incident on a sheet of thermal paper shown in Figure 1. As a result of the discontinuity between the wave impedance in the material to the wave impedance in the surrounding air, there are reflecting waves at both boundaries of the material in addition to the transmitted waves.

The total electric field in the absorbing material can be described as the summation of the positive traveling wave transmitted from the incident wave through the material boundary and the negative traveling wave resulting from a reflection of the transmitted wave off the back side of the absorbing material. Mathematically, this is represented as:

$$E_2 = E_2^+ e^{-\gamma_2 z} + E_2^- e^{-\gamma_2 z} \quad (3)$$

where

$$\gamma_2 = j\omega\sqrt{\mu_2\varepsilon_2} \sqrt{1 + \frac{\sigma_2'}{j\omega\varepsilon_2}} = \alpha_2 + j\beta_2.$$

The square of this electric field is therefore:

$$E_2^2 = |E_2^+|^2 e^{-2\alpha_2 z} + |E_2^-|^2 e^{2\alpha_2 z} + 2 \operatorname{Re} \left\{ E_2^+ E_2^{-*} e^{-j^2 \beta_2 z} \right\} \quad (4)$$

Using this result in equation 2 and integrating, the total absorbed power per square meter in the Teledeltos paper is:

$$P_{abs} = \frac{\sigma}{4} \left[\frac{|E_2^-|^2}{\alpha_2} (e^{2\alpha_2 d} - 1) - \frac{|E_2^+|^2}{\alpha_2} (e^{-2\alpha_2 d} - 1) + \frac{2}{\beta_2} \operatorname{Re} \left\{ E_2^+ E_2^{-*} j (e^{-j^2 \beta_2 d} - 1) \right\} \right] \quad (5)$$

Through the application of boundary conditions, E_2^+ and E_2^- can be determined from the original tangential incident electric field, E_{inc}^+ as:

$$\begin{aligned} E_2^+ &= E_{inc}^+ \frac{\Gamma + 1}{1 - \Gamma^2 P^2} \\ E_2^- &= E_{inc}^+ \frac{-\Gamma P^2 (\Gamma + 1)}{1 - \Gamma^2 P^2} \end{aligned} \quad (6)$$

where, for normal incidence, $P = e^{-\gamma_2 d}$, $\Gamma = (\eta_2 - \eta_0)/(\eta_2 + \eta_0)$, and η_2 is the intrinsic wave impedance in the material.

$$\eta = \sqrt{\frac{j\omega\mu}{\sigma + j\omega\epsilon}} \quad (7)$$

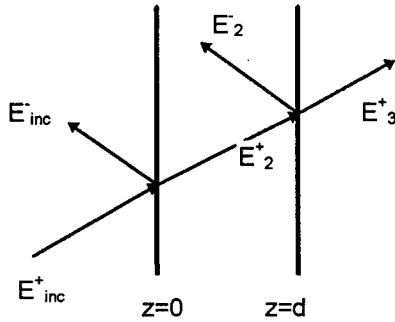


Figure 1 - Geometry of E-Field Incident on a Material

Due to energy conservation, this absorbed power must be balanced in equilibrium by the power lost through thermal convection, thermal conduction and thermal radiation, as described below.

3.1 Thermal Convection

Convection is the loss of heat to the material surrounding the thermal paper. Previous thermal imaging work [4, 5, 6, 7, 8, 9] has shown that convection is adequately described by Newton's law of cooling:

$$q = hA(T_s - T_a) \quad (8)$$

where q is the heat in Watts, h is the convection heat transfer coefficient in W/m^2K , A is the surface area in m^2 , T_s is the surface temperature in K, and T_a is the ambient temperature in K.

In general, this convective heat loss occurs on all six sides of a block of material. The edges of the thin resistive paper used for these tests, however, have a negligible surface area; thus, convective losses from the edges of the paper were ignored. Additionally, the thermal paper was mounted on two layers of artist's poster board (total thickness of 1.0 cm). The poster board, therefore, represents a thick, electromagnetic (EM) transparent, thermally insulative layer (low convection heat transfer coefficient)

between the paper and the radiating antenna. Thus, convection off the back side of the resistive paper was reduced to a negligible value. Convective heat loss was then essentially limited to the front side of the thermal paper.

The heat transfer coefficient, h , is dependent on environmental factors such as the movement of air around the thermal paper (the capacity of the surrounding air to remove heat from the thermal paper); however, in this work, since all thermal measurements were performed in an enclosed anechoic chamber, a fixed value of $h=0.93$ as determined by Metzger [4] was used. In future work it may be possible to measure certain environmental factors to determine an accurate value of h at the time of the thermal measurement, and then use this value to balance the thermal paper heating equation. It is anticipated that some form of real-time determination of h such as this will be required in order to transfer the thermal measurement technology from the (controlled) laboratory to a field measurement system.

A second problem with thermal convection is that, as the heat in the thermal paper is transferred to the surrounding air, the air decreases in density and, therefore, begins to rise. With the thermal paper oriented vertically, the rising, warmed, air tends to convect heat back into cooler areas of the thermal paper; thus, distorting the upper portion of the thermal image. This distortion can be clearly seen in Figure 2, which shows a close up thermal image of the radiating field from an array. The contour lines around the perimeter of the array in this image should be fairly rectangular, but as can be seen, the contour lines are deformed on the upper edge of the image. It may be possible to reduce or remove the effects of this distortion by data processing. In addition, a modification of the screen with cells or baffles

to reduce or eliminate air currents along the face of the screen may be possible. In this work, distortion from rising, warmed air was eliminated by orienting the thermal screen horizontally.

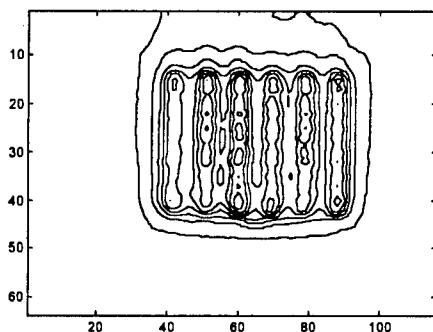


**Figure 2 - Close-up IR Image of an Array
Showing the Distortion from Rising Warmed Air**

3.2 Thermal Conduction

Conduction is the flow of heat within a material from hotter regions to cooler regions resulting in a "defocusing" of the thermal picture.

The effect of conduction can be seen in the comparison of thermal measurements to either hard-wired measurements or calculations as warmer than expected minimums (nulls) and cooler than expected maximums [10, 11]. Thermal conduction is described mathematically by Fourier's law of heat conduction:

$$q_x = -kA \frac{\partial T}{\partial x} \quad (9)$$

where q_x is the heat flow in the x direction in W, k is the thermal conductivity of the material in W/mK, A is the cross-sectional surface area in m^2 and T is the temperature in K.

Metzger [4] mentions that it may be possible to use thermal transport finite differencing methods to remove the thermal conduction distortions from the measurement data. Other work, however, has shown that, in general, for low electrical conductivity thermal paper such as used in the measurements in this research, the thermal conductivity, k , is also low [12]. For this work, therefore, the effects of thermal conduction were considered negligible.

3.3 Thermal Radiation

The Stefan-Boltzman law states that the total hemispherical emissive power of a blackbody is related to the temperature of the blackbody by[13]:

$$q = \sigma_b AT^4 \quad (10)$$

where q is in W, σ_b is the Stefan-Boltzman constant ($5.669E-8 \text{ W/m}^2\text{K}^4$), A is the surface area in m^2 , and T is the surface temperature in K.

The net power radiated by a gray body surrounded by several other gray bodies at different temperatures is extremely complicated and, therefore, difficult to accurately compute for a test set-up like that used for this work. A reasonably accurate first order approximation can be made, however, for a gray body with emissivity ϵ_r (the Teledeltos paper), radiating into a larger body (the anechoic chamber) maintained at a uniform ambient temperature, T_a . Using this approximation, the net radiated power is given by:

$$q = \epsilon_r \sigma_b A(T_s^4 - T_a^4) \quad (11)$$

3.4 Thermal Equilibrium

The final (thermal equilibrium) temperature of a sheet of Teledeltos paper in an EM field is then the result of a balance between the EM power absorbed by the paper and the power lost due to thermal convection and thermal radiation. Equations 8 and 11 therefore, can be combined as:

$$P_{abs} = \epsilon_r \sigma_b A(T_s^4 - T_a^4) + h(T_s - T_a) \quad (12)$$

where P_{abs} is given by equations 5 and 6.

Rather than attempting to find a closed form solution to the above equations for E_{inc} in terms of the thermal paper surface temperature, a three step process was performed. First, the above equations and constants were programmed into MATLAB and using the built in MAPLE symbolic solver, an array of surface temperature values were then calculated for an array of E_{inc} values. This data was

then fit (via a built in least squares type polynomial fit function) to a 2nd order polynomial in surface temperature.

Using this code, the best least-squares 2nd order polynomial fit for the Teledeltos paper was:

$$3.1 \times 10^{-5} (E_{inc}^2) + 3.5 \times 10^{-3} (E_{inc}) - 0.302 = \Delta T \quad (13)$$

where $\Delta T = T_s - T_a$ is the temperature rise in K above ambient.

Figure 3 shows a comparison of this polynomial (equation 13) to the computation of equation 12 (including equations 5 and 6). As shown in this figure, the fit is quite good with the exception of the lowest temperature values. The disagreement in the curves at the low temperature values is, however, partially offset by the thermal resolution limitations of the UCCS AGA 780 thermal camera (about 0.3 K in the setup used). If a thermal camera with a greater thermal sensitivity were used, then a different process of converting temperature rise to incident E-field values would be necessary. For example, equations 5, 6, and 12 could be programmed into an iterative minimization routine that uses the polynomial derived values (equation 13) as a starting point to provide a more accurate computation of the incident E-field from a measured temperature rise.

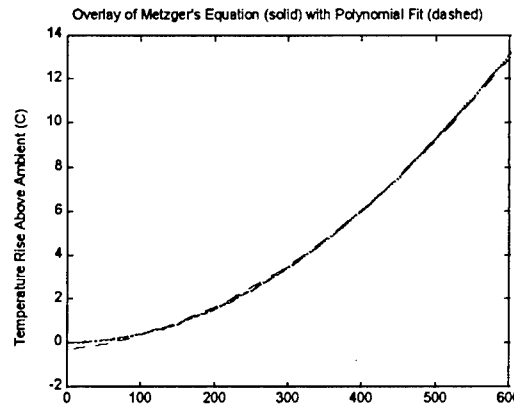


**Figure 3 - Temperature Rise in
Teledeltos Paper vs. E_{inc}**

4. Magnitude Results

An example of the comparison between the E-field determined from an IR thermogram measurement and the expected result based on NIST near-field measurements [14] is shown in Figure 4. This data is of the magnitude of the electric field 45.1 cm in front of a 36 element patch array antenna operating at 4 GHz. As shown in this figure, agreement between the curves is quite good down to about 18 to 20 dB below the peak, as expected from the thermal dynamic range of the AGA 780 camera, as discussed in more detail in [3].

5. Phase Measurements

Several algorithms have been proposed in recent years to retrieve phase information from phaseless (magnitude only) measurements. These algorithms can be grouped into minimization techniques, iterative Fourier techniques, and stochastic modeling techniques. A comparison of some of the practical algorithms and an overview of the mathematical basis of phase retrieval can be found in [15, 16].

Two closely related error-reduction techniques, known as the Gerchberg-Saxton [17] and the Input-Output [16] methods, require magnitude measurements in both the near field and in the far field; thus, they are not practical for the thermal imaging technique (which requires high power levels), and, therefore, were not further investigated in this study.

An iterative Fourier technique known as the Misell algorithm [18] requires two far-field measurements with the antenna beam "defocused." This technique, therefore, is also impractical for consideration with a thermal imaging technique.

PTP phase retrieval, however, was specifically developed for near-field measurements of antennas. A closely related phase retrieval algorithm has been successfully implemented by Yaccarino and Rahmat-Samii with a bi-polar planar hard-wired near-field measurement system using magnitude-only data measured over two planes separated by only 2.560λ [19]. Further modifications and improvements to this technique have been carried out by Rahmat-Samii, et al. [20] and Junkin et al. [21, 22, 23]. The uniqueness of the solution obtained from a plane-to-plane phase retrieval algorithm has been addressed by several authors, most notably Isernia, Leone, and Pierri [24, 25]. This study presents an application of PTP to the IR thermographic measurements of near-field antenna fields.

The PTP phase retrieval process is illustrated in Figure 5. First, various variables and constants are defined and an estimate of the magnitude and phase of the aperture field is made. This estimate is then propagated to measurement plane 1 by a Fourier transformation. A convergence error is then calculated as:

$$\xi = \frac{\sum |A| - M|^2}{\sum M^2}$$

where M is the measured magnitude data and |A| is the calculated magnitude data at each pixel location in the plane of interest. The calculated magnitude is then replaced with the measured magnitude with

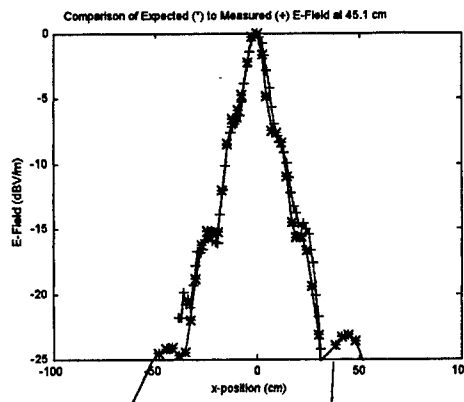


Figure 4 - Comparison of IR Measured E-Field to Expected Levels

the calculated phase retained. These complex data are then propagated by Fourier techniques back to the original aperture plane. All data outside the antenna aperture are then truncated, and the truncated data are propagated to the second measurement plane. Again the convergence error is calculated and the calculated magnitude data replaced with the measured magnitude at plane 2 with the calculated phase retained, and these data are then propagated back to the aperture plane. At this point in the process, the change in the convergence error from the previous iteration is checked, and if the change in convergence error is less than a set tolerance, the iterations are stopped. If, however, the change in convergence error is still sufficiently large, the iteration is repeated, starting with a truncation of data outside the antenna aperture.

Junkin has recently suggested [22] that a "phase change acceleration procedure" be imposed between iterations. This procedure reduces the possibility of PTP algorithm stagnation due to a local minimum, which is an increasing problem with decreasing scan plane separation. In our work, however, the scan plane separation used was over 1.5 wavelengths, or about $0.066 D^2/\lambda$ (the scan plane separation used by Junkin was $0.0033 D^2/\lambda$); thus the utility of incorporating the phase change acceleration procedure may be minimal. In addition, Junkin and Trueba [23] have also suggested a center-of-gravity type algorithm to help in the alignment of the two planes of measurements, which becomes more critical with increasing antenna operating frequency.

The PTP algorithm discussed above is based on planar near-field to far-field transformations which are the result of the pioneering work of Kerns and his development of the plane-wave scattering matrix theory [26]. The planar near-field measurement was the first of the near-field techniques to be developed, verified, and implemented as an operational method of obtaining antenna parameters. An excellent review of the history of near-field antenna measurements is given by Yaghjian in [27].

The fields exterior to a radiating antenna are typically divided into three regions. The specific transitions from one region to the next are not sharply defined, and vary based on the antenna type and the acceptable uncertainty in the use of the data. Very close to the antenna, that is, within about one wavelength, is the region called the reactive near-field or sometimes the evanescent region. In this region, the imaginary part of the complex Poynting vector, which is typically proportional to the inverse of the radial distance to the power of 3 or greater, is not negligible. It is this region that contributes to the reactive part of the antenna input impedance, and is, therefore, why this region is called the reactive near field. Beyond about one wavelength and out to, typically, a radial distance of about $2 D^2/\lambda$ is a region called the radiating near field, or sometimes the Fresnel

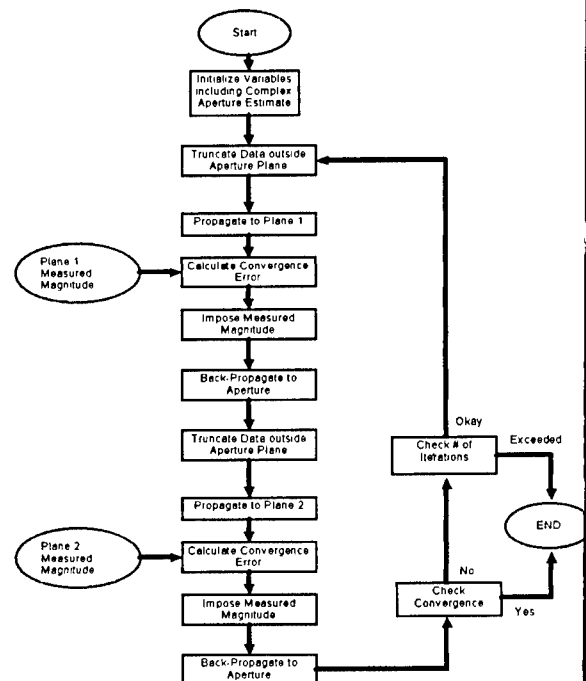


Figure 5 - Plane-to-Plane Phase Retrieval Process

region. In this region, the electric and magnetic fields are propagating, but do not yet exhibit the e^{ikr}/r dependence characteristic of the far field. This region is where the near-field measurements in this study were made. Finally, the far-field region, sometimes called the Fraunhofer region, is that volume that extends from a radial distance of about $2 D^2/\lambda$ from the antenna out to infinity.

The basic idea of near-field to far-field transformations is that: (1) the far-field region is that region where the radiating field phase front is locally very nearly planar, (2) energy leaving an antenna always propagates in a straight line in a uniform medium, (3) near-field measurements of the magnitude and phase determine the phase front of the radiating energy and this can be transformed into an angular spectrum of plane waves, (4) this angular spectrum of plane waves is *equivalent* to the antenna far-field pattern [28].

Using the concept of superposition, the field at a distance $z = d_1$ in front of a radiating antenna is a combination of a series of plane waves (analogous to the idea that a time domain waveform is the superposition of a combination of frequency spectral signals). Mathematically, this can be written as [29]:

$$B_o(x, y, z = d_1) = \int_{-\infty}^{\infty} \int_{-\infty}^{\infty} \bar{T}(k_x, k_y) \cdot \bar{S}(k_x, k_y) e^{i\gamma d_1} e^{i(k_x x + k_y y)} dk_x dk_y$$

where B_o is the output of a probe at position (x, y, z) , $T(k)$ is the plane-wave spectrum (which is equivalent to the far-field pattern of the antenna), $S(k)$ is the vector receive pattern of the probe antenna (set to unity for the thermal paper), and $\gamma = [(2\pi/\lambda)^2 - (k_x^2 + k_y^2)]^{0.5}$ is the wavenumber in the z direction (k_z is often used in the literature instead of γ). A slight re-arrangement of the equation above with a replacement of $D(k_x, k_y) = T(k_x, k_y) \cdot S(k_x, k_y)$ gives:

$$B_o(x, y, z = d_1) = \int_{-\infty}^{\infty} \int_{-\infty}^{\infty} e^{i\gamma d_1} D(k_x, k_y) e^{i(k_x x + k_y y)} dk_x dk_y$$

This integral equation is the same as an inverse Fourier transform with the added multiplication of an $e^{i\gamma d_1}$ term. The Fourier transform pair to this equation is:

$$D(k_x, k_y) = \frac{e^{-i\gamma d_1}}{4\pi^2 A} \int_{-\infty}^{\infty} \int_{-\infty}^{\infty} B_o(x, y, z = d_1) e^{-i(k_x x + k_y y)} dx dy$$

where A is a measurement insertion loss correction constant used to determine the absolute gain of the antenna.

These equations provide the means for transforming from phase front (near-field) measurements to the angular spectrum (which is an equivalent representation of the antenna far field) and back. Since these equations are integral equations, they imply that measurements must be made over a continuous (nondiscrete) surface. It turns out, however, that since the angular spectrum is band-limited, near-field data sampling can be performed at intervals of $\lambda/2$ in x and y and the discrete Fourier transform (DFT) used with no loss of generality [26, 30].

Since a discrete Fourier transform can be used, standard fast Fourier transform (FFT) routines can be used to transform complex near-field data to the far field, or an inverse FFT (IFFT) used

to transform from the far field in to the near field. Planar near-field, far-field transformations using a modern, complex, matrix-oriented language are, therefore, quite simple to implement and reasonably efficient (a complete PTP loop, which includes four FFT-IFFT operations as well as convergence error calculations and magnitude replacements for a non-power-of-2 57x57 element data matrix on a 486DX2-100 processor is performed in about 4 seconds).

A 36 element patch array antenna was used as a test antenna for the data measurements. The thermal paper, with its backing thermal insulator (poster board), is centered directly below the array antenna, oriented horizontally, and sitting on a wooden perimeter frame. At the bottom of the frame is the thermal imaging camera.

The two measurement planes selected for the 36 element patch array antenna were at a distance of 32.4 cm and 45.0 cm. Since the array operates at a frequency of 4 GHz, these distances were approximately 4.3λ and 6λ from the aperture. The exact distances were arbitrary, with the goals of being well outside the reactive near-field and having a plane separation of greater than one wavelength, but not so far apart as to result in a large difference in peak thermal paper temperatures.

6. Phase Results

The phase was simulated and measured (in a previous effort) at RL.

6.1 Simulations

A set of simulations was performed before processing the thermally measured data. First, the array antenna was measured by NIST/Boulder on their near-field antenna test range. The near-field to far-field FFT processing method discussed above was then used to compute the magnitude and phase of the fields of the array at the two measurement planes selected for the IR thermal measurements (32.4 cm and 45.0 cm). The magnitudes of these data were then used as an initial simulation of the capabilities of the PTP algorithm.

Figure 7 is an overlay of the far-field pattern of the array as determined by the PTP algorithm (dashed *) and from the original NIST complex data (solid +). As the figure illustrates, the agreement between the PTP determined far-field pattern and the real far-field pattern of the array is excellent.

The PTP algorithm was then rerun with the NIST magnitude data truncated at amplitudes below 20 dB down from the peak as an estimate of the dynamic range of the thermal camera at UCCS. The result of this simulation is shown in Figure 7. As illustrated in this figure, the PTP algorithm was able to only reconstruct the antenna's main lobe and provide an indication of the location of the first two side-lobes (but not the correct amplitudes for the side-lobes).

Obviously, the results from the simulations of the expected dynamic range from the UCCS thermal camera are only marginally useful; however, modern 12-bit digitizing thermal cameras should have at least a 30 dB RF dynamic range. The results of the PTP algorithm applied to data with a 30 dB dynamic range are substantially better than those for data with only a 20 dB dynamic range, as shown in the simulation results of Figure 8. As shown in these simulations, data from thermograms collected with a camera having a 30 dB RF dynamic range should be adequate for the PTP algorithm to faithfully reproduce the far-field pattern of antennas such as the array tested in this paper. Future work will show the validity of this simulation, and additional work will focus on investigating the utility of the algorithm for other antennas, including some with lower side-lobes.

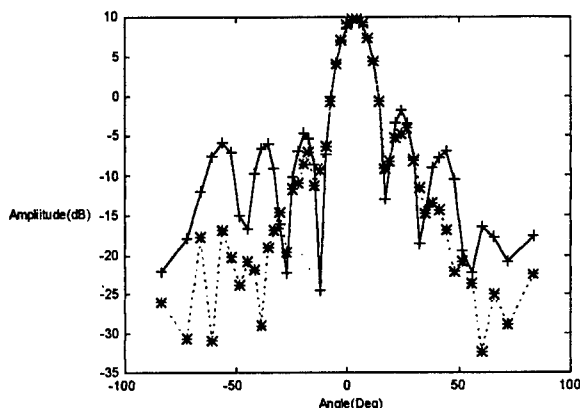


Figure 7 - PTP Results Using NIST Magnitude Data Truncated to 20 dB Dynamic Range.

6.2 Experiments

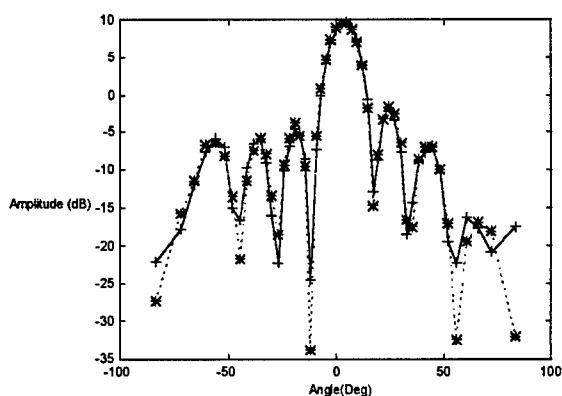


Figure 6 - PTP Generated Far-Field from NIST Magnitude Data.

Actual IR thermograms were taken over these same measurement planes (in a previous effort). Direct comparison of the field magnitudes from the thermograms to the expected values based on the NIST/Boulder measured data confirmed that the thermal measurements from the thermal camera at UCCS resulted in about 18-20 dB of usable dynamic range. The result of the PTP algorithm on these data are shown in Figure 10. The result of processing these thermograms is very encouraging as it is approximately the same as the 20 dB dynamic range simulation.

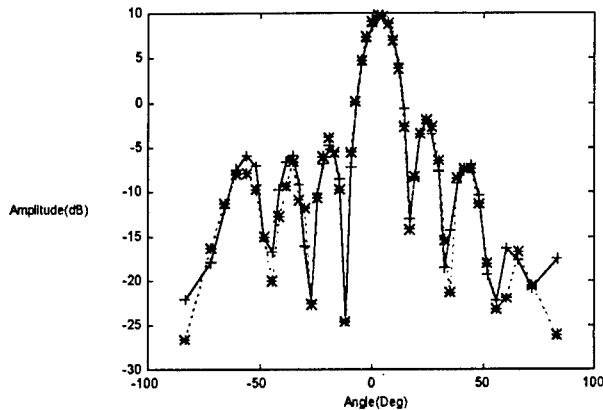


Figure 8 - PTP Results from Simulated 30 dB Dynamic Range Data.

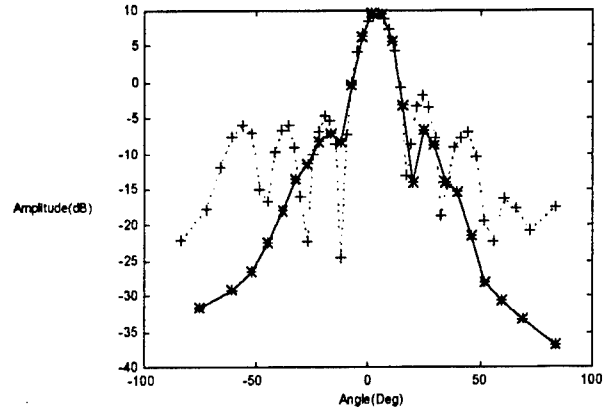


Figure 9 - PTP Results for Thermograms from the Camera at UCCS.

Another useful measure of the success of the PTP algorithm is a plot of the convergence error metric. Figure 10 shows an overlay of the convergence error metric of the PTP algorithm for the four cases discussed above (full range simulation, 30 dB dynamic range simulation, 20 dB dynamic range simulation, and UCCS thermogram data). Several observations can be made from this figure. First, the convergence metric settles to a stable value for each case in less than 40 iterations, which represents only 2-3 minutes of processing time on a 486DX2-100 processor for these matrix sizes. Second, the convergence metric stays stable for many iterations (all runs were taken out for 200 iterations and all remained stable). Third, it appears that the value of the convergence metric is a usable measure of how well the algorithm was able to reconstruct the antenna far-field pattern. Since in actual practice, the antenna pattern will be unknown to the user, the convergence metric may be very useful in determining the reliability of the PTP algorithm results.

7. Conclusions

Despite thermal errors caused by conductive heating within the thermal paper and convective heating of the air surrounding the thermal paper, proper selection of screen conductivity and test set-up have been shown to produce measurements of the magnitude of antenna near fields over an approximate 20 dB range with accuracy to within ± 1 dB as compared with standard near field probe techniques. The main advantage of this technique is that the fields over a large planar area can be determined very quickly and with high spatial resolution. Work continues to increase

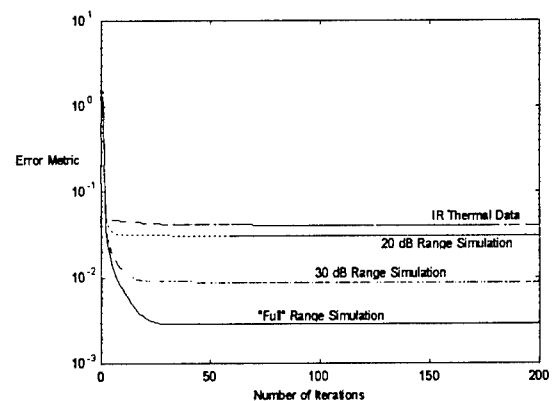


Figure 10- Overlay of Convergence Error Metrics for Various PTP Runs.

the accuracy and dynamic range of these measurements[3].

The PTP iteration algorithm appears very well suited to the reconstruction of the holographic far-field pattern from thermographic measurements on 2 near-field planes.

8. Future Work

Additional research in the PTP technique should be pursued. First, a camera with greater dynamic range should be used to verify the results of the 30 dB dynamic range simulation shown in this study. Furthermore, several antenna styles with different side-lobe amplitudes should be measured in order to build confidence in this technique.

The microwave holographic interference technique also should be simulated and tested in a manner similar to the tests reported here for the PTP technique. This phaseless measurement work is being done in conjunction with NIST/Boulder.

9. Publications

The papers published on this project during the AFOSR Summer Research Program are listed in the Appendix.

Acknowledgments

The author would like to acknowledge the support of the AFOSR Summer Research Program on this IR project and the help of Michael Seifert at RL and Carl Stubenrauch at NIST/Boulder.

REFERENCES

-
- [1] J.Norgard, "Infrared/Microwave Correlation Study," *Optical Engineering*, 33(1), pp. 86-94, January 1994.
 - [2] J.Will, J. Norgard, C. Stubenrauch, K. MacReynolds, M.Seifert, and R. Sega, "Phase Measurements of Electromagnetic Fields Using Infrared Imaging Techniques and Microwave Holography," *Proceedings of the SPIE Aerosense Conference*, Conference 2766, April 1996.
 - [3] J. E. Will, "Antenna Pattern Measurements using Infrared Imaging and Microwave Holography," Ph.D. Thesis for the University of Colorado, Colorado Springs, 1996.
 - [4] D.W. Metzger, "Quantification of the Thermographic Mapping of Microwave Fields", Ph.D. Thesis for the University of Colorado, Colorado Springs, 1991.
 - [5] R.M. Sega and J.D. Norgard, "Infrared Measurements of Scattering and Electromagnetic Penetration Through Apertures", *IEEE Transactions on Nuclear Science*, Vol. NS-33, No. 6, pp. 1658-1663, Dec. 1986.
 - [6] R.M. Sega and J.D. Norgard, "Expansion of an Infrared Detection Technique using Conductive Mesh in Microwave Shielding Applications", *SPIE Vol. 819 Infrared Technology XII*, pp. 213-219, 1987.
 - [7] J.D. Norgard and R.M. Sega, "Microwave Fields Determined from Thermal Patterns", *SPIE Vol. 780 Thermosense IX*, pp. 156-163, 1987.

-
- [8] V.M. Martin, C.V. Stewart, and R.W. Burton, "An Optimized Conductive Coating for Thermographic Measurement of Microwave Induced Surface Currents", *Proceedings: IEEE Region 5 Conference and Exposition*, pp. 182-185, May 1982.
 - [9] G.D. Wetlaufer, "Optimization of Thin-Screen Material Used in Infrared Detection of Microwave Induced Surface Currents at 2-3 GHz", MSEE Thesis, University of Colorado, Colorado Springs, 1985.
 - [10] J.D. Norgard, D.C. Fromme, and R.M. Sega, "Correlation of Infrared Measurement Results of Coupled Fields in Long Cylinders with a Dual Series Solution", *IEEE Transactions on Nuclear Science*, Vol. 37, No. 6, pp. 2138-2143, Dec. 1990.
 - [11] W.C. Diss, "Techniques for Measuring Microwave Interference Using Infrared Detection and Computer Aided Analysis", MSEE Thesis, University of Colorado, Colorado Springs, 1984.
 - [12] R.M. Sega, V.M. Martin, D.B. Warmuth, and R.W. Burton, "Infrared Application to the Detection of Induced Surface Currents", *SPIE*, Vol. 304, Modern Utilization of Infrared Technology VII, pp. 84-91, 1981.
 - [13] R. Segal and J. Howel, "Thermal Radiation Heat Transfer", McGraw-Hill, 1972.
 - [14] Measured near-field data provided by C. Stubenrauch and K. MacReynolds of NIST, Boulder, CO.
 - [15] L.S. Taylor, "The Phase Retrieval Problem," *IEEE Transactions on Antennas and Propagation*, Vol 29, pp. 386-391, March 1981.
 - [16] J.R. Fienup, *Applied Optics*, Vol. 21, pp. 2758-2769, August 1982.
 - [17] R.W. Gerchberg and W.O. Saxton, *Optik*, Vol. 35, pp. 237-246, 1972.
 - [18] D.L. Misell, "A Method for the Solution of the Phase Problem in Electron Microscopy", *Journal of Physics D, Applied Physics*, Vol. 6, pp. L6-L9, 1973.
 - [19] R.G. Yaccarino and Y. Rahmat-Samii, "Phaseless Near-Field Measurements Using the UCLA Bi-Polar Planar Near-Field Measurement System," *16th Annual Antenna Measurement Techniques Association Symposium*, pp. 255-260, October 1994.
 - [20] R.G. Yaccarino and Y. Rahmat-Samii, "Phaseless Bi-polar Near-field Measurements: A Squared Amplitude Interpolation/Iterative Fourier Algorithm," *1995 Antenna Measurements Techniques Association 17th Meeting and Symposium*, Williamsburg, pp. 195-200, Nov 13-17, 1995.
 - [21] C.A.E. Rizzo, G. Junkin, and A.P. Anderson, "Near-field/Far-field Phase Retrieval Measurements of a Prototype of the AMSU-B Space-Borne Radiometer Antenna at 94 GHz," *1995 Antenna Measurements Techniques Association 17th Meeting and Symposium*, Williamsburg, pp. 385-389, Nov 13-17, 1995.
 - [22] G. Junkin, A.P. Anderson, C.A.E. Rizzo, W.J. Hall, C.J. Prior, and C. Parini, "Near-field/Far-field Phase Retrieval Measurement of a Prototype of the Microwave Sounding Unit Antenna AMSU-B at 94 GHz," *ESTEC Conference on Millimeter Wave Technology and Applications*, Noordwijk, Netherlands, 1995.
 - [23] G. Trueba, G. Junkin, "A Numerical Beam Alignment Procedure for Planar Near-field Phase Retrieval," *Electronics Letters*, 1995.
 - [24] T. Isernia, G. Leone, R. Pierri, "Phaseless Near-field Techniques: Uniqueness Conditions and Attainment of the Solution," *Journal of Electromagnetic Waves and Applications*, Vol. 8, No. 7, pp. 889-908, 1994.
 - [25] R. Barakat and G. Newsam, "Algorithms for Reconstruction of Partially Known, Band-limited Fourier-transform Pairs from Noisy Data," *Journal of the Optical Society of America*, Vol. 2, No. 11, pp. 2027-2039, 1985.
 - [26] D.M. Kerns, "Plane-wave Scattering-matrix Theory of Antennas and Antenna-antenna Interactions", *National Bureau of Standards Monograph 162*, June 1981.
 - [27] A.D. Yaghjian, "An Overview of Near-field Antenna Measurements," *IEEE Transactions on Antennas and Propagation*, Vol. AP-34, No. 1, pp. 30-45, Jan. 1986.
 - [28] D. Slater, "Near-Field Antenna Measurements", *Artech House*, 1991.
 - [29] J.J. Lee, E.M. Ferren, D.P. Woollen, and K.M. Lee, "Near-field Probe Used as a Diagnostic Tool to Locate Defective Elements in an Array Antenna", *IEEE Transactions on Antennas and Propagation*, Vol. 36, No. 6, pp. 884-889, June 1988.

-
- [30] A.D. Yaghjian, "Efficient Computation of Antenna Coupling and Fields Within the Near-field Region", *IEEE Transactions on Antennas and Propagation*, Vol. AP-30, No. 1, Jan 1982.

APPENDIX

A. *Papers Presented:*

1. Norgard (Invited Paper)
"Electromagnetic Complex Magnitude & Phase from Infrared Thermograms"
AeroSpace Conference, Snowmass, CO, February 1997.
2. Will, Norgard, Sega, Stubenrauch, MacReynolds, Seifert
"Phaseless Measurements of Antenna Near Fields from Infrared Images Using
Holographic Phase Retrieval Techniques"
SPIE/Thermosense XVII International Conference, Orlando, FL, April, 1997.
(2nd Place Award - Best Paper Prizes).
3. Norgard, Will, Seifert, Pesta, Cleary
"Determining Antenna Near-Field Magnitude Data Using Infrared
Thermographic Measurements"
GOMACS Conference, Las Vegas, NV, May, 1997.
4. Will, Norgard, Seifert, Pesta, Cleary
"Near-Field Phase Reconstruction Using Plane-to-Plane Iterative Fourier
Processing and Infrared Thermograms of Electromagnetic Fields"
GOMACS Conference, Las Vegas, NV, May, 1997.
5. Norgard, Will, Seifert, Pesta, Cleary

"Near-Field Phase Reconstruction Using Infrared Thermograms: A Comparison of Plane-to-Plane Iterative Fourier Processing Techniques and Microwave Holography"

Dual Use and Applications Conference, Syracuse, NY, June, 1997.

6. Seifert, Norgard
"Code Validation using Infrared Imaging Techniques"
AAE Symposium, Urbana-Champaign, IL (U of Illinois), September, 1997.

B. *Seminars Presented*

1. "Infrared Images of Electromagnetic Fields"
US Air Force Academy
Department of Electrical Engineering
Colorado Springs, CO
June 1997

C. *Journal Articles Published:*

1. Norgard, Will, Stubenrauch, MacReynolds, Seifert, Sega
"Infrared (IR) Imaging Techniques for the Measurement of Complex Near-Field Antenna Patterns"
EuroTherm Quantitative Infrared Measurement Journal, January 1997